

Doctoral Thesis

**Nonlinear Modeling of Piezoelectric Transducers
under High-power Operation**

(ハイパワー駆動時における圧電振動子の非線形モデルに関する研究)

LIU Yaoyang

劉耀陽

Abstract

Piezoelectric materials, especially hard-type piezoelectrics are required in high power and high frequency applications, such as ultrasonic motors, transformers, resonators, and so on. Owing to the concerns on environmental protection and human health, lead-free materials have gain great attention; niobates are one of the most promising families owing to the high Curie temperature and high piezoelectric performance.

For high power applications, the largest limitation of potassium sodium niobate is the low quality factor. In previous studies, CuO was used as a dopant to enhance the quality factor. In this dissertation, on the one hand, aiming at the quality factor, we proposed a method and succeeded in enhancing the quality factor again. On the other hand, in order to estimate high power performance, we studied the nonlinear behavior at high power operation first. The main results are as follows.

CuO-(K_{0.48}Na_{0.52})NbO₃ (CuO-KNN) ceramics were prepared via hydrothermal method and solid state sintering. Comparing with pure (K_{0.48}Na_{0.52})NbO₃ (KNN) ceramics, the quality factor was greatly enhanced. The effect of a post-annealing process was studied. In the experiments, it was noticed that although the crystal phase of the CuO-KNN ceramics was not changed by the post-annealing process, the intense transition resulted in a significant change in the quality factor, corresponding to the rearrangement of oxygen vacancies in the domains. A post-annealing process in argon was utilized and proved to be efficient in enhancing the quality factor. On the opposite, a post-annealing process in oxygen can decrease the quality factor.

In high power operation, nonlinear behavior has significant influence; despite of which, the present models cannot describe the nonlinear phenomena very well. Before the estimation of high power performance of CuO-KNN transducers, the nonlinear behavior of Pb(Zr,Ti)O₃ (PZT) transducers was investigated. In burst mode results, both the decay rate and resonant frequency are velocity dependent; indicating the existence of nonlinearity. Admittance curves at high voltages corroborated the presence of nonlinearity in PZT transducers. For both hard-type and soft-type PZT the symmetry of admittance curves was broken. Especially in the admittance curves of the hard-type transducer, a jumping phenomenon and an admittance hysteresis between different sweep directions appeared. A nonlinear model was proposed and utilized to fit the admittance curves. This model proves to be effective in describing the admittance curves at high power and determining the nonlinear coefficients. The mechanical nonlinearity is the main source instead of dielectric and piezoelectric nonlinearities in the admittance curves. The model is

also feasible in estimating the high power characteristics of CuO-KNN transducers. Compared with the PZT transducers, lead-free CuO-KNN transducers are less dependent on high-velocity condition. Along with high quality factor, CuO-KNN is a promising material for high-power applications.

To illustrate the nonlinear phenomena in piezoelectrics, simulations were carried out. The procedures of estimating nonlinearity were presented first; using the proposed nonlinear model, the simulation of current jumping in frequency response and voltage response were realized. ξ , η , and V_0 can affect the jumping phenomena separately and together. For easier estimation of the nonlinear level, a simplified method was proposed. The nonlinear coefficients can be determined via simple calculation from the typical points in low voltage and high voltage admittance curves instead of the curve fitting. Owing to the jumping of admittance curves at high power operation, the definition of quality factor was discussed; based on the nonlinear level it is also possible to determine Q_m at high power condition. The comparison of nonlinearities between the present study and previous literatures; simulations of polarization-field hysteresis loop and strain-field loop were realized. The results supported our discussion that the essential of admittance hysteresis was different from that of polarization-field hysteresis loops.

Keywords: lead-free piezoelectric, hardening, nonlinear phenomena, nonlinear modeling, high power characteristics

Contents

1	Introduction	3
1.1	Piezoelectrics	4
1.1.1	Principle and history	4
1.1.2	Piezoelectric constitutive equations	5
1.1.3	Applications	7
1.1.4	Lead-containing piezoelectrics	8
1.1.5	Lead-free piezoelectrics	8
1.2	Niobates	9
1.2.1	Potassium niobate and sodium niobate	9
1.2.2	Potassium sodium niobate and its derivatives	11
1.3	Synthesis Methods	14
1.3.1	Solid-state reaction method	14
1.3.2	Hydrothermal method: history, merits and shortcomings	14
1.3.3	Hydrothermal reactions of niobates	15
1.4	High Power Piezoelectric Properties	16
1.4.1	Conventional characteristics	16
1.4.2	Drive methods	17
1.4.3	High-power applications	18
1.4.4	High power characteristics	19
1.4.5	Constant voltage and constant current method	20
1.4.6	Burst mode method	21
1.5	Thesis Motivation	22
1.6	Thesis Structure	23
2	Experimental and Analysis Procedures	25
2.1	Synthesis of KN and NN Powders	26
2.2	Synthesis of KNN and CuO-KNN Ceramics	27
2.2.1	Synthesis of KNN ceramics	28
2.2.2	Synthesis of CuO-KNN ceramics	31

2.3	Physical Characteristics and Ceramic Processing	31
2.3.1	X-ray diffraction	31
2.3.2	Density test	33
2.3.3	Ceramics processing	33
2.3.4	Plate and bar transducers	36
2.4	Determination of Electrical Properties	37
2.4.1	Permittivity	37
2.4.2	Admittance curve	37
2.4.3	Equivalent circuit	40
2.4.4	Resonant-antiresonant method	42
2.5	Burst Mode Method	44
3	Properties and Hardening of CuO-KNN	49
3.1	Background	50
3.2	KNN Powders and Ceramics	52
3.3	CuO-KNN Powder and Ceramics	54
3.4	Post-annealing in Air	57
3.5	Post-annealing in Argon	61
3.6	Brief Summary	66
4	Nonlinear Behavior in PZT Transducers	67
4.1	Background	68
4.2	Admittance Curve under High Voltage	70
4.3	Burst Mode Measurement and Results	74
4.4	Analysis of Burst Mode Results	76
4.5	Modeling of Nonlinearity in Piezoelectrics	79
4.6	Fitting Results and Nonlinear Coefficients	82
4.7	Discussion on the conclusions	85
4.8	Derivation of Nonlinear coefficients	90
4.8.1	Derivation of q	90
4.8.2	Derivation of decay rate	92
4.8.3	Derivation of p	94
4.9	Brief Summary	95
5	Nonlinear Behavior in CuO-KNN Transducers	97
5.1	Background	98
5.2	Admittance Curve under High Voltage	99
5.3	Fitting Results and Nonlinear Coefficients	103
5.4	Predictions and Confirmation	107
5.5	Burst Mode Measurement and Results	109
5.5.1	Burst mode measurements	110

5.5.2	Results determined from velocity-time curve	110
5.5.3	Results determined from current-time curve	111
5.6	Further Analysis of Burst Mode Results	112
5.7	Brief Summary	115
6	Simulation	117
6.1	Background	118
6.2	<i>G-B</i> circle	120
6.3	Jumping Current-Frequency Curve	121
6.4	Jumping Current-Voltage Curve	124
6.5	Methods of Estimating Nonlinear Level	125
6.6	High Power Characteristics	132
6.6.1	Quality factor	132
6.6.2	Energy density	135
6.7	Simulation of Hysteresis Loops	136
6.7.1	Polarization-field loop	136
6.7.2	Strain-field loop	139
6.8	Brief Summary	140
7	Conclusions and Prospects	141
7.1	Conclusions	142
7.2	Prospects	144

- Symbols and Units

Symbol	Physical Quantity	SI Unit (Other units)
A	Force factor	N/V
B	Susceptance	S (μ S, mS)
C	Capacitance	F (pF, nF)
C_0	Linear Capacitance	F (pF, nF)
C_d	Damped Capacitance	F (pF, nF)
c_{ij}	Stiffness	Nm ⁻² (GPa)
D	Electrical Displacement	Cm ⁻² (μ Cm ⁻²)
d_{ij}	Piezoelectric d Coefficient	m/V, C/N (pm/V, pC/N)
E	Electrical Field	V/m (kV/cm)
E_r	Real Part of Young's Modulus	Nm ⁻²
E_i	Imaginary Part of Young's Modulus	Nm ⁻²
e_{ij}	Piezoelectric e Coefficient	Cm ⁻²
f_a	Anti-resonant Frequency	Hz (kHz)
f_r	Resonant Frequency	Hz (kHz)
G	Conductance	S (μ S, mS)
g_{ij}	Piezoelectric g Coefficient	Vm/N
h	Height	m (mm)
h_{ij}	Piezoelectric h Coefficient	Cm ⁻²
i	Current	A (mA)
i_d	Damped Current	A (mA)
i_0	Motional Current	A (mA)
j	Imaginary Unit	1
K	Spring Constant	N/m
k	Wavenumber	m ⁻¹
k_{ij}	Coupling Factor	1
L	Equivalent Inductance	H (mH)
l	Length	m (mm)
M	Mass	kg (g)
m	Equivalent Mass	kg (g)
N	Frequency Constant	m·Hz
P	Polarization	Cm ⁻² (μ Cm ⁻²)
p	Nonlinear Coefficient	s/m
Q_m	Quality Factor	1
q	Nonlinear Coefficient	s/m
R	Resistance	Ω
r	Equivalent Resistance	Ω
S	Strain	1

Symbol	Physical Quantity	SI Unit (Other units)
s_{ij}	Compliance	m^2/N (pm^2/N)
T	Stress	Nm^{-2} (MPa)
t	Time	s (ms)
$\tan \delta$	Loss	1
u	Displacement	m
V	Voltage	V
v	Velocity	m/s
w	Width	m (mm)
X	Reactance	H (mH)
Y	Admittance	S (μS , mS)
Z	Impedance	Ω
Z_e	Electrical Impedance	Ω
Z_m	Mechanical Impedance	Ω
β	Decay Rate	s^{-1}
β_0	Linear Decay Rate	s^{-1}
Γ	Power Density	Jm^{-3}
δ	Phase Delay	rad
Δ	Discriminant of Cubic Polymomial	1
ϵ_0	Vacuum Permittivity	F/m
ϵ_r	Relative Permittivity	F/m
ϵ' (ϵ'')	Real (Imaginary) Complex Permittivity	F/m
ζ	Damping Ratio	1
η	Nonlinear Coefficient	ΩA^{-2}
θ	Phase Delay	rad
λ	Wavelength	m
ξ	Nonlinear Coefficient	ΩA^{-2}
ρ	Density	kgm^{-3}
σ^E	Poisson's Ratio	1
ϕ	Phase Delay	rad
φ	Phase Delay	rad
ω	Angular Frequency	rad/s
ω_r	Resonant Angular Frequency	rad/s
ω_a	Anti-resonant Angular Frequency	rad/s

CHAPTER 1

Introduction

1.1 Piezoelectrics

1.1.1 Principle and history

Piezoelectricity, or piezoelectric effect is an effect that electric charges of certain materials accumulate as a consequence of applying mechanical stress. Piezoelectric materials have two properties that are defined as direct piezoelectric effect and converse piezoelectric effect, respectively. On the basis of pyroelectricity, P. Curie and J. Curie demonstrated the direct piezoelectric effect in quartz in 1880 [1]. In 1881, G. Lippmann theoretically deduced the converse piezoelectric effect from fundamental thermodynamic principles [2]; which was experimentally validated by the Curie brothers in the same year [3]. The direct and converse piezoelectric effect can be illustrated by Fig. 1.1. In Fig. 1.1(a), a piezoelectric specimen can generate a voltage when it is deformed (or, driven by stress); while applying voltage also enables the deformation of the disk, as indicated by Fig. 1.1(b).

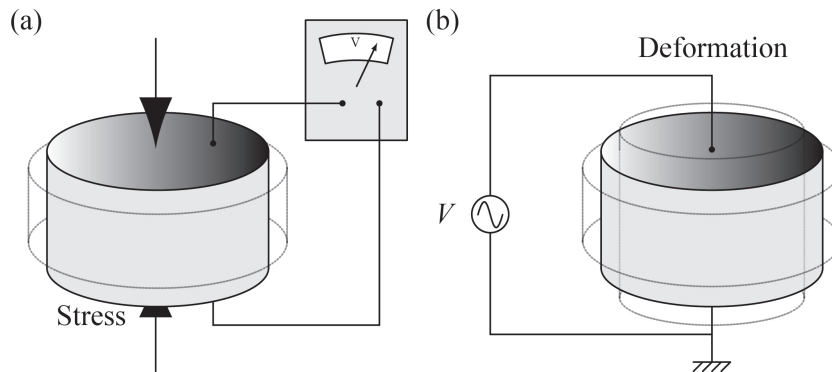


Figure 1.1: Schematic diagram of (a) direct and (b) converse piezoelectric effect; change of the shape in piezoelectric disks is greatly exaggerated.

The essence of the piezoelectric effect is the electric dipole moments in various materials. Twenty one classes of thirty two point groups are non-centrosymmetric; except for the cubic class 432, twenty of them exhibit the piezoelectric effect [4]. Ten of these twenty classes are polar crystal classes that exhibit a spontaneous polarization even under zero mechanical stress, named by pyroelectrics (with the ability to generate a temporary electrical field when they are heated or cooled) [5]. If the spontaneous polarizations can be reversed by a sufficient high electrical field, the material is called ferroelectric [5]. The relationship between the dielectrics, piezoelectrics, pyroelectrics, and ferroelectrics is illustrated in Fig. 1.2.

Beginning with the fabrication and phenomenological theory study of the first piezo-ceramics BaTiO_3 in 1940s [6], various piezoelectric materials were synthesized. Among them, lead zirconate titanate ($\text{Pb}(\text{Zr}_x\text{Ti}_{1-x})\text{O}_3$, $0 \leq x \leq 1$, PZT)

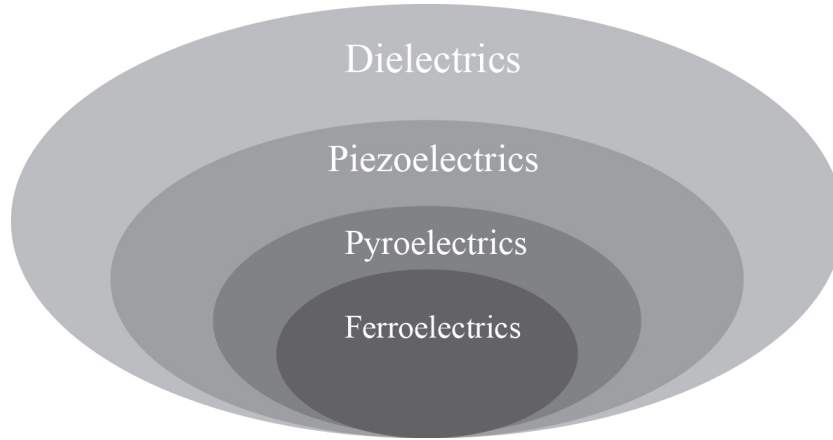


Figure 1.2: Relationship between the dielectrics, piezoelectrics, pyroelectrics and ferroelectrics.

system has played an important role until now [7]. On the basis of PZT system, various ternary and quaternary system ceramics have emerged [8]. Nowadays, they are widely used due to their excellent performance, simple technology, and most important, low cost. One important advantage of such multicomponent systems is the adjustable piezoelectric properties; e.g., in PZT system, different component results in large performance variation.

1.1.2 Piezoelectric constitutive equations

Define (1, 2, 3) as three axes corresponding to (x, y, z) in the Cartesian coordinates, the components of stress T and strain S in the Cartesian, cylindrical, and polar coordinates are shown in Table 1.1.

Table 1.1: Components of T and S in Cartesian, cylindrical, and polar coordinates.

	Normal Stress			Shear Stress		
Cartesian coordinates	T_1	T_2	T_3	T_4	T_5	T_6
Cartesian coordinates	T_{xx}	T_{yy}	T_{zz}	T_{yz}	T_{zx}	T_{xy}
Cylindrical coordinates	T_{rr}	$T_{\theta\theta}$	T_{zz}	$T_{\theta z}$	T_{zr}	$T_{r\theta}$
Polar coordinates	T_{rr}	$T_{\theta\theta}$	$T_{\phi\phi}$	$T_{\theta\phi}$	$T_{\phi r}$	$T_{r\theta}$
	Normal Strain			Shear Strain		
Cartesian coordinates	S_1	S_2	S_3	S_4	S_5	S_6
Cartesian coordinates	S_{xx}	S_{yy}	S_{zz}	S_{yz}	S_{zx}	S_{xy}
Cylindrical coordinates	S_{rr}	$S_{\theta\theta}$	S_{zz}	$S_{\theta z}$	S_{zr}	$S_{r\theta}$
Polar coordinates	S_{rr}	$S_{\theta\theta}$	$S_{\phi\phi}$	$S_{\theta\phi}$	$S_{\phi r}$	$S_{r\theta}$

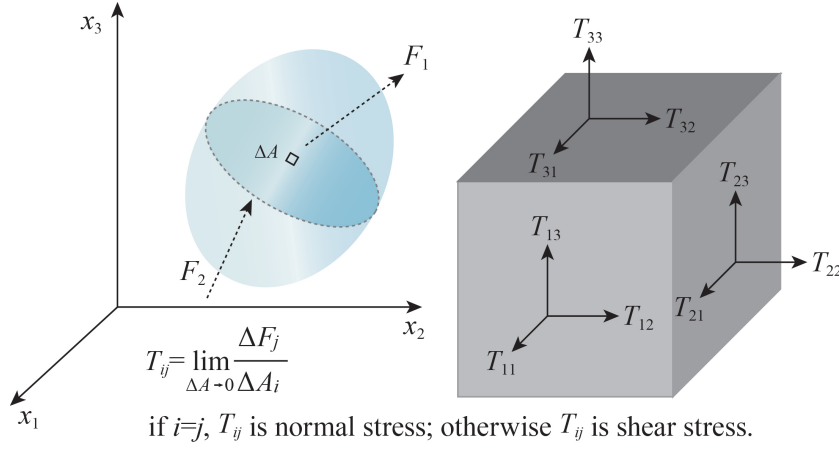


Figure 1.3: The definition and directions of stress and strain in the piezoelectrics.

The stress T and strain S in the Cartesian coordinates are illustrated in Fig. 1.3. The electric field E , electric displacement D , T , and S can be expressed by

$$E = \begin{pmatrix} E_1 \\ E_2 \\ E_3 \end{pmatrix}, D = \begin{pmatrix} D_1 \\ D_2 \\ D_3 \end{pmatrix}, T = \begin{pmatrix} T_1 \\ T_2 \\ T_3 \\ T_4 \\ T_5 \\ T_6 \end{pmatrix}, S = \begin{pmatrix} S_1 \\ S_2 \\ S_3 \\ S_4 \\ S_5 \\ S_6 \end{pmatrix}. \quad (1.1)$$

The relationship between S , T , E , and D in the piezoelectric materials can be expressed by the following equations:

$$\begin{cases} S = s^E T + d_t E, \\ D = d T + \varepsilon^T E, \end{cases} \quad (1.2)$$

where d is piezoelectric coefficient, s^E is elastic compliance constant, and ε^T is permittivity; d_t is the transposed matrix of d . Equation 1.2 has four different forms [9], as shown in Table 1.2.

Table 1.2: Four forms of piezoelectric constitutive equations.

d format	$S = s^E T + d_t E$	$D = d T + \varepsilon^T E$
e format	$T = c^E T - e_t E$	$D = e S + \varepsilon^S E$
g format	$S = s^D T + g_t D$	$E = -g T + \beta^T D$
h format	$T = c^D S - h_t D$	$E = -h S + \beta^S D$

The coefficients in Table 1.2 are not all independent [10]; the relationships are

summarized in Equation 1.3.

$$\left\{ \begin{array}{l} s^E - s^D = g_t d = d_t g, \\ c^D - c^E = h_t e = e_t h, \\ \varepsilon^T - \varepsilon^S = e d_t = d e_t, \\ \beta^S - \beta^T = g h_t = h g_t, \\ \\ s^D = \frac{1}{c^D}, \\ s^E = \frac{1}{c^E}, \\ \varepsilon^T = \frac{1}{\beta^T}, \\ \varepsilon^S = \frac{1}{\beta^S}, \\ \\ d = \varepsilon^T g = e s^E, \\ e = d c^E = \varepsilon^S h, \\ g = h s^D = \beta^T d, \\ h = \beta^S e = g c^D. \end{array} \right. \quad (1.3)$$

Based on the dynamic equations of the piezoelectric ceramics derived from the above piezoelectric constitutive equations, it is possible to simulate and analyze various piezoelectric vibrating modes.

1.1.3 Applications

Rapid development in the property improvement and mass production of materials has aroused intense application interest. To date, piezoelectric materials, including single crystals, ceramics, and films have been utilized in the applications such as generators, actuators [11], frequency control devices, surface acoustic wave devices, and so on [12]. Transducers are designed to convert energy from one form to another form. Basically, these applications can be categorized into three series depending on the energy transformation direction.

The first, piezoelectric actuators convert electrical energy to mechanical energy, usually referred to as “motors” [13]; the autofocus system for cameras is a typical example. The second, piezoelectrics sensors [14] convert mechanical energy into electrical energy, usually referred to as “generators”; one common example is the cigarette lighters. And the last one combines the previous two directions; like in filters [15], the electrical signal converts to mechanical signal and then converts back to electrical signal.

Among these applications, the progress of high power ultrasonic devices is remarkable. The ultrasonic transducers and actuators (motors) exploit the resonant

vibrations of piezoelectrics. Unlike present widely used electromagnetic motors, the miniaturization demand for motors can be satisfied by the ultrasonic motors [16]. The ultrasonic motors can be categorized to standing wave type and propagating wave type [17]; both of them are driven by the tangential stress along the interface between stator and rotor [18, 19]. The main advantages of ultrasonic motors include high torque, low speed, quick response, hard brake without backlash, high power density, and most important, small size [20]. However, the high power ultrasonic motors have shortcomings; such as demand for high frequency power source, bad durability, and the performance reduction at high power [20]. The nonlinear behavior was reported in an ultrasonic transducer [21], which might be another limitation for ultrasonic applications.

1.1.4 Lead-containing piezoelectrics

$\text{Pb}(\text{Zr}_{1-x}\text{Ti}_x)\text{O}_3$ (PZT) and related compositions have occupied a large proportion in various piezoelectric applications [7]. PZT is the solid solution of PbZrO_3 (PZ) and PbTiO_3 (PT), which are antiferroelectric and ferroelectric at room temperature, respectively [22]. PZT ceramics were found to exhibit anomalously high dielectric and piezoelectric properties when the composition is near a morphotropic phase boundary (MPB, $x=0.48$), which separates rhombohedral and tetragonal phases [23]. The properties of PZT-system were modified by the usage of various dopants: isovalent dopants, acceptor dopants, and donor dopants [24]. Doping with donor dopant Nb^{5+} and acceptor dopants Fe^{3+} (Fe^{2+} , Mn^{3+}) can reduce and enhance the quality factor, resulting in soft-type PZT and hard-type PZT, respectively [25]. Other lead-containing materials also possess excellent piezoelectric and dielectric properties; for example, $\text{Pb}(\text{Zn}_{1-x}\text{Nb}_x)\text{O}_3$ (PZN), $\text{Pb}(\text{Mn}_{1-x}\text{Nb}_x)\text{O}_3$ (PMnN), and $\text{Pb}(\text{Mg}_{1-x}\text{Ta}_x)\text{O}_3$ (PMT) [26]. The PMnN single crystal was reported to have large coupling factor $k_{33}=92\%$ and large piezoelectric coefficient $d_{33}=1500$ pC/N [27].

1.1.5 Lead-free piezoelectrics

Despite of the great piezoelectric properties of PZT based systems, the high content of toxic lead composition is against environmental regulations and raises safety concerns [23]. Lead and its inorganic compound is stable and their metabolism and degradation are difficult. The concentration of lead in polluted water, air, and food chain finally affects human beings [28]. Human body does not need the element “lead” (Pb); on the contrary, the blood, nervous, digestive, and immune systems suffer from the intake of excess lead. Especially for children, excess lead results in hyperactivity, lower intelligence quotient, and shorter average height.

In July 2006, the Restriction of Hazardous Substances Directive (RoHS 1) took effect. The purpose is to restrict the relevant manufacturers in the discharging and

using of six toxic substances including Pb. Since then, the investigation on lead-free piezoelectric materials has become motivated and indispensable [29]. It has been summarized that the general considerations of lead-free materials includes cost, toxicity, crystal structure, electronic structure, and phase diagram [30]. Nowadays, the most promising candidates can be mainly categorized into three families: $(\text{Na}_x\text{Bi}_{1-x})\text{TiO}_3$ (NBT) family, BaTiO_3 (BTO) family, and $(\text{K}_x\text{Na}_{1-x})\text{NbO}_3$ (KNN) family [31].

1.2 Niobates

PZT-based materials have tunable piezoelectric properties owing to the adjustable composition. Two ends of PZT, PbZrO_3 (PZ) and PbTiO_3 (PT) are in rhombohedral phase and tetragonal phase, respectively. It has been suggested that the piezoelectric properties become optimal around the morphotropic phase boundary (MPB). As one of the most promising lead-free piezoelectrics, niobates have been systematically investigated [31]. It's easy to notice that KNbO_3 and NaNbO_3 are exactly the same as the former case. This section presents the structure of the two ends of the KNN solid solution and the properties of KNN-based systems.

1.2.1 Potassium niobate and sodium niobate

Ferroelectricity of potassium niobate (KNbO_3 , KN) was reported by B. T. Matthias in 1949 [32]. The crystal structures of KN are shown in Table 1.3; KN undergoes the phase transitions from cubic to tetragonal, tetragonal to orthorhombic, and orthorhombic to rhombohedral with decreasing temperature, respectively [33]. At room temperature, as shown in Fig. 1.4, the crystal structure of KN is orthorhombic (perovskite-like), in space group Bmm2, with lattice parameters $a = 5.697 \text{ \AA}$, $b = 3.971 \text{ \AA}$, and $c = 5.721 \text{ \AA}$ [34]. Theoretical density can be determined to be 4.618 g/cm^3 .

Table 1.3: Phase transitions of potassium niobate.

Temperature Range	Crystal System	Space Group	Phase
$> 435 \text{ }^\circ\text{C}$	Cubic	Pm3m	Paraelectric
$225 \sim 420 \text{ }^\circ\text{C}$	Tetragonal	Pamm	Ferroelectric
$-10 \sim 225 \text{ }^\circ\text{C}$	Orthorhombic	Bmm2	Ferroelectric
$< -10 \text{ }^\circ\text{C}$	Rhombohedral	R3m	Ferroelectric

Although KNbO_3 is difficult to synthesize, it has been reported to express good acousto-optic, electro-optic, and nonlinear optical properties; usually utilized for frequency doubling of low and medium power lasers owing to the large nonlinear

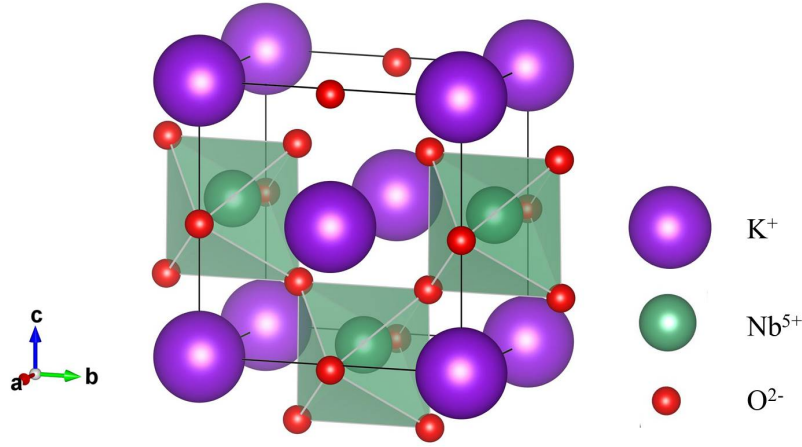


Figure 1.4: Crystal structure of potassium niobate; the enclosed units denote the NbO_6 octahedra.

Table 1.4: Phase transitions of sodium niobate.

Temperature Range	Crystal System	Space Group	Phase
$> 640\text{ }^\circ\text{C}$	Cubic	Pm3m	Paraelectric
$575 \sim 640\text{ }^\circ\text{C}$	Tetragonal	P4/mbm	Paraelectric
$520 \sim 575\text{ }^\circ\text{C}$	Orthorhombic	Ccmm	Paraelectric
$480 \sim 520\text{ }^\circ\text{C}$	Orthorhombic	Pnmm	Paraelectric
$370 \sim 480\text{ }^\circ\text{C}$	Orthorhombic	Pmnm	Paraelectric
$-103 \sim 370\text{ }^\circ\text{C}$	Orthorhombic	Pbma	Antiferroelectric
$< -103\text{ }^\circ\text{C}$	Rhombohedral	R3c	Ferroelectric

optical coefficient [35]. In addition, high temperature stability and high coupling factor ($k_t = 0.69$) make KN single crystals promising for ultrasonic and acoustic wave applications [35].

Another end of KNN, sodium niobate (NaNbO_3 , NN) was found to be antiferroelectric by Matthias [36]. In the antiferroelectrics the adjacent electric dipoles are antiparallel, resulting in zero net polarization and hence zero piezoelectricity. The crystal structures of NN are shown in Table 1.4; with decreasing temperature, NN undergoes the phase transitions from cubic to tetragonal, tetragonal to orthorhombic, and orthorhombic to rhombohedral, respectively. It's worth mentioning that four different space structures appear in orthorhombic structure; only in Pbma NN shows antiferroelectricity.

Investigations on NN are much less than on KN; unlike KN, the crystal structure of NN is more complex. At room temperature, two kinds of crystal structures have been reported, as shown in Fig. 1.5. One is orthorhombic unit cell in space group

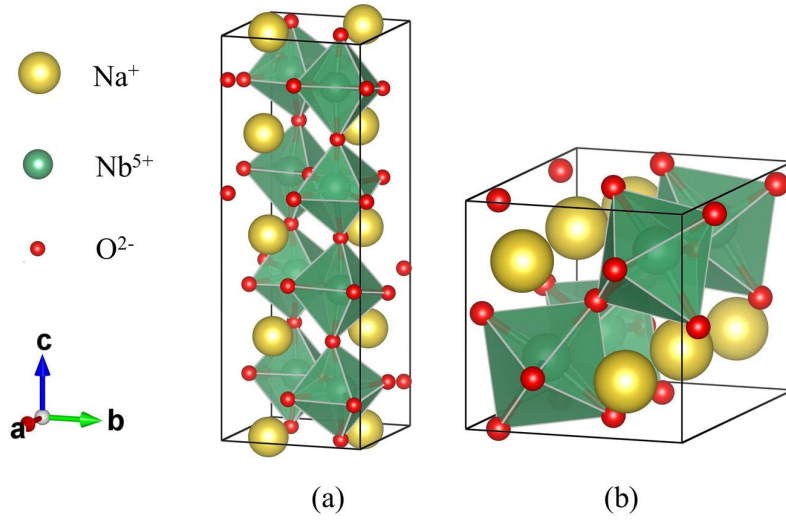


Figure 1.5: Crystal structure of sodium niobate in space group (a) $Pbcm$ and (b) $Pmc2_1$; the enclosed units denote the NbO_6 octahedra.

$Pbcm$, with $a = 5.506 \text{ \AA}$, $b = 5.566 \text{ \AA}$, and $c = 15.520 \text{ \AA}$; while the other is a polar space group $Pmc2_1$, with $a = 5.569 \text{ \AA}$, $b = 7.790 \text{ \AA}$, and $c = 5.518 \text{ \AA}$ [37]. In space group $Pmc2_1$ the material exhibits ferroelectricity, which was usually considered as a result of polarization of NN crystal [37].

1.2.2 Potassium sodium niobate and its derivatives

$(K_{1-x}Na_x)NbO_3$ (KNN) has a high Curie temperature ($T_c = 420 \text{ }^\circ\text{C}$), excellent ferroelectric property, and large electro-mechanical coupling factor [38]. At room temperature, the crystal structure of KNN is orthorhombic, as shown in Fig. 1.6. For the composition $(K_{1-x}Na_x)NbO_3$, when x is less than a critical value (about 0.1 and dependent on the temperature), the compound is in antiferroelectric phase; otherwise it is in ferroelectric phase. Despite of the large difference between KN and NN properties, the Curie temperature is almost constant [39], as shown in the phase diagram [30] (Fig. 1.7). Although it's clear that the MPB in KNN system must exist, the corresponding composition is still controversial; usually x is thought to be around 0.5 [30].

In recent years, the investigation on KNN-based materials can be mainly categorized into three groups.

(1) Modify the composition and adjust it to the MPB so that the properties can be optimized. One advantage of the KNN-system is that the MPB only has slight variation with increasing temperature, as shown in Fig. 1.7 [30]. Effects of single

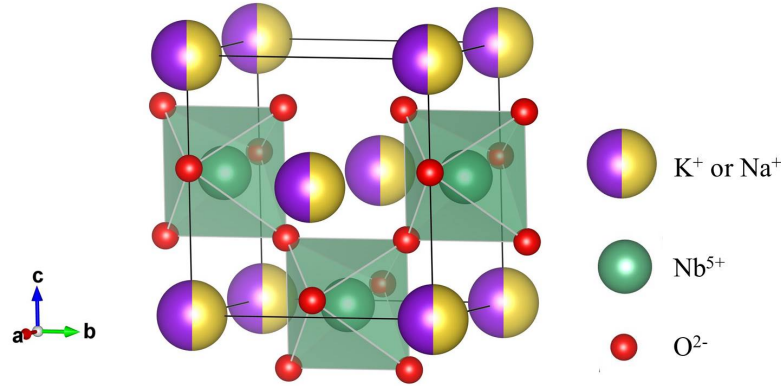


Figure 1.6: Crystal structure of potassium sodium niobate; the enclosed units denote the NbO₆ octahedra; and purple-yellow bicolor balls represent the occupation of either potassium or niobate ions.

element doping were summarized by Damjanovic et al. [30]. For example, replacing niobium with tantalum enhances the electrostrictive effects and unipolar strain [40]. Doping with manganese can decrease the dielectric loss and relative permittivity and improves the mechanical quality factor Q_m and k_p [41]. Alkaline earth dopants are more complex: doping with strontium and calcium can improve the sinterability while magnesium oxide hinders it [42].

(2) Improve the sinterability of KNN-based materials by using sintering aids because the melting point of KNbO₃ is relative low (1050 °C) comparing to other piezoelectrics [43]. This limitation of low temperature makes it difficult to obtain ceramics of high quality or to control the composition in solid solutions. Using sintering aids is one of the methods to improve the ceramic quality. The introduction of liquid phase sintering aids (e.g. CuO, K₄CuNb₈O₂₃, and K_{5.4}CuTa₁₀O₂₉) can decrease the required sintering temperature and hence result in more compact KNN ceramics with a density up to 97.5% theoretical density [44]. Except for Cu²⁺ ions, ZnO, MnO, MnO₂, SnO₂, and many other compounds can be used as sintering aids. An alternative is to prohibit the vaporization of KNbO₃ by using low temperature fabrication methods, e.g. hydrothermal method [6].

(3) The other researches attempt to promote the practical usage, for example, the fabrication of various chemical structures, the device designing using KNN-based materials and so on. The synthesis and test of CuO-added K_{0.5}Na_{0.5}NbO₃ 1-3 fiber/epoxy piezo-composites was realized by E. M. Alkoy et al. [45]. KNN-based thick films [46] and thin films [47] were prepared via aerosol deposition and dry etching, respectively. Domain orientation controlled KNN ceramics was fabricated

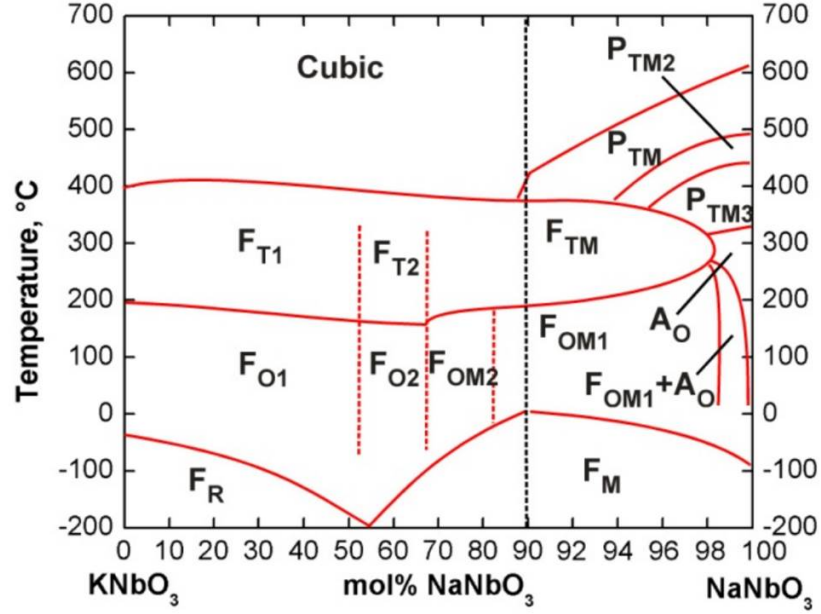


Figure 1.7: Phase diagram of the KNN solid solution [39].

by employing a SrTiO_3 single crystal substrate [48]. Acoustic emission sensors [49] and a shear mode ultrasonic motor [50] using KNN-based materials were reported. E. A. Patterson et al. studied the unipolar fatigue behavior of pure and CuO-doped $(\text{K,Na,Li})(\text{Nb,Ta,Sb})\text{O}_3$ ceramics [51].

Table 1.5: Typical characteristics of some KNN-based materials.

Material	T_c (°C)	$\varepsilon_{33}^T/\varepsilon_0$ 1	k_p %	d_{33} pC/N	P_r $\mu\text{C}/\text{cm}^2$	E_c kV/mm	Reference
KNN	420	496	46	127	33	4.7	[52]
KNN-LS	368	1380	50	265	25	18.5	[52]
KNN-Mn		207	34	114			[53]
KNN-BT	358	1003	29	104	7.5	1.2	[54]
KNN-Ta	210	967	45	205			[40]
KNN-(Li,Ta,Sb)	338	689	35.6		8.7	0.2	[55]
KNN-Mn	193	1490	45	240			[56]
KNN-Cu		285	38	94			[57]
KNN-KCT	402	200	39	180	20	1.3	[44]

The typical characteristics (Curie temperature T_c , relative permittivity $\varepsilon_{33}^T/\varepsilon_0$, coupling factor k_p , piezoelectric coefficient d_{33} , remanent polarization P_r , and coercive field E_c) of some modified KNN materials are shown in Table 1.5.

1.3 Synthesis Methods

1.3.1 Solid-state reaction method

Among the piezoelectric materials, polycrystalline ceramics occupy a large portion in the practical applications owing to the simple procedure and relative low cost. The polycrystalline ceramics can be prepared via several methods.

Solid-state reaction method is the most widely used method for the synthesis of polycrystalline ceramics from the mixture of solid raw materials [22]. Usually, the raw materials do not react together (or very slowly) at room temperature. High temperature (~ 1000 °C, sometimes up to 1800 °C) is necessary to accelerate the reaction process. The selection of raw materials mainly depends on the toxicity, the melting point, the reaction rate, the feasibility of by-product separation, and the cost. In the synthesis of some materials, solid-state reaction method is inapplicable.

Taken the synthesis of KNbO_3 ceramics as an example, raw materials K_2CO_3 and Nb_2O_5 powders are usually employed. KN powders can be obtained through mixing, ball-milling, and sintering; the KN powders are then pressed into desired shape and sintered [58]. There are several disadvantages in the solid-state reaction method [58]. As one of the raw materials for KN, K_2CO_3 is hygroscopic, which is inconvenient for storage. The synthesis processes might bring in impurities, e.g., the fragment of ZrO_2 balls and container used in the ball-milling process. The most important limitation is, in the sintering process (~ 1000 °C), the evaporation of K^+ results in the deviation from the stoichiometry ($\text{K}:\text{Nb} = 1:1$) [59]. In addition, the lack of K^+ might lead to the appearance of a by-product $\text{K}_4\text{Nb}_6\text{O}_{17}$ [60]. In other potassium-containing ceramics, for example, $(\text{K},\text{Na})\text{NbO}_3$, the evaporation of K^+ is also a limitation to the quality of the ceramics [61]. To prevent from this phenomenon, excess K^+ was used to compensate the K^+ loss [62]. Sintering under high alkaline vapor pressure atmosphere was suggested as another solution [63]. In the preparation of Pb- or Bi-containing ceramics, the same strategy was used [64]. Low temperature sintering also proved to be efficient in preventing from the K^+ evaporation [22].

1.3.2 Hydrothermal method: history, merits and shortcomings

Hydrothermal method was first adopted by mineralogists to simulate a similar condition to the crust so that the formation and growth of minerals and rocks became possible [65]. Since 1970s, the hydrothermal synthesis has become an important tool for ceramic processing. In subsequent studies the synthesis of PZT and similar oxide ceramics were found to be effective [65].

Hydrothermal method was introduced as one synthesis method of piezoelectric

materials in 1980s [66]. PZT thin films [67], BaTiO₃ thin films [68] and powders [69], bismuth sodium titanate powder [70], niobate thin films [46] and powders [71] synthesized via hydrothermal method, and related devices [72] have been reported in the last three decades. Comparing with conventional powder synthesis method, hydrothermal method has several merits [73]. The low temperature (i.e., low energy consumption) in hydrothermal synthesis is useful for the mass industrial production; it is also helpful for the prohibition of K⁺ vaporization in KNbO₃ fabrication [74] and Bi⁺ vaporization in (Bi,Na)TiO₃-based system [70]. The significantly reduced aggregation level of the prepared powders may result in optimized properties [73]. High purity is also an advantage: the impurities tend to be rejected by the growing crystallites and stay in the solution; while in solid-state reactions the impurities would mix with reaction product if not vaporized [73]. The hydrothermal method also helps to investigate the crystal growth mechanism when it became possible to monitor the synthesis in recent years. Actually, earlier this used to be taken as the main its shortcoming, because the equipment setup had a nature of black-box [65].

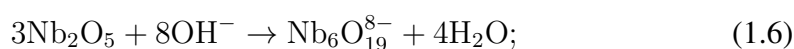
However, hydrothermal method also has some dismerits. It has long synthesis period owing to its relative low processing temperature comparing with conventional synthesis methods. In order to compensate the limitation of the long reaction time, ultrasonic power assistance was utilized to irradiate the raw solutions to accelerate the reaction [75]. The nature of the hydrothermal method decides that all the raw materials are required to be soluble in water or other solvents. It has been claimed that although Nb₂O₅ is most accessible and cheap Nb source, its low solubility is one drawback of the homogeneous reaction [76]. Soluble niobium pentachloride (NbCl₅) was suggested to substitute for Nb₂O₅ as one of raw materials in the fabrication of KNbO₃ and NaNbO₃ powders [76].

1.3.3 Hydrothermal reactions of niobates

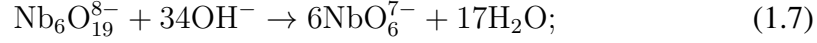
In the hydrothermal method, the synthesis process is usually believed to follow the particle nucleation and growth theory [65]. The nuclei formed in the raw solution may dissolve or grow depending on the free energy [77]. However, the reactions in the hydrothermal method are highly system-dependent. The mechanisms in the synthesis of alkali metal niobates have been revealed [71, 78, 79].

The reactions in the synthesis of KNbO₃ powders using raw materials Nb₂O₅ powders and KOH solution are listed in the following [71].

(1) Dissolution process



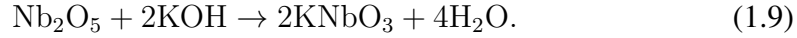
(2) Monomer generation



(3) Integration

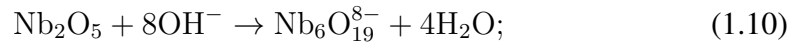


(4) Overall reaction

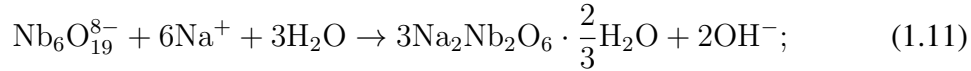


Similar structural evolution in the hydrothermal synthesis of NaNbO_3 powders has been reported by X-ray diffraction (XRD) [78]. However, with the help of scanning electron microscope (SEM), nuclear magnetic resonance (NMR) and other techniques, a metastable intermediate structure ($\text{Na}_2\text{Nb}_2\text{O}_6 \cdot 2/3\text{H}_2\text{O}$ fibers) was observed [79]. The reactions after dissolution process are also listed as follows [79].

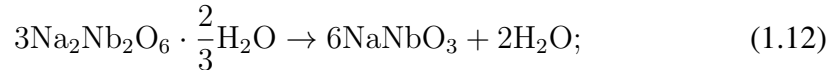
(1) NbO_6 octahedra rupture



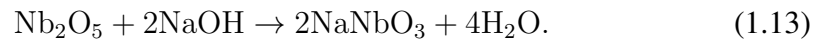
(2) Unstable microporous $\text{Na}_2\text{Nb}_2\text{O}_6 \cdot 2/3\text{H}_2\text{O}$ fibers



(3) Stable NaNbO_3



(4) Overall reaction



1.4 High Power Piezoelectric Properties

1.4.1 Conventional characteristics

Given a piezoelectric material (or a piezoelectric specimen), the properties in Table 1.6 are usually necessary to describe the characteristics [80]. The applications of materials depend on one or more of these properties. For instance, the PZT-based systems have an enormous application range owing to their high coupling factor, high d coefficients, and large density.

Table 1.6: Key characteristics of piezoelectric materials and devices.

Parameters	Symbols
Coupling factors	$k_p, k_{31}, k_{33}, k_t, k_{15}$
Frequency constants	$N_p, N_{31}, N_{33}, N_t, N_{15}$
Permittivity	$\varepsilon_{33}^T, \varepsilon_{11}^T$
Piezoelectric d coefficients	d_{31}, d_{33}, d_{15}
Piezoelectric g coefficients	g_{31}, g_{33}, g_{15}
Young's modulus	E_{11}, E_{33}, E_{55}
Poisson's ratio	σ_{ij}
Mechanical quality factor	Q_m
Dielectric loss	$\tan \delta$
Curie point	T_c
Density	ρ

Especially, large quality factor (Q_m) is a necessity for some piezoelectric applications. In piezoelectrics, Q_m is usually used as the criterion to separate hard-type and soft-type materials. Although no clear boundary has been claimed, the materials with a Q_m larger than 500 are considered as “hard” while the ones with a Q_m smaller than 100 are considered as “soft”. The concepts of “hard” and “soft” came from the ferromagnetic materials [81, 82]. The low or high coercive magnetic field (H_c) depicted in the magnetization-field curve [83] corresponds to soft- or hard-type magnetic materials, respectively. The similarity between ferroelectrics and ferromagnetics prompted the criterion of E_c . For piezoelectrics, the “hard” and “soft” are represented by high or low Q_m , the derivation of which is the same as the E_c (details seen in chapter 3).

1.4.2 Drive methods

Based on the energy transformation direction, piezoelectric devices can be classified into three groups (seen in section 1.1.3). It is worth mentioning that piezoelectric applications relying on the converse piezoelectric effect can also be categorized by driving method. For one certain piezoelectric device, it has singular or plural resonant frequencies. Two driving methods are normally adopted in piezoelectric devices, depending on whether the driving voltage is close to or away from the resonant frequency, as seen in Fig. 1.8. It was suggested that in these two types of applications the strain was induced by different mechanisms [17]. For example, in the piezoelectric actuators, large deformation can be achieved by two strategies: driving materials with small piezoelectric coefficient d , large quality factor Q_m , and high coercive field E_c at resonant frequency or driving materials with large d and large dielectric constant at low frequency [22], as illustrated in Fig. 1.8. The

former materials are hard-type piezoelectrics, the deformation is proportional to the value $d_{ij}Q_m$; large Q_m ensures a large deformation [84], represented by the transducer, transformer, and Langevin actuator [17]. The latter ones are soft-type piezoelectrics; which are usually assembled in multilayer structures (e.g., multilayer actuator, bimorph actuator, and so on) [85].

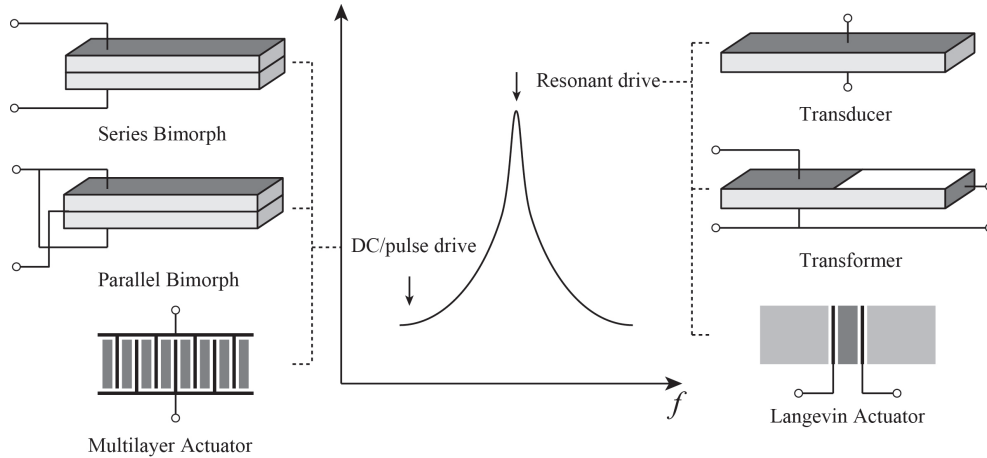


Figure 1.8: Examples of applications driven under two modes.

1.4.3 High-power applications

The miniaturization trends nowadays arouse the pursuing for high power density devices, such as piezoelectric actuators, piezoelectric transformers, and ultrasonic motors [86]. They are normally driven by a relatively high electrical field so that large stress (force) or large strain (deformation) can be achieved. As a prerequisite, the materials need to exhibit high power performance and stability at the same time. Due to the demand for high power density, the soft-type piezoelectrics are inappropriate because of its large energy dissipation ratio (or low Q_m). Hence, the hard-type piezoelectrics including ceramics, films, and single crystals are used in high-power devices.

In the applications of the piezoelectric devices, in addition to high performance, high reliability is also required owing to the continuous operation. Especially for the high power operating devices, high reliability is a necessity. Figure 1.9 shows one example of a mechanically broken PZT transducer when operated under high voltage condition. During the continuous operation, the induced large stress is also a burden for the devices; in extreme situations the devices might broke near the maximum stress.

However, in previous investigations, only limited attention has been paid to the reliability of high-power piezoelectric applications. Nagata et al. investigated on the

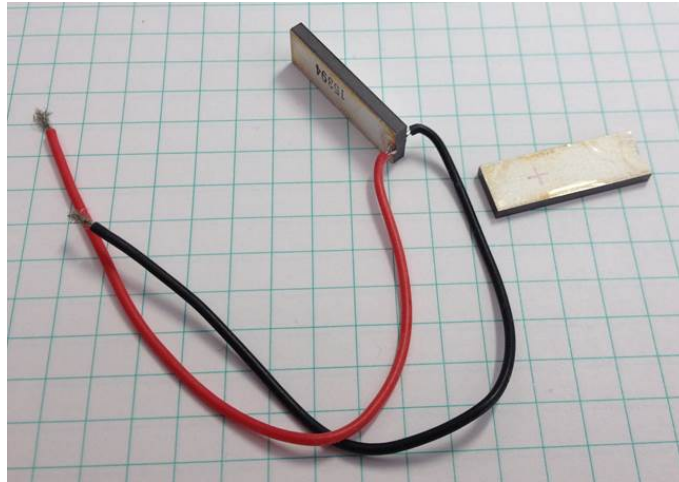


Figure 1.9: A mechanically broken PZT transducer.

breakage reason and life expectancy of piezoelectric devices and pointed out that for different devices the main reason was probably not the same [22]. Two main causes of breakage are high applied electrical field (electric breakage) and large stress when vibrating (mechanical breakage). In the piezoelectric actuators, the breakage was suggested to result from space charge, inner stress, and nonlinearity [22]. Although the theoretical prediction of lifetime is almost impossible, an empirical prediction can be realized by analyzing the breakage data [22]. The lifetime of the piezoelectric transformers was studied and proved to be load-dependent [87]. These investigations reveals that the properties of piezoelectrics operated at high voltage are quite different from low voltage condition and that the former ones also need attention.

1.4.4 High power characteristics

In high power piezoelectric devices, comparatively high voltages are employed to obtain high deformation or large force [86]. High power characteristics of the piezoelectrics have been carried out for various materials. The properties including piezoelectric coefficients, coupling factor, and quality factor show large voltage dependence [92]. Moreover, the vibration velocity dependent resonant frequency shift [88, 89], dissipation power density [88], mechanical quality factor [90], and electrical field dependent piezoelectric constant [91] have been observed in different materials, as shown in Fig. 1.10. Hence, the conventional characteristics in Table 1.6 proved to be not enough to describe the piezoelectric materials.

However, it is noticed that the high power characteristics of piezoelectrics still lack standard criteria; probably because of the controversial understanding of the

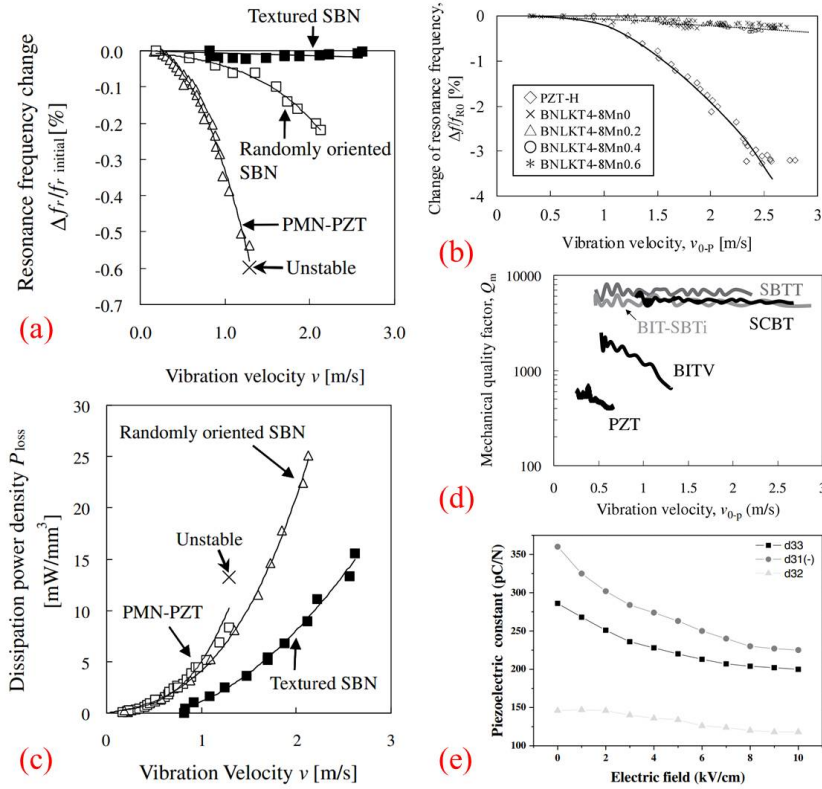


Figure 1.10: The high power characteristics in piezoelectrics: velocity-dependent (a)-(b) resonant frequency shift [88, 89], (c) dissipation power density [88], (d) mechanical quality factor [90], and (e) electrical field-dependent piezoelectric constant [91].

nonlinear behavior under high-power operation. In the practical applications, high voltage driving results in large current, large stress, and large temperature rise; the effects of which are difficult to separate from each other.

To satisfy the requirement of high power characteristics, the following measurement techniques were proposed.

1.4.5 Constant voltage and constant current method

The piezoelectric properties can be determined via a resonant-antiresonant method (details seen in section 2.4.4). In the resonant-antiresonant method, two different schemas are used: constant voltage method and constant current method [93].

In the constant voltage method, the sample is excited by a constant-amplitude AC voltage, which is provided by a voltage source with low output impedance [93], as shown in Fig. 1.11(a). The current in the circuit is measured as a voltage drop on a resistor r . When the frequency of driving voltage sweeps, the result is impedance

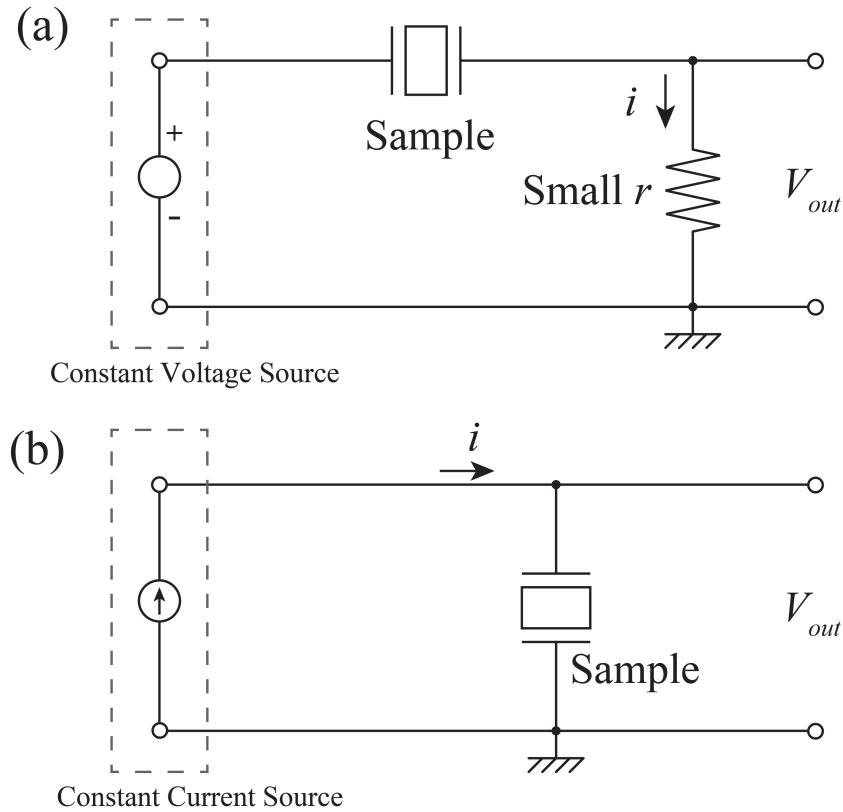


Figure 1.11: Schematic diagrams of (a) constant voltage method and (b) constant current method.

curve (or admittance curve) given by the impedance analyzer.

Around the resonant frequency of the specimen, the vibration amplitude is proportional to the current instead of voltage. Using the constant voltage method to determine the electro-mechanical coupling parameters might cause inaccuracy; thus a constant current method was introduced.

In the constant current method, a constant-amplitude AC current from a current source is applied on the sample instead of the AC voltage [93], as shown in Fig. 1.11(b). The voltage drop on the sample is detected and the impedance curve or admittance curve of the sample is obtained. The constant current method has been utilized to measure the high-power properties in 2000s [94–98].

1.4.6 Burst mode method

In some piezoelectric devices, the temperature increases dramatically when they are driven continuously, especially driven by high voltage [99]. The heat results from the energy loss while the electrical energy is converted to mechanical energy [100].

Continuous operating at high temperature leads to undesired effects, for example, the partial depolarization of piezoelectric devices, degradation in key properties, and so on [100]. In practical applications, the temperature rise is difficult to eliminate because the continuous running is required. However, it is important to separate the temperature effect from the other effects so that they can be investigated one by one.

A transient response method was suggested to measure the high power properties with negligible temperature rise [101]. In the method, a sinusoidal voltage is applied on the sample (for only several cycles) until the vibration velocity is sufficiently high [101]. The waveforms of current or velocity after the excitation can provide the necessary characteristics [101].

Similar to the transient method, a pulse drive method was proposed to determine the quick and precise response of piezoelectric actuators [86, 102]. A step voltage or a voltage pulse applied on a piezoelectric actuator gives the transitional response of the actuator.

1.5 Thesis Motivation

Piezoelectrics are widely employed in various applications; including high power devices, such as ultrasonic motors, transducers, transformers, and so on. They are driven at resonant frequency to achieve large deformation (strain) or force (stress). Therefore, the high power characteristics are very important in this case. However, most previous studies focused on the low power level and there's limited literatures concerning the properties under high power condition. This dissertation focused on the estimation of high power properties.

In recent years, the concerns on human health and environmental protection have aroused the development of lead-free piezoelectric materials, as substitutes for lead-based systems. Most lead-free piezoelectrics usually taken as promising substitutes for lead-containing compositions exhibit unsatisfactory properties (e.g., smaller d coefficients, lower coupling factor, lower density, and so on) under low power level. On the other hand, it has been suggested that the lead-free materials possessed higher vibration amplitude under high power condition; indicating that different criteria are required for low power level and high power level. In high power applications, the piezoelectrics need high and stable quality factor. In the attempt of analyzing and improving the high power properties in piezoelectrics, the following problems were encountered and relevant solutions were explored:

(1) In the previous papers, usually two methods were used to enhance the Q_m of the ceramics: doping with low valence ions and adding sintering aids. Noticing that the essential of both the two methods is increasing the charge defects, it's convincing that other methods to increase the charge defects are also promising in the hardening of piezoelectric ceramics. So we wanted to investigate the influence

of post-annealing in argon since it might enable the increasing of oxygen vacancies (one type of the various charge defects).

(2) For evaluating the lead-free materials, some criteria were introduced, such as d coefficient, g coefficient, k_p , ε_r , and so on. In low power region, IEEE standard on piezoelectricity [103] approved in 1988 and its revision [104] in 1997 were adopted as the guidance on the determination of piezoelectric properties. However, despite the factor that most hard-type piezoelectric materials and devices need to be operated under high voltage, in most literatures low voltage properties are still taken as only criteria. Although in recent years attention has been shifted to high power piezoelectric characteristics that are dependent on the voltage (nonlinear), yet there's no uniform criterion or model that can describe the high power properties very well. Grounded on the contradiction between the demand and lack of a standard in high power region, we attempted to find a model to explain the nonlinear phenomena distinguishing from low voltage properties. The model should satisfy the following two demands. First, it should be consistent with the experimental results given by admittance curve and burst mode measurements, which are two effective methods to estimate the properties around the resonant frequency. Second, it should allow the quantification of nonlinear level in various samples so that the comparison between them is available.

(3) Using the proposed model, we wanted to estimate the high power properties of CuO-KNN transducers and to compare that with the PZT materials.

(4) In both academic researches and mass production, a simple and convenient method for property estimation is important; on the basis of the proposed model, we tried to give standardized procedures for estimating nonlinear levels. Besides, noticing that in piezoelectric materials, except for the nonlinearity depicted above, the polarization-field hysteresis loop and strain-field loop are also inherently nonlinear; we wanted to discuss the relation and distinction between them. To illustrate that clearly, we carried out simulations.

1.6 Thesis Structure

In this thesis, we present the properties of CuO-KNN ceramics synthesized via the hydrothermal method. Particularly, the hardening effect and nonlinear phenomena of CuO-KNN ceramics are described. This thesis is organized as follows.

In chapter 1, the background of piezoelectrics, niobate lead-free piezoelectrics, and hydrothermal method are introduced. High power characteristics and related evaluation methods are then presented. At last the motivation and structure of this thesis are described.

In chapter 2, the experimental details of the hydrothermal synthesis, burst mode measurement, and property estimation are first presented. Then the derivation and

calculation of electrical properties are introduced.

In chapter 3, the synthesis and hardening of CuO-KNN ceramics are presented. The effects of post-annealing in air and argon atmospheres are discussed separately. Post-annealing in air reveals the transitions of charge dipole distributions in the domain. By adding a post-annealing process in argon, the hardening of CuO-KNN ceramics is realized; the quality factor increases to 1500 from 870.

In chapter 4, prior to the estimation of the high power characteristics for the CuO-KNN ceramics, the investigation on nonlinear behavior in PZT transducers is carried out. The nonlinearity in high voltage admittance curves and burst mode method are presented and discussed, respectively. A nonlinear model is proposed on the basis of the burst mode results; the feasibility of which is systematically demonstrated and discussed. It proves to be effective in describing the admittance hysteresis and jumping phenomenon. The main source of the nonlinear behavior in the transducers is mechanical nonlinearity, instead of dielectric or piezoelectric nonlinearities. Dimensionless coefficients are suggested by theoretical derivation of the piezoelectric constitutive equations.

In chapter 5, using the proposed nonlinear model in chapter 4, we present the estimation results of fabricated CuO-KNN transducers; the proposed model is also effective for CuO-KNN. The comparison of nonlinear level between PZT and CuO-KNN transducers is given and discussed. Compared with the hard-type and soft-type PZT transducers, CuO-KNN has lower nonlinear level. The piezoelectric coefficients and compliance are also determined by burst mode results.

In chapter 6, for better understanding of the appearing nonlinearity, we carry out simulations of nonlinear circuits. The technological procedures of estimating nonlinearity is presented; and for practical usage a simplified method is given. At the end of this chapter, we also present the comparison of nonlinearities between the present study and other conditions; a simulation of ferroelectric hysteresis loop is adopted to reveal the difference in essence.

In chapter 7, abovementioned results are summarized; concluding remarks and prospects are made.

At last, acknowledgements, appendices including the programs used for the fitting in chapter 3-5 and the simulation in chapter 6 are listed.

CHAPTER 2

Experimental and Analysis Procedures

This chapter first introduces the hydrothermal method synthesis of powders and subsequent ceramics fabrication via solid state method; then presents the physical characteristic method, processing of the ceramics, and the determination method of electrical properties. In the last section of this chapter we also introduce the burst mode method.

2.1 Synthesis of KN and NN Powders

Prior to the fabrication of piezoelectric ceramics, powders with same composition should be synthesized; after that, the ceramics can be prepared by pressing and sintering of the powders. In this section we introduce the fabrication of KNbO_3 and NaNbO_3 powders via hydrothermal method [58]. The powders can be prepared in the following order:

(1) Preparing potassium hydroxide and sodium hydroxide aqueous solutions:

NaOH pellets (97.0%, Kanto Chemical), KOH pellets (86.0%, Kanto Chemical), and Nb_2O_5 powders (99.95%, Kanto Chemical) were used as raw materials. Except for water, the main impurities in these raw materials were Na_2CO_3 (1.0%) in NaOH pellets and K_2CO_3 (1.0%) in KOH pellets, respectively. In the case of KOH solution, 252.95 g KOH pellets were weighed and placed in one graduated cylinder; distilled water was poured into the graduated cylinder until total volume became 500 mL; in the case of NaOH solution, 179.95 g NaOH pellets were used instead of KOH pellets. The concentrations of the KOH and NaOH solutions were calculated based on the purity of the reagents; which were 7.6 N and 8.7 N, respectively. Distilled water was trickled to compensate the decreasing volume while stirring until complete dissolution of the pellets. When the solutions cooled down, stored them in bottles.

(2) Hydrothermal reaction process:

Since we need to fabricate the powders in high temperature, high pressure, and strong alkali condition, two high pressure resistant containers (Taiatsu Techno TAF-SR Type) were adopted.

As illustrated in Fig. 2.1, Nb_2O_5 powder and alkaline solutions were mixed in a Teflon vessel, which was placed inside a pressure container. To synthesize KNbO_3 powder, 9.18 g Nb_2O_5 powder and 140 mL of KOH solution (7.6 N) were placed into one vessel (300 mL); while to synthesize NaNbO_3 powder 37.2 g of Nb_2O_5 powder and 70 mL of NaOH solution (8.7 N) were placed in another vessel (100 mL). Each vessel was placed in a constant temperature oven (Yamato DKN 302) pre-heated to 210 °C for 24 h reaction. After the reaction, the reaction container was taken out from the constant temperature oven and cooled by flowing water for 30 minutes. Then the slurry (except the pellucid alkaline solution in the upper layer) was moved into the beaker.

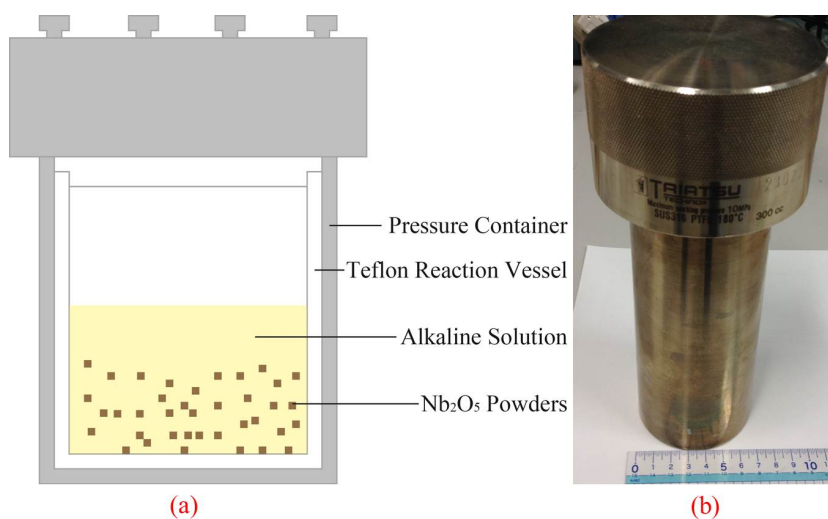


Figure 2.1: (a) Schematic diagram of hydrothermal method and (b) photo of the container.

(3) Filtering and drying process:

Distilled water was poured into the beaker containing the slurry and a stir bar was used to mix them until the slurry became suspension. Then the powders were separated using a Teflon filter paper with a pore size $0.45 \mu\text{m}$ (Millipore Corporation Millipore Omnipore Membrane Filters). The remnant in the beaker was washed into the filter using distilled water. After filtering, the separated wet powders were dried in a constant temperature oven (Yamato DKN 302) under 130°C for several hours.

(4) Neutralizing process:

After drying the powder, the powders (along with the residual K^+ , Na^+ and OH^- ions) were dissolved into distilled water again. The pH value of the solution was monitored using a pH meter (A&D Ap-20). To eliminate residual contaminants, HCl solution (0.01 mol/L) was used in a neutralization process after washing the mixture with distilled water; usually less than 100 mL HCL solution was needed. After the neutralizing, the solution was dried as described in step (3).

The powders were then used for crystal structure analysis or further fabrication.

2.2 Synthesis of KNN and CuO-KNN Ceramics

Subsequent to the hydrothermal synthesis of KNbO_3 and NaNbO_3 powders, solid-state reaction method is adopted to prepare $(\text{K,Na})\text{NbO}_3$ and $\text{CuO}-(\text{K,Na})\text{NbO}_3$ ceramics. The present section introduces the experimental details of the ball milling, pressing, and the sintering processes [58].

2.2.1 Synthesis of KNN ceramics

Using the hydrothermal synthesized powders, ceramics were prepared as follows:

(1) After the reaction, cooling, and neutralization, the KNbO_3 and NaNbO_3 powders were mixed in a molar ratio of 48:52, which proved to be the morphotropic phase boundary (MPB) in KNbO_3 - NaNbO_3 system with a high piezoelectric coefficient d_{33} [58]. In one synthesis, 11.0000 g KNbO_3 powders and 10.8502 g NaNbO_3 powders were usually used.

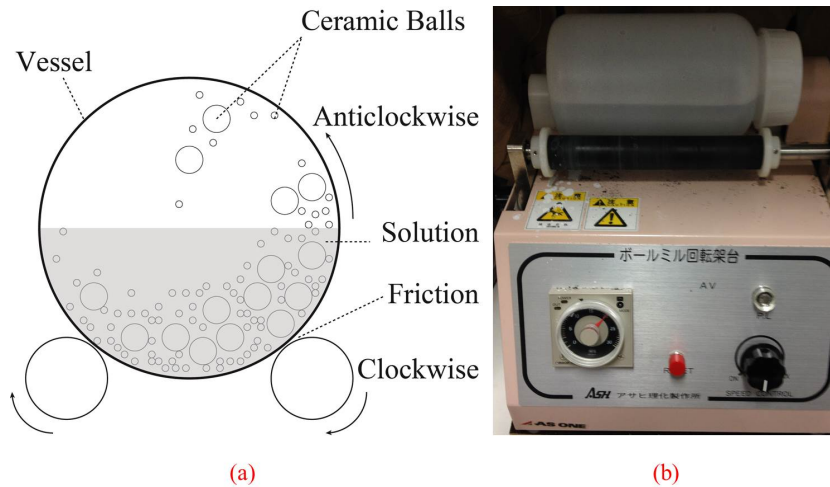


Figure 2.2: (a) Schematic diagram and (b) photo of ball milling process.



Figure 2.3: Photo of 425 μm sieve.

(2) The mixture was ball milled for 24 h to obtain a powder mixture with more uniform particle size. The powder mixture was then placed into a polyethylene

bottle with 200 mL distilled water, 100 radius-10 mm zircon balls, and 100 g radius-2 mm zircon balls. Then the bottle was laid on a ball milling rotator (Asahi Mill Pot Rotator AV-1) and ball milling was performed for 24 hours. The schematic diagram and photo of ball milling are shown in Fig. 2.2.

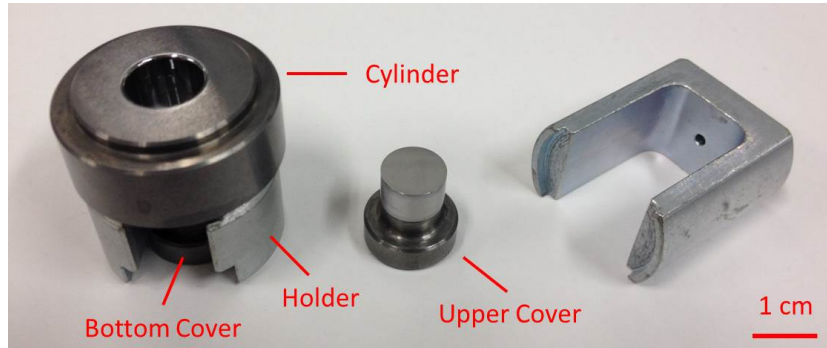


Figure 2.4: Photo of ceramic pressing mold.

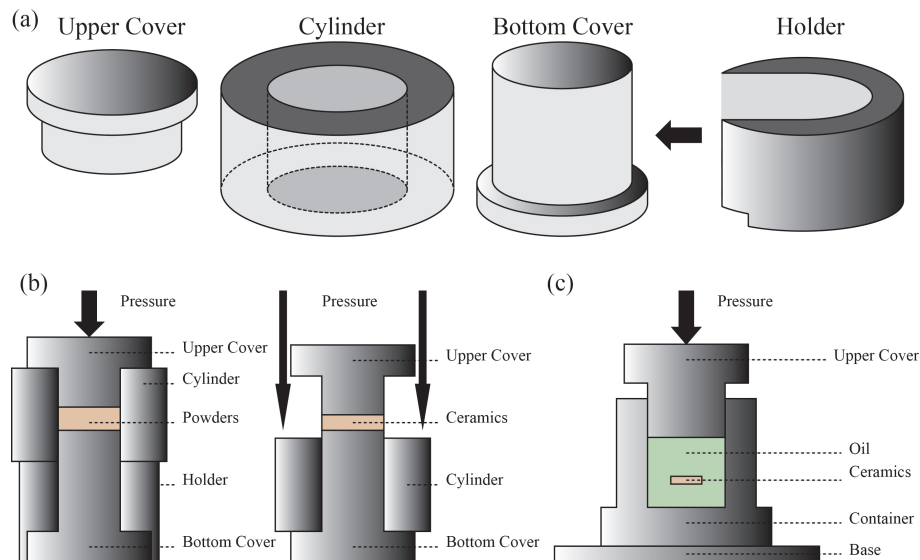


Figure 2.5: Schematic diagram of (a) four part of pressing mold, (b) ceramic pressing procedures, and (c) cold isostatic pressing.

(3) Filtering with a Teflon filter paper with a pore size $0.45 \mu\text{m}$ (Millipore Corporation Millipore Omnipore Membrane Filters) was carried out to eliminate the distilled water and zircon balls (left in the polyethylene bottle). The wet powders were dried in a constant temperature oven (Yamato DKN 302) under $130 \text{ }^\circ\text{C}$ for several hours.

(4) The powders were crushed in a mortar to prevent from caking. Then the powders were sieved with a $425\ \mu\text{m}$ sieve (as shown in Fig. 2.3). For each disk ceramic 0.3 g mixed powders were pre-weighed.

(5) These powders were placed into a mould (Super Hard Mould NPA System) as shown in Fig. 2.4 and the schematic diagram of four parts is show in Fig. 2.5 (a). The powders in the mould were uniaxially pressed into 10 mm-diameter and 2-mm-thick disks under 128 MPa by an oil press (AS ONE AH-2003) for 10 seconds. The schematic diagram of the pressing process is shown in Fig. 2.5 (b); at first the powers were pressed into a pellet; then the holder was removed and the cylinder was pressed to the bottom so that we could reach the pellet.

(6) The disks were pressed by a cold isostatic pressing or CIP (NPa system CPP-35), the schematic diagram of which is show in Fig. 2.5 (c). Prior to that, to prevent oil contamination the pellets were placed into the finger part of vinyl gloves, which were sealed by a vacuum packing machine (Sansho Industry BMV-280A). Then the pellets in the vinyl packing were placed in the container of CIP and pressed under 200 MPa for 3 minutes. Here, to prevent corrosion, the aqueous solution containing corrosion inhibitor (Tomyx Japan Tomyx water) was used.

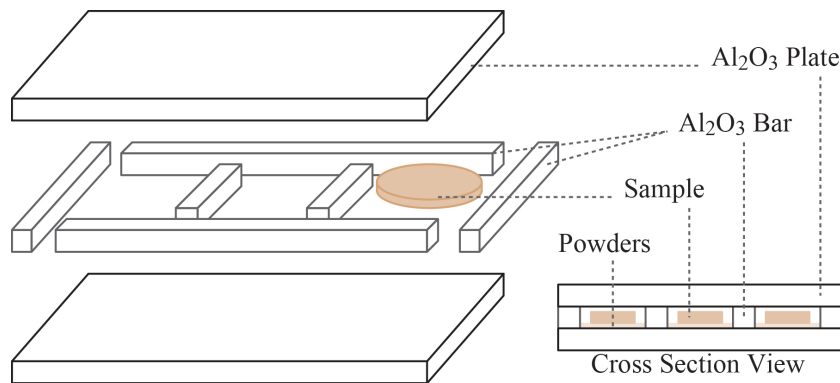


Figure 2.6: Schematic diagram of ceramics sintering.

(7) Since the vaporization of KNbO_3 powders in the sintering process is a significant obstacle, it's necessary to prevent the vaporization of KNbO_3 as possible as we can. The configuration in Fig. 2.6 was adopted; the pellets were located into narrow spaces separated from each other and the outside. Then the whole part in Fig. 2.6 was located in an Al_2O_3 crucible.

(8) The pellets in the Al_2O_3 crucible were then sintered at $1125\ ^\circ\text{C}$ for 2 hours in a muffle furnace (Yamada Denki TSR-430). Before reaching the sintering temperature, the samples were fired at $600\ ^\circ\text{C}$ for 4 hours to stabilize the disk shape (avoiding distortion due to fast shrinking) [58]. The heating and cooling rates were 150 and $100\ ^\circ\text{C}/\text{h}$, respectively. The programmed temperature curve of the furnace

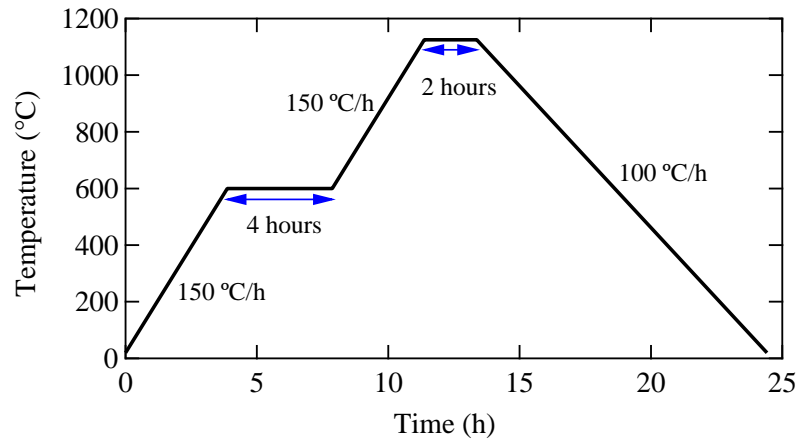


Figure 2.7: The temperature curve in the muffle furnace programming.

is shown in Fig. 2.7.

2.2.2 Synthesis of CuO-KNN ceramics

Doping with CuO was introduced to enhance to quality factor and 1.2 mol% CuO doping KNN ceramics exhibited a large quality factor [105]. The fabrication of CuO-(K,Na)NbO₃ ceramics was similar to that of (K,Na)NbO₃ ceramics [105]. For the doping of CuO, in the powders 1.2 mol% of CuO powder (99.9%, Kanto Chemical) was also mixed. After the mixing and ball milling, pH should be tested and neutralizing process should be used again if necessary. Besides, the sintering temperature adopted was 1050 °C instead of 1125 °C.

2.3 Physical Characteristics and Ceramic Processing

This section first introduces the determination of physical properties of the ceramics, including crystal structure analysis and density test; then provide the processing processes of ceramics, such as poling, polishing, and cutting.

2.3.1 X-ray diffraction

X-ray diffraction (usually referred to as XRD) is a method used for identifying the molecular and atomic structure of a material [106]. The principle is that the atoms in the material result in the diffraction of the incident X-ray beam in multiple specific directions [106]. By measuring the angle-dependent intensities of the diffracted X-ray beams, a three-dimensional spectrum of the electron density in the material can

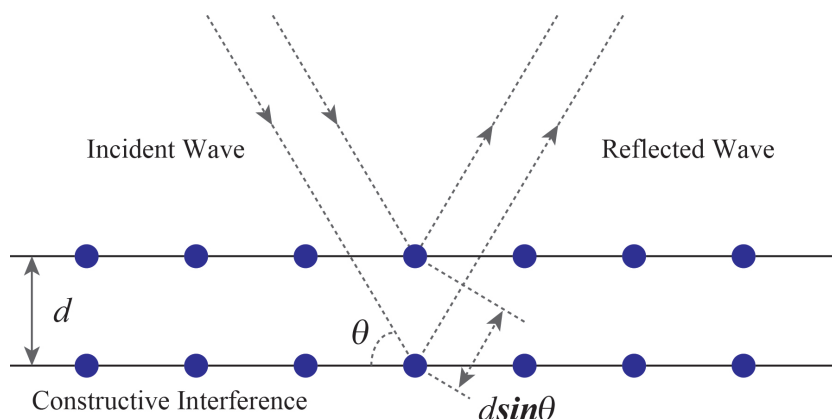


Figure 2.8: Bragg's law.

be obtained. In the X-ray spectra of crystals, the signals are much stronger than the amorphous samples due to the periodicity. For crystals (powders or ceramics), based on the electron density spectrum the mean positions of the atoms in the crystal can be determined, as well as the crystal system, the space group, the lattice parameters, and other information. Although in most directions the destructive interference results in weak intensity, strong intensity appears in a few specific directions due to constructive interference, determined by Bragg's law (Fig. 2.8), as expressed by the following equation [106]:

$$2d \sin \theta = n\lambda, \quad (2.1)$$

where d , θ , and λ are spacing between the planes in the atomic lattice, angle between the incident X-ray and interface, and wavelength of the incident X-ray, respectively; and n is an integer. In this study, crystal structural characterization was performed using a desktop X-ray diffractometer (Rigaku MiniFlex II).

Table 2.1: XRD measurement conditions.

X-Ray	CuK α
Voltage	30 kV
Current	15 mA
Scan mode	2θ - θ
Divergence slit	1.25 °
Soller slit	1.25 °
Receiving slit	0.8 mm
Step size	0.0005 °

(1) To measure the XRD spectrum of powders, a glass holder was used. The powders after grinding were placed in the recess of the holder. Another glass slide

was used to planish the powders and the holder was loaded into XRD chamber and fixed by the magnetic clamps. The adopted measurement conditions were listed in Table 2.1.

(2) To measure the XRD spectrum of ceramics, since usually the thickness of ceramics is about 1 mm, larger than the depth of the holder recess (0.3 mm), an aluminum plate was used to adjust the surface of the ceramic and the holder to the same plane. The other steps were the same as (1).

2.3.2 Density test

Compactness is an important prerequisite for piezoelectric ceramics and has a significant influence on the various properties; materials that are too porous or loose may exhibit insufficient piezoelectric performance and would thus be unsuitable for practical applications. For ceramics, density can be categorized to theoretical density, apparent density, bulk density, and so on [107]. The theoretical density is grounded on the assumption of ideal arrangement lattices; which can be determined from the type and number of atoms in the unit cell volume. In ceramics, there are pores and defects; the measured volume of the ceramics may be affected by rough surface, inner pores, the space between particles, and space between particles and container. Because the inner pores cannot be removed easily, the volume including particle size, particle-particle space, and inner pores is used to calculate the apparent density.

In this study, the density of ceramics is measured using an electronic densimeter (Alfamirage SD-200L). The principle is Archimedes' principle, which indicates that the upward buoyant force exerted on an object immersed in any fluid equals to the weight of the fluid displaced by the object [108]. At first, the ceramics was dried and weighed in air; then the weight in water was recorded when the weight becomes stable. The measurement should be carried out at room temperature (about 20 °C) to avoid weight fluctuation. The average value of three measurements was used.

The sample density ρ can be expressed by

$$\rho = \rho_0 \frac{W_0}{W_0 - W_1}, \quad (2.2)$$

where ρ_0 , W_0 , and W_1 are water density (10^3 kg/m^3), sample weight in air, and sample weight in the fluid, respectively.

2.3.3 Ceramics processing

Subsequent to sintering, the pellets were polished to remove the convex and concave on the surfaces with water-resistant sandpapers (Grit designation: 1000, and 2000) on a glass disk plate. The pellets were polished following the "8"-shaped pattern to

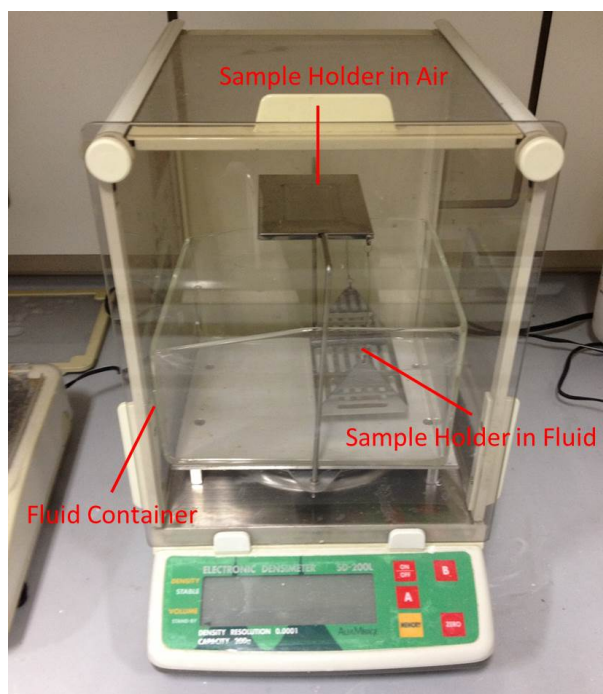


Figure 2.9: Photo of the electronic densimeter (Alfamirage SD-200L).

ensure their exactly the same thickness. This procedure was repeated from coarser sandpaper to finer sandpaper and repeated the same processing for another side of the pellets until desired thickness was reached. After that the pellets were cleaned in acetone using ultrasonic cleaning for 5 minutes and then were dried in the oven. The dimensions of the samples were measured using a micrometer.

Electrodes on the surface of the ceramics are necessary to measure electrical properties. Au electrodes were sputtered on both sides of the ceramics via a quick coater (Sanyu Electron Quick Coater SG-701) shown in Fig. 2.10. Here, to protect the pellet flank from being sputtered, we used a thermal compression tube (G-APEX GS(F) E255532 125 °C VW-1, 10 mm) to cover the flank. The air flow was controlled so that the current was around 10 mA. For each side sputtering was carried out for 15 minutes. The thermal compression tube was then removed.

Figure 2.11 shows the poling system. Poling procedure was carried out in an oil bath (Tokyo Rika Kogyo OHB-100G); in which silicon oil (Shin-Etsu Chemical KF-54) was preheated to 100 °C to prevent from breakdown. The oil bath was in a protection cover used to separate the heat transfer and prevent high voltage. The pellets were placed on the sample holder and poled by a high-voltage power supply (Matsusada Precision HARb-30P1). For different specimens, the applied electrical field varied from 2 kV/mm to 4 kV/mm; poling time lasted for 10-20 minutes.



Figure 2.10: Photo of the quick coater.

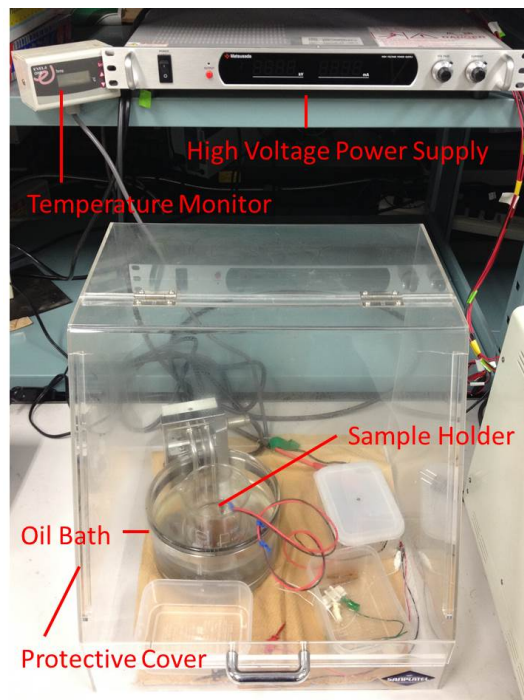


Figure 2.11: Photo of the poling equipment.

2.3.4 Plate and bar transducers

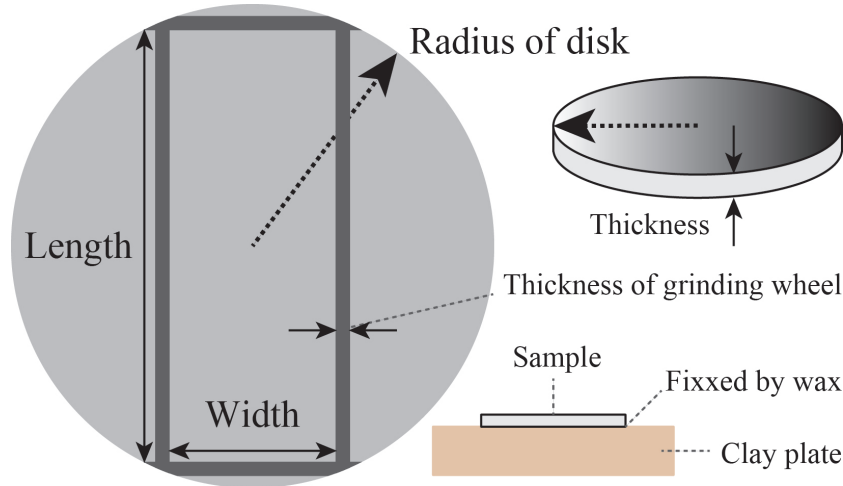


Figure 2.12: Schematic diagram of cutting process.

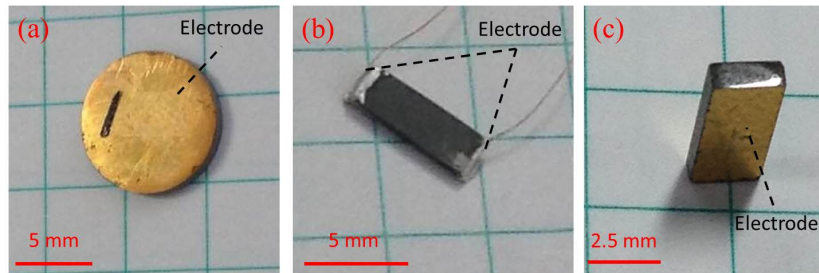


Figure 2.13: Photos of the prepared (a) disk, (b) bar, and (c) plate transducers.

Plate and bar transducers are required to analyze the 31 and 33 vibration mode properties. After polishing, the disk pellet was adhered to a clay plate using a hot-melt adhesive (Nikka Seiko solid wax). Then the pellet along with the clay plate (to help the horizontal-vertical leveling) was cut into plate or bar with desired size using a precision cutter (Musashino Denshi MPC-130). The schematic diagram of cutting is shown in Fig. 2.12. The desired size was marked on the disk with considering the thickness of the grinding wheel. A soldering iron was used to melt the wax to separate the cut ceramics from the clay plate.

The cutting sections of the plate and bar transducers were then polished using water-resistant sandpapers (Grit designation: 1000 and 2000); finer sandpapers (Grit designation: 5000 and 10000) were used then so that the surface can reflect laser (useful later). The photos of disk, bar, and plate transducers are shown in Fig. 2.13 (a)-(c), respectively.

2.4 Determination of Electrical Properties

This section introduces the method to measure and calculate the electrical properties of piezoelectric ceramics.

2.4.1 Permittivity

Disk-shaped ceramics with diameter D and thickness t are usually used to determine the permittivity coefficient. The static capacity C_p and dielectric loss $\tan \delta$ can be obtained from the 1 kHz $C_p - D$ measurement via a precision impedance analyzer (Agilent Technologies 4294A) [109]. Relative permittivity coefficient ε_r is given by

$$\varepsilon_r = \frac{\varepsilon_{33}^T}{\varepsilon_0} = C_p \frac{4t}{\varepsilon_0 \pi D^2}, \quad (2.3)$$

where ε_{33}^T is the absolute permittivity of the material; and $\varepsilon_0 = 8.854 \times 10^{-12}$ (F/m) is vacuum permittivity. For a non-ideal capacitor the imperfections results in energy dissipating, expressed by a parallel equivalent resistance R_p [109]. The relationship between dielectric loss $\tan \delta$ and the equivalent circuit parameters can be expressed by

$$\tan \delta = \frac{1}{\omega C_p R_p}. \quad (2.4)$$

2.4.2 Admittance curve

The electrical property around the resonant frequency of the transducer can be given by the admittance curve (or impedance curve). When a plate transducer is driven by an AC voltage, the schematic diagram of the fundamental vibration in the transducer is illustrated in Fig. 2.14. As shown in Fig. 2.14(b), the poling direction is along the thickness (z axis) and the stress, strain, and displacement are along the x axis. In the fundamental vibration, the maximum stress (and strain) is at the middle of the transducer; while the maximum displacement (and velocity) appears at both ends of the transducer.

The admittance curves of piezoelectric materials at low voltage are measured via a precision impedance analyzer (Agilent Technologies 4294A). The adopted measuring voltage is $0.5 V_{pp}$. A typical admittance curve of a PZT disk transducer (Fuji Ceramics C-203) is shown in Fig. 2.15, from which resonant frequency f_r and antiresonant frequency f_a can be obtained.

The admittance curve is equivalent to the admittance circle [35], as shown in Fig. 2.16. The horizontal and vertical axis are the real part (electrical conductance

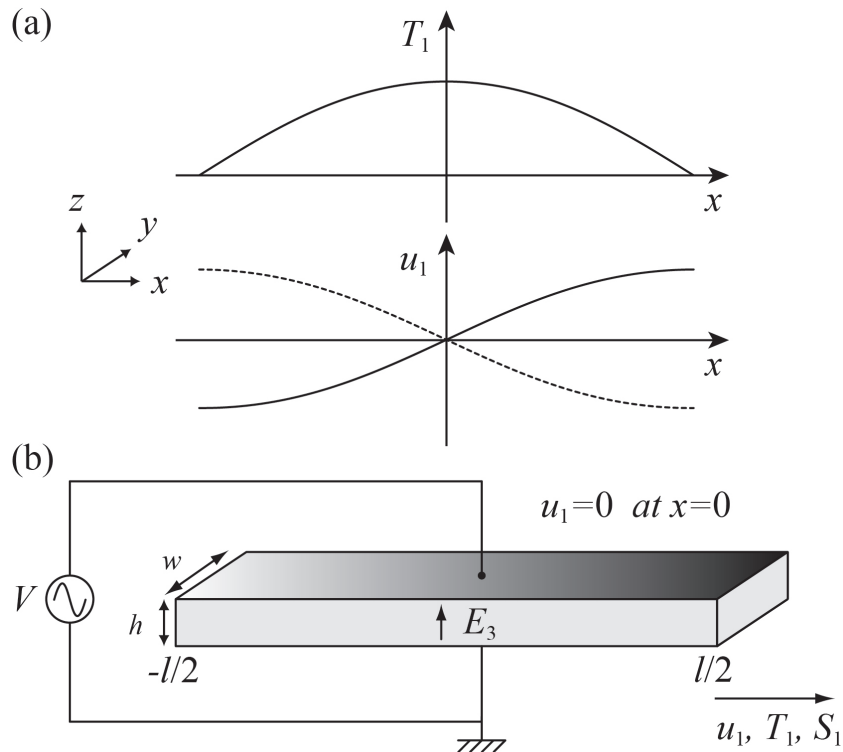


Figure 2.14: Schematic diagram of (a) stress T_1 , displacement u_1 , and (b) plate transducer driven by an electric field E_3 .

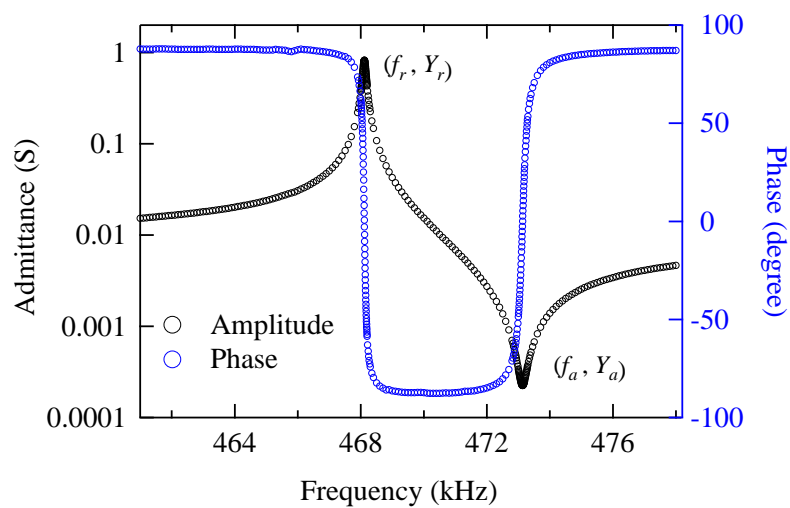


Figure 2.15: The admittance curve (amplitude and phase) of a PZT disk transducer, the resonant and antiresonant frequencies are f_r and f_a , respectively.

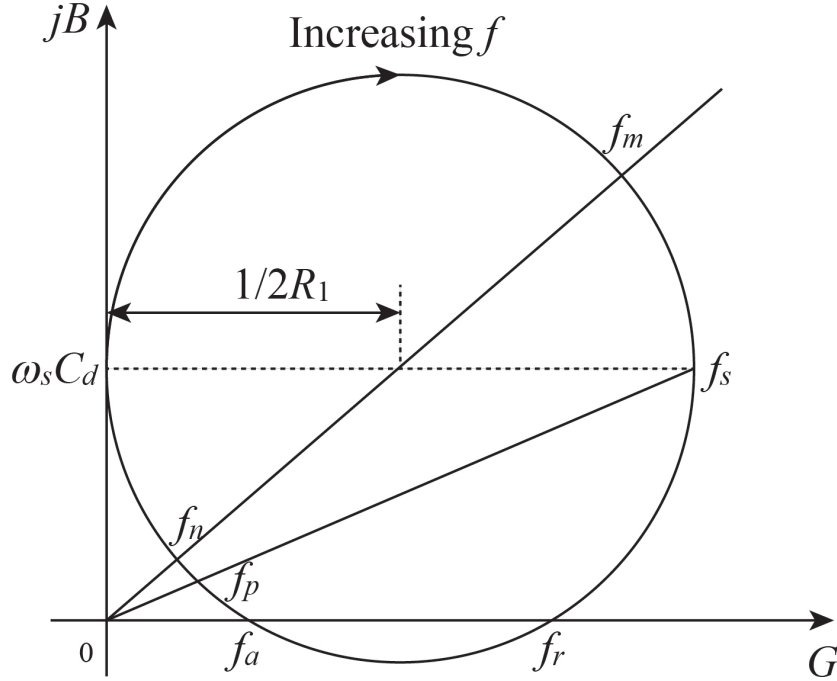


Figure 2.16: Admittance circle.

G) and imaginary part (electrical susceptance B) of the admittance, respectively. The frequencies f_r and f_a are defined when the phase is 0:

$$B = \omega C_d + B_1 = 0. \quad (2.5)$$

The mechanical vibration of piezoelectric transducers is similar to LC circuit; series resonant frequency f_s and parallel resonant frequency f_p are defined when

$$B_1 = 0. \quad (2.6)$$

In practical experiments, the observed frequencies are f_m and f_n , corresponding to the maximum and minimum admittance values. The three series of frequencies are located in different places of the admittance circle (Fig. 2.16). It is easy to prove that the three series of frequencies are not the same when the equivalent resistance R in the equivalent circuit (Fig. 2.18) is not zero. The relationships between f_r , f_a and f_s , f_p can be expressed by

$$f_r^2 \approx f_s^2 \left(1 + \frac{R^2 C_d}{L}\right), \quad (2.7)$$

$$f_a^2 \approx f_p^2 \left(1 - \frac{R^2 C_d}{L}\right). \quad (2.8)$$

Similarly, the relationships between f_m , f_n and f_s , f_p can be expressed by

$$f_m^2 \approx f_s^2 \left(1 - \frac{R^2 C_d}{L}\right), \quad (2.9)$$

$$f_n^2 \approx f_p^2 \left(1 + \frac{R^2 C_d}{L}\right). \quad (2.10)$$

So, when $R \neq 0$, the six frequencies are in the following order:

$$f_m < f_s < f_r, \quad (2.11)$$

$$f_n > f_p > f_a. \quad (2.12)$$

Since it is most convenient to determine f_m and f_n ; considering usually we have $R^2 C_d/L \ll 1$ because

$$\frac{R^2 C_d}{L} = \frac{C_d \omega_r^2 L^2}{L Q_m^2} = \frac{1}{Q_m^2} \frac{C_d}{C} \ll 1, \quad (2.13)$$

we can take the f_m and f_n values to be f_r and f_a [35]. Here we use the expression of quality factor $Q_m = \omega_r L/R$, which will be explain in next subsection.

2.4.3 Equivalent circuit

The mechanical vibration of the piezoelectric transducers is similar to the simple harmonic motion of a spring-mass system (as shown in Fig. 2.17(a)). For an ideal one-dimensional harmonic vibration, the solution satisfies

$$m \frac{d^2 x}{dt^2} = -kx + F, \quad (2.14)$$

where m , k , x , and F are inertial mass, spring constant, displacement, and applied force in the system, respectively. Similarly, the LC circuit in Fig. 2.17(a) follows the equation

$$L \frac{d^2 Q}{dt^2} = -\frac{Q}{C} + V, \quad (2.15)$$

where L , Q , C , and V are inductance, charge, capacitance, and voltage, respectively.

When the damping cannot be neglected, the behavior can be expressed by

$$m \frac{d^2 x}{dt^2} = -kx - \zeta \frac{dx}{dt} + F, \quad (2.16)$$

where ζ is the damping ratio. Similarly, a resistance R can be introduced to the LC circuit when taking the damping into account:

$$L \frac{d^2 Q}{dt^2} = -\frac{Q}{C} - R \frac{dQ}{dt} + V. \quad (2.17)$$

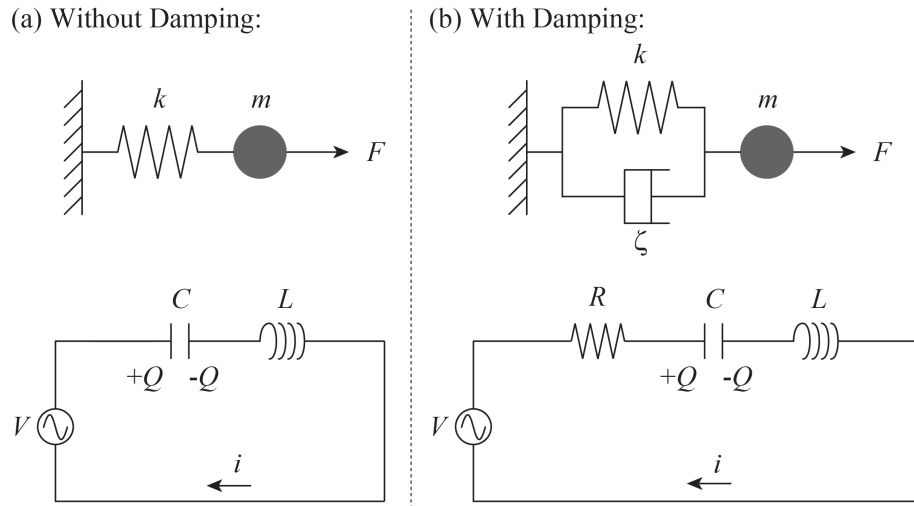


Figure 2.17: The equivalent circuits of spring-mass system (a) without damping and (b) with damping.

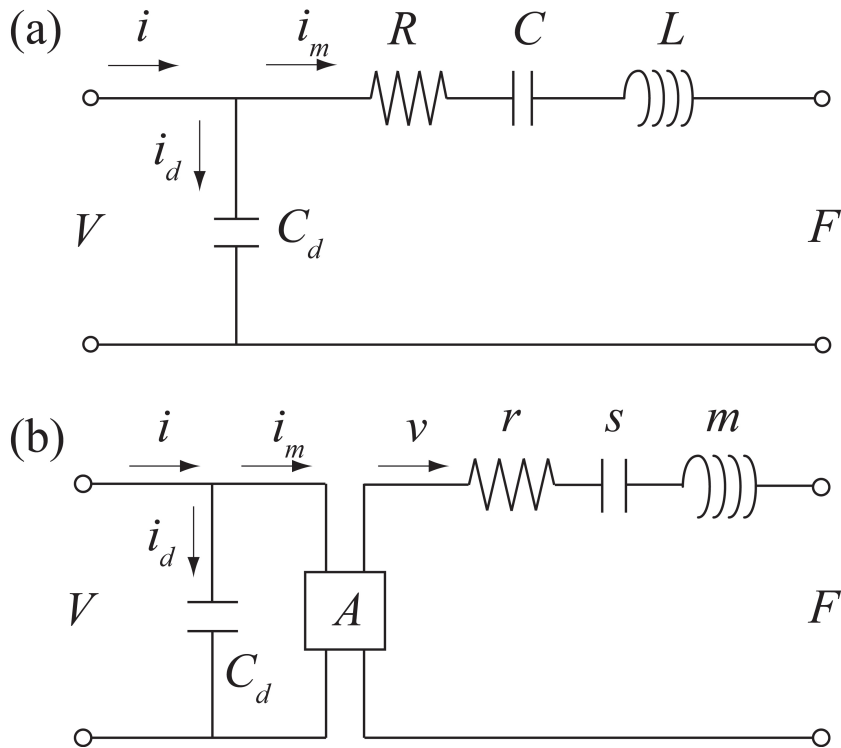


Figure 2.18: The conventional equivalent circuit of a piezoelectric transducer driven by an AC voltage.

Besides, as explained before, the transducer has a static capacitance, which is only dependent on the size and dielectric constant (or permittivity) at low electrical field. Hence, for a piezoelectric transducer driven by an AC voltage (shown in Fig. 2.14), the fundamental vibration is usually described by an equivalent circuit in Fig. 2.18(a); R , C , and L are equivalent resistance, capacitance, and inductance, respectively. Here, force factor A is usually used to represent the piezoelectric effect; as shown in Fig. 2.18(b). In Fig. 2.18(b), the left half is the electrical branch and the right half is the mechanical branch, i_m , v , F , and V are motional current (the current flowing in the mechanical branch), velocity, force, and voltage, r , s , m are equivalent mechanical loss, equivalent spring constant, and equivalent mass, respectively. The force factor A is defined by

$$A = \frac{i_m}{v} = \frac{F}{V}. \quad (2.18)$$

Relationships between R , C , L in Fig. 2.18 (a) and r , s , m in Fig. 2.18 (b) can be expressed by

$$R = \frac{r}{A^2}, \quad (2.19)$$

$$C = \frac{A^2}{s}, \quad (2.20)$$

$$L = \frac{m}{A^2}. \quad (2.21)$$

Except for the fundamental vibration, high mode vibrations also exist; similar to Fig. 2.18, each high mode vibration can be considered as one LCR series circuit [93], which is parallel to each other.

2.4.4 Resonant-antiresonant method

Evaluation of piezoelectric properties is based on the IEEE resonant-antiresonant method [104]. The method to determine piezoelectric coefficients, elastic stiffness coefficients, electromechanical coupling factors, and permittivity coefficient are given as follows.

For a disk transducer with a radius a , the stiffness coefficient c_{11}^E is given by the following equation:

$$f_r = \frac{2.05}{2\pi a} \sqrt{\frac{c_{11}^E}{\rho(1 - \sigma^2)}}, \quad (2.22)$$

where ρ is the density and σ is Poisson's ratio. For the perovskite materials, the Poisson's ratio is about 0.3 [93]. For a bar transducer with a length l , the stiffness

coefficient c_{33}^E can be determined by the following equation:

$$f_r = \frac{1}{2l} \sqrt{\frac{c_{33}^E}{\rho}}. \quad (2.23)$$

The electrical-mechanical coupling factor k_{31} and k_{33} can be determined by the resonant frequency f_r and anti-resonant frequency f_a [35], expressed by

$$\frac{1}{k_{ij}^2} = a \frac{f_r}{f_a - f_r} + b, \quad (2.24)$$

where, a and b are parameters depending on the vibration mode; for radial mode (a, b) = (0.395, 0.574); for 31 mode (a, b) = (0.405, 0.595); and for longitudinal mode (a, b) = (0.405, 0.810). Piezoelectric d coefficients in radial and longitudinal mode are determined by corresponding coupling factor, relative permittivity coefficient, and stiffness coefficients:

$$d_{31} = k_{31} \sqrt{\varepsilon_{33}^T / c_{11}^E}, \quad (2.25)$$

$$d_{33} = k_{33} \sqrt{\varepsilon_{33}^T / c_{33}^E}. \quad (2.26)$$

Mechanical quality factor (Q_m) is a dimensionless parameter describing the energy dissipation ratio in mechanical vibrations, the definition of which is

$$Q_m = 2\pi \times \frac{\text{Energy Stored}}{\text{Energy dissipated per Cycle}}. \quad (2.27)$$

For simplicity, using the equivalent circuit in Fig. 2.18, the quality factor can be given by:

$$Q_m = \frac{2\pi f_r L}{R}, \quad (2.28)$$

where L , C , R , and C_d can be determined by the admittance curve. As shown in Fig. 2.18, two typical points (f_r, Y_r) and (f_a, Y_a) or (ω_r, Y_r) and (ω_a, Y_a) are used. Since

$$Y(\omega) = j\omega C_d + \frac{1}{j\omega L + R + \frac{1}{j\omega C}}, \quad (2.29)$$

when $\omega = \omega_r$, $Y(\omega)$ reaches the maximum, neglecting R we have

$$\omega_r^2 = \frac{1}{LC}. \quad (2.30)$$

Similarly, when $\omega = \omega_a$, $Y(\omega)$ reaches the minimum, also neglecting R we have

$$j\omega_a C_d + \frac{1}{j\omega_a L + \frac{1}{j\omega_a C}} = 0; \quad (2.31)$$

$$\omega_a^2 = \frac{1}{L} \left(\frac{1}{C_d} + \frac{1}{C} \right). \quad (2.32)$$

Combining Eqs. 2.30 and 2.32 we have

$$L = \frac{1}{C_d} \frac{1}{\omega_a^2 - \omega_r^2}, \quad (2.33)$$

$$C = C_d \frac{\omega_a^2 - \omega_r^2}{\omega_r^2}. \quad (2.34)$$

Both (ω_r, Y_r) and (ω_a, Y_a) satisfy Eq. 2.29. When $\omega = \omega_r$ we have

$$Y_r = \sqrt{\left[\omega_r C_d - \frac{\omega_r L - \frac{1}{\omega_r C}}{R^2 + \left(\omega_r L - \frac{1}{\omega_r C} \right)^2} \right]^2 + \left[\frac{R}{R^2 + \left(\omega_r L - \frac{1}{\omega_r C} \right)^2} \right]^2}, \quad (2.35)$$

using Eqs. 2.33-2.34, Eq. 2.35 becomes

$$R = \frac{1}{\sqrt{Y_r^2 - \omega_r^2 C_d^2}}. \quad (2.36)$$

When $\omega = \omega_a$ we have

$$Y_a = \sqrt{\left[\omega_a C_d - \frac{\omega_a L - \frac{1}{\omega_a C}}{R^2 + \left(\omega_a L - \frac{1}{\omega_a C} \right)^2} \right]^2 + \left[\frac{R}{R^2 + \left(\omega_a L - \frac{1}{\omega_a C} \right)^2} \right]^2}, \quad (2.37)$$

using Eq. 2.36, Eq. 2.37 becomes

$$Y_a^2 = \frac{\omega_a^4 C_d^4}{Y_r^2}, \quad (2.38)$$

$$C_d = \frac{\sqrt{Y_r Y_a}}{\omega_a}. \quad (2.39)$$

The parameters L, C, R, C_d in the equivalent circuit can be given by Eqs. 2.33-2.34, 2.36, and 2.39, respectively.

2.5 Burst Mode Method

As mentioned in section 1.4.6, the heat generation of piezoelectric devices under high voltage operation results in a large temperature rise. This is inappropriate for property evaluation because the saturated temperature might be very different when driving frequency has a slight shift. To observe and study the pure high power effects, the temperature effect in the experiments should be negligible.

The burst mode method was suggested by M. Umeda et al. [110] to eliminate the heat generation so that the high voltage effect under room temperature can be separated from the temperature influence.

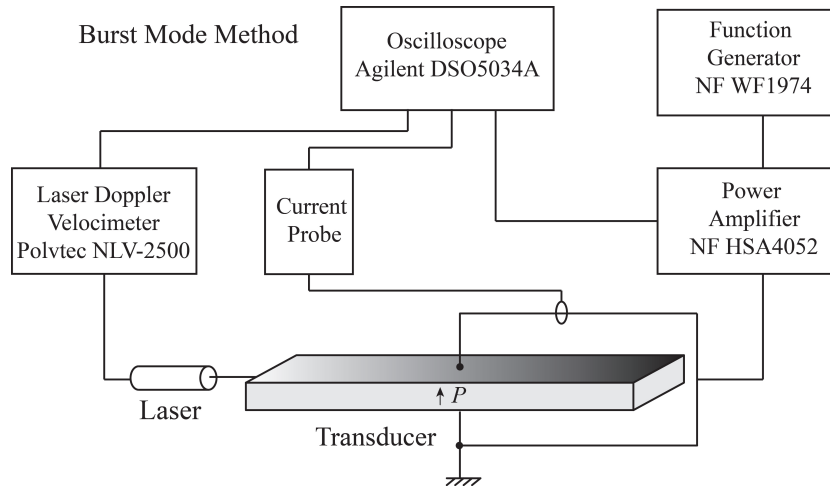


Figure 2.19: Schematic diagram of burst mode measurement system.

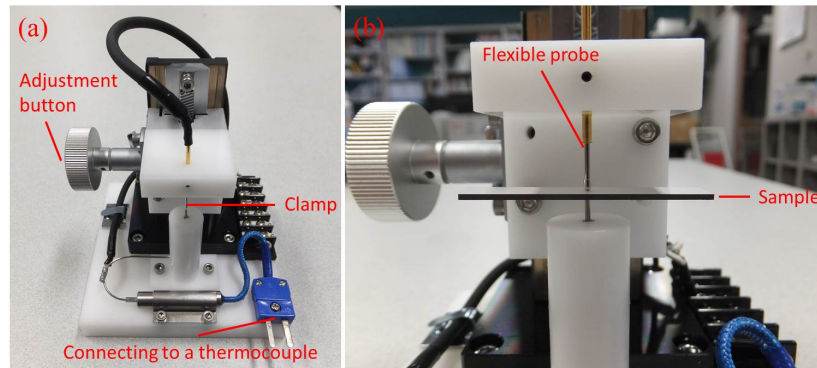


Figure 2.20: Photos of the holder: (a) front image and (b) with the sample.

The schematic diagram of burst mode measurement setup is shown in Fig. 2.19. In burst mode measurements, the samples were driven by a function generator (NF WF1974) connected by a power amplifier (NF HSA4052). The transducer vibration velocity was measured by a laser Doppler vibrometer (Polytec NLV-2500). The driving voltage, current, and vibration velocity were monitored and recorded by an oscilloscope (Agilent DSO5034A). The driving signal was set in the burst trigger mode. After each trigger signal, subsequent to sinusoidal waves (1000 cycles), the electrical driving port was shortened. Different driving voltages were chosen; and the frequency of the driving voltage was determined to be close to the resonant frequency measured by the NF FRA5097 prior to this procedure. The current was detected by a current probe amplifier (Tektronix TCP A300). The temperature on the surface of the transducers during the measurements was monitored and recorded by a multifunctional logger (Graphtec midi logger GL200), the resolution of which

was 0.1 °C. The samples were clamped in the holder shown in Fig. 2.20.

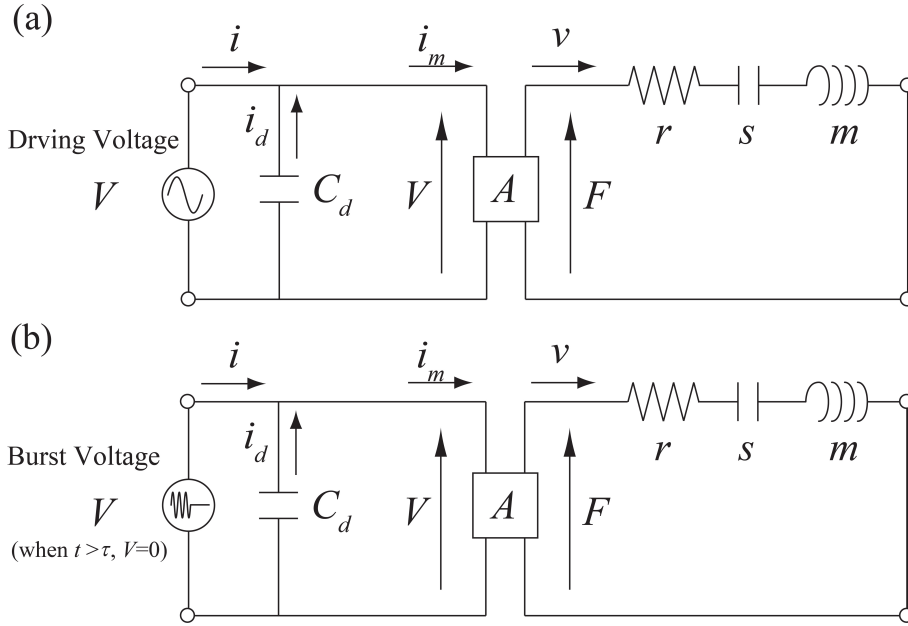


Figure 2.21: The equivalent circuits of (a) continuous driving and (b) burst mode measurement system.

When a continuous voltage is applied on the transducer, the transducer gets excited and vibrates under the driving, as shown in Fig. 2.21(a). On the opposite, in the burst mode measurement, the burst voltage only lasts for a short time; given by the driving frequency and set cycles. After the excitation, the electrical branch is shortened, as shown in Fig. 2.21 (b). In this case, the damped current i_d is

$$i_d = 0. \quad (2.40)$$

And total current i equals to the motional current i_m :

$$i = i_m. \quad (2.41)$$

The schematic diagram of burst mode results is shown in Fig. 2.22. In Fig. 2.22, the burst voltage stops at the time t_0 ; while the transducers continues vibrating (free vibration), as indicated by the velocity and the current. Owing to the existence of damping, both velocity and current decrease with time. Based on the burst mode results, many properties can be determined as follows.

In the free vibration, the vibration velocity at the end of the transducer can be expressed by

$$v = v_0 \exp(-\beta t) \sin \omega_r t, \quad (2.42)$$

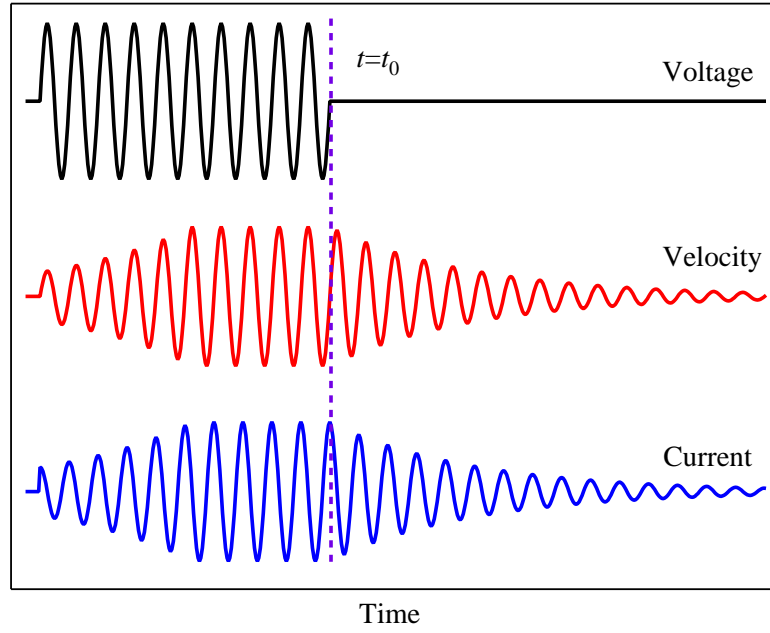


Figure 2.22: Schematic diagram of driving voltage, vibration velocity, and current in burst mode results.

where v_0 , β , and ω_r are the velocity amplitude, velocity decay rate, and angular resonant frequency, respectively. The velocity-time curve gives the value of β and ω_r ; which can be used to determine r and s (Fig. 2.21):

$$r = 2m\beta, \quad (2.43)$$

$$s = m\omega_r^2, \quad (2.44)$$

where equivalent mass m is the half of transducer mass M . Quality factor Q_m can be determined by

$$Q_m = \frac{\omega_r}{2\beta}. \quad (2.45)$$

The compliance coefficient s_{11}^E is given by

$$s_{11}^E = \frac{\pi^2}{l^2\omega_r^2\rho} = \frac{1}{4l^2f_r^2\rho}, \quad (2.46)$$

where f_r is the resonant frequency.

The maximum stress T_m appears at the middle of the transducer and can be expressed by

$$T_m = \sqrt{\frac{\rho v_0^2}{s_{11}^E}} = \rho c v_0. \quad (2.47)$$

Based on the motional current i_m , the determination of current amplitude i_0 , β and ω_r are also available, which is also useful for further analysis. Force factor A is given by

$$A = \frac{i_0}{v_0}. \quad (2.48)$$

Using A and r , s , m we have

$$L = \frac{m}{A^2}, \quad (2.49)$$

$$C = \frac{A^2}{s}, \quad (2.50)$$

$$R = \frac{r}{A^2}. \quad (2.51)$$

The piezoelectric d coefficient is given by compliance coefficient s_{11}^E :

$$d_{31} = \frac{s_{11}^E A}{2w}. \quad (2.52)$$

where w is the width of the plate transducer.

Detailed analysis of the results in burst mode will be shown in chapter 4-5.

CHAPTER 3

Properties and Hardening of CuO-KNN

3.1 Background

The piezoelectrics are usually divided into two groups; which are referred to as “hard-type” (or “hard”) and “soft-type” (or “soft”) piezoelectrics. The essential is the mobility of the charge dipoles and domains, which affects the ferroelectric and piezoelectric properties. As mentioned in chapter 2, in the piezoelectrics, the quality factor Q_m is a physical quantity used to describe the energy dissipation ratio in mechanical vibration.

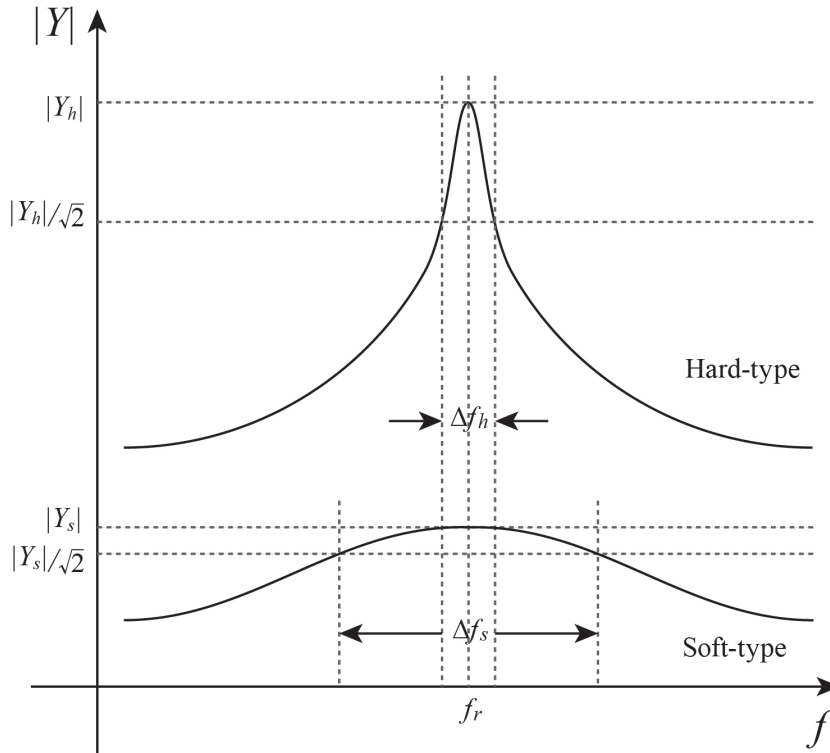


Figure 3.1: Determination of Q_m in hard-type and soft-type piezoelectrics.

For piezoelectrics, Q_m can be determined by Fig. 3.1. In the resonant range of the admittance curves, the admittance amplitude decreases dramatically with the deviating from the resonant frequency. Define the maximum amplitude as $|Y_0|$, two frequencies corresponds to the amplitude $|Y_0|/\sqrt{2}$; the range between them is the half bandwidth Δf . Q_m can be expressed by

$$Q_m = \frac{f_r}{\Delta f} \quad (3.1)$$

As shown in Fig. 3.1, in hard-type piezoelectrics, Δf is relatively smaller and Q_m is larger; while in soft-type piezoelectrics, Δf is relatively larger with a lower

Q_m . To date, no obvious boundary has been taken for separating the hard-type and soft-type piezoelectrics; however, normally soft-type piezoelectrics have a Q_m less than 100 while that of hard-type piezoelectrics is higher than 500 [80]. For simplicity, Q_m can also be calculated using the equivalent circuit parameters of piezoelectrics (chapter 2). For the record, in high power operation, it is difficult to calculate Q_m using abovementioned method or equivalent circuit owing to the deformation of admittance curves. An improved method to determine Q_m will be given in chapter 6.

Except for Q_m , it has been pointed out that soft-type piezoelectrics have relatively larger piezoelectric constants, permittivity (dielectric constant, loss), electro-mechanical coupling factors, and electrical resistance while exhibiting lower coercive fields, strong nonlinearity, and easier polarization process [111]. These distinctions are exactly the reason for the different applications of these two groups. Hard-type piezoelectrics are potential candidates for high power operated devices owing to their large piezoelectric coupling factors, high mechanical quality factor, and low dielectric loss; while soft-type piezoelectrics are suitable for actuators and sensors due to the easy polarization and high domain mobility.

(K,Na)NbO₃, as a potential lead-free substitute, has a drawback of low Q_m . Although it was suggested that to develop substitutes for hard- and soft-type PZT separately seemed to be also optional [30], attempts of modification has been made. Similar as PZT-based materials, doping is one of the most efficient methods employed to improve various properties, including enhancement of the Q_m [25]. Doping with low valence ions (acceptor impurities) in A sites (Pb²⁺) or B sites (Zr⁴⁺, Ti⁴⁺) of PZT can enhance the Q_m (hardening), whereas low valence doping can soften the materials (reducing the Q_m).

In the KNN system, two methods prove to be feasible in enhancing the Q_m . One of them is doping with low valence ions; oxides such as ZnO, CuO and MnO₂ have all been demonstrated to be effective for the improvement of the Q_m and other related piezoelectric properties [112]. We should notice that the hardening effect of CuO or MnO was also reported in other piezoelectrics, like Li/Ta-modified KNN [113], (K,Na)(Nb,Ta)O₃ [114], (Ca,Ba)TiO₃ [115], and so on.

Another method is using sintering aids. The addition of K_{5.4}Cu_{1.3}Ta₁₀O₂₉ (KCT) [57] and K₄CuNb₈O₂₃ (KCN) [116], has also been reported to be functional in enhancing Q_m . Both KCT and KCN, as additives, are working owing to the formation of a liquid phase in KNN during the sintering procedure [117], which leads to a significant improvement in the sinterability of the KNN ceramics and better piezoelectric properties.

It seems to be convincing that the Cu²⁺ ions in KCT and KCN also play an important role in increasing Q_m . In addition, increasing grain size and improved grain growth behavior might indicate that Cu²⁺ also has the effect of sintering aids

[118]. In this chapter, another method of enhancing Q_m is proposed, demonstrated, and discussed.

3.2 KNN Powders and Ceramics

Prior to the fabrication of (K,Na)NbO₃ ceramics, KNbO₃ and NaNbO₃ powders were prepared separately via hydrothermal method. The XRD patterns are shown in Fig. 3.2, which indicate an orthorhombic single phase for both KNbO₃ and NaNbO₃ powders; no evidence of impurity or secondary phase is observed.

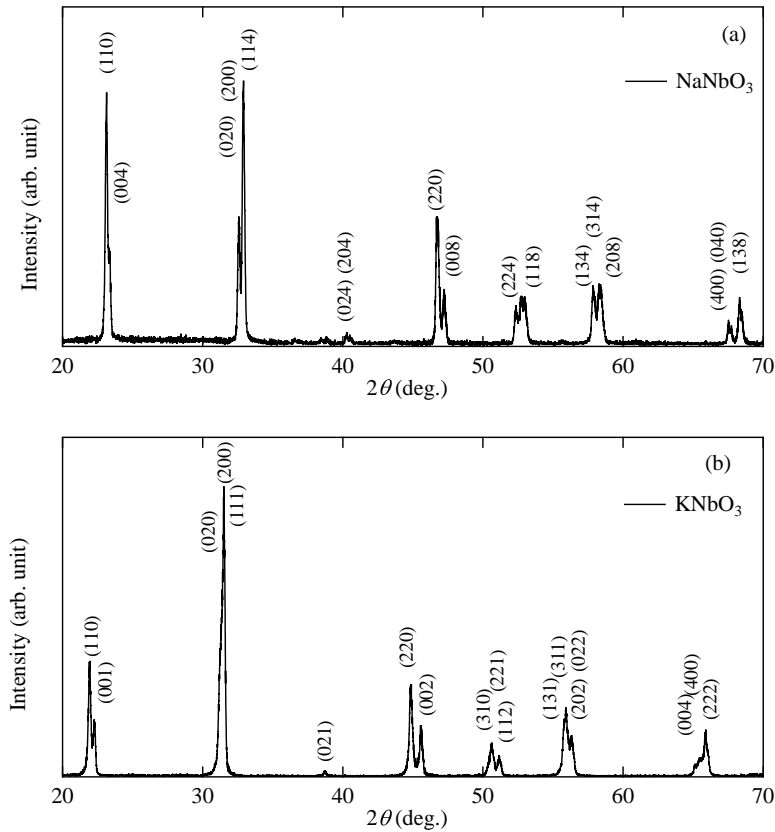


Figure 3.2: XRD spectra of (a) NaNbO₃ and (b) KNbO₃ powders.

(K,Na)NbO₃ ceramics were then prepared via solid-state reaction method (details seen in chapter 2). The XRD pattern is shown in Fig. 3.3, suggesting a pure orthorhombic phase. The spectrum is different from the one of KN and NN mixture powders; indicating that the whole reaction had been realized. The lattice parameters of the two powders and one ceramic are listed in Table 3.1.

The density of (K,Na)NbO₃ is about 4.46 g/cm³; which is about 98.9% of

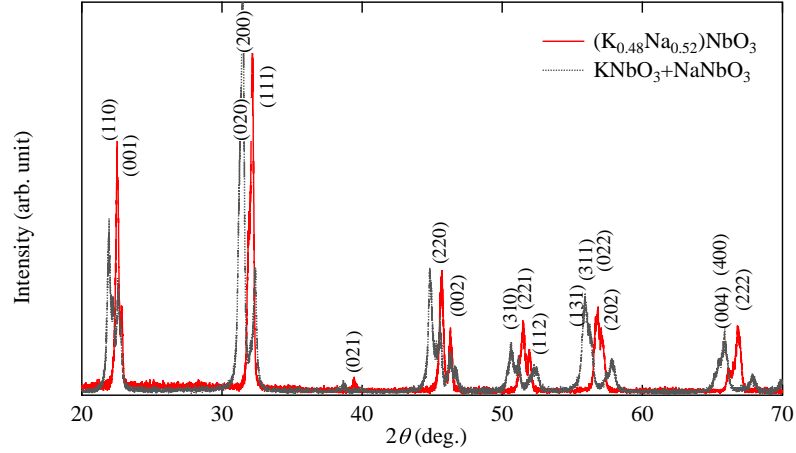


Figure 3.3: XRD spectrum of KNN ceramics.

Table 3.1: Lattice parameters of KNbO_3 , NaNbO_3 powders, and KNN ceramics.

	a (Å)	b (Å)	c (Å)
KNbO_3	5.706	5.736	4.000
NaNbO_3	5.504	5.569	15.490
$(\text{K,Na})\text{NbO}_3$	5.564	5.598	3.921

the theoretical value (4.51 g/cm^3). This high percentage of theoretical density obtained for these ceramics could be related to the uniform particle size of the powders synthesized via the hydrothermal method and few pores in the sintered ceramics. Figures 3.4(a)-(b) are the admittance curves of $(\text{K,Na})\text{NbO}_3$ disk and bar transducers. The fitting of Fig. 3.4 using the equivalent circuit mentioned in chapter 2 enables the determination of various parameters, as shown in Table 3.2.

Table 3.2: Equivalent circuit parameters of KNN transducers.

	L (mH)	R (Ω)	C (pF)	C_d (pF)
Radial	2.17	89.2	62.6	42.8
Longitudinal	255.6	13885	0.291	0.934

Table 3.3: Properties of KNN ceramics.

k_p	k_{33}	$\varepsilon_{33}^T/\varepsilon_0$	$\tan \delta$	d_{31}	d_{33}	Q_m	ρ
1	1	1	%	pC/N	pC/N	1	g/cm^3
0.40	0.53	453	2.5	-44	123	66	4.46

Based on the experiments, the piezoelectric properties of KNN ceramics are

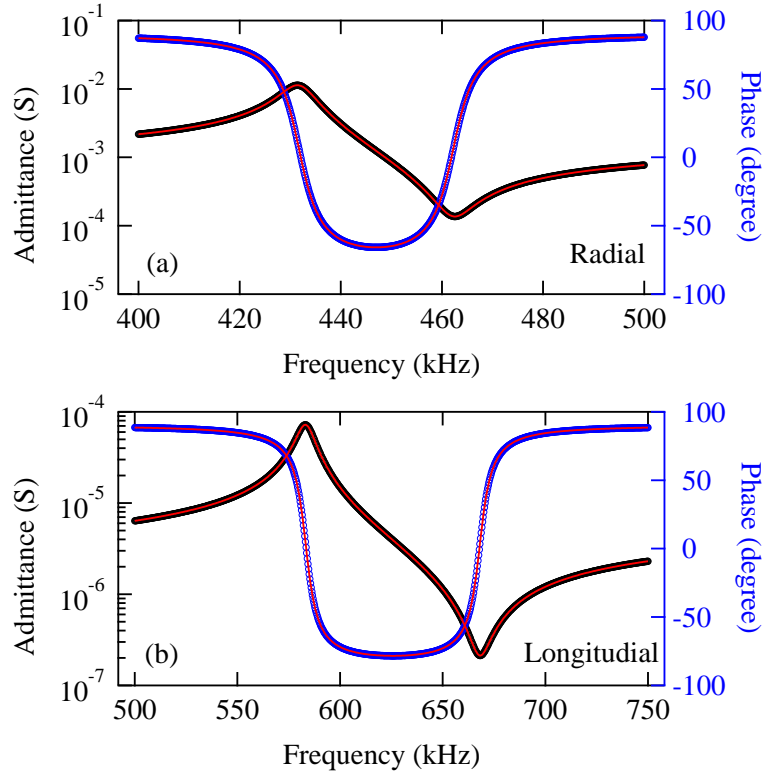


Figure 3.4: Admittance curves of KNN (a) disk and (b) bar transducers.

shown in Table 3.3; which is consistent with the previous studies [58, 119]. Q_m is 66, indicating that KNN is a soft-type material.

3.3 CuO-KNN Powder and Ceramics

$\text{CuO}-(\text{K}_{0.48}\text{Na}_{0.52})\text{NbO}_3$ powder and ceramics were then obtained by doping with CuO. The density of the $\text{CuO}-(\text{K},\text{Na})\text{NbO}_3$ ceramic is 4.48 g/cm^3 , which is slightly larger than the density of the pure $(\text{K}_{0.48}\text{Na}_{0.52})\text{NbO}_3$ ceramics.

Table 3.4: Lattice parameters of $\text{CuO}-(\text{K},\text{Na})\text{NbO}_3$ ceramics.

	a (Å)	b (Å)	c (Å)
$(\text{K},\text{Na})\text{NbO}_3$	5.564	5.598	3.921
$\text{CuO}-(\text{K},\text{Na})\text{NbO}_3$	5.579	5.627	3.925

Figure 3.5 shows the XRD pattern for 1.2% CuO-doped $(\text{K}_{0.48}\text{Na}_{0.52})\text{NbO}_3$ ceramic, of which the peaks are similar to those of pure $(\text{K}_{0.48}\text{Na}_{0.52})\text{NbO}_3$ ceramic. The XRD pattern corresponds to an orthorhombic single phase and no evidence of

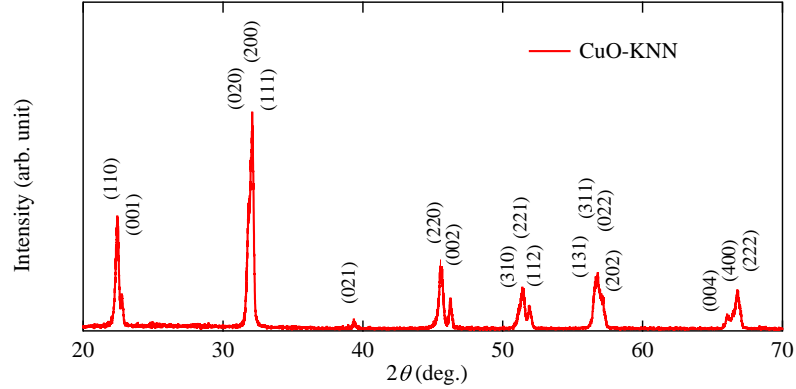
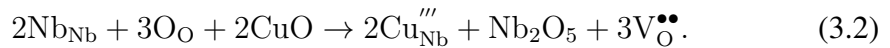


Figure 3.5: XRD spectrum of CuO-KNN ceramics.

impurity or secondary phase was observed.

As shown in Table 3.4, the calculated lattice parameters increased slightly from $a = 5.564$, $b = 5.598$, and $c = 3.921$ Å to $a = 5.579$, $b = 5.627$, and $c = 3.925$ Å. The ionic radius of Nb^{5+} is 0.68 Å and that of Cu^{2+} is 0.73 Å, while the ionic radii of K^+ and Na^+ are 1.38 and 1.02 Å, respectively; therefore, if Cu^{2+} enters the crystal lattice and substitutes for Nb^{5+} , the lattice parameters would become slightly larger, whereas if Cu^{2+} substituted for K^+ or Na^+ , the lattice parameters would become smaller. Therefore, the results suggest that Cu^{2+} successfully enters the crystal lattice and substitutes for Nb^{5+} as an acceptor type dopant in CuO-KNN, instead of substituting for K^+ or Na^+ as a donor type dopant. Oxygen vacancies are simultaneously formed to satisfy the charge neutrality. This doping behavior can be described by Eq. 3.2 using Kroger-Vinks notation:



The admittance curves of CuO-KNN disk and bar transducers are given in Fig. 3.6(a); from which equivalent parameters were obtained and shown in Table 5.1.

Table 3.5: Equivalent circuit parameters of KNN transducers.

	L (mH)	R (Ω)	C (pF)	C_d (pF)
Radial	11.71	37.45	10.57	96.05
Longitudinal	717.45	6410.58	0.138	0.492

In this case, Q_m is about 880, much larger than that of pure KNN transducers. This is consistent with the previous studies [120]: the dopants with low valence ions can enhance the Q_m . The schematic diagram of the domain structure in CuO-KNN ceramics is given in Fig. 3.7. When Cu^{2+} ions substitute Nb^{5+} sites, oxygen

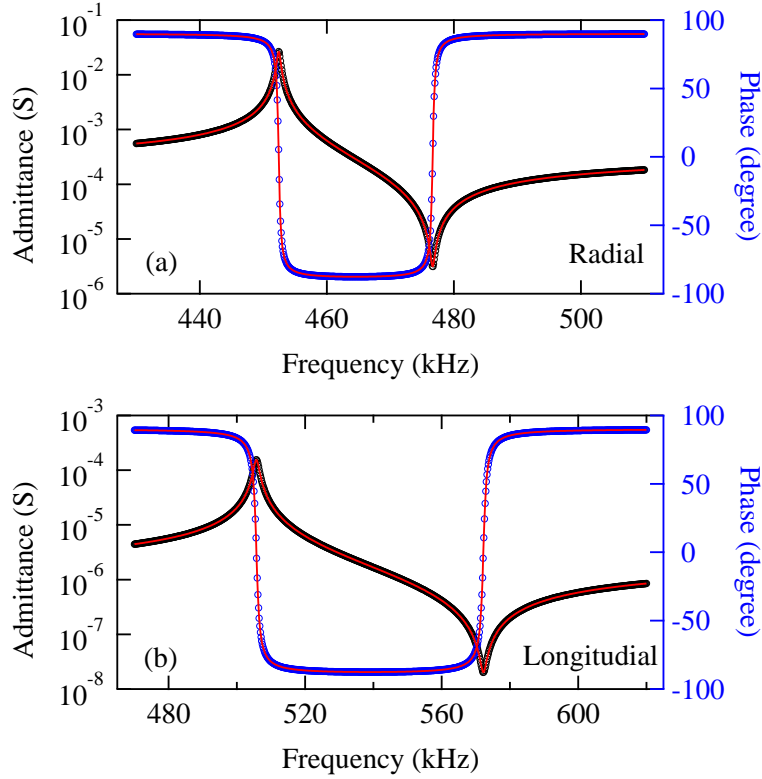


Figure 3.6: Admittance curves of CuO-KNN (a) disk and (b) bar transducers.

vacancies are formed to balance the electro-neutrality (Eq. 3.2), which, along with the Cu^{2+} ions, would constitute charge dipoles. These charge dipoles are inclined to be relatively stable around the domain boundaries and generate the pinning effect. The pinning effect could be so strong that the domain walls would become more difficult to move, even under applied electric fields. The soft-type and hard-type piezoelectrics are categorized based on this effect (seen in 1.1.3). As shown in Fig. 3.7, in soft-type piezoelectrics the pinning effect is weak and the domain walls are still easy to move; while in hard-type specimens the pinning effect impedes the moment of the domain walls. In one word, pure KNN has high mobility domain walls and CuO-KNN has low mobility domain walls due to the charge dipoles.

The piezoelectric properties are shown in Table 3.6. Compared with undoped KNN, $\epsilon_{33}^T/\epsilon_0$ and $\tan \delta$ for CuO-KNN shown in Table 3.6 demonstrate that doping with Cu^{2+} can observably decrease both values, which correspond to the proposed explanation of mobility suppression. However, it is noticed that the properties are still not comparable to PZT ceramics.

High power characteristics of CuO-KNN are also necessary; the results of CuO-KNN plate transducers will be presented in chapter 5. But prior to that, it's

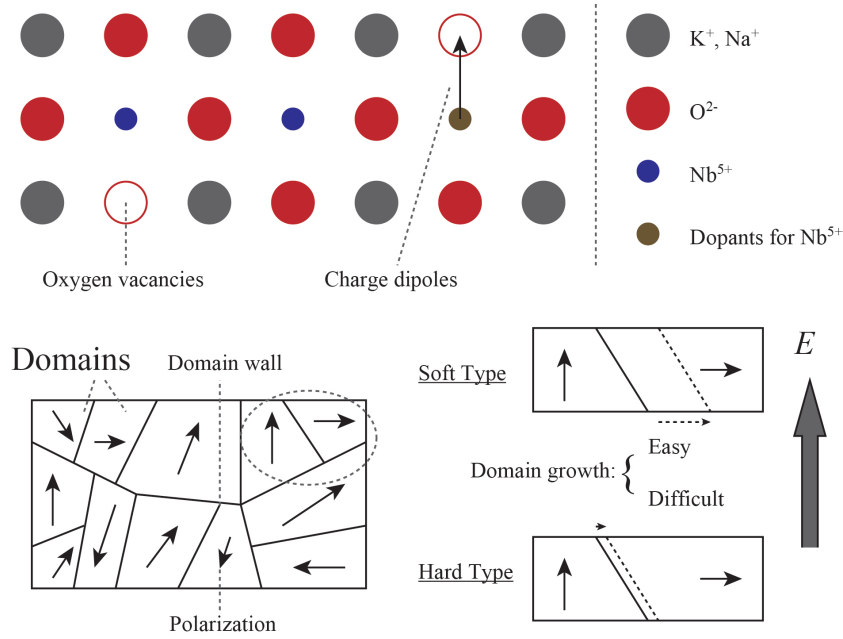


Figure 3.7: Schematic diagram of charge dipoles in domains and their influence.

Table 3.6: Properties of KNN, CuO-KNN, soft-, and hard-type PZT ceramics.

	k_p	k_{33}	$\varepsilon_{33}^T/\varepsilon_0$	$\tan \delta$	d_{31}	d_{33}	Q_m	ρ
	1	1	1	%	pC/N	pC/N	1	g/cm ³
KNN	0.40	0.53	453	2.5	-44	123	66	4.46
CuO-KNN	0.35	0.50	257	0.5	-27	99	890	4.48
Soft PZT [80]	0.66	0.76	2130	1.6	-210	472	80	7.65
Hard PZT [80]	0.59	0.71	1450	0.3	-145	325	2000	7.70

important to find out the estimation method for high power characteristics; so we investigated the high power properties in hard-type and soft-type PZT transducers (chapter 4).

3.4 Post-annealing in Air

In this section, the effect of the post-annealing in air is presented. As we explained in section 3.3, the “ Q_m enhancing” effect of Cu^{2+} ions corresponds to the pinning effect of charge dipoles. However, in the experiments it was noted that aggregation of the charge dipoles to the domain boundaries may take a certain period of time, during which Q_m of the sample would increase gradually (in other word, the Q_m is not always a constant).

To observe this transition, a post-annealing process was utilized to provide the

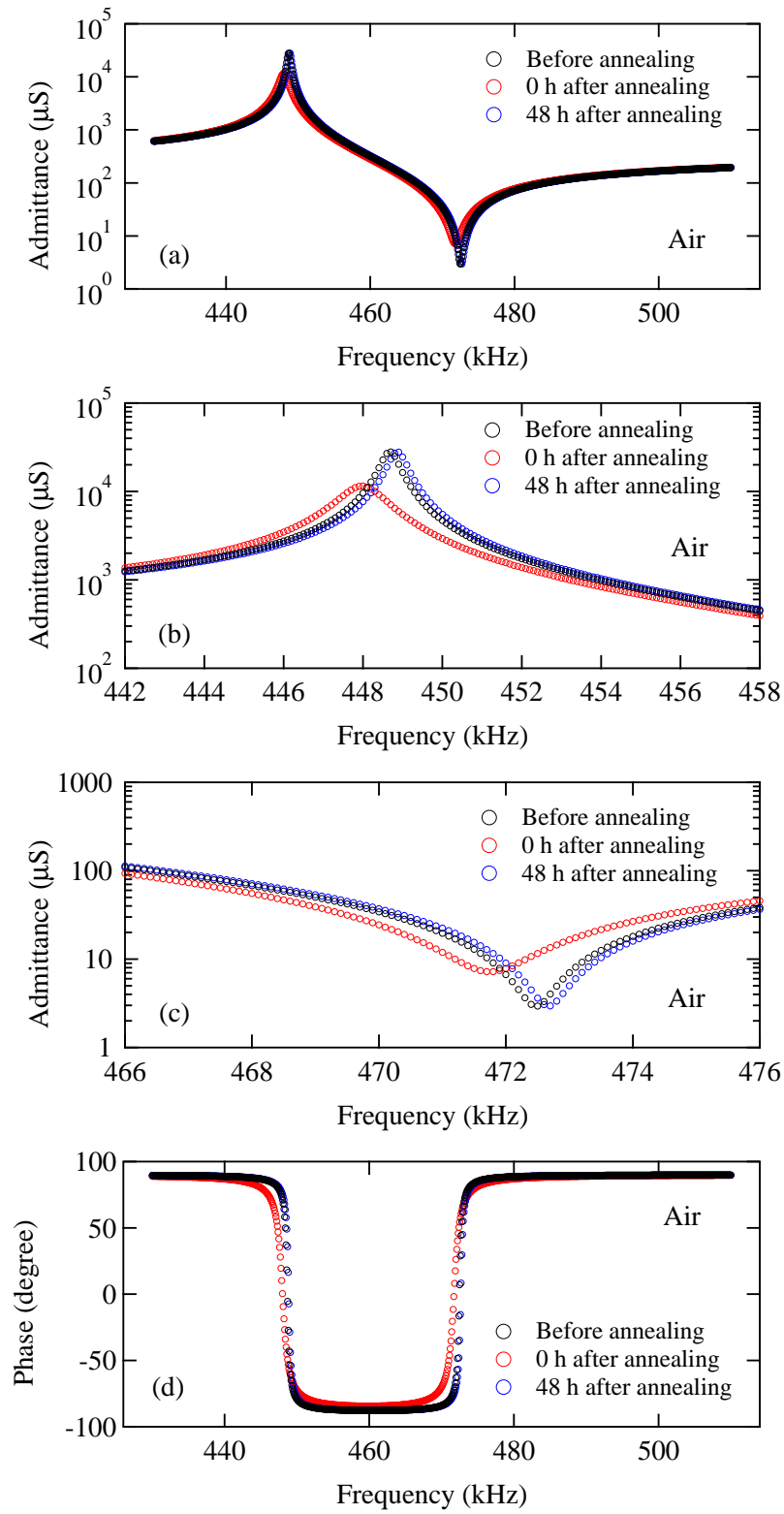


Figure 3.8: The admittance (a)-(c) amplitude and (d) phase curves of CuO-KNN before, 2h after, and 48 h after the post-annealing in air; (b) and (c) are the enlarged view of (a) around resonant and antiresonant frequency, respectively.

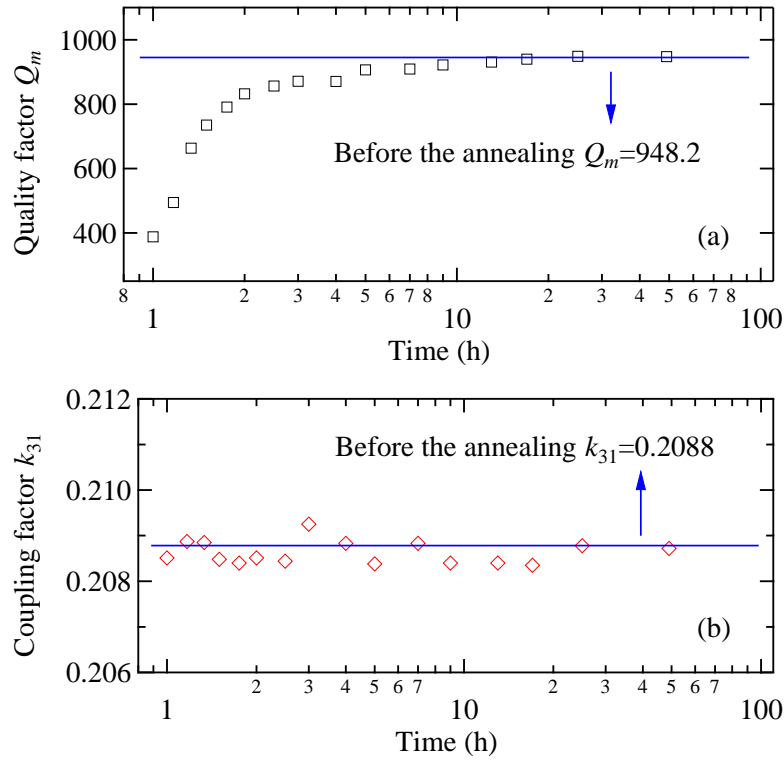


Figure 3.9: The change in (a) Q_m and (b) k_{31} of CuO-KNN in 24 h after the post-annealing in air.

condition necessary for aggregation of the charge dipoles. The sample was located in an electric furnace (Yamada Denki Co. Ltd. TSR-430) and annealed at 400 °C for 24 h. This temperature was selected as both sufficiently high to enable domain reorientation and sufficiently low to suppress grain regrowth.

Figure 3.8 shows the change in the admittance curve of the CuO-KNN ceramics before the post-annealing in air, right after, and 48 h after the post-annealing. Right after the post-annealing, the curves show great distinction from the ones before the post-annealing; from the enlarged view around the resonant and antiresonant frequency in Figs. 3.8(b)-(c) we can observe a smaller maximum value and a greater minimum value of admittance amplitude right after the post-annealing process. The admittance curve of the sample 48 h after the post-annealing in air is almost the same as that before the post-annealing. Similar situation was also observed in the phase curve in Fig. 3.8(d).

For detailed information, the admittance curves after the post-annealing were measured and analyzed. The change in Q_m and the coupling factor (k_{31}) for CuO-KNN disks in 48 h after the post-annealing is shown in Fig. 3.9. In Fig. 3.9(a), the

line $Q_m = 950$ denotes the Q_m value before the post-annealing. The temperature of the post-annealing (400 °C) is sufficiently high for the domains to change the original direction and become depolarized; therefore, a re-poling procedure was necessary after the annealing and cooling, which, would take around 1 hour. After poling, the sample was tested immediately and over the following 48 h (0 min, 10 min, 20 min, 30 min, 45 min, 1 h, 1.5 h, 2 h, 3 h, 4 h, 6 h, 8 h, 12 h, 16 h, 24 h, and 48 h). In Fig. 3.9, the poling time is taken into account (from 1h to 49 h). Q_m decreased to less than 400 at the first test (1 h). However, Q_m recovered gradually over the following several hours; the values at 24 and 48 h were almost exactly the same as the original value. This is attributed to the rearrangement of oxygen vacancies in the domains. The rate of increase in Q_m was fast at first and then became slow, which indicated the change in the rate of rearrangement in the ceramics. This is consistent with the reported Q_m results for PZT-based materials [121]. In addition, we should keep in mind that this investigation may show different results (different rate of change of Q_m and the value of Q_m immediately after the post-annealing) due to different heat treatment histories. To minimize this uncertainty, all data provided here were obtained after the first post-annealing of each different sample.

Oxygen vacancies have been considered to play an important role in the variance of Q_m . Meanwhile, as we know, oxygen vacancies also contribute to many other properties, such as fatigue [122], electrostriction, and aging [123] in ferroelectrics. However, despite the similar origin of the high Q_m and aging phenomenon in these materials, these phenomena have barely been linked together in the literatures. As one of the proofs, the double hysteresis loops (also known as antiferroelectric-like hysteresis loops and pinched hysteresis loops and so on) in CuO-doped KNN ceramics and other hard-type piezoelectric ceramics are usually given [124,125]. In other systems the similar phenomenon was also reported [25].

There are three main mechanisms [123, 126] for the aging phenomenon in ferroelectrics; the bulk effect, domain wall effect, and interface effect. The common feature of these three models is the rearrangement and locating of charge carriers and the defect dipoles related to them. However, there are slight differences in the displacement distances of and the ultimate location of mobile charge defects: locating between multiple adjacent domains in the bulk effect; around the domain walls in the domain wall effect; and at the grain boundaries, external perimeters, or other interfaces in the interface effect [127]. Controversies in the prioritizing of these three effects have existed for decades and each argument has substantial evidence. It has been argued that the main mechanisms in the PZT system and lead-free system could be different; however, no strong evidence has been provided to substantiate this [50]. Recently, it has been suggested that probably more than one mechanism is working in a single material.

In the present case, the most important charge defects are oxygen vacancies and

the decrease of Q_m shown in Fig. 3.9(a) may contribute to a de-aging phenomenon, which is promoted by the annealing process. During this procedure, the oxygen vacancies already located around the grain boundaries or domain walls are able to recover the mobility lost in the aging process. Similar de-aging behavior of Fe-doped PZT after adjustment of the defect structure by heat treatment in an oxygen depleted atmosphere has been reported [128].

In addition, it is noticed that, different from the situation of Q_m , the k_{31} value keeps relatively stable with time, as shown in Fig. 3.9(b).

3.5 Post-annealing in Argon

As we discussed, the initial of the previous two methods for hardening is the charge dipoles. If any other method can realize the increase of the charge dipoles, it might be helpful in enhancing the quality factor. In this case, the charge dipoles originate from the oxygen vacancies, the amount of which can be controlled. For example, the usage of atmospheres enables the control of oxygen vacancy density, as shown in Fig. 3.10.

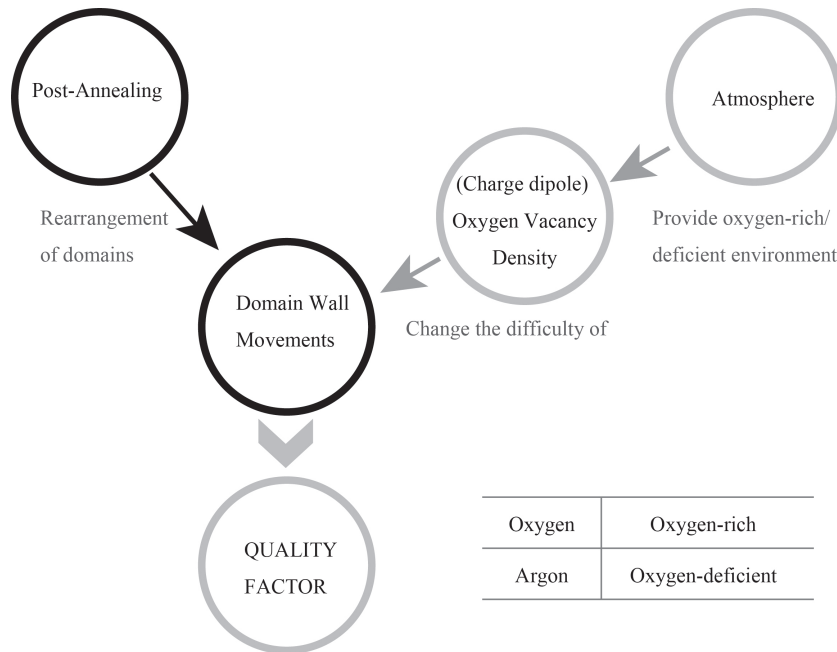


Figure 3.10: Schematic diagram of the influence of post-annealing process on Q_m .

One investigation on CuO-doped KNN ceramics sintered in air and argon atmospheres has been reported and it was proposed that when the ceramics were sintered in argon, a large portion of Cu^{2+} ions could be reduced to Cu^+ ions that can

then replace Na^+ , which would not realize the demand here for increasing oxygen vacancies [129]. Therefore, considering that the sintering atmosphere could result in the substitution of Cu^{2+} ions into B sites, an extra post-annealing process in argon atmosphere (Suzusho Gas Center Argon) after the sintering process was utilized instead. Subsequent to the post-annealing, a re-poling procedure was performed owing to the same reason given above. As a control group, for another CuO-KNN specimen the same procedure was performed, except that an oxygen atmosphere (Chiba ND Gas Center Oxygen) was utilized. Since the post-annealing proved to be efficient in promoting the domain rearrangement (section 3.4), with controlled oxygen vacancy density it might be possible to adjust the Q_m , as illustrated in Fig. 3.10. This section deals with this assumption.

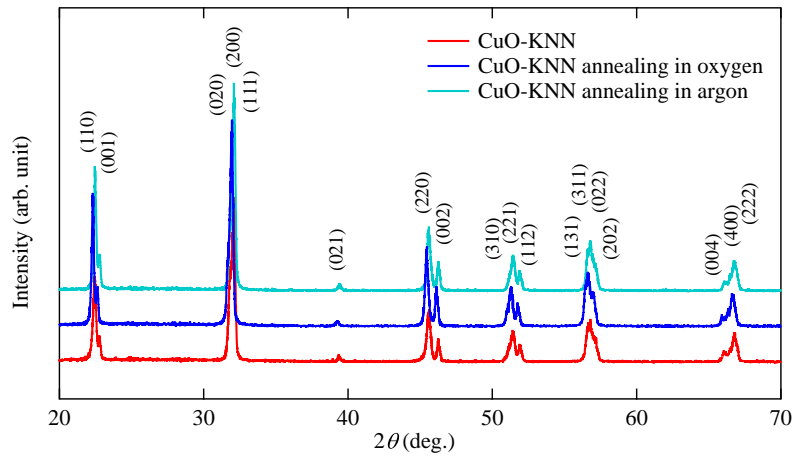


Figure 3.11: Comparison of XRD spectrum of CuO-KNN before and after the post-annealing (in argon and oxygen).

First of all, Fig. 3.11 shows the comparison of XRD patterns of the ceramics before the post-annealing, after the post-annealing in argon, and after the post-annealing in oxygen, which indicate that no phase transition occurs during the post-annealing process.

The admittance curve for CuO-KNN 24 h after the post-annealing in argon is shown in Fig. 3.12(a), while Figs. 3.12(b) and 3.12(c) show the contrasting Q_m and k_{31} before, 2 h after, and 24 h after the post-annealing. The post-annealing process with argon can significantly enhance Q_m for CuO-KNN to approximately 1500. Due to the existence of aging phenomenon we mentioned earlier, the data were measured before annealing, in addition to 2 h after and 24 h after the post-annealing; the calculated Q_m values were 870, 730, and 1500, respectively. Q_m decreases to a low value after the post-annealing, which is consistent with the aforementioned

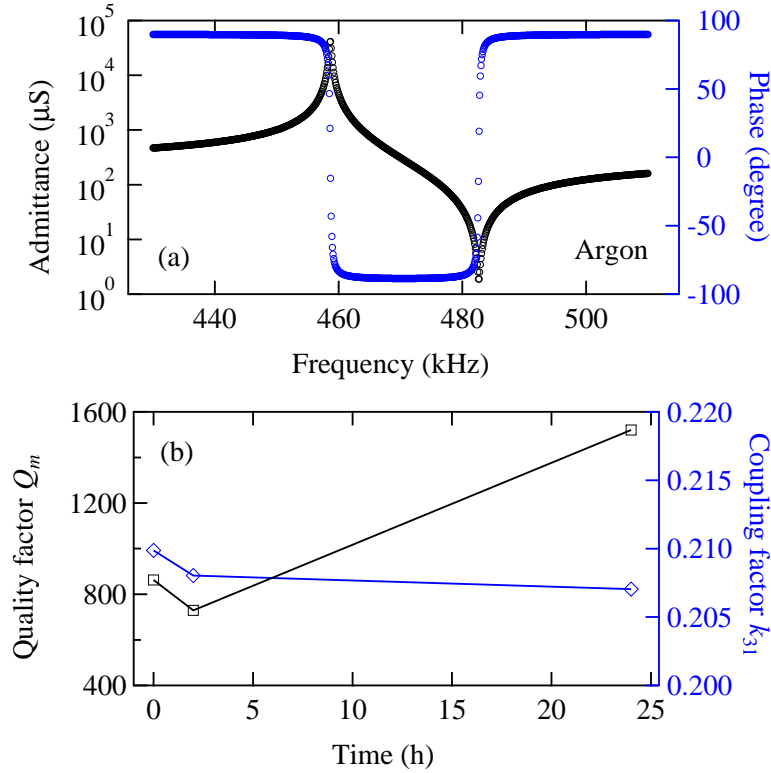


Figure 3.12: The (a) admittance curve, (b) Q_m , and k_{31} of CuO-KNN in 24 h after post-annealing in argon.

model of oxygen vacancy reorientation. During the post-annealing process, domain rearrangement becomes possible, while the argon atmosphere provides an oxygen deficient environment. As a result, annealing in argon atmosphere can increase the amount of oxygen vacancies, which has a significant influence on the stability of domain structure. The increase of oxygen vacancies strengthens the suppression of domain wall moment and thus enlarges the value of Q_m .

The coupling factor k_{31} , shown in Fig. 3.12(c) remains relatively stable after the post-annealing. In most cases, Q_m and k_{31} change with opposite tendencies. In softening processes by doping (high valence ion substitution), Q_m decreases and k_{31} increases, whereas in hardening processes by doping (low valence ion substitution), the Q_m increases and k_{31} decreases. However, it should be noted that in some cases, such as in hard PZT, $\text{Pb}(\text{Sb}_{2/3}\text{Mn}_{1/3})\text{O}_3$ (PSM), and Yb co-doped PZT, k_{31} remains stable while Q_m increases [121].

As a comparison, the change in the admittance curve for CuO-KNN 24 h after the post-annealing in oxygen is shown in Fig. 3.13(a). Figures 3.13(b) and 3.13(c) show Q_m and k_{31} before and after the post-annealing. Q_m before the post-annealing

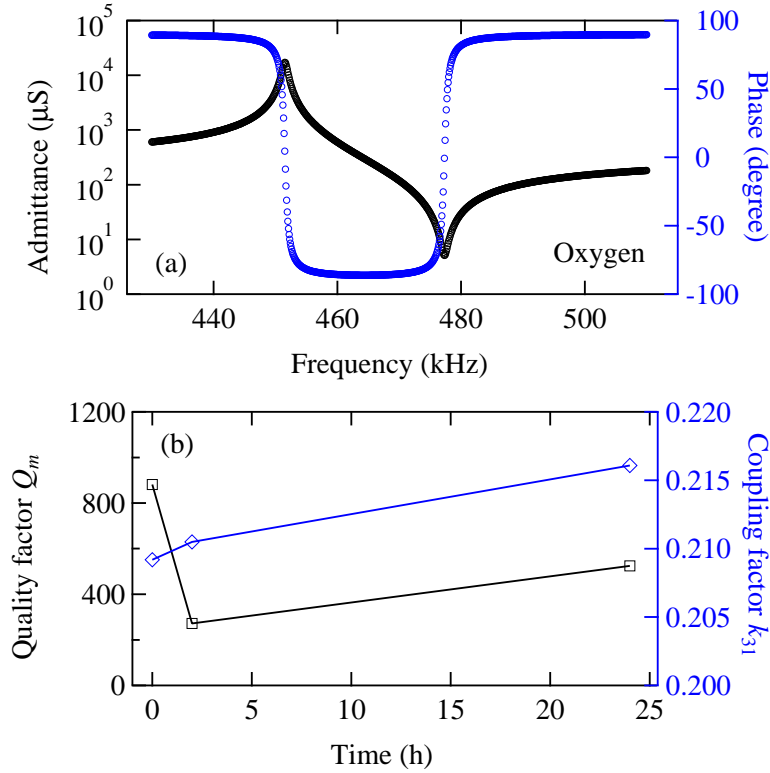


Figure 3.13: The (a) admittance curve, (b) Q_m , and k_{31} of CuO-KNN in 24 h after post-annealing in oxygen.

was 880, while 2 h and 24 h after the annealing, Q_m was 270 and 520, respectively. Q_m decreases immediately after the post-annealing process; while k_{31} remains almost unchanged, as was the case for post-annealing in argon. However, Q_m 24 h after the annealing in oxygen was lower than that before the annealing, whereas that when annealed in argon was larger 24 h after the annealing than that before the annealing. This may result from the disappearance of a portion of the oxygen vacancies during annealing in an oxygen environment.

Soaking the CuO-KNN ceramics in aqueous hydrogen peroxide solution (H_2O_2) has a similar influence as post-annealing in an oxygen atmosphere, because it also provides an oxygen-rich environment. Q_m decreases after such a soaking period (not shown here), while k_{31} remains relatively stable.

The influence of the post-annealing in atmospheres was summarized in Fig. 3.14. As we discussed in section 3.4, the hardening effect (increasing Q_m) and softening effect (decreasing Q_m) correspond to the aging and de-aging processes. In our case, the period after or before the post-annealing can be taken as aging process while during annealing takes charge during the post-annealing. In the

aging, the charge dipoles (constituted by Cu^{2+} ions and oxygen vacancies) move to the surfaces (domain walls, substrate surfaces, and grain boundaries), which will impede the domain wall moments, resulting in more stable domain structure and larger Q_m . On the opposite, in the de-aging, the rearrangement (into domains) of the charge dipoles tends to make the domain walls easier to move, which of course means lower Q_m .

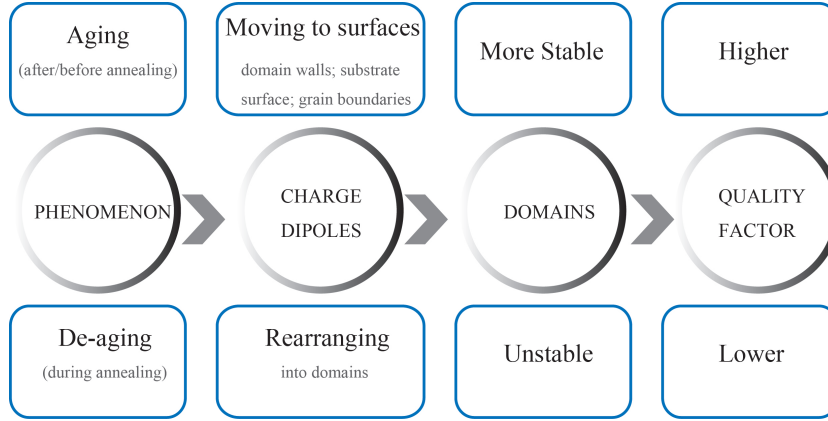


Figure 3.14: The influence of post-annealing with atmospheres on Q_m .

The measured piezoelectric properties of the CuO-KNN specimens after the post-annealing are listed in Table 3.7. Except for the hardening effect mentioned before, the charge dipoles (formed by oxygen vacancies and doped ions) may also have an important influence on other ferroelectric and piezoelectric properties. The comparison of the properties of CuO-KNN before and after the post-annealing in oxygen and argon atmospheres revealed no evidence for any considerable change except Q_m .

Table 3.7: Properties of CuO-KNN ceramics: a-c represent CuO-KNN before the annealing, CuO-KNN after the annealing in argon and oxygen, respectively.

	k_p	k_{33}	$\varepsilon_{33}^T/\varepsilon_0$	$\tan \delta$	d_{31}	d_{33}	Q_m	ρ
	1	1	1	%	pC/N	pC/N	1	g/cm ³
a	0.35	0.50	257	0.5	-27	99	880	4.48
b	0.35	-	269	0.4	-27	-	1500	4.48
c	0.35	-	267	0.5	-27	-	520	4.48

For most hard-type piezoelectric ceramics like hard-type PZTs [80], Q_m is between 500 and 2000. In previous literatures, doping with acceptor ions, Q_m was enhanced to 600-1200 in most cases [41, 129–131]; of course there were exceptions: as low as 200-300 [113, 118] or as high as 2500-3000 [57, 124]. The value of Q_m

here is comparable to these studies. Therefore, the proposed method is useful to obtain piezoelectric materials with higher Q_m , especially when we combine the method of acceptor doping and annealing in oxygen deficient atmospheres.

3.6 Brief Summary

Pure and CuO-doped ($\text{K}_{0.48}\text{Na}_{0.52}$) NbO_3 powders and ceramics were prepared. The effectiveness of a new method to enhance the Q_m of CuO-KNN ceramics was investigated and discussed. The main results are summarized as follows:

(1) 1.2 mol% CuO-doped ($\text{K}_{0.48}\text{Na}_{0.52}$) NbO_3 ceramics was fabricated via a hydrothermal method and solid state sintering. The phase of CuO-KNN is similar to that of pure KNN and corresponds to an orthorhombic single phase without any impurities.

(2) Post-annealing does not change the phase of the CuO-KNN ceramics. However, intense transitions of the domains in the ceramics that occur after post-annealing result in a change in Q_m . Q_m had a decrease after the post-annealing and recovered gradually over several hours. This phenomenon is attributed to the rearrangement of oxygen vacancies in the domains.

(3) We proposed that post-annealing in an oxygen-deficient atmosphere could increase the amount of oxygen vacancies, which would impede movement of the domain structure, even under applied electrical fields, and thus increased the value of Q_m . In the case of annealing in argon, Q_m increased to approximately 1500 from 870, whereas post-annealing in oxygen resulted in a decrease of Q_m .

CHAPTER 4

Nonlinear Behavior in PZT Transducers

4.1 Background

Under high power operation, piezoelectrics show deviations from low power characteristics, resulting from multiple sources. In the previous literatures, nonlinear phenomena have been reported and analyzed.

Phenomenon of current jumping in lead zirconate titanate vibrator was reported by K. Ishii et al. [96, 132–134]. The frequency response of current amplitude near the resonant frequency is shown in Fig. 4.1(a); the measuring and jumping directions are marked by arrows [132]. Moreover, influence of various surrounding media (acetone, silicone oil, and diffusion pump oil) on current jumping phenomenon was revealed; the minimum driving voltage required for the current jump rises with increasing media viscosity [135].

Systematical investigations on nonlinear piezoelectric resonators were carried out by A. Albareda et al. [139–143]. The additional nonlinear impedance terms (both real part and imaginary part) were found to be motional current dependent

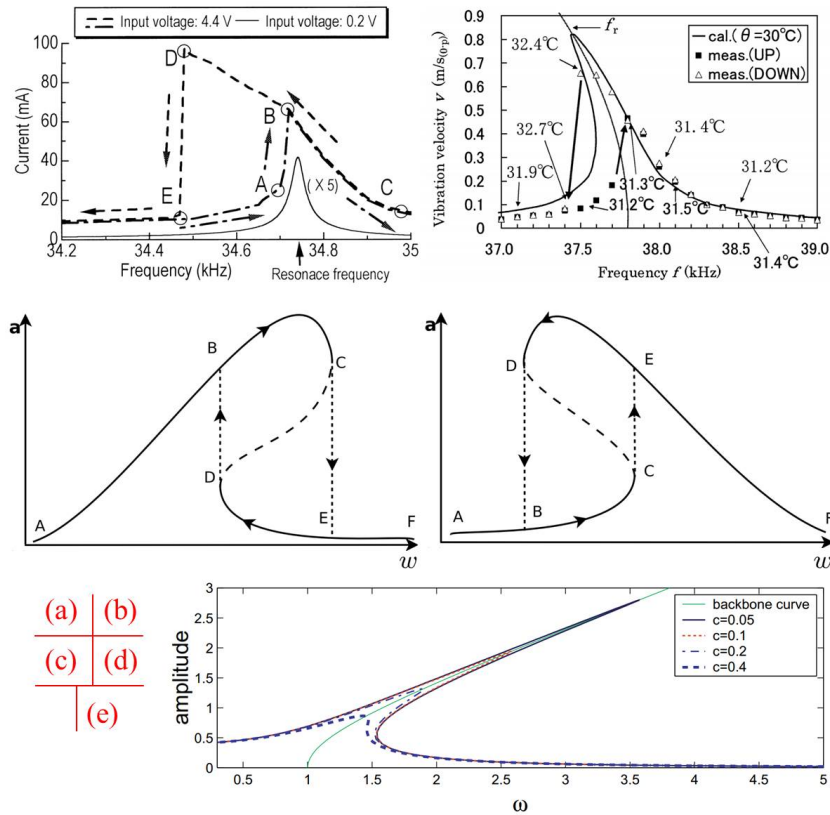


Figure 4.1: Previous studies on nonlinear phenomena: (a) jumping and hysteresis of current [132], (b) jumping and hysteresis of velocity [136], (c) soft spring [137], (d) hard spring [137], and (e) forced vibration in a nonlinear system [138].

[139]. Using motional impedance plane the characteristics of nonlinearity were enabled [142]. The jumping and dropping phenomena of piezoelectric transducers were studied using the electrical equivalent circuit constants in high vibration amplitude level, as shown in Fig. 4.1(b) [136]. Complex material constants were used to fit the G - B curves for specimens with high and low quality factor [144].

The jumping phenomenon appears not only in piezoelectric transducers; in nonlinear oscillators or other nonlinear systems it is also possible to observe the jumping. The nonlinearity in oscillators was studied using a renormalization group method and the stability of the fixed points of amplitude equation was enabled [137]. According to the bending directions of the resonant peaks shown in Figs. 4.1(c)-(d), it was suggested that the amplitude-frequency curves correspond to soft spring and hard spring, respectively [137]. What makes nonlinear systems distinct from linear systems includes various effects, such as multiple steady states in response to the same input, jump phenomena, response at frequencies other than driving frequency, internal resonances, self-sustained oscillations, and extremely sensitive response (chaos) [138]. Amplitude response was found to be dependent on the nonlinear coefficients and periodic input signal, as shown in Fig. 4.1(e) [138].

Drive level dependence of the resonant frequency in quartz resonators was illustrated by introducing a current amplitude dependent resonant angular frequency [145]. Similarly, current dependence was adopted by other researchers [132, 139]. An assumption that polarization is proportional to strain without phase delay was made when analyzing the losses in piezoelectric ceramics [146]. Different sets of admittance formulas [147] and complex material constants [144] were used in the fitting of admittance curves. A third order term modified piezoelectric constitutive equations was proposed to explain the nonlinear phenomena; the effects under low voltages can be explained [84]. Other forms of modified piezoelectric constitutive equations were also introduced [96, 147]. J. F. Blackburn and M. G. Cain, on the other hand, claimed that these quasilinear theories relating to various parameters were inappropriate; as a substitute, they proposed a model derived from constitutive equations [97].

Although various models have been proposed to explain the phenomena in deformed frequency response properties at high power operation, two important points are still missing:

- (1) The origination of jumping phenomenon: in almost all the previous theories, jumping cannot be described very well.

- (2) The physical source of nonlinearity: which one is more important, dielectric nonlinearity, piezoelectric nonlinearity, or mechanical nonlinearity? The exploited models distinct with each other, but didn't provide enough experimental evidence.

In this chapter, prior to the high power estimation of CuO-KNN transducers, high power characteristics of standard PZT transducers were investigated first.

4.2 Admittance Curve under High Voltage

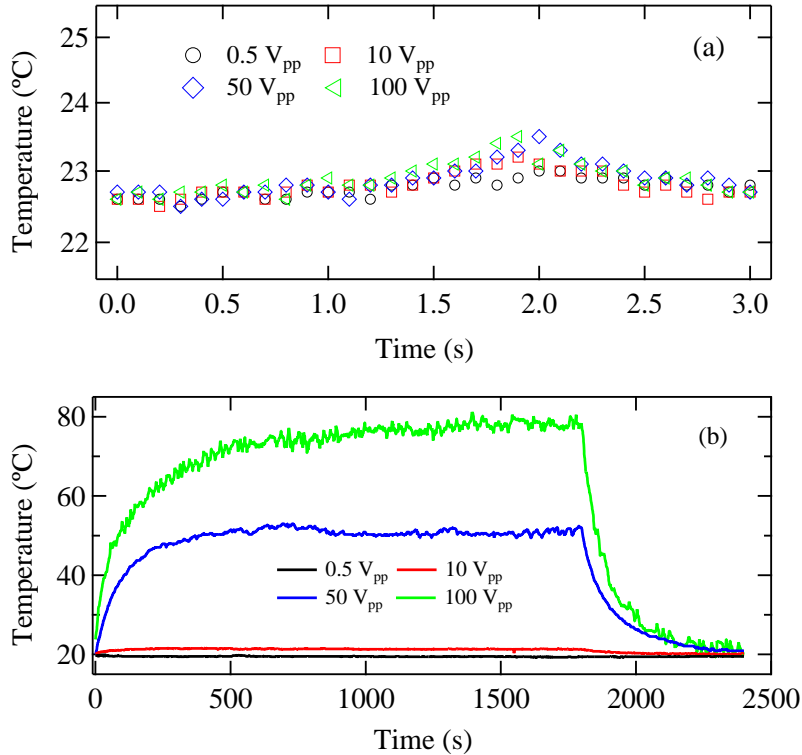


Figure 4.2: Temperature rise of hard-type PZT transducer in (a) admittance curve measuring and (b) continuous driving at various voltages.

Two kinds of transducers were used, including hard-type PZT transducers (Fuji Ceramics, C-203, $43 \times 7 \times 2$ mm³) and soft-type PZT transducers (Fuji Ceramics, C-6, $43 \times 7 \times 2$ mm³) poled along the thickness direction (2 mm), which were excited in the longitudinal mode with the 31 effect.

The admittance curves for both PZT transducers were measured by a frequency response analyzer. Measurements were carried out rapidly (only 100 steps for each measurement, less than 3 s). Before and after the measurements, the driving voltage was off. As mentioned in chapter 1, the heat generation needs to be eliminated to prevent its influence on the study of high voltage effect. The temperature rise at the center of the hard-type PZT transducer was measured and shown in Fig. 4.2. The temperature has a small rise (less than 2 °C) around the resonant frequency and decreases quickly after the resonant frequency, as shown in Fig. 4.2(a). As a comparison, the temperature rise during continuous driving is shown in Fig. 4.2(b). At the voltage of 0.5 and 10 V_{pp} the saturated temperature rises are small; while at

50 and 100 V_{pp} the temperature rises and becomes saturated gradually (the saturated temperature rise is about 30 °C at 50 V_{pp} and 50 °C at 100 V_{pp}, respectively). The time scale in Fig. 4.2(b) is consistent to a previous study [100].

It is noticed that the velocity of the transducer is large only near the resonant frequency; e.g., in only 0.15 s the admittance amplitude is larger than one tenth of the maximum amplitude at 0.5 V_{pp} (Fig. 4.3). Given this fact and the time scale of heat generation in Fig. 4.2(b), the effect of heat generation in this procedure could be neglected.

Table 4.1: Equivalent circuit parameters of two PZT transducers.

	L (mH)	R (Ω)	C (pF)	C_d (pF)
Hard PZT	100.44	16.04	193.20	2028.60
Soft PZT	63.84	132.45	367.15	3154.80

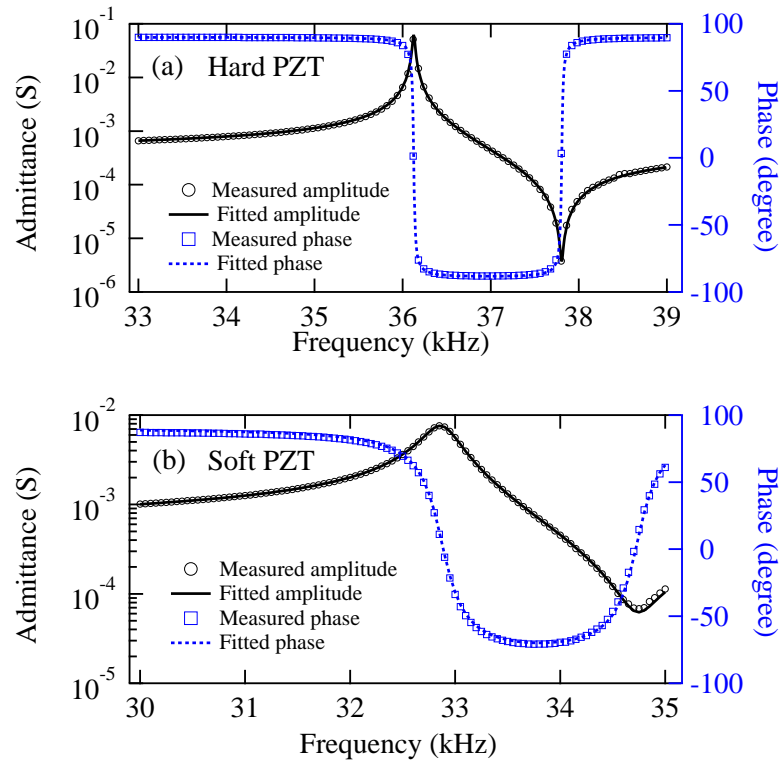


Figure 4.3: Measured and fitted admittance amplitude and phase curve of (a) hard- and (b) soft-type PZT transducers at 0.5 V_{pp}. Measured curves are denoted by circles and fitted curves are lines.

The admittance curves of both PZT transducers at low voltage (0.5 V_{pp}) are shown in Fig. 4.3. The admittance amplitude and phase curves of hard-type PZT are

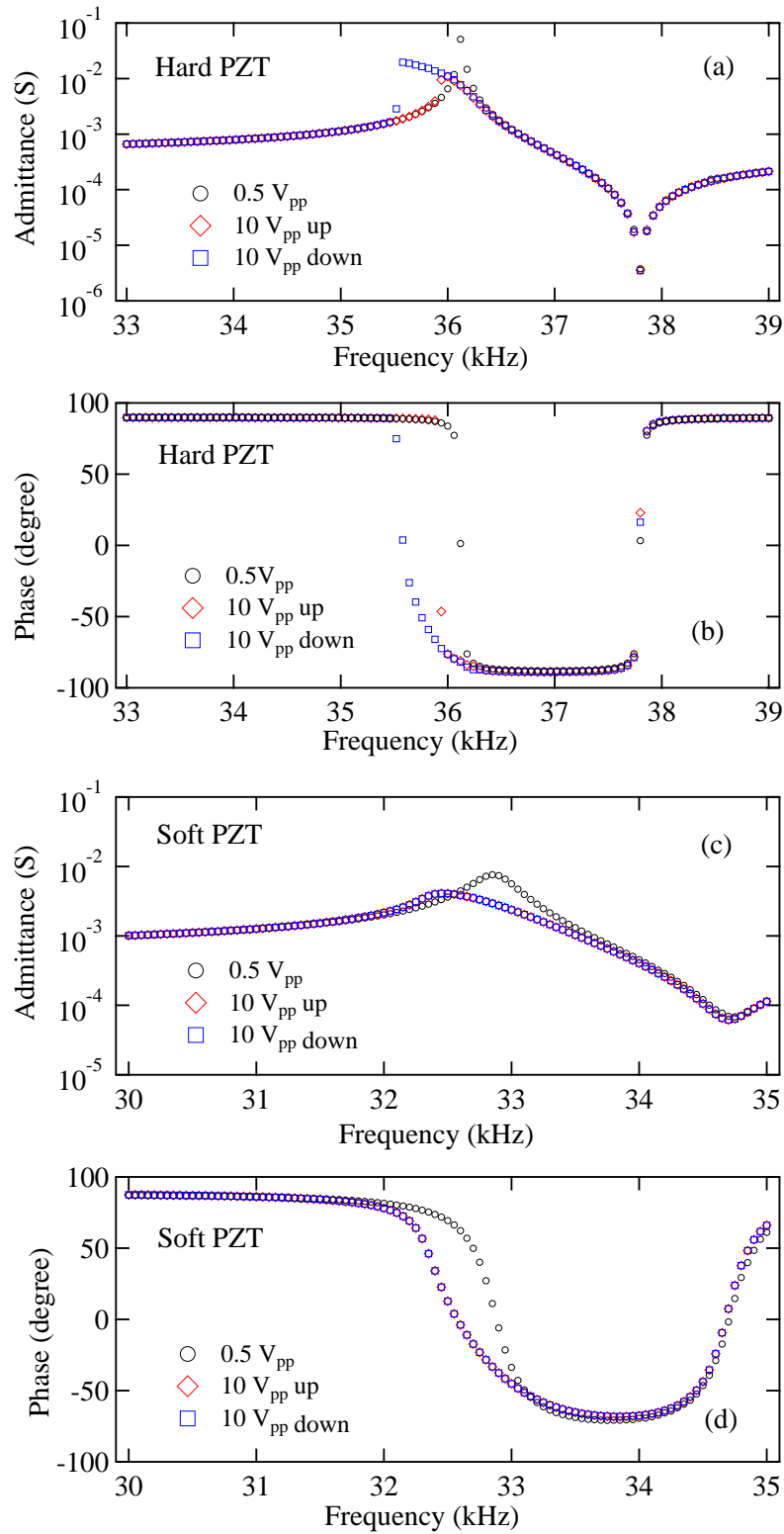


Figure 4.4: Admittance amplitude and phase curves for (a-b) hard and (c-d) soft PZT transducers at 0.5 and 10 V_{pp} (up sweep and down sweep).

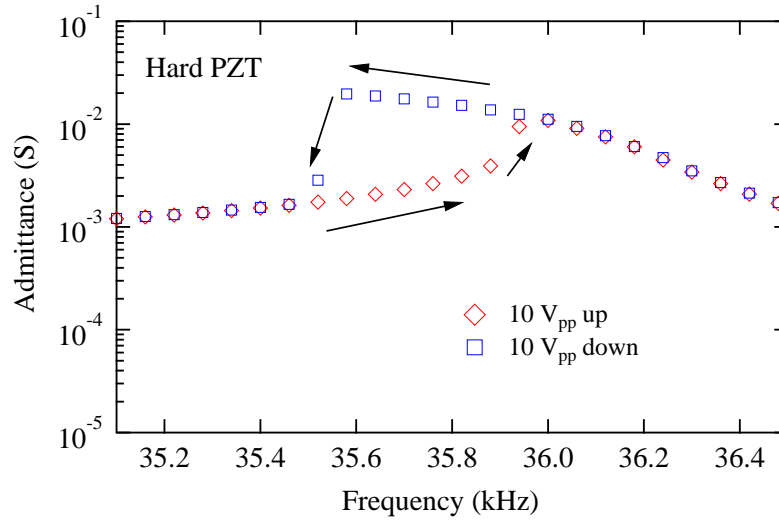


Figure 4.5: An enlarged version of the hard-type PZT admittance curve in the region around the resonant frequency; the arrows denote the directions of sweeping and jumping.

shown in Fig. 4.3(a). The equivalent circuit introduced in chapter 2 can be utilized to describe the curves; the lines in Fig. 4.3(a) are fitted results, showing consistence with the measured curves. Similarly, the measured and fitted admittance amplitude and phase curves of soft-type PZT are illustrated in Fig. 4.3(b). The parameters determined from the fitting are listed in Table 4.1, from which Q_m can be obtained. Q_m of hard-type PZT is about 1420 and that of soft-type PZT is about 100.

The admittance curves for both transducers at high voltage ($10 V_{pp}$) are shown in Fig. 4.4. In Fig. 4.4(a), compared to the symmetric admittance curve at $0.5 V_{pp}$, the curves at $10 V_{pp}$ clearly lost their symmetry. The admittance values around the resonant frequency are not consecutive like at other points, which is often referred to as a jumping phenomenon [141]. In addition, upward sweep and downward sweep measurements give different results, forming an admittance hysteresis. The phase curves exhibits a similar behavior, as shown in Fig. 4.4(b). The admittance amplitude and phase curves of the soft PZT transducer are shown in Fig. 4.4(c)-(d). Although in Fig. 4.4(c), the resonant peak also shifts to lower frequencies, the situation is different from Fig. 4.4(a); the jumping phenomenon is not observed, neither is the admittance hysteresis between the upward and downward sweep results.

An enlarged version of the hard-type PZT admittance curve in the region around the resonant frequency is shown in Fig. 4.5; the arrows denote the directions of the sweeping and jumping.

It is clear that the conventional equivalent circuit fails to describe the deformed

admittance curves in Fig. 4.4, no matter how we adjust the parameters in Table 4.1. Similar phenomena have been reported, which are usually believed to be related to nonlinear effect. Due to the nonlinear effect it is inconvenient to estimate the property at high power operation; for instance, the calculation method of quality factor Q_m and force factor A becomes inaccurate. These phenomena suggest that the conventional equivalent circuit needs improvement.

4.3 Burst Mode Measurement and Results

Before further study on admittance curves, the nonlinearity in burst mode measurements was investigated. In the burst mode measurements, the frequencies of the driving signals in the function generator were set to the resonant angular frequencies of the transducers determined by the admittance curves at low voltage (Fig. 4.3), which were about 2.27×10^5 rad/s for the hard-type PZT and 2.07×10^5 rad/s for the soft-type PZT. It should be noted that although the resonant frequency of the forced vibration might deviate from this value at $10 V_{pp}$, the resonant frequency in the free vibration part would not change.

The driving signal (1000 cycles) began at 0 ms and excited the transducers. After releasing the driving voltage, the transducers started to exhibit free vibration, whose velocity is shown in Fig. 4.6. The starting time of the free vibration (and in Fig. 4.6) was around 27.7 ms for the hard-type PZT and 30.6 ms for the soft-type PZT. It can be seen that the velocity decreased once the burst voltage was released. The vibration velocity of the soft transducer decreases much faster than that of the hard-type transducer (notice that the time scales of two figures are different). For each transducer, we measured the velocity at two voltages (10 and 100 V_{pp}). In the beginning, the maximum velocity amplitude is 0.5, 1.1 m_{pp}/s for hard-type PZT and 0.15, 0.5 m_{pp}/s for soft-type PZT, respectively. In the linear system, the vibration velocity amplitude v_0 is clearly subject to an exponential decay, which can be expressed by a differential equation

$$\frac{dv_0}{dt} = -\beta t, \quad (4.1)$$

where β is a positive rate called the exponential decay rate.

In Fig. 4.6, the higher the voltage is, the higher the beginning velocity and decay rate are; suggesting that the decay rate is not a constant but the function of time

$$\beta = \beta(t), \quad (4.2)$$

Considering the driving signal is sinusoidal voltage, the instantaneous velocity can be expressed by

$$v(t) = v_0 \sin [\omega_r(t)(t + \varphi)] \exp^{-\beta(t)(t-\tau)}, \quad (4.3)$$

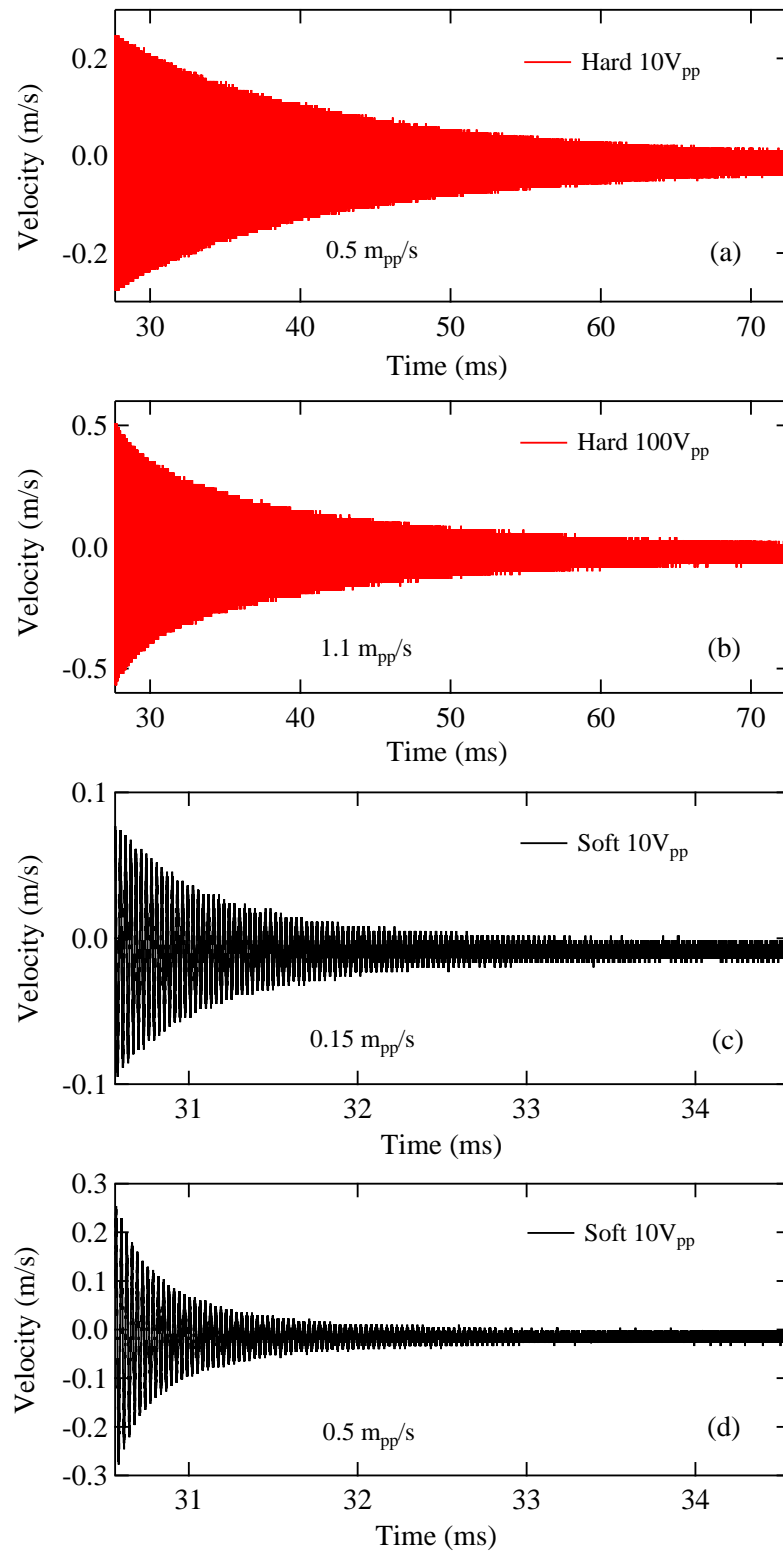


Figure 4.6: Vibration velocity of hard-type PZT transducer at (a) 10, (b) 100 V_{pp} and soft-type PZT transducer at (c) 10, (d) 100 V_{pp}.

where ω_r is the angular resonant frequency of the vibration, also a function of time; τ is the beginning time of free vibration. Given the vibration velocity wave, the parameters in Eq. 4.3 can be determined.

4.4 Analysis of Burst Mode Results

Parameters were determined from the velocity-time curves by curve fitting. For the hard-type PZT transducer, the fitting was performed for every 20,000 data points (or about 2 ms) after the driving signal stopped, during which ω_r and β were considered to have constant values. The fitting results are shown in Fig. 4.7(a). The time shown in the figure is the middle point of each period. As illustrated by the error bar, in the beginning the error was negligible, but it increased with time, which corresponds to a relatively stronger background in the low-velocity range.

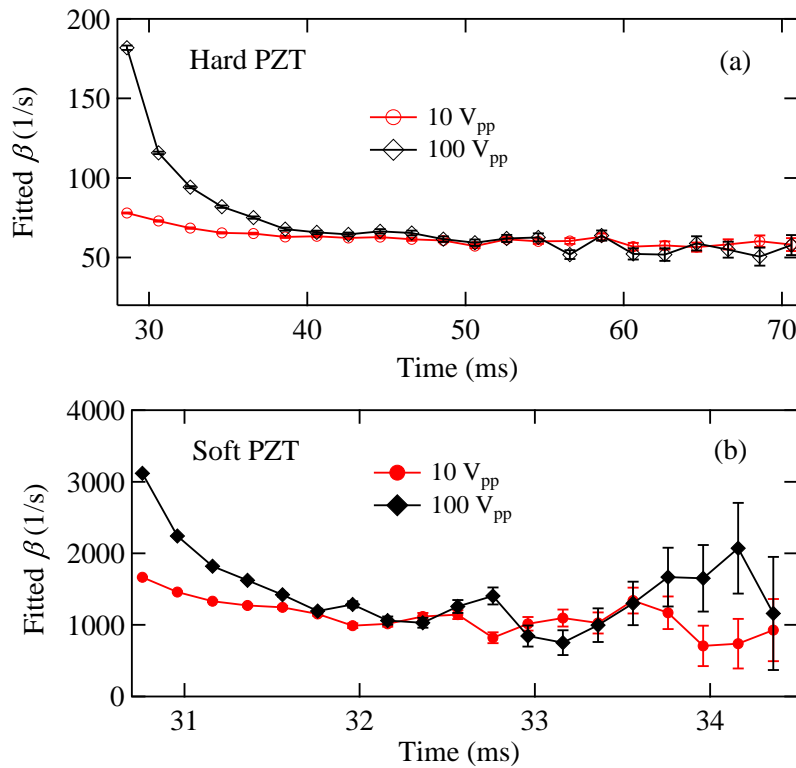


Figure 4.7: Time-dependent β value and error for hard PZT transducer at (a) 10 V_{pp} (hollowed circles), 100 V_{pp} (hollowed squares) and (b) soft PZT transducer at 10 V_{pp} (filled circles), 100 V_{pp} (filled squares).

As a comparison, the corresponding results for the soft-type PZT transducer are shown in Fig. 4.7(b). Since the velocity of the soft PZT transducer decreased much

Table 4.2: m , β , and ω_r in the beginning of free vibration for both transducers.

	m (g)	β (s^{-1})	ω_r (rad/s)
Hard PZT 10 V_{pp}	2.318	78	2.26×10^5
Hard PZT 100 V_{pp}	2.318	182	2.25×10^5
Soft PZT 10 V_{pp}	2.303	1667	2.04×10^5
Soft PZT 100 V_{pp}	2.303	3118	2.01×10^5

faster, the time scale is shorter and the fitting was carried out for every 10,000 data points (or about 0.2 ms). The same two driving voltages were adopted. In Fig. 4.7(b) a much larger β value is shown; the errors are found to be larger than those of the hard-type transducer owing to the lower velocity. The equivalent mass m , β , and ω_r values of the first point (highest velocity) for each condition are listed in Table 4.2. As seen in Table 4.2, the ω_r of both PZT transducers shifts to lower frequencies, and this effect is more obvious in the soft-type specimen. For both PZT transducers, β increases with increasing voltage. For the soft PZT specimen, β is much larger.

The tendencies of fitted β and ω_r values in Fig. 4.7 suggest that both of them are vibration velocity dependent. Figure 4.8 plots β and ω_r of the hard-type PZT transducer as functions of vibration velocity; Fig. 4.8(a) gives the β curves of the hard-type PZT at 10 and 100 V_{pp} . A similar β - v curve was reported by Umeda et al. [148]. Although the curve at 10 V_{pp} lacks some points in high velocity range and the curve at 100 V_{pp} has fewer points in low velocity range, these two curves show the same tendency, indicating high reliability and repeatability of our burst mode measurement. The exhibited increasing trend with velocity of β suggests a quadratic relationship, which is confirmed by curve fitting with a first-order coefficient of zero and consistent with a previous study [149]. This relationship can be expressed by

$$\beta = \beta_0 + p \frac{v_0^2}{l}, \quad (4.4)$$

where v_0 is the amplitude of the vibration velocity; p is a real nonlinear coefficient; l is the length of the transducer. Similarly, as shown in Fig. 4.8(b), ω_r also follows a quadratic function of vibration velocity, as expressed by

$$\omega_r = \omega_0 + q \frac{v_0^2}{l}, \quad (4.5)$$

where q is also a real nonlinear coefficient. Here, l is used so that p and q are not size dependent (details seen in section 4.8).

Equations 4.4 and 4.5 are also valid for the soft PZT transducer, with larger p and q (absolute value), which is different from the previous study [149], where a linear relationship was suggested. However, as illustrated in Fig. 4.9(a), both linear and

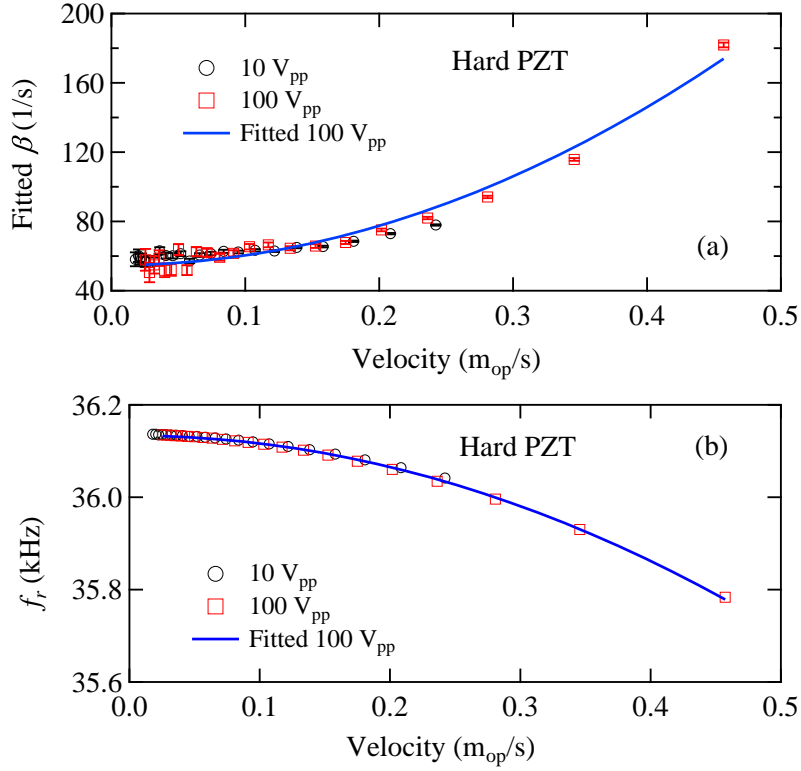


Figure 4.8: Velocity-dependent (a) β and (b) ω_r for hard PZT transducer.

quadratic fitting seem to be feasible. For simplicity, in this study we use quadratic relationships for both transducers. The values of p and q can be determined from the fitting, as shown in Table 4.3.

Table 4.3: Parameters of both transducers determined from burst mode results.

	β_0 (s^{-1})	p (s/m)	ω_0 (rad/s)	q (s/m)
Hard PZT	55	2.45×10^1	2.27×10^5	-4.34×10^2
Soft PZT	1293	4.75×10^3	2.05×10^5	-8.52×10^3

In the fundamental vibration of plate transducers, the maximum stress T_m (at the center) can be derived from the velocity amplitude v_0 at the end.

$$T_m = \frac{v_0 E}{c} = \rho c v_0, \quad (4.6)$$

where E , c , ρ are the Young's modulus, wave speed, and density of the transducer, respectively.

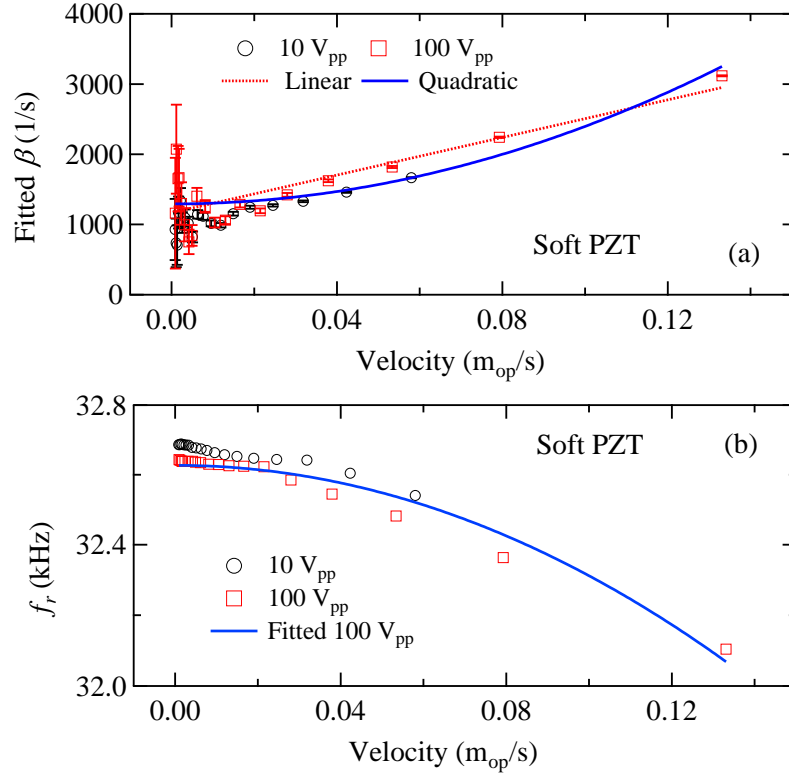


Figure 4.9: Velocity-dependent (a) β and (b) ω_r for soft PZT transducer.

Hence, equations 4.4 and 4.5 are equivalent to the following equations:

$$\beta = \beta_0 + p \frac{T_m^2}{\rho l E}, \quad (4.7)$$

$$\omega_r = \omega_0 + q \frac{T_m^2}{\rho l E}. \quad (4.8)$$

4.5 Modeling of Nonlinearity in Piezoelectrics

In section 4.1 we've already mentioned the previous models for explaining the jumping phenomena in frequency response curves of admittance (or impedance, velocity, current, and so on). The researchers tried to start with solving the revised piezoelectric constitutive equations, or to analyze the experimental results. In the first pathway [96, 97, 147], nonlinear terms were introduced to the conventional constitutive equations (Eq. 1.2, Table 1.2):

$$\begin{cases} S = s^E T + s^{E'} T^2 + s^{E''} T^3 + dE, \\ D = dT + \varepsilon^T E, \end{cases} \quad (4.9)$$

or

$$\begin{cases} E = -hS + \beta^s D + \gamma_D D + \xi_D D^3, \\ T = c^D S - hD + \chi_D D^2 + \delta_D D^3, \end{cases} \quad (4.10)$$

or

$$\begin{cases} E = \beta D - gT + \frac{1}{2}\beta^* D^2 + \gamma DT, \\ S = sT + gD + \frac{1}{2}s^* T^2 - \frac{1}{2}\gamma D^2 - \alpha DT. \end{cases} \quad (4.11)$$

However, it is noticed that there's no evidence supporting the introduced nonlinear terms. On the other hand, the fitting results of the measured frequency response curves didn't show great consistency with the experimental data [97, 144, 147].

In one word, the previous nonlinear models are unsatisfactory in describing the jumping and hysteresis and determining the nonlinear level. To avoid that, we attempted to establish a nonlinear model with the help of burst mode results.

When only linear terms are considered, the conventional *LCR* equivalent circuit can describe the electrical properties of motional admittance, expressed by Kirchhoff's second law:

$$L \frac{di}{dt} + Ri + \frac{1}{C} \int idt = V, \quad (4.12)$$

where $V = V_0 \cos \omega t$ is the driving voltage, $i = i_0 \cos(\omega t + \theta)$ is the motional current, and θ is the phase delay between current and voltage. However, the results of the burst-mode measurement suggest that nonlinearity needs to be considered in this occasion and that β and ω_r are velocity dependent, as expressed by Eqs. 4.4 and 4.5. The value of equivalent loss r and equivalent spring constant s can be determined from the burst mode results. s is expressible in terms of ω_r :

$$s = m\omega_r^2 = m \left(\omega_0 + \frac{qv_0^2}{l} \right)^2 \approx m\omega_0^2 + \frac{2m\omega_0 q}{l} v_0^2. \quad (4.13)$$

Here, the quartic term of v_0 is neglected because $qv_0^2/l\omega_0 \approx 0$, which can be confirmed by Fig. 4.8(b) and Fig. 4.9(b) (the change in ω_r is very small). And r , which is related to the decay rate β , can be expressed by

$$r = 2m\beta = 2m \left(\beta_0 + \frac{pv_0^2}{l} \right). \quad (4.14)$$

Equations 4.13 and 4.14 are based on the assumption that the nonlinear terms of β and ω_r do not influence each other. In the equivalent circuit we have

$$R = \frac{r}{A^2}, C = \frac{A^2}{s}, L = \frac{m}{A^2}, \quad (4.15)$$

where A is taken as a constant, which will be explained later.

Then the nonlinear R and C are obtained from r and s . Equation 4.12 can be revised as

$$L \frac{di}{dt} + R_0 i + \eta i^3 + \frac{1}{C_0} \int i dt + \xi \omega^3 \left(\int i dt \right)^3 = V, \quad (4.16)$$

where R_0 and C_0 are linear resistance and linear equivalent capacitance, η and ξ are the nonlinear coefficients corresponding to p and q , respectively. The relationships between η and ξ with p and q can be expressed by

$$\eta = \frac{2Lp}{lA^2}, \xi = \frac{2Lq}{lA^2}. \quad (4.17)$$

To obtain Eq. 4.17, the approximation $\omega \approx \omega_0$ was used. By substituting the expressions $V = V_0 \cos \omega t$ and $i = i_0 \cos(\omega t + \theta)$ into Eq. 4.16, we get

$$\begin{aligned} & R_0 i_0 \cos(\omega t + \theta) - \omega L i_0 \sin(\omega t + \theta) + \\ & \frac{i_0 \sin(\omega t + \theta)}{\omega C_0} + \eta i_0^3 \cos^3(\omega t + \theta) \\ & + \xi i_0^3 \sin^3(\omega t + \theta) = V_0 \cos \omega t. \end{aligned} \quad (4.18)$$

Using the trigonometric equations

$$\cos^3 \varphi = \frac{3 \cos \varphi + \cos 3\varphi}{4}, \quad (4.19)$$

$$\sin^3 \varphi = \frac{3 \sin \varphi - \sin 3\varphi}{4}. \quad (4.20)$$

Equation 4.18 reveals that there is a high harmonic vibration, similarly to the findings of [132] and [150]. By eliminating the high harmonic terms and merging similar items, Eq. 4.18 can be rewritten as

$$\begin{aligned} & \left(-\omega L i_0 + \frac{i_0}{\omega C_0} + \frac{3\xi i_0^3}{4} \right) \sin(\omega t + \theta) \\ & + \left(R_0 i_0 + \frac{3\eta i_0^3}{4} \right) \cos(\omega t + \theta) = V_0 \cos \omega t. \end{aligned} \quad (4.21)$$

Since we have

$$\cos \omega t = \sin(\omega t + \theta) \sin \theta + \cos(\omega t + \theta) \cos \theta, \quad (4.22)$$

to satisfy Eq. 4.21, we need to assume

$$\begin{aligned} & \left[\left(-\omega L i_0 + \frac{i_0}{\omega C_0} + \frac{3\xi i_0^3}{4} \right) - V_0 \sin \theta \right] \sin(\omega t + \theta) \\ & + \left[\left(R_0 i_0 + \frac{3\eta i_0^3}{4} \right) - V_0 \cos \theta \right] \cos(\omega t + \theta) = 0; \end{aligned} \quad (4.23)$$

since $\sin(\omega t + \theta)$ and $\cos(\omega t + \theta)$ are linearly independent, then

$$\left(-\omega L i_0 + \frac{i_0}{\omega C_0} + \frac{3\xi i_0^3}{4}\right) = V_0 \sin \theta, \quad (4.24)$$

$$\left(R_0 i_0 + \frac{3\eta i_0^3}{4}\right) = V_0 \cos \theta. \quad (4.25)$$

Then we have

$$\left(-\omega L i_0 + \frac{i_0}{\omega C_0} + \frac{3\xi i_0^3}{4}\right)^2 + \left(R_0 i_0 + \frac{3\eta i_0^3}{4}\right)^2 = V_0^2, \quad (4.26)$$

$$\begin{aligned} \theta &= \arctan \frac{\left(-\omega L i_0 + \frac{i_0}{\omega C_0} + \frac{3\xi i_0^3}{4}\right)}{\left(R_0 i_0 + \frac{3\eta i_0^3}{4}\right)} \\ &= \arctan \frac{\left(-\omega L + \frac{1}{\omega C_0} + \frac{3\xi i_0^2}{4}\right)}{\left(R_0 + \frac{3\eta i_0^2}{4}\right)}. \end{aligned} \quad (4.27)$$

The value of motional current amplitude i_0 can be determined from Eq. 4.26, which is a cubic equation of the square of the current. All the cubic equations have three solutions, among which one or three are real solutions. In our case, when for a certain frequency range (around the resonant frequency), the equation has three real solutions, the jumping phenomenon is observed. The medium solution is unstable, while the other two are stable. Depending on the initial conditions, one of the two stable solutions can be observed in the measurement, resulting in the admittance hysteresis between different sweep directions. Meanwhile, the phase is determined by Eq. 4.27. Motional admittance Y_m is given by

$$Y_m = G_m + jB_m = \frac{i_0}{V_0} \cos \theta + j \frac{i_0}{V_0} \sin \theta, \quad (4.28)$$

where G_m and B_m are the real and imaginary part of Y_m , respectively. The total admittance Y_{total} is the parallel of motional admittance and a damped capacitance

$$Y_{total} = Y_m + j\omega C_d, \quad (4.29)$$

where C_d is also considered as a constant; the reason will be given in section 4.7.

The measured admittance amplitude is $|Y_{total}|$, while the measured phase curve corresponds to $\arctan(B_{total}/G_{total})$, B_{total} and G_{total} are imaginary and real part of Y_{total} , respectively.

4.6 Fitting Results and Nonlinear Coefficients

Using the model described above, curve fitting was performed for the admittance curves measured at 10 V_{pp} (Fig. 4.4). According to Eqs. 4.26-4.29, one series

of parameters can determine the total admittance of the transducer, including the amplitude $|Y_{total}|$ and phase $\arctan(B_{total}/G_{total})$. For the hard-type PZT transducer, since the admittance hysteresis reflects the nonlinearity, the same series of parameters should be used for both the upward and downward sweep curves. The fitting was carried out for the upward admittance amplitude curve; the downward admittance amplitude curve and both phase curves were calculated from the parameters obtained in the upward sweep. Figures 4.10(a)-(b) plot the fitting and calculation results for the hard-type PZT transducer. In Fig. 4.10(a), the jumping phenomenon and admittance hysteresis are described very well. The measured and fitted phase curves are presented in Fig. 4.10(b). The calculated curves are found to be consistent with the measured curves; while in previous studies [97, 144, 147], the fitted (or calculated) admittance curves usually exhibited deviation from the experimental results.

The fitting results of the admittance and phase curves for the soft-type PZT transducer are shown in Fig. 4.10(c) and Fig. 4.10(d). Both the fitted admittance and phase curve overlap with the experimental results. Unlike the curves of hard-type PZT shown in Fig. 4.10(a)-(b), there is no jumping or admittance hysteresis. As mentioned above, a cubic equation might have three real solutions or only one. In this case, only one real solution satisfies the equation, so there is no jumping or admittance hysteresis.

The fitted parameters including force factor A , damped capacitance C_d (both taken as constants, as explained in next section), and nonlinear coefficients ξ , η are shown in Table 4.4. The two nonlinear coefficients, ξ and η , of the soft-type PZT transducer are much larger than those of the hard-type PZT transducer. The value of β_0 for soft PZT transducer is also larger than that of hard PZT transducer, which is consistent with the burst-mode measurement results. The ω_0 values of two transducers are close to the angular resonant frequencies of each sample at $0.5 V_{pp}$ (also the driving frequency in the burst mode measurements).

Table 4.4: Force factor and nonlinear coefficients of PZT transducers determined from the admittance curve fitting.

Sample	A (N/V)	β_0 (s^{-1})	η (ΩA^{-2})	ω_0 (rad/s)	ξ (ΩA^{-2})	C_d (nF)
Hard PZT	0.153	54	5.07×10^3	2.27×10^5	-9.57×10^4	2.06
Soft PZT	0.191	1037	4.09×10^5	2.06×10^5	-8.83×10^5	3.12

In addition, p and q can be calculated from ξ and η . Though not identical, they are comparable to the results obtained from the fitting in Fig. 4.8 and Fig. 4.9, as summarized in Table 4.5. This demonstrates the effectiveness of the proposed model in predicting the nonlinearity. Besides, the two methods could be substitutes for each other in estimating nonlinearity level. Here, force factor A is taken as a

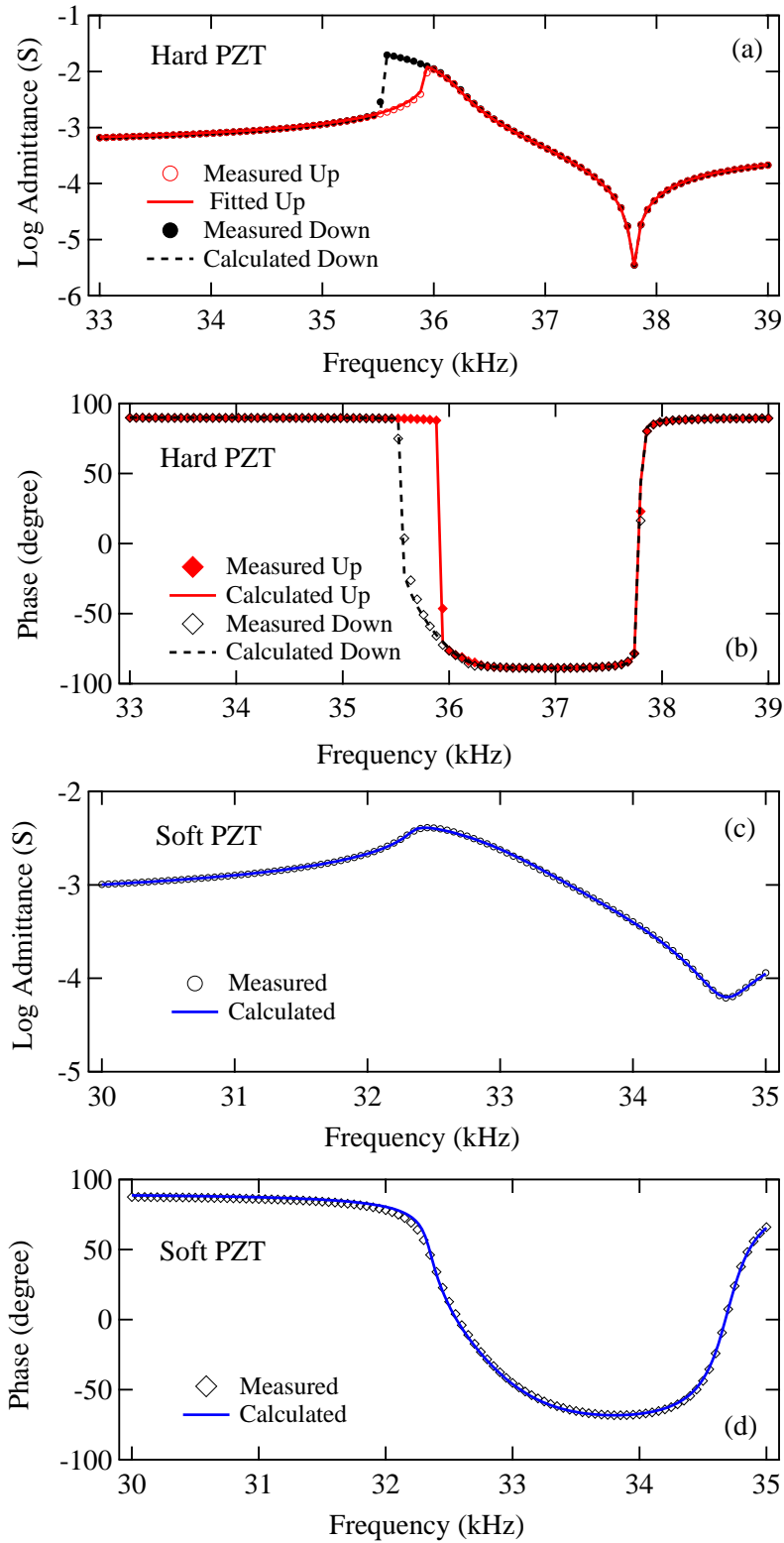


Figure 4.10: Fitted results of admittance curves: (a) amplitude, (b) phase of hard-type PZT transducer and (c) amplitude, (d) phase of soft-type PZT transducer.

real constant without any loss or stress dependence, indicating that the piezoelectric e coefficient is a real constant; which demonstrates the assumption of M. Hagiwara et al. [151].

Table 4.5: Comparison of coefficients determined from burst mode results and admittance curve fitting.

Sample	Method	β_0 (s ⁻¹)	p (s/m)	ω_0 (rad/s)	q (s/m)
Hard PZT	Burst Mode	55	2.45×10^1	2.27×10^5	-4.34×10^2
Hard PZT	Admittance	54	2.58×10^1	2.27×10^5	-4.86×10^2
Soft PZT	Burst Mode	1293	4.75×10^3	2.05×10^5	-8.52×10^3
Soft PZT	Admittance	1293	5.03×10^3	2.06×10^5	-1.08×10^4

4.7 Discussion on the conclusions

In the previous sections, the nonlinear behavior in the burst mode measurement and the admittance curves was presented and analyzed. The proposed model with nonlinear terms proves to be efficient and enables the description and prediction of admittance curves. The jumping phenomenon and hysteresis in the admittance curves derives from the multiple solutions at one frequency. However, the physical source of the nonlinearity here is still unclear; in this section we want to discuss about the source of nonlinearity. Before considering the details of the nonlinearity sources, it is important to emphasize our research target again. In the practical applications, there are mainly two types of piezoelectric devices; one is DC drive and the other is resonant drive (section 1.4.2). This thesis treats the latter one, the resonant drive type.

There are three kinds of losses in piezoelectric materials: the dielectric loss, the mechanical loss, and the piezoelectric loss. The dielectric and mechanical losses are considered to be independent; while the piezoelectric loss exists on the basis of the other two losses [152]. The dielectric, mechanical, and piezoelectric coefficients and corresponding losses might be dependent on the stress or the electrical field. The nonlinearity in piezoelectrics results from one of them or the combination of them; one or more of them are dominant depending on the condition.

It is noticed that the jumping and hysteresis phenomena appears in various systems. For example, in ferroelectrics the polarization-field hysteresis loop [153] and strain-field curve [153] are typical characteristics, as shown in Fig. 4.11. In Fig. 4.11(a), the net polarization is zero before any electrical field treatment (initial state, point a). The domain structure stays unchanged and the ions are only shifted around the equilibrium position when applied electrical field is sufficiently low; switching process is initiated when electrical field is large enough, resulting fast

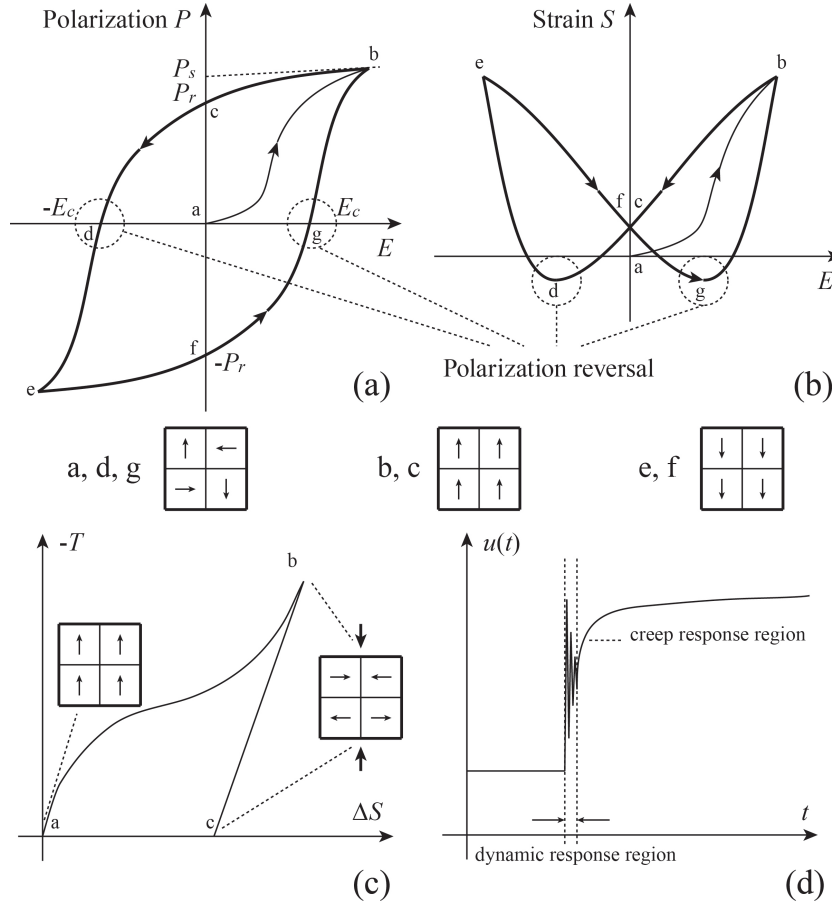


Figure 4.11: Schematic diagram of (a) polarization-field hysteresis loop, (b) strain-field curve, (c) stress-strain curve, and (d) creep response for a typical ferroelectric material.

increase of the net polarization; finally all the microscopic polarizations are aligned in the electrical field ($a \rightarrow b$). With decreasing electrical field, the domains gradually deviate from the electrical field owing to the demand for energy minimization; when the electrical field reaches zero, the net polarization is called residual polarization ($b \rightarrow c$). To switch the aligned polarization again, an opposite direction electrical field is required ($c \rightarrow d$); with increasing the opposite direction electrical field, the directions of the domains are aligned in the opposite direction ($d \rightarrow e$). Following process ($e \rightarrow f \rightarrow g \rightarrow b$) is similar to the process ($b \rightarrow c \rightarrow d \rightarrow e$) [153]. Similarly, the strain-field curve is shown in Fig. 4.11(b). Other typical phenomena include stress-strain curve [153], creep response [154, 155], and so on.

The switching process is the source of the dielectric nonlinearity, suggesting that the dielectric nonlinearity needs high electrical field so that the domain switching can be realized. In addition, the piezoelectric nonlinearity derives from the change

in strain associated with the switching of the spontaneous polarizations [92, 156].

The initial sources of these nonlinearities might be different, probably corresponding to widely varying driving conditions. In this study, three voltages (0.5, 10, and 100 V_{pp}) were used; given the thickness of the samples is 2 mm, the applied electrical fields were 0.125, 2.5, and 25 V/mm, respectively. Comparing with the coercive field (E_c) of the PZT samples (about 1.72 kV/mm for hard-type PZT and 1.05 kV/mm for soft-type PZT, provided by the manufacturer Fuji Ceramics), in this study the experiments were carried out at much lower electrical field (burst mode method: lower than 1/40 coercive field; admittance curve measurement: lower than 1/400 coercive field). Our sample locates in one of the two regions denoted by the blue circles in the P - E ferroelectric hysteresis loop, as shown in Fig. 4.12. In these two regions, even if the dielectric nonlinearity (in our study) exists, our experimental results clarified that it is negligible because the domains are almost not affected by the electrical field. In other regions, of course the dielectric nonlinearity is large due to the domain movement resulting from the electrical field.

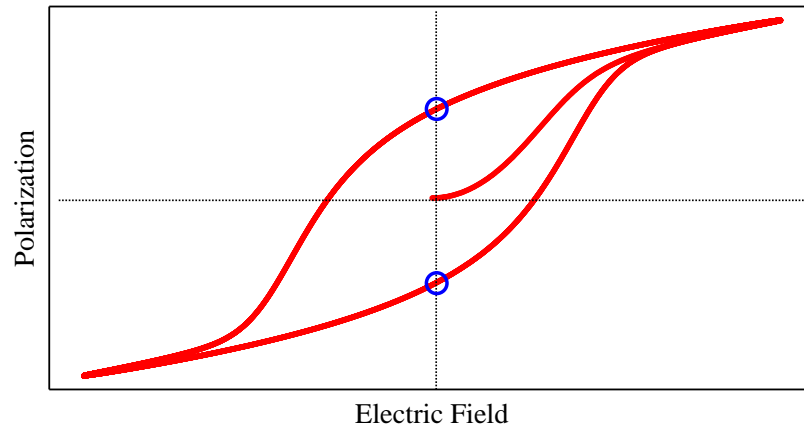


Figure 4.12: Schematic diagram of a P - E hysteresis loop; the blue circles represent the regions investigated in our study.

On the other hand, the mechanical nonlinearity in this study is much more significant than the nonlinearity in the P - E ferroelectric hysteresis measurement, because the driving frequencies are very close to the resonant frequency. In our study the driving frequency is near the resonant frequency (≈ 36 kHz for hard PZT and 33 kHz for soft PZT); while in the P - E ferroelectric hysteresis measurement, the driving frequency is usually about 100 Hz (away from the resonant frequency). So, comparing with the P - E ferroelectric hysteresis measurement, the vibration velocity in our study is much larger, indicating much larger stress (≈ 20 MPa) at the center of the transducers. So, instead of large electrical field, the large stress is the source of nonlinearity.

As we introduced in section 4.1, the nonlinear phenomena are widespread in nature (e.g., in the nonlinear oscillators). The jumping behavior appears in the oscillators when the nonlinear perturbation is large enough [137]. The mechanical vibration may exhibit other nonlinear behavior when the nonlinear force became more significant [138]. This is similar to our study except that no piezoelectric effect is involved in this situation.

In short, when sufficiently high electrical field strength and low frequency (small stress) is applied, the P - E hysteresis loops can be observed [92]; whereas relatively low electrical field with a driving frequency near the resonant frequency of the transducer (indicating large stress) is applied, the admittance jumping and hysteresis can be observed. Hence, in former case, dielectric nonlinearity is dominant; and in latter case, mechanical nonlinearity is more important, which is demonstrated by the burst mode and admittance curve fitting results.

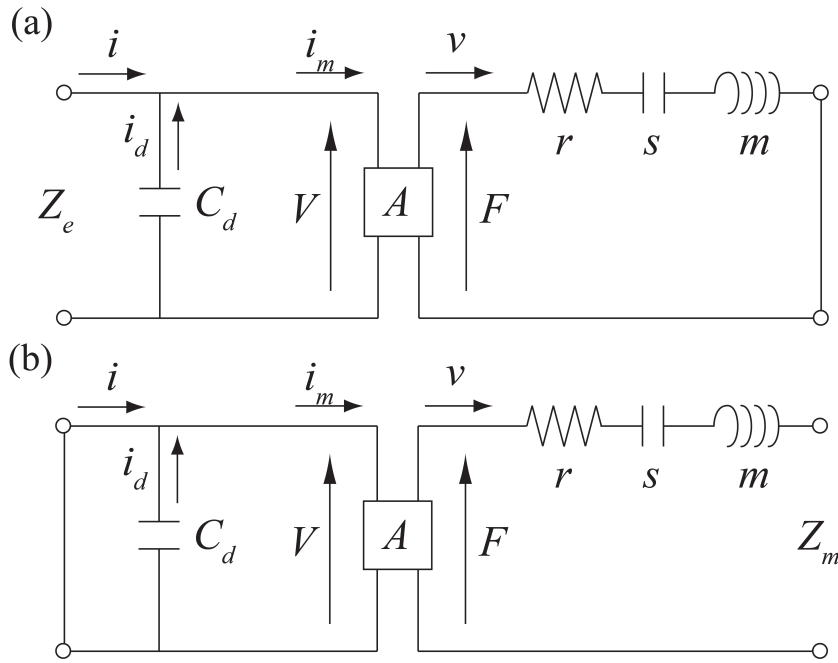


Figure 4.13: Equivalent circuits of (a) dielectric and (b) mechanical nonlinearity.

In burst mode measurement, when the burst voltage is released, the electrical branch is shortened, and the contribution of the dielectric nonlinearity is zero as well as the damping capacitance. As seen in Fig. 4.13(a), when the electrical branch is not shortened, the total impedance Z_e is

$$Z_e = j\omega C_d + \frac{V}{i_m} = j\omega C_d + \frac{1}{A^2} \frac{F}{v}; \quad (4.30)$$

while in the case of Fig. 4.13(b) the electrical branch is shortened, the impedance

Z_m can be expressed by

$$Z_e = r + j\omega m + \frac{s}{j\omega} + \frac{F}{v} = r + j\omega m + \frac{s}{j\omega} + A^2 \frac{V}{i_m} = r + j\omega m + \frac{s}{j\omega}. \quad (4.31)$$

It means that the burst mode result only reveals the information of mechanical vibration and the existence of the mechanical nonlinearity. The equivalent circuits of both dielectric nonlinearity and mechanical nonlinearity are given in Fig. 4.14; corresponding to field-dependent R , C [157], and stress-dependent k , ζ , respectively. It should be noticed that in systems even without piezoelectric effect also have similar jumping phenomenon [137].

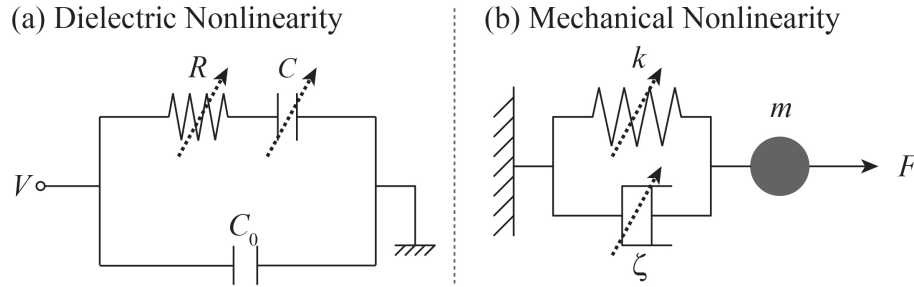


Figure 4.14: Equivalent circuits of (a) dielectric and (b) mechanical nonlinearity; R , C in (a) and k , ζ in (b) are variables.

Conversely, if dielectric and piezoelectric nonlinearities exist, the values (real and imaginary) of the dielectric coefficient (or damped capacitance C_d) and the piezoelectric coefficient (or force factor A) in the modeling must be field (or voltage) dependent. However, in this study, the model was found to be successful when both of them were assumed to be real constants. The fitting of admittance curves and burst mode results gave almost same coefficients (Table 4.5), so the C_d and A (used in the nonlinear model) should be constants. This is different from the conventional polarization-field hysteresis loops and creep phenomena: in ferroelectrics the C_d is dependent on the electrical field because it is related to the domain movements.

In view of above discussion, we've mentioned that:

- (1) Small electrical field;
- (2) Large stress;
- (3) Burst mode results only reveal the information of mechanical vibration;
- (4) Fitting of admittance curve gave the same results as burst mode method;
- (5) Constant C_d and A proved to be feasible.

So, we believe that the nonlinearity found in burst mode results and admittance curves derives from the mechanical nonlinearity, while the dielectric nonlinearity and piezoelectric nonlinearity can be neglected.

4.8 Derivation of Nonlinear coefficients

In section 4.4-4.5, the nonlinear phenomena in burst mode results and admittance curves were analyzed. Two nonlinear coefficients p and q were used; we mentioned that they were dimensionless. This section presents the derivation of p and q from the vibration equations.

4.8.1 Derivation of q

A plate transducer shown in Fig. 4.15 is considered, with length l , width w , height h , section area wh , and Young's modulus E .

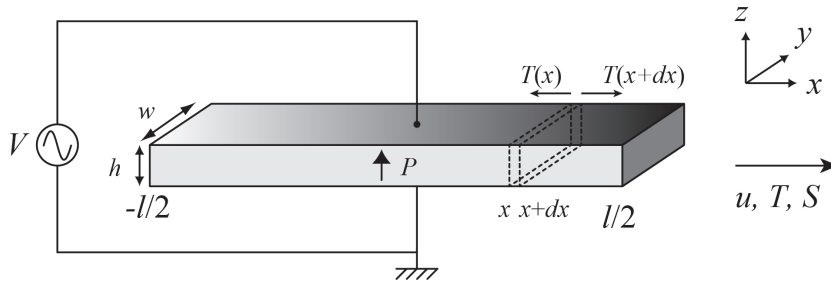


Figure 4.15: Schematic diagram of a piezoelectric plate transducer.

Considering a small section of the transducer $x \rightarrow x + dx$, the motion equation of this section is

$$\rho wh \frac{\partial^2 u}{\partial t^2} dx = wh (T(x + dx) - T(x)) = wh \frac{\partial T}{\partial x} dx, \quad (4.32)$$

where ρ , u , and T are the density, displacement, and stress of the transducer. Both u and T are functions of x and t . In the linear case, Eq. 4.32 can be revised as

$$\rho wh \frac{\partial^2 u}{\partial t^2} dx = Ewh \frac{\partial^2 u}{\partial x^2} dx. \quad (4.33)$$

Multiply both sides by $\frac{\partial u}{\partial t}$ and integrate with respect to x ,

$$\int_{-\frac{l}{2}}^{\frac{l}{2}} \rho wh \frac{\partial^2 u}{\partial t^2} \frac{\partial u}{\partial t} dx - \int_{-\frac{l}{2}}^{\frac{l}{2}} Ewh \frac{\partial^2 u}{\partial x^2} dx = 0, \quad (4.34)$$

where,

$$\int_{-\frac{l}{2}}^{\frac{l}{2}} \rho wh \frac{\partial^2 u}{\partial t^2} \frac{\partial u}{\partial t} dx = \int_{-\frac{l}{2}}^{\frac{l}{2}} \rho wh \frac{\partial v}{\partial t} v dx = \frac{\partial}{\partial t} \left(\int_{-\frac{l}{2}}^{\frac{l}{2}} \rho wh v^2 dx \right), \quad (4.35)$$

and

$$\int_{-\frac{l}{2}}^{\frac{l}{2}} Ewh \frac{\partial^2 u}{\partial x^2} dx = -\frac{\partial}{\partial t} \int_{-\frac{l}{2}}^{\frac{l}{2}} \frac{1}{2} \left(\frac{\partial u}{\partial x} \right)^2 dx, \quad (4.36)$$

where, integration by parts was adopted. Using the expressions of the velocity and the displacement:

$$v = v_0 \sin kx \exp j\omega t = v_t \sin kx, \quad (4.37)$$

$$u = \frac{v_0}{j\omega} \sin kx \exp j\omega t = u_t \sin kx, \quad (4.38)$$

where $k = \pi/l$ is the wavenumber of the fundamental mode.

Equation 4.34 can be simplified as

$$\frac{\partial}{\partial t} \left(\frac{1}{2} m v_t^2 + \frac{1}{2} K u_t^2 \right) = 0, \quad (4.39)$$

where, $m = \rho whl = M/2$, $K = k^2 Ewhl$ are equivalent mass and spring constant, respectively. The two terms in the brackets on the left side of Eq. 4.39 are kinetic energy and potential energy, respectively. m and K are both dependent on the size of the transducer.

Taking the nonlinear term into account,

$$T = E_1 \frac{\partial u}{\partial x} + E_3 \left(\frac{\partial u}{\partial x} \right)^3 + \dots \quad (4.40)$$

If only E_1 is not zero, it is linear case; here we introduce the third order term to represent the third order vibration; higher order terms are neglected. The motion equation (Eq. 4.32) can be revised as

$$\begin{aligned} \rho wh \frac{\partial^2 u}{\partial t^2} dx &= wh E_1 \frac{\partial^2 u}{\partial x^2} + wh E_3 \frac{\partial \left(\frac{\partial u}{\partial x} \right)^3}{\partial x} \\ &= wh E_1 \frac{\partial^2 u}{\partial x^2} + 3wh E_3 \frac{\partial^2 u}{\partial x^2} \left(\frac{\partial u}{\partial x} \right)^2. \end{aligned} \quad (4.41)$$

Integrate the terms on both sides, similar as Eq. 4.39, at last we have

$$\frac{\partial}{\partial t} \left(\frac{1}{2} m v_t^2 + \frac{1}{2} K_1 u_t^2 + \frac{1}{2} K_3 u_t^4 \right) = 0, \quad (4.42)$$

where,

$$K_1 = \frac{E_1 whl k^2}{2}, \quad (4.43)$$

$$K_3 = \frac{3E_3 whl k^4}{16}. \quad (4.44)$$

Introducing a parameter k' , which satisfies

$$\begin{aligned} \frac{1}{2}K_1u_t^2 + \frac{1}{2}K_3u_t^4 &= \frac{1}{4}E_1whlk^2u_0^2 + \frac{3}{32}E_3whlk^4u_0^4 \\ &= \frac{1}{4}E_1whl(k')^2u_0^2. \end{aligned} \quad (4.45)$$

Then, we have

$$k + \frac{3}{16} \frac{E_3}{E_1} k^3 u_0^2 = k', \quad (4.46)$$

or

$$\omega_0 + \frac{3}{16} \frac{E_3}{E_1} \frac{\omega_0^3}{c^2} u_0^2 = \omega_r, \quad (4.47)$$

where, the approximation $E_3/E_1 \ll 1$ and $k = \omega_0/c$ is used. Noticing

$$c^2 = \frac{E}{\rho}, \quad (4.48)$$

we have

$$\Delta\omega = \omega_r - \omega_0 = \frac{3}{16} \frac{E_3}{E_1} \frac{\omega_0^3}{c^2} u_0^2 = -\frac{3}{16} \frac{\rho\omega_r E_3}{E_1^2} v_0^2, \quad (4.49)$$

where, the expressions of the displacement and velocity (Eqs. 4.37-4.38) and the approximation $\omega_r \approx \omega_0$ are used. So we have

$$\frac{q}{l} = -\frac{3\rho\omega E_3}{16E_1^2}. \quad (4.50)$$

Noticing that in the expression of $\Delta\omega$, only ω_r is proportional to l^{-1} because

$$\omega_r = 2\pi f_r = 2\pi \frac{c}{2l} = \frac{\pi c}{l} \propto l^{-1}. \quad (4.51)$$

So, the coefficient in Eq. 4.49 is proportional to l^{-1} ; here we use q/l to represent the coefficient, then q should be a parameter independent on size and can be used for comparison between samples with different sizes.

4.8.2 Derivation of decay rate

In Eq. 4.32, taking the loss into account, Young's modulus E should be a complex parameter instead of a real one, as expressed by

$$E = E_r + jE_i. \quad (4.52)$$

Using the expression of damped vibration

$$u = u_0 \sin kx \exp(j\omega t - \beta t), \quad (4.53)$$

and put Eqs. 4.52-4.53 into Eq. 4.32, we have

$$\begin{aligned} & \rho wh(j\omega - \beta)^2 u_0 \sin kx \exp(j\omega t - \beta t) \\ &= (E_r + jE_i)^2 wh(-k^2) u_0 \sin kx \exp(j\omega t - \beta t). \end{aligned} \quad (4.54)$$

Noticing $\beta/\omega \ll 1$ when $Q_m \gg 1$, then

$$-\rho\omega^2 = -E_r k^2, \quad (4.55)$$

$$-2j\rho\omega\beta = -E_i k^2; \quad (4.56)$$

hence we have

$$\beta = \frac{-jE_i k^2}{-2j\rho\omega} = \frac{-jE_i}{-2j\rho\omega} \frac{-\rho\omega^2}{-E_r} = \frac{\omega E_i}{2E_r}. \quad (4.57)$$

The following is another method to derive β .

Still, we need to consider the Young's modulus as a complex parameter (since later the nonlinearity needs to be taken into account, where we need to use nonlinear term E_3 ; here we use E_1 instead of E), and

$$E_1 = E_{1r} + jE_{1i}, \quad (4.58)$$

$$\rho wh \frac{\partial^2 u}{\partial t^2} dx = (E_{1r} + jE_{1i}) wh \frac{\partial^2 u}{\partial x^2} dx. \quad (4.59)$$

Similar to Eqs. 4.34-4.36, the integrations give a result similar to Eq. 4.39,

$$\begin{aligned} \frac{\partial}{\partial t} \left(\frac{1}{2} m v_t^2 + \frac{1}{2} K u_t^2 \right) &= \frac{\partial}{\partial t} \left(\int_{-\frac{l}{2}}^{\frac{l}{2}} jE_{1i} \frac{\partial^2 u}{\partial x^2} \frac{\partial u}{\partial t} dx \right) \\ &= -\frac{1}{4} jE_{1i} wh l k^2 2u_t v_t \approx -\frac{1}{2} E_{1i} wh l \frac{\omega}{E_{1r}} v_t^2, \end{aligned} \quad (4.60)$$

where, the expression of u and v should be revised as

$$v = v_0 \sin kx \exp(j\omega t - \beta t) = v_t \sin kx, \quad (4.61)$$

$$u = \frac{v_0}{j\omega} \sin kx \exp(j\omega t - \beta t) = u_t \sin kx. \quad (4.62)$$

Noticing that the coefficient on the right side is related to β_0 (the decay rate without considering nonlinear terms), and we have

$$\beta = \frac{\zeta}{2m}, \quad (4.63)$$

where, ζ is damping ratio and m is equivalent mass. Details about Eq. 4.63 will be given later. Hence, we have

$$\beta_0 = \frac{-\frac{1}{2}E_{1i}\rho whl \frac{\omega}{E_{1r}}}{2 \times \frac{\rho whl}{2}} = -\frac{\omega E_{1i}}{2E_{1r}}. \quad (4.64)$$

The following is the derivation of Eq. 4.63. Considering a damped spring-mass system, expressed by

$$m \frac{\partial^2 x}{\partial t^2} = -Kx - \zeta \frac{\partial x}{\partial t}. \quad (4.65)$$

Using the expression $x = x_0 \exp(j\omega t)$, Eq. 4.65 can be revised

$$-m\omega^2 + j\zeta\omega + K = 0. \quad (4.66)$$

The solution of Eq. 4.66 is

$$\omega = \frac{j\zeta \pm \sqrt{-\zeta^2 + 4mK}}{2m} \approx \pm \sqrt{\frac{K}{M}} + j\frac{\zeta}{2M}. \quad (4.67)$$

Separate the complex frequency by using $x = x_0 \exp(j\omega t - \beta t)$, we have

$$\omega_0 = \pm \sqrt{\frac{K}{m}}, \quad (4.68)$$

$$\beta = \frac{\zeta}{2m}, \quad (4.69)$$

which is the same as Eq. 4.63.

4.8.3 Derivation of p

In Eq. 4.32, if we take the effects of nonlinear E (as expressed by Eq. 4.40) and complex E (as expressed by Eq. 4.58) at the same time, we have

$$E_1 = E_{1r} + E_{1i}, \quad (4.70)$$

$$E_3 = E_{3r} + E_{3i}. \quad (4.71)$$

Similar to Eq. 4.60, we have

$$\begin{aligned} & \frac{\partial}{\partial t} \left(\frac{1}{2}mv_t^2 + \frac{1}{2}K'u_t^2 \right) \\ &= \frac{\partial}{\partial t} \left(\int_{-\frac{l}{2}}^{\frac{l}{2}} jE_{1i} \frac{\partial^2 u}{\partial x^2} \frac{\partial u}{\partial t} dx + \int_{-\frac{l}{2}}^{\frac{l}{2}} 3jE_{3i} \frac{\partial^2 u}{\partial x^2} \left(\frac{\partial u}{\partial x} \right)^2 \frac{\partial u}{\partial t} dx \right) \\ &= -\frac{1}{4}jE_{1i}whlk^2 2u_t v_t - \frac{9}{32}jE_{3i}whlk^4 4u_t^3 v_t \\ &\approx -\frac{1}{2}whl\rho \frac{\omega E_{1i}}{E_{1r}} v_t^2 - \frac{3}{8}jE_{3i}whl \frac{\omega^4}{E_{1r}^2} \rho^2 \frac{1}{-j\omega^3} v_t^4 \\ &= -\frac{1}{2}whl\rho \frac{\omega E_{1i}}{E_{1r}} v_t^2 - \frac{3}{8}whl\rho^2 \frac{\omega E_{3i}}{E_{1r}^2} v_t^4. \end{aligned} \quad (4.72)$$

The coefficients of first term and second term on the right side of Eq. 4.72 are related to β_0 and p/l , respectively. We have

$$\beta_0 = -\frac{\omega E_{1i}}{2E_{1r}}, \quad (4.73)$$

$$\frac{p}{l} = \beta - \beta_0 = -\frac{3}{8} \frac{E_{3i}}{E_{1r}^2} \rho \omega_r. \quad (4.74)$$

Similar to Eq. 4.50, using Eq. 4.51, the parameter p is also independent on the size. Above theoretical derivation demonstrates that the introduced nonlinear parameters p and q are size independent and can be utilized for the comparison of samples with different sizes.

Finally, the relationships between the parameters and Young's modulus are summarized and shown in Table 4.6. Real parts of E_1 and E_3 determine the linear resonant frequency and nonlinear resonant frequency; while imaginary parts give the linear decay rate and the nonlinear decay rate, respectively.

Table 4.6: Relationships between parameters and Young's modulus.

	Resonant Frequency	Decay Rate
Linear	$\omega_0 (E_{1r})$	$\beta (E_{1i})$
Nonlinear	$\Delta\omega (E_{3r})$	$\Delta\beta (E_{3i})$

4.9 Brief Summary

In this chapter, the nonlinearity in PZT transducers was investigated and a method to determine the nonlinear coefficients was proposed. Two main conclusions are as follows:

(1) The burst mode method was used at first to measure the vibration velocity of the transducers after excitation by a burst voltage. The equivalent mechanical loss and the equivalent spring constant were determined by the decay rate of the vibration velocity and the resonant frequency, respectively. Both of them were found to be functions of velocity amplitude, suggesting that nonlinearity should be considered when the transducers are driven at high voltage (in this case, 10 and 100 V_{pp}).

(2) Admittance curves at high voltage (10 V_{pp}) corroborated the existence of nonlinearity in PZT transducers. In the admittance curves of the hard-type PZT transducer, a jumping phenomenon and an admittance hysteresis between different sweep directions appeared. A model with nonlinear terms was proposed and used to fit the admittance curves. This model proves to be effective in describing the admittance hysteresis and jumping observed in the case of the hard-type PZT

transducer and the deformation in admittance curves for both PZT transducers. Curve fitting yielded the nonlinear coefficients and force factor.

The present method can be used to analyze the nonlinearity in piezoelectrics; the two nonlinear coefficients can be regarded as criteria for assessing transducers driven under large stress. The comparable results of admittance curve measurement and burst mode method suggest that the two methods can replace each other in estimating the nonlinearity level. The feasibility of the model without considering the dielectric nonlinearity and piezoelectric nonlinearity indicates that the jumping and admittance hysteresis in the admittance curves results from the mechanical nonlinearity.

CHAPTER 5

Nonlinear Behavior in CuO-KNN Transducers

5.1 Background

Lead-free piezoelectrics, as potential substitutes for PZT-based piezoelectrics, have been widely investigated and utilized. Although some lead-free based piezoelectrics have been claimed to exhibit comparable properties to that of PZT-based materials, an overview of present developments in lead-free piezoelectrics [23] pointed out that there is still long way to go. The values of dielectric permittivity, piezoelectric coefficient, and coupling factor at room temperature are summarized as functions of Curie temperature T_c , as illustrated in Fig. 5.1 [23]. From Fig. 5.1 it is noticed that the performance of these key characteristics in lead-free materials is unsatisfactory comparing with PZT system.

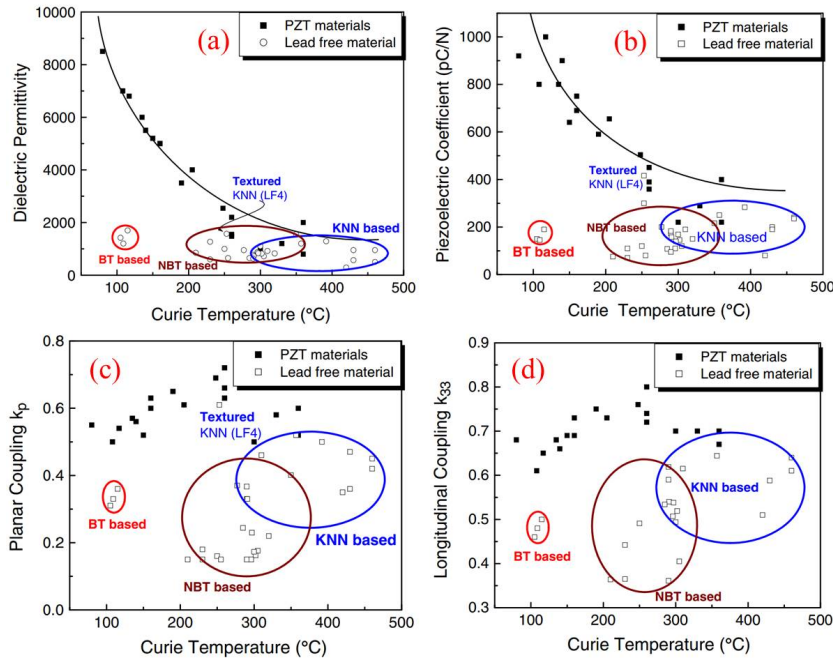


Figure 5.1: Comparison of (a) dielectric permittivity, (b) piezoelectric coefficient, (c) planar coupling factor, and (d) longitudinal coupling factor between PZT and lead-free materials [23].

Despite of abovementioned disadvantages, the lead-free piezoelectric materials also have some merits that should not be overlooked. As shown in Fig. 5.2(a)-(b), with increasing vibration velocity, the change of resonant frequency of PZT is much larger than some lead-free materials [90, 158]; in some lead-free systems the resonant frequency has an opposite shift direction [161]. Meanwhile, the quality factors of some lead-free materials stay relatively stable, whereas the performance of PZT-based materials are disappointing [159, 160], as shown in Fig. 5.2(c)-(d). In addition, PZT-based materials have other shortcomings like fatigue and aging

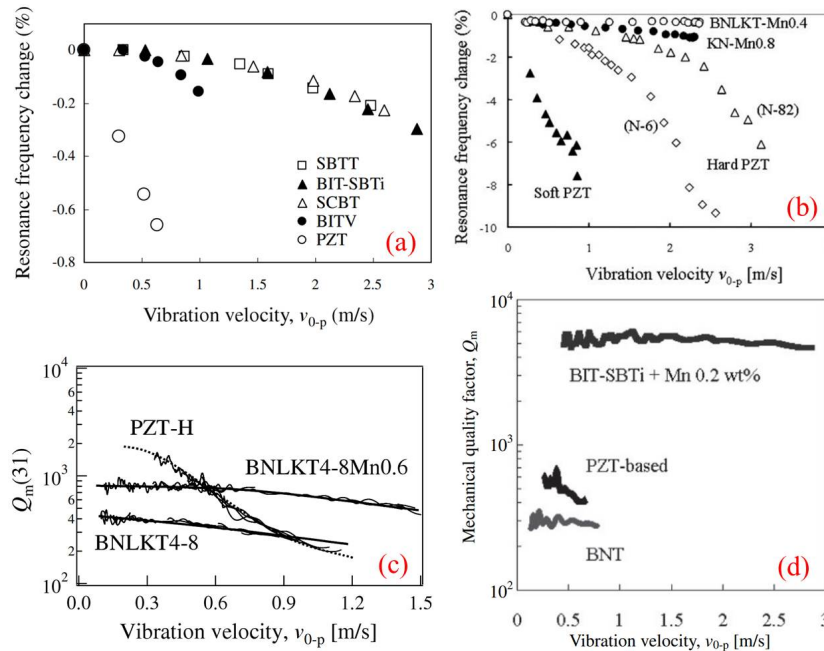


Figure 5.2: Comparison of (a)-(b) resonant frequency shift [90, 158] and (c)-(d) quality factor decrease [159, 160] between PZT and lead-free materials.

[162], which might be overcome by lead-free piezoelectrics. In one word, lead-free piezoelectrics are potential if their disadvantages can be solved.

5.2 Admittance Curve under High Voltage

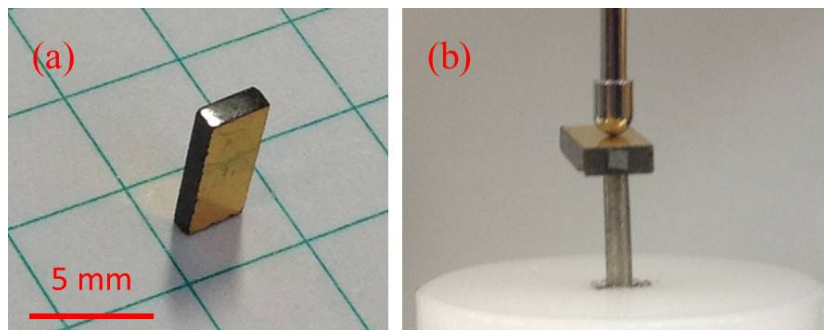


Figure 5.3: CuO-(K,Na)NbO₃ transducer (a) without and (b) with reflection sheet.

A CuO-(K,Na)NbO₃ transducer with a size of $6.33 \times 2.54 \times 0.99$ mm³ was cut from CuO-KNN disk. It was poled in the thickness direction (0.99 mm) and excited in the longitudinal mode with the 31 effect. Figure 5.3(a) shows the photo of one CuO-KNN transducer; the section of which was polished using water-resistant sandpapers. Notice that its size is smaller than PZTs used in chapter 4.

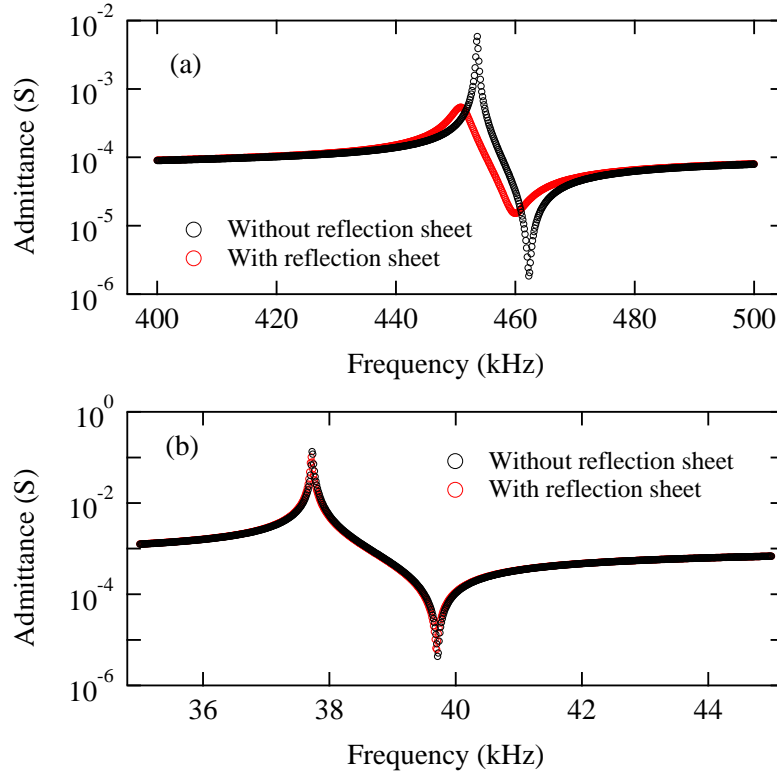


Figure 5.4: Admittance curves of (a) CuO-KNN and (b) hard-type PZT transducers with and without reflection sheet at $0.5 V_{pp}$.

For measuring the mechanical properties, usually a reflection sheet is adopted to reflect the laser beam, as shown in Fig. 5.3(b). However, it is found that the admittance curves with and without the reflection sheet are different from each other, as shown in Fig. 5.4(a), suggesting that the capacitance of reflection sheet cannot be neglected comparing with that of the transducer. This phenomenon didn't appear in PZT transducers, as shown in Fig. 5.4(b), probably corresponding to the much larger capacitance comparing with CuO-KNN transducer. The influence of the same reflection sheet on PZT transducers is relatively smaller than on CuO-KNN transducers.

The admittance curve measurements for CuO-KNN transducers were carried out rapidly (200 steps for each measurement, less than 5 s in total). The temperature rise during the admittance curve measurements and constant driving is shown in Fig. 5.5. During measuring admittance curves, the temperature rise of CuO-KNN transducer is negligible. As shown in Fig. 5.5(a), the temperature is almost constant at voltages of 0.5 and $10 V_{pp}$; while at voltages of 50 and $100 V_{pp}$ it increases by less than 0.6°C around the resonant frequency and decreases quickly after the resonant frequency.

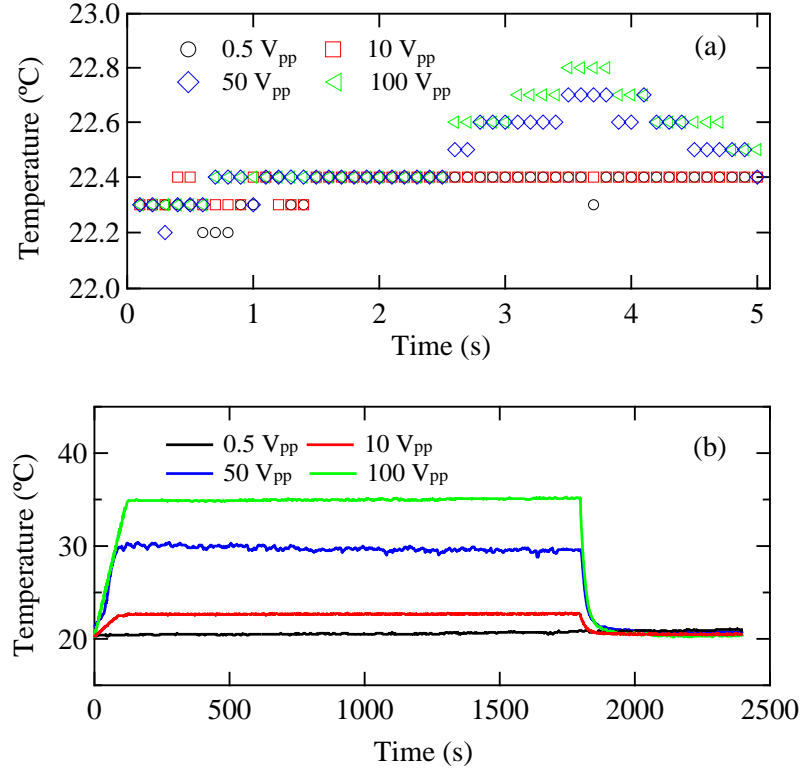


Figure 5.5: Temperature rise of CuO-KNN transducer in (a) admittance curve measuring and (b) continuous driving at various voltages.

Figure 5.5(b) shows the temperature rise during continuous driving. The driving at a constant voltage of 0.5 V_{pp} results in a negligible temperature rise; while during continuous driving at 10, 50, and 100 V_{pp} the temperature rises and becomes saturated gradually (the saturated temperature rise is about 2.5, 10, and 15 °C at 10, 50, and 100 V_{pp}, respectively). The voltage was released in 30 minutes and the temperature decreased rapidly. The time scale in Fig. 5.5(b) is consistent to that in PZT transducer (chapter 4) and the previous study [100]. It is noticed that the temperature rise curve of CuO-KNN transducer is slight different from the curve of hard-type PZT, probably owing to the smaller size and higher velocity.

The admittance curve of the CuO-KNN transducer at a low voltage (0.5 V_{pp}) is given in Fig. 5.6. The resonant and antiresonant frequencies are about 455.6 and 458.5 kHz, respectively. Using the equivalent circuit introduced in chapter 2 or the following equation

$$Y_{total} = j\omega C_d + \frac{1}{R + j\omega L + \frac{1}{j\omega C}}, \quad (5.1)$$

the admittance amplitude curve was fitted, the line in Fig. 5.6(a) shows consistence with the measured curves. In addition, the measured and fitted phase curves are

shown in Fig. 5.6(b).

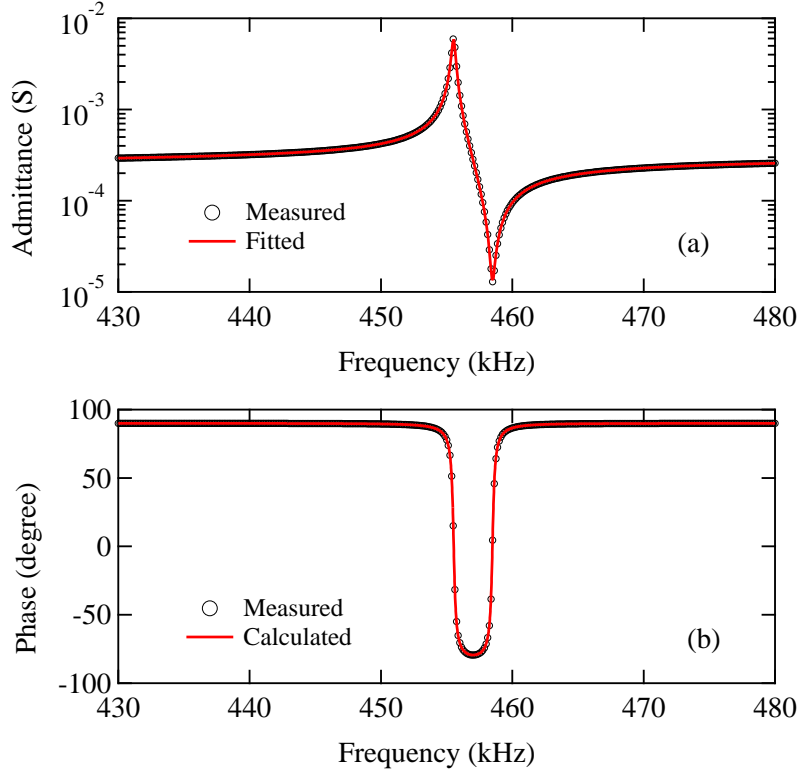


Figure 5.6: Measured and fitted admittance (a) amplitude and (b) phase curves of the CuO-KNN transducers at $0.5 V_{pp}$. Measured curves are denoted by circles and fitted curves are lines.

The parameters determined from the fitting are listed in Table 5.1. Comparing with hard- and soft-type PZT, the C_d value is much smaller. This may be the reason of Fig. 5.4; with the same reflection sheet, its influence on CuO-KNN (small C_d) is more significant than on PZT (large C_d).

Table 5.1: Equivalent circuit parameters of the PZT transducers and the CuO-KNN transducer.

	L (mH)	R (Ω)	C (pF)	C_d (pF)
Hard PZT	100.44	16.04	193.20	2028.60
Soft PZT	63.84	132.45	367.15	3154.80
CuO-KNN	99.67	166.47	1.2628	96.839

Using the parameters shown in Table 5.1 and the following equation

$$Q_m = \frac{2\pi f_r L}{R}, \quad (5.2)$$

the quality factor Q_m of CuO-KNN is determined to be 1662.

The admittance curves at 0.5, 10, 20, 50, and 100 V_{pp} are shown in Fig. 5.7. Compared with the low-voltage (0.5 V_{pp}) case (Fig. 5.6), the curves at high voltages clearly lost the symmetry. The admittance values near the resonant frequency (Fig. 5.6(a,c)) are not consecutive, which is the jumping phenomenon mentioned in the hard-type PZT transducer (chapter 4). In addition, the upward sweep and downward sweep measurements gave different results, forming a hysteresis. The phase curves exhibited similar behavior, as shown in Fig. 5.7(b,d). With increasing voltage, the resonant frequency shifts and the hysteresis range becomes larger and larger.

An enlarged version of the admittance curves in the region around the resonant frequency measured at 10 and 100 V_{pp} is shown in Fig. 5.8; the arrows in Fig. 5.8(a) mark the sweeping and jumping directions. Notice is taken that unlike the high voltage admittance curve of hard-type PZT (chapter 4) and Fig. 5.8(a), in the upward admittance curve the jumping at 100 V_{pp} is not as obvious as that of the former ones. However, the conventional equivalent circuit still fails to describe the deformed admittance curves in Fig. 5.8, no matter how we adjust the parameters in Table 5.1. The equivalent circuit with nonlinear terms is necessary.

5.3 Fitting Results and Nonlinear Coefficients

Using the nonlinear model derived in chapter 4, the current amplitude and phase of the admittance curve can be expressed by

$$\left(-\omega L i_0 + \frac{i_0}{\omega C_0} + \frac{3\xi i_0^3}{4}\right)^2 + \left(R_0 i_0 + \frac{3\eta i_0^3}{4}\right)^2 = V_0^2, \quad (5.3)$$

$$\begin{aligned} \theta &= \arctan \frac{\left(-\omega L i_0 + \frac{i_0}{\omega C_0} + \frac{3\xi i_0^3}{4}\right)}{\left(R_0 i_0 + \frac{3\eta i_0^3}{4}\right)} \\ &= \arctan \frac{\left(-\omega L + \frac{1}{\omega C_0} + \frac{3\xi i_0^2}{4}\right)}{\left(R_0 + \frac{3\eta i_0^2}{4}\right)}, \end{aligned} \quad (5.4)$$

The curve fitting was performed for the admittance curves of the CuO-KNN transducer at a voltage of 100 V_{pp} (Fig. 5.8(c-d)). Since the hysteresis in admittance and phase curves reflects nonlinearity, the same series of parameters should be used for both upward and downward sweep curves. The curve fitting was carried out for the downward sweep results first, and the upward sweep admittance curve was calculated from the parameters obtained in the downward sweep.

Figure 5.9 shows the plots of the fitting and calculation results for the CuO-KNN transducer. To help the comprehending of the jumping phenomenon, the

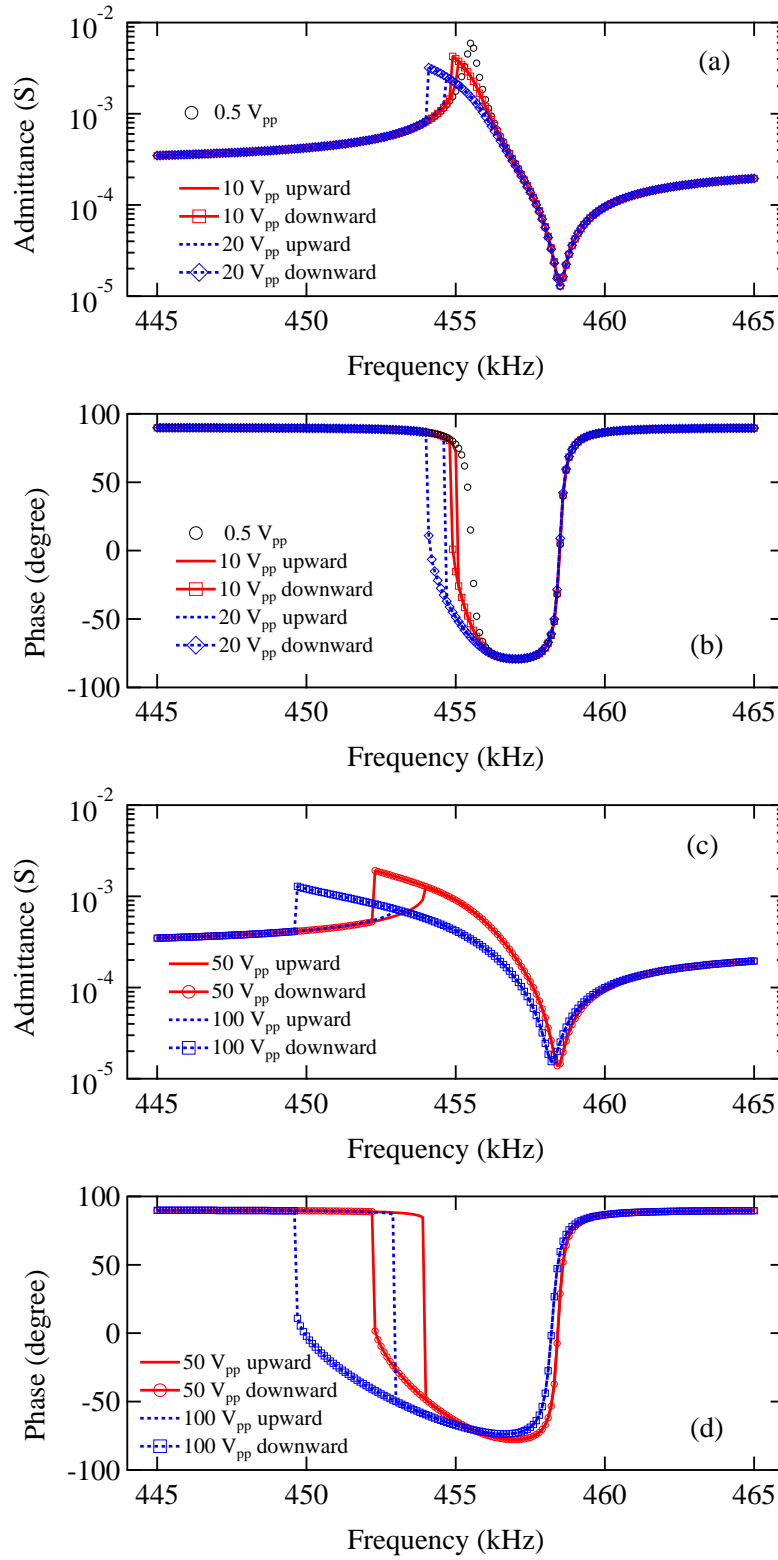


Figure 5.7: Admittance amplitude and phase curves for CuO-KNN transducers at (a-b) 0.5, 10, 20, and (c-d) 50, 100 V_{pp} (up sweep and down sweep).

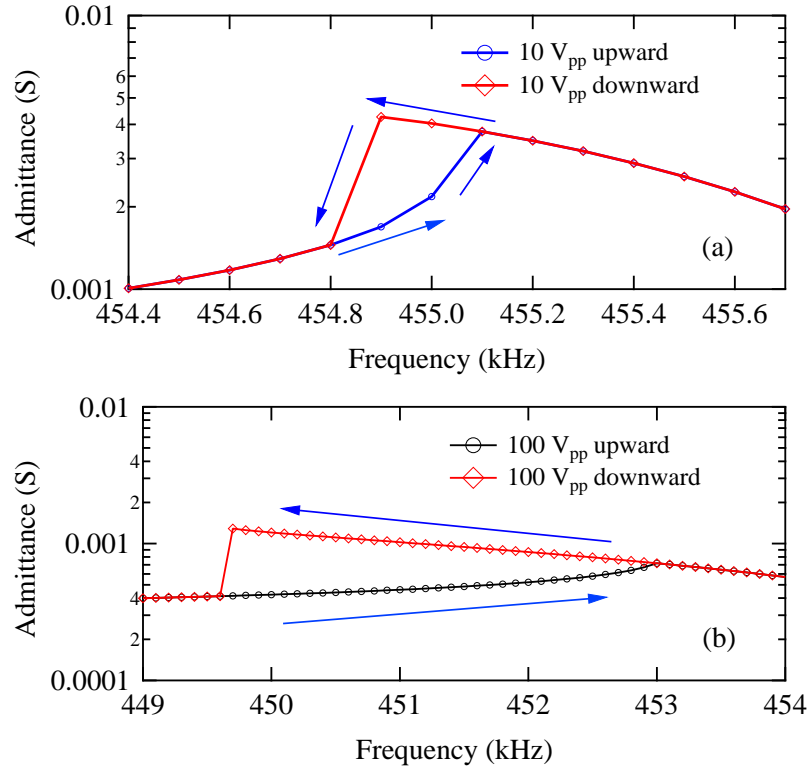


Figure 5.8: Enlarged view of admittance curve of the CuO-KNN transducer at (a) 10 and (b) 100 V_{pp} near the resonant frequency.

current values yielded from Eq. 5.3 are shown in Fig. 5.9(a). The unstable solutions connect the smaller solutions and larger solutions; however, the sweep of frequency determines that the unstable solutions cannot be observed, instead the jumping phenomenon appears.

The measured, fitted, and calculated admittance and phase curves shown in Fig. 5.9(b)-(c) indicate good description of the jumping phenomenon and admittance hysteresis. In Fig. 5.9(b), for the frequency range between 449.7 and 452.9 kHz, the cubic equation has three real solutions. In the upward sweep, the admittance value jumps at 452.9 kHz from smaller solutions to larger solutions; in the downward sweep, the values jumps at 449.7 kHz from larger solutions to smaller solutions, forming the hysteresis. The measured and calculated phase curves are depicted in Fig. 5.9(c). Both phase curves were determined from the aforementioned series of parameters; the calculated curves are also found to be consistent with the measured curves.

The fitted parameters including the force factor A , the nonlinear coefficients ξ and η , and the damped capacitance C_d are shown in Table 5.2. ω_0 values are close

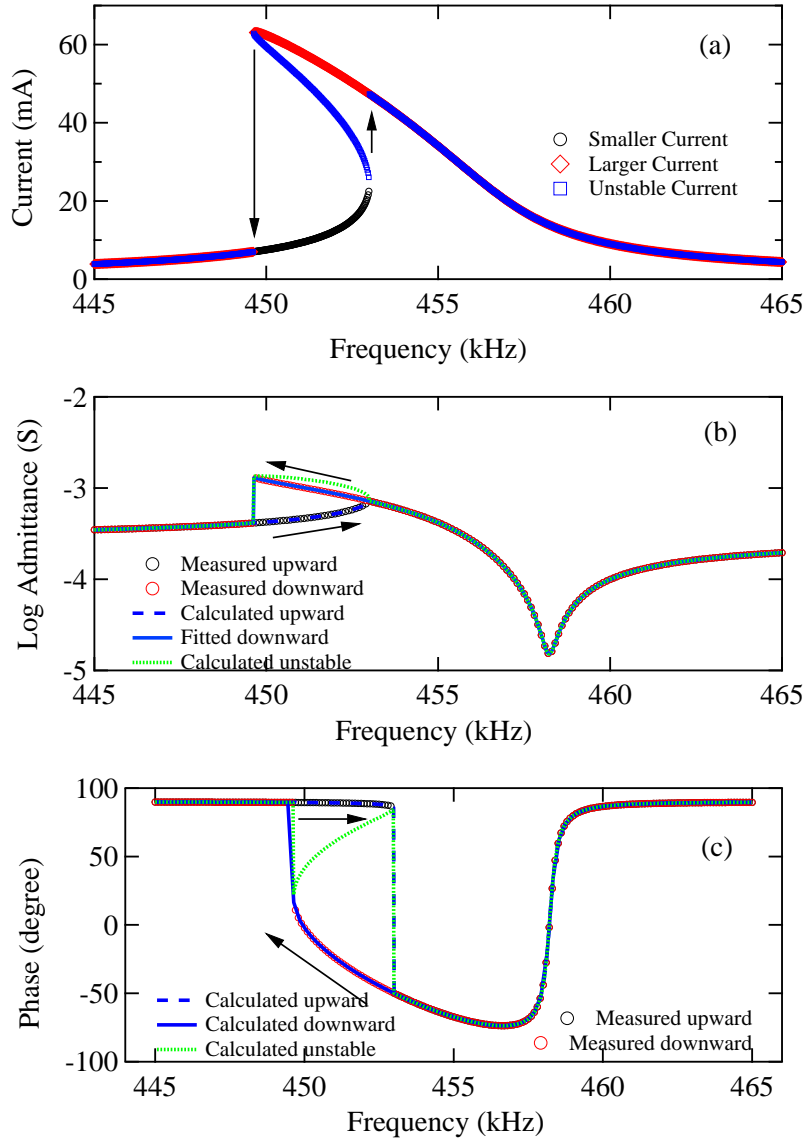


Figure 5.9: (a) Calculated current, (b) fitting admittance amplitude, and (c) phase curves of CuO-KNN transducers.

to the resonant frequency of each sample at $0.5 V_{pp}$ (also the driving frequency in the burst mode). Using the values of ω_0 and β_0 , the quality factor Q_m at low voltage can also be determined by

$$Q_m = \frac{\omega_0}{2\beta_0}; \quad (5.5)$$

which is 1662, the same as the value determined using Eq. 5.2.

In Table 5.2 it is noticed that the values of C_d are almost the same as those in Table 5.1; indicating that C_d is independent on the velocity (or current) amplitude.

The force factor A at low voltage can be calculated by L in Table 5.1 and the mass M (or equivalent mass $m = M/2$)

$$A = \sqrt{\frac{M}{2L}}. \quad (5.6)$$

At low voltage and high voltage A is almost the same, too; suggesting that A is not dependent on the velocity, either. The constant values of C_d and A demonstrate that the dielectric nonlinearity and piezoelectric nonlinearity can be neglected in the admittance curves, as explained in chapter 4.

Table 5.2: Coefficients of CuO-KNN transducers determined from the admittance curve fitting.

Sample	A (N/V)	β_0 (s ⁻¹)	η (ΩA^{-2})	ω_0 (rad/s)	ξ (ΩA^{-2})	C_d (pF)
Hard PZT	0.153	54	5.07×10^3	2.27×10^5	-9.57×10^4	2060
Soft PZT	0.191	1037	4.09×10^5	2.06×10^5	-8.83×10^5	3120
CuO-KNN	0.0189	861	2.08×10^5	2.862×10^6	-2.39×10^6	96.9

5.4 Predictions and Confirmation

The determined series of parameters shown in Table 5.2 can be used to predict the admittance curves at different voltages (0.5, 10, and 50 V_{pp}), as shown in Fig. 5.10. In Fig. 5.10(a), the calculated curve at a low voltage (0.5 V_{pp}) shows great consistence with the measured curve, confirming the negligible nonlinear effect under this condition. In contrast, the nonlinearity cannot be neglected at voltages of 10, 20, and 50 V_{pp}, as indicated by the jumping phenomenon and hysteresis in the curves in Fig. 5.10(b)-(d). With increasing voltage, the hysteresis range (or the frequency range with three real solutions) expands rapidly. At voltages of 10 and 20 V_{pp}, the calculated curves overlap with the measured curves.

However, as shown in Fig. 5.10(d), the calculated curves at 50 V_{pp} are slightly different from the measured curves in the region near the resonant frequency, as marked by an ellipse. The point where the admittance amplitude jumps from larger solutions to smaller ones in the downward curve has a small shift, which might correspond to the slight deviation of nonlinear coefficients at different voltages.

It is noticed that although the curve fitting of high voltage admittance curves enables the determination of nonlinear coefficients, it takes time to prepare the fitting program. And in the fitting process the initial values of all parameters are supposed to be provided; without proper initial parameters the fitting might be unsuccessful. In chapter 6, we will present an easier method for estimating the nonlinear coefficients using only the feature points in the admittance curves (for example, resonant and antiresonant points).

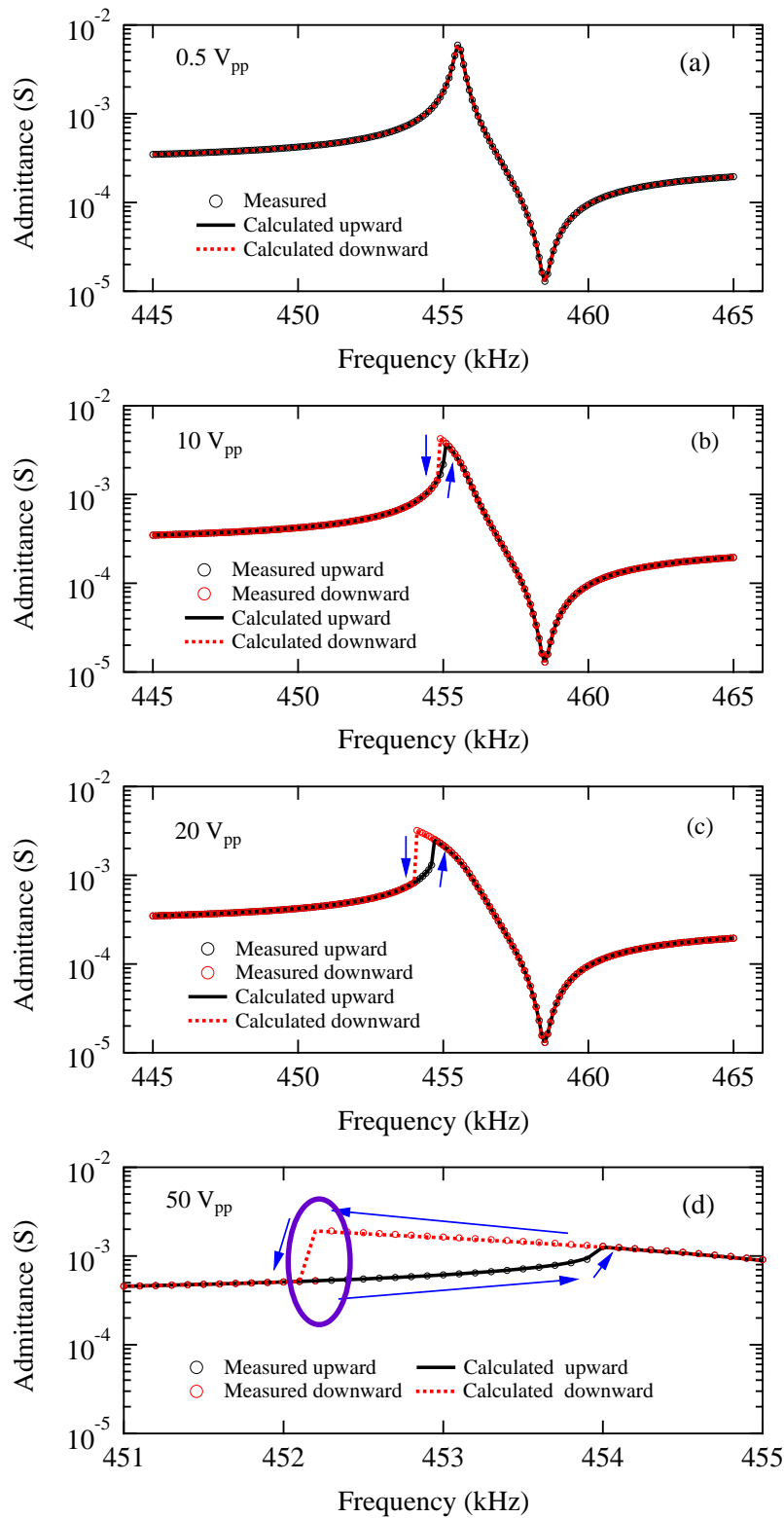


Figure 5.10: Prediction of admittance curves at (a) 0.5, (b) 10, (c) 20, and (d) 50 V_{pp} given by the determined coefficients.

5.5 Burst Mode Measurement and Results

In chapter 4, the nonlinearity in PZT transducers appears in the burst mode result. Here we present the nonlinearity of the CuO-KNN transducer in the burst mode measurement. Since only detecting velocity in the burst mode measurements might result in information loss, here both vibration velocity and current were measured. By combining them more parameters can be obtained.

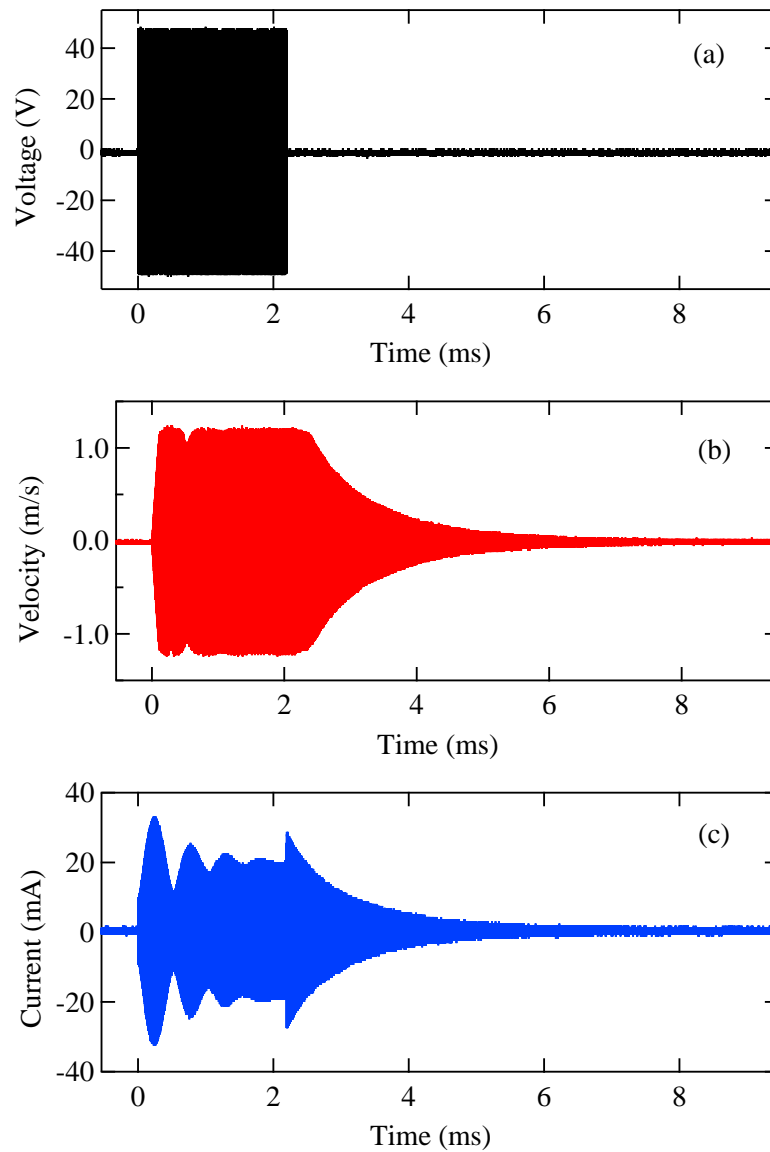


Figure 5.11: The burst mode results: (a) driving voltage, (b) vibration velocity, and (c) current of CuO-KNN transducer at 100 V_{pp}.

5.5.1 Burst mode measurements

In the burst mode measurements, the heat generation can also be neglected owing to the very short driving time (about 2.2 ms). The driving frequency is determined by the admittance curves measured at respective voltages (Fig. 5.7). The results at 10, 20, 50, and 100 V_{pp} were similar and the latter ones are shown in Fig. 5.11. In the beginning, as shown in Fig. 5.11(a), the burst voltage excited the transducer. After releasing the voltage signal, the transducer started free vibration; both the velocity in Fig. 5.11(b) and the current in Fig. 5.11(c) decreased with time. Filtering was carried out for the velocity and current with a bandwidth of 100 kHz to eliminate the background noise.

5.5.2 Results determined from velocity-time curve

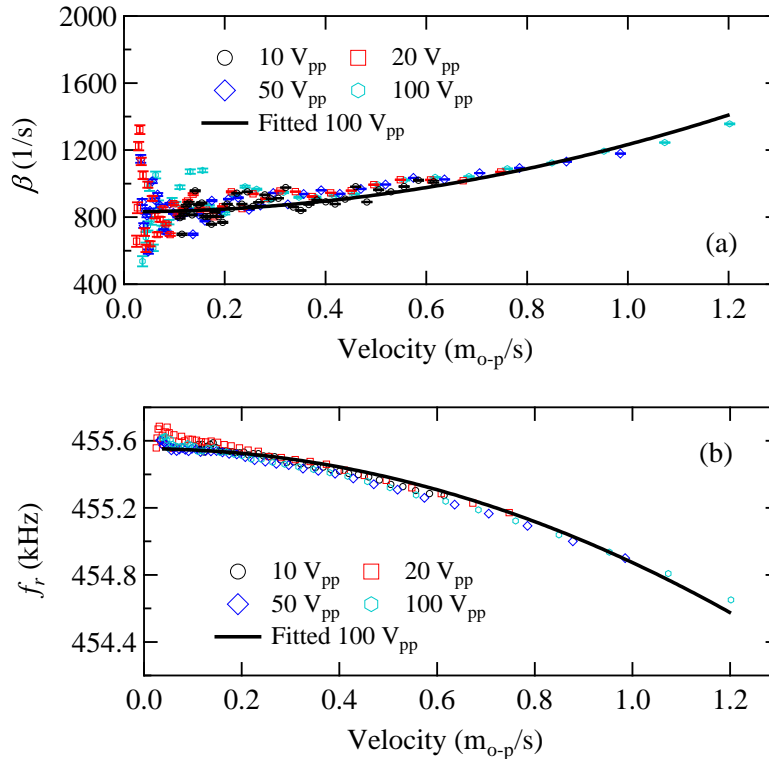


Figure 5.12: The determined (a) β and (b) f_r of CuO-KNN transducer at 10, 20, 50, and 100 V_{pp}.

From Fig. 5.11(b) and Fig. 5.11(c) it is possible to determine resonant frequency f_r and decay rate β . In Fig. 5.11(b) using the following equation

$$v(t) = v_0 \sin [\omega_r(t)(t + \varphi)] \exp^{-\beta(t)(t-\tau)}, \quad (5.7)$$

where $\omega_r = 2\pi f_r(t)$ and $\beta(t)$ are functions of time, v , v_0 , φ , and τ are the vibration velocity, velocity amplitude, initial phase, and the beginning time of free vibration, respectively.

Through the similar procedures as shown in chapter 4, the relationships between β , ω_r and velocity amplitude is given in Fig. 5.12. The quadratic relationships can be expressed by

$$\beta = \beta_0 + \frac{pv_0^2}{l}, \quad (5.8)$$

$$\omega_r = \omega_0 + \frac{qv_0^2}{l}, \quad (5.9)$$

where p and q are two real nonlinear coefficients.

Using curve fitting, the parameters in Eqs. 5.8-5.9 were determined and shown in Table 5.3. The values of p and q of the CuO-KNN transducer are smaller than the hard-type and soft-type PZTs, suggesting better stability of the CuO-KNN transducer. Along with high quality factor, CuO-KNN is a promising material for high-power applications; further estimation will be presented in chapter 6.

Table 5.3: Parameters of the CuO-KNN transducer obtained from burst mode result.

	β_0 (s ⁻¹)	p (s/m)	ω_0 (rad/s)	q (s/m)
CuO-KNN	832	2.60×10^0	2.862×10^6	-2.70×10^1

In addition, p and q can also be calculated from ξ and η , which were determined by the admittance curves. As shown in Table 5.4, although not identical, they are comparable to the results in Table 5.3, which are obtained from the fitting shown in Fig. 5.9. This is similar to the case of the hard-type and soft-type PZTs. Since the admittance curves can give results similar to those obtained by the burst-mode method, in this respect the two methods can be mutual substitutes.

Table 5.4: Comparison of parameters determined from the burst mode result and admittance curve fitting in the CuO-KNN transducer.

Method	β_0 (s ⁻¹)	p (s/m)	ω_0 (rad/s)	q (s/m)
Burst Mode	832	2.60×10^0	2.862×10^6	-2.70×10^1
Admittance	861	2.44×10^0	2.862×10^6	-2.79×10^1

5.5.3 Results determined from current-time curve

The above analysis also works for the current-time curve in Fig. 5.11(c). Using the function

$$i(t) = i_0 \sin [\omega_r(t)(t + \varphi)] \exp^{-\beta(t)(t-\tau)}, \quad (5.10)$$

the parameters can also be determined; where i and i_0 are the current and current amplitude, respectively. The velocity and current dependence of β and f_r are given in Fig. 5.13. The scale of the top axis (current amplitude) is given by the scale of the bottom axis (velocity amplitude) and the force factor A because we have

$$A = \frac{i}{v}. \quad (5.11)$$

The value A in Table 5.2 ($A = 0.0189$) is adopted; that is, the scale of bottom axis is $0 < v_0 < 1.3 \text{ m}_{\text{op}}$ and the scale of top axis $0 < i_0 < 0.02457 \text{ A}$. It is found that for both β and f_r curves determined from velocity and current are the same. It suggests that either velocity or current can provide the mechanical information.

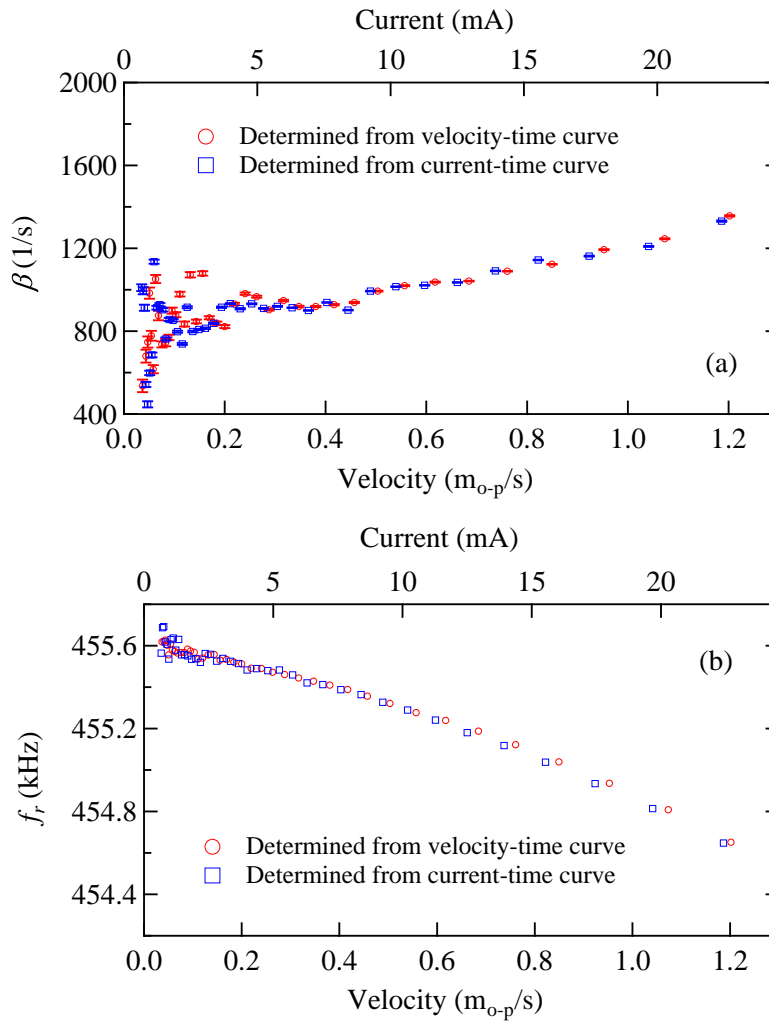


Figure 5.13: The (a) β and (b) f_r values of CuO-KNN transducer determined by velocity-time curve and current-time curve measured at $100 \text{ V}_{\text{pp}}$; the bars in (a) are the error bars of β .

5.6 Further Analysis of Burst Mode Results

Combining the velocity and current, the other parameters can be obtained based on the equations in chapter 2:

$$s_{11}^E = \frac{1}{4\rho l^2 f_r^2}, \quad (5.12)$$

$$T_m = v_0 \sqrt{\frac{\rho}{s_{11}^E}} = 2\rho l f_r v_0. \quad (5.13)$$

Using the stress as the independent variable, the velocity and current amplitudes are shown in Fig. 5.14. Despite of the slight decrease in f_r with increasing velocity, the approximate linear function correlations are still valid.

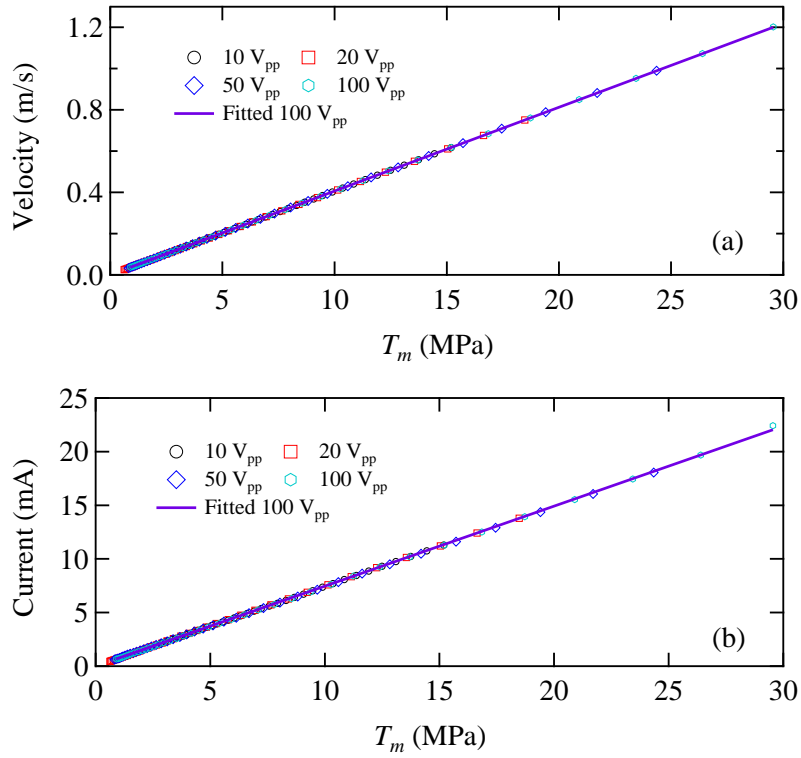


Figure 5.14: The fitted (a) velocity amplitude and (b) current amplitude as functions of T_m .

The linear relationships can be expressed by

$$v_0 = 4.0635 \times 10^{-8} T_m, \quad (5.14)$$

$$i_0 = 7.4594 \times 10^{-10} T_m. \quad (5.15)$$

The values of s_{11}^E determined at the same voltages are given in Fig. 5.15, which exhibits an approximate quadratic relationship, as expressed by

$$s_{11}^E = 7.0376 \times 10^{-12} + 3.4761 \times 10^{-29} T_m^2. \quad (5.16)$$

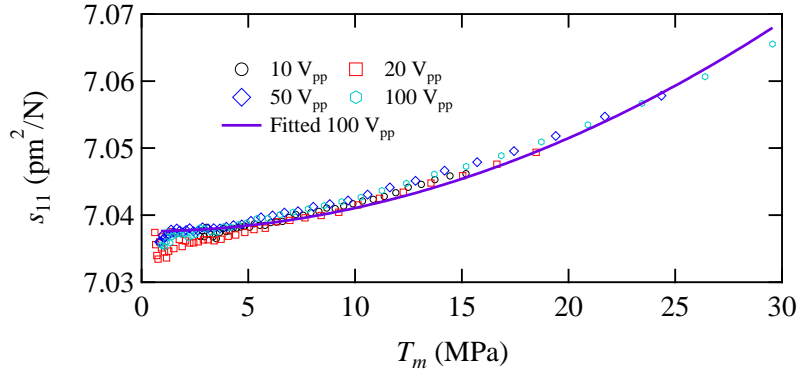


Figure 5.15: s_{11}^E values as functions of T_m .

The force factor A can be calculated to be 0.01836 N/V, almost the same as A given by the fitting of admittance curve (Table 5.2). In plate transducers, A can be expressed by

$$A = \frac{2wd_{31}}{s_{11}^E}. \quad (5.17)$$

Using Eq. 5.17, d_{31} can be calculated from A and s_{11}^E , as shown in Fig. 5.16.

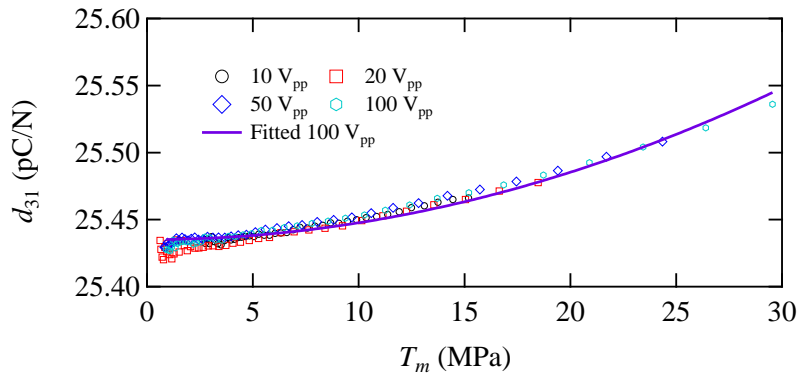


Figure 5.16: d_{31} values as functions of T_m .

In Fig. 5.16, d_{31} also follows an approximate quadratic relationship, which can be demonstrated by the fitting and expressed by

$$d_{31} = 2.5435 \times 10^{-11} + 1.2563 \times 10^{-28} T_m^2. \quad (5.18)$$

At last, it should be pointed out that the change of s_{11}^E and d_{31} values are small; at 30 MPa the relative variety is less than 0.5%. This corresponds to the small change of resonant frequency f_r (seen in Fig. 5.12-5.13). So, for rough calculations s_{11}^E and d_{31} can be taken as constants.

5.7 Brief Summary

The nonlinearity in lead-free CuO-KNN transducers was analyzed in this chapter. Three main conclusions are as follows:

(1) The admittance curves of lead-free CuO-KNN transducers at high voltages have serious deformation compared with the curves at low voltage. The broken symmetry cannot be explained by the conventional equivalent circuit. Around the resonant frequency the curves show a significant jump; while the different results in two sweep directions formed a hysteresis. The nonlinear model enables the fitting of admittance curves; and yielded coefficients allow the prediction of admittance curves at other voltages.

(2) In the burst-mode method, the nonlinearity at high voltages was confirmed. After excitation by a burst voltage, the transducers began free vibration, during which, both the decay rate and resonant frequency changed with time (or velocity amplitude). Quadratic relationships proved to be feasible in describing the results. The nonlinear coefficients obtained from the burst mode method are consistent with the admittance curve measurements. Combining the velocity and current curve, the other parameters can be calculated.

(3) Compared with PZT transducers, lead-free CuO-KNN transducers are less dependent on high-velocity condition.

CHAPTER 6

Simulation

6.1 Background

As mentioned in section 4.7, nonlinear behavior plays an important role in various phenomena, such as aperiodic oscillation, chaos, multi-state, amplitude attenuation, vanishment, and so on. Despite of many unique mechanisms of nonlinearity, some of the methods prove to be mutual. It is found that for most nonlinear phenomena, the corresponding differential equations are impossible to find an exact solution. Therefore, numerical simulation is adopted to find the approximate solutions of the differential equations. The stability of a damped Duffing oscillator was investigated using a renormalization group method, which enables the analysis of fixed points in the differential equations [137].

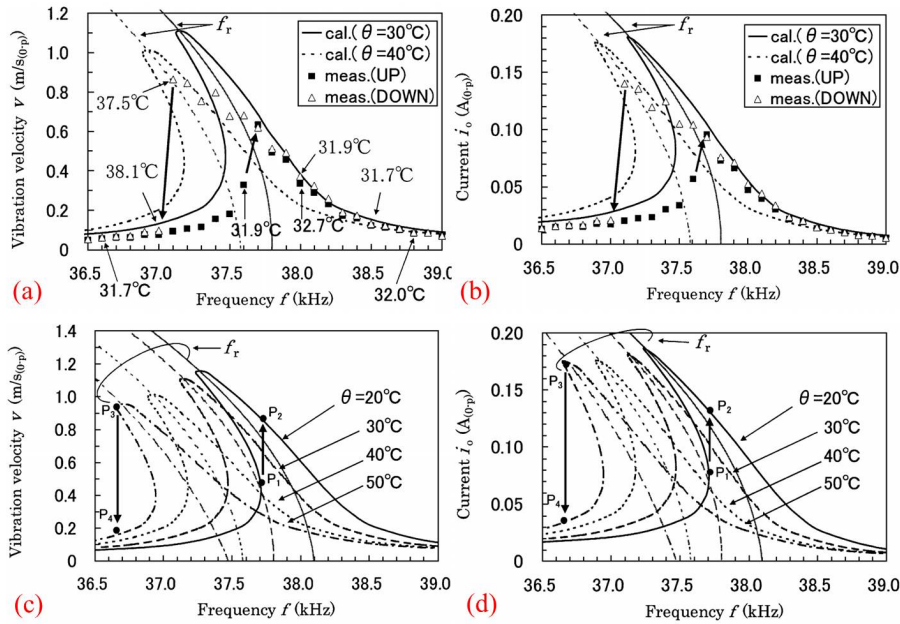


Figure 6.1: Simulation of (a) vibration velocity and (b) current at $10 V_{op}$ and the temperature dependence of (c) vibration velocity and (d) current [136].

A simulation on jumping and dropping phenomena of piezoelectric transducers at high vibration level was conducted based on the equivalent circuit constants [136]. The burst mode measurement suggested the velocity level dependent force factor A , equivalent resistance, inductance, and capacitance R , L , C ; using which the frequency responses of velocity (Fig. 6.1(a)), current (Fig. 6.1(b)), temperature dependence of velocity (Fig. 6.1(c)) and current (Fig. 6.1(d)) were calculated and discussed [136].

In piezoelectric or ferroelectric materials, the most common nonlinear behavior is P - E hysteresis loop, which might seem to be confusing with the nonlinearity in our study. Since Landau theory is feasible in the description of the phase transitions;

it was introduced to ferroelectrics by Devonshire [35]. However, thermodynamic theories are not suitable for polycrystalline ferroelectric materials, which are most used in the practical applications. Attempts to explain the P - E hysteresis loops of polycrystalline ferroelectrics have aroused the proposal of numerous models.

An equivalent circuit of ferroelectric capacitors is shown in Fig. 6.2(a); using the Landau free energy the P - E hysteresis loops could be calculated with proper parameters [157]. As shown in Fig. 6.2(b), the unipolar domain wall motions were considered to be analogy to mechanical dry friction, which allowed the simulation of P - E hysteresis loops [163]. In another model, a ferroelectric capacitor was considered as a bilayer structure constructed by a switching ferroelectric layer and two non-switching dielectric layers near the electrodes as shown in Fig. 6.2(c); the predications exhibited consistence with the experimental data [164]. Preisach distribution in Fig. 6.2(d) was introduced and improved for the calculation of field-induced strain and polarization curves [165, 166]. A two-dimensional simulation also proved to be feasible in the description of polarization switching [167].

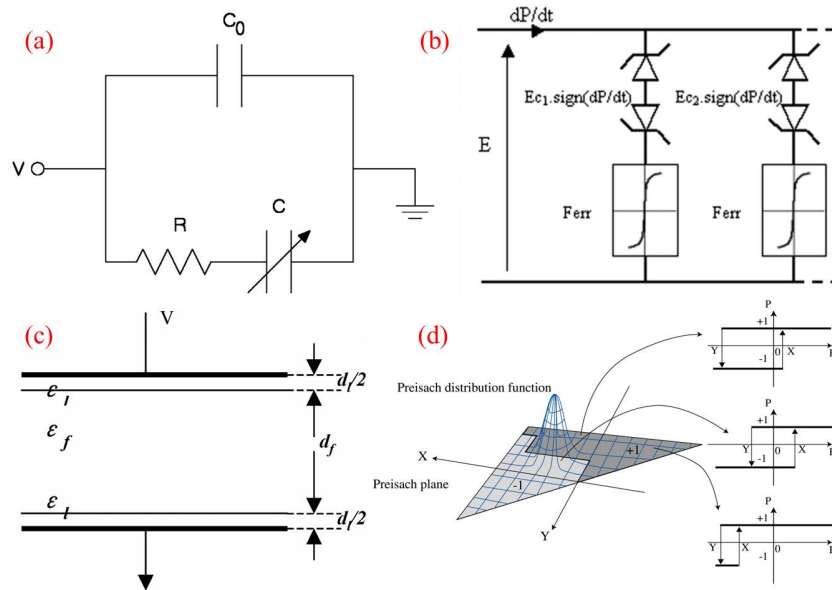


Figure 6.2: Ferroelectric hysteresis models: (a) equivalent circuit of ferroelectric capacitors [157], (b) dry friction model [163], (c) ferroelectric capacitance model [164], and (d) Preisach model [165].

High precision positioning is one of the most widely investigated applications in piezoelectric actuators, which, however, is significantly limited by aforementioned nonlinear hysteresis effect and creep effect resulting from the switching and domain wall movements [156]. Numerous compensation techniques are adopted to balance the influences of hysteresis and creep. To describe the creep, both nonlinear and linear creep models were introduced [156].

6.2 G - B circle

In chapters 4-5, the jumping in admittance curves is found in hard-type PZT and CuO-KNN plate transducers. Further explanation of jumping phenomenon is presented in this section and next two sections.

The admittance curves are equivalent to the G - B circles because

$$Y = G + jB, \quad (6.1)$$

where conductance G and susceptance B are the real and imaginary parts of the admittance, respectively. The G - B circles can be calculated from the admittance curves using

$$G = |Y| \cos \phi, \quad (6.2)$$

$$B = |Y| \sin \phi, \quad (6.3)$$

where $|Y|$ and ϕ are the admittance amplitude and phase, respectively.

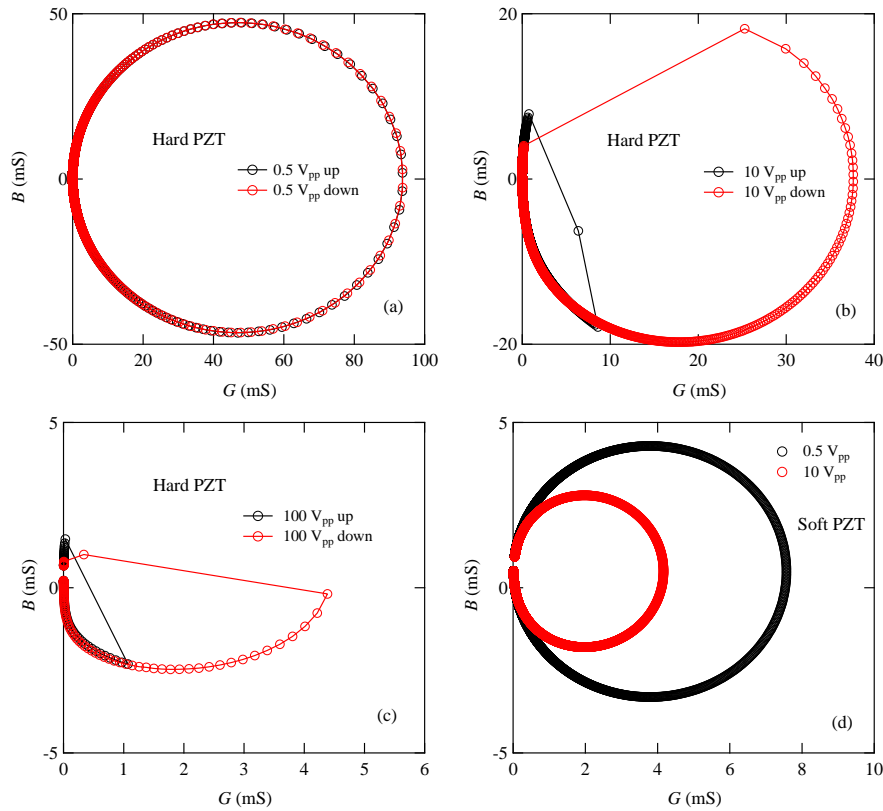


Figure 6.3: G - B circles of hard-type PZT at (a) 0.5, (b) 10, and (c) 20 V_{pp} and (d) soft-type PZT at 0.5 and 10 V_{pp} .

On the opposite, admittance curves can also be calculated from the G - B circles because

$$|Y| = \sqrt{G^2 + B^2}, \quad (6.4)$$

$$\phi = \arctan \frac{B}{G}. \quad (6.5)$$

The G - B circles of hard-type and soft-type PZT transducers are shown in Fig. 6.3. For hard-type PZT, at low voltage (0.5 V_{pp}), the upward sweeping and downward sweeping give overlapping circles, as shown in Fig. 6.3(a); while at high voltage (10 and 100 V_{pp}) shown in Fig. 6.3(b)-(c), the circles are not perfect anymore. The missing arcs represent the jumping in the admittance curve; while the staggered upward and downward circles correspond to the admittance hysteresis. For soft-type PZT, as shown in Fig. 6.3(d), no jumping or hysteresis appears. However, we should notice that for both PZTs the radius of the G - B circles (or the amplitude of the admittance) decreases with increasing voltage.

6.3 Jumping Current-Frequency Curve

To help the understanding of jumping, here we try to solve the following equation

$$\left(-\omega L i_0 + \frac{i_0}{\omega C_0} + \frac{3\xi i_0^3}{4}\right)^2 + \left(R_0 i_0 + \frac{3\eta i_0^3}{4}\right)^2 = V_0^2, \quad (6.6)$$

which can be revised to a cubic equation

$$\begin{aligned} \left(\frac{9\xi^2}{16} + \frac{9\eta^2}{16}\right) (i_0^2)^3 - 2 \left[\left(\omega L - \frac{1}{\omega C_0}\right) \frac{3\xi}{4} + R_0 \frac{3\eta}{4} \right] (i_0^2)^2 \\ + \left[\left(\omega L - \frac{1}{\omega C_0}\right)^2 + R_0^2 \right] (i_0^2)^1 - V_0^2 = 0, \end{aligned} \quad (6.7)$$

where, both ξ and η are involved in the polynomial coefficients; for each ω Eq. 6.7 is a different cubic equation.

For a cubic equation

$$aX^3 + bX^2 + cX + d = 0, \quad (6.8)$$

the roots of the cubic equation depend on the discriminant Δ [168], where

$$A = b^2 - 3ac, \quad (6.9)$$

$$B = bc - 9ad, \quad (6.10)$$

$$C = c^2 - 3bd, \quad (6.11)$$

$$\Delta = B^2 - 4AC. \quad (6.12)$$

When $A = B = 0$, the equation has a triple real root; when $\Delta > 0$, the equation has one real root and two conjugated imaginary roots; when $\Delta = 0$, the equation has three real roots and two of them are the same; when $\Delta < 0$, the equation has three different real roots.

Table 6.1: Parameters used in the simulation: frequency sweeping.

V_0 (V)	L (mH)	R_0 (Ω)	C_0 (nF)
5	100	10	1

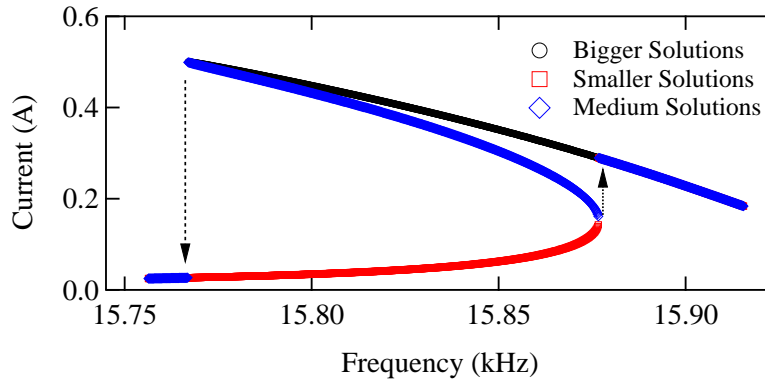


Figure 6.4: Simulation of jumping in current-frequency curve; the arrows mark the jumping directions.

In the simulation, the adopted parameters are shown in Table 6.1; the values of ξ and η (the units are both ΩA^{-2}) were set at -1000 and 0 , respectively. The currents around the resonance frequency obtained from Eq. 6.7 are depicted in Fig. 6.4. In the frequency range between 99064 and 99756 rad/s, three roots of Eq. 6.7 are all real; in other frequency ranges the equation has only one real root. In the upward sweep, current jumps from smaller roots to larger roots at 99756 rad/s; while in the downward sweep, current jumps from larger roots to smaller roots at 99064 rad/s. Noticed that the medium roots shown in Fig. 6.4 cannot be detected in the experiments because they are unstable.

Clearly, given a set of parameters shown in Table 6.1, the nonlinear level is determined by the two nonlinear coefficients ξ and η . The influence of ξ and η is given in Fig. 6.5. As shown in Fig. 6.5(a), when η is limited to zero, ξ with negative values makes the current deforms. With increasing ξ (the absolute value) the resonance frequency shifts to low frequency range while the maximum current decreases. As a comparison, ξ with positive values has a similar influence except for the opposite resonance frequency shift, as shown in Fig. 6.5(b). This effect corresponds to the soft-spring and hard-spring effect [137]. The soft-spring effect

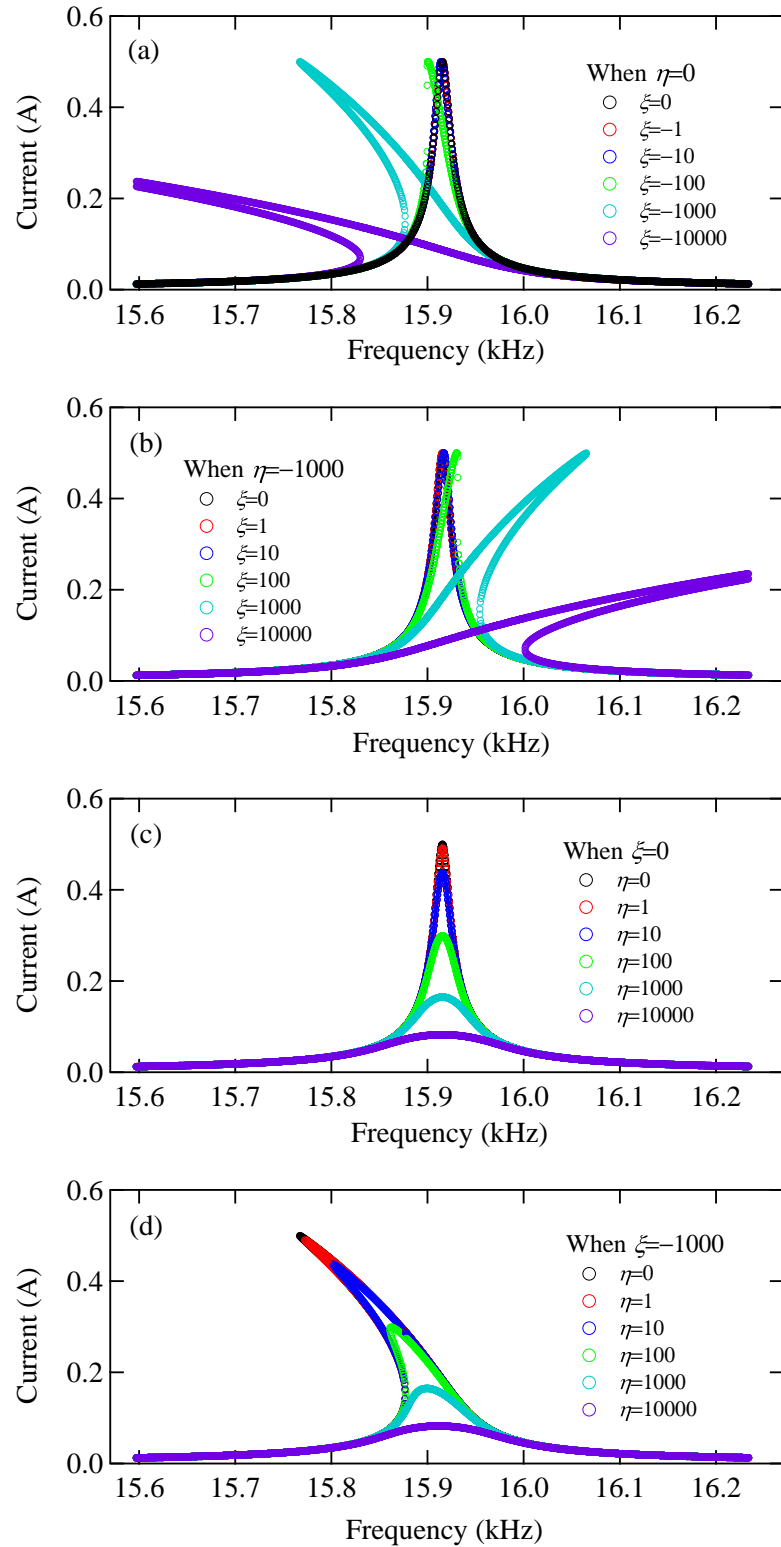


Figure 6.5: Influence of ξ and η to jumping in current-frequency curves: (a) $\xi < 0$, $\eta = 0$, (b) $\xi < 0$, $\eta = 0$, (c) $\xi = 0$, $\eta > 0$, and (d) $\xi = -1000$, $\eta > 0$.

exists in most piezoelectrics; while hard-spring effect was also reported in some piezoelectrics. Based on the experiments, the samples used in our study show soft-spring effect, while $(\text{Sr,Ca})_2\text{NaNb}_5\text{O}_{15}$ ceramics show hard-spring effect [98, 169].

When ξ is limited to 0, the influence of η is depicted in Fig. 6.5(c). Since in high power operation R usually increase, η should be positive. With an increasing η the maximum current amplitude decreases without changing the resonance frequency, which results in decreasing quality factor. When ξ is -1000 and η are not 0, the current amplitude also decreases; meanwhile the resonance frequency shifts to high frequency range, as shown in Fig. 6.5(d).

The simulation suggests that both ξ and η have significant influence on the current around resonance frequency while having negligible contribution in other regions. Both of them can decrease the amplitude and shift the resonance frequency (except for $\xi = 0$).

The current determined from the admittance curve of CuO-KNN transducer at $100 V_{pp}$ is illustrated in Fig. 6.6, which shows consistence with the simulated curves using the coefficients determined from the fitting.

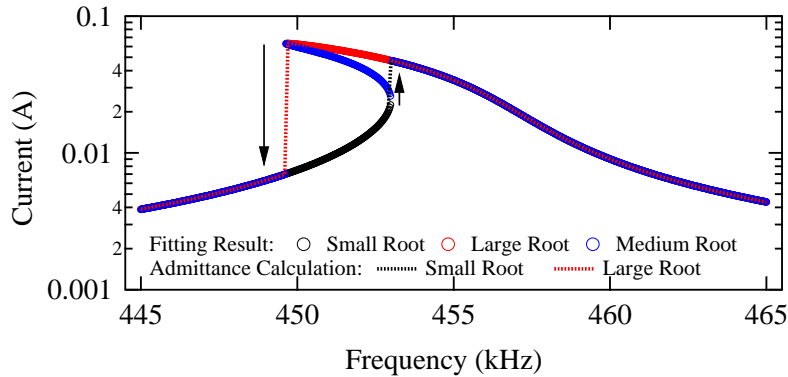


Figure 6.6: Comparison of current given by the simulation and experiments.

6.4 Jumping Current-Voltage Curve

In the previous section, the frequency sweeping is shown with a constant voltage amplitude V_0 in Eq. 6.7. In this section, the voltage sweep behavior is studied with a constant angular frequency ω in Eq. 6.7. In the simulation, the adopted parameters are shown in Table 6.2; the values of ξ and η (the units are both ΩA^{-2}) were set at -100 and 10, respectively. The currents with sweeping voltage calculated from Eq. 6.7 are shown in Fig. 6.7. Jumping and current hysteresis also appear in Fig. 6.7. In the voltage range between 22.5 and $45.5 V_{op}$ three roots are all real; in other ranges the equation has one real root and two complex conjugated roots.

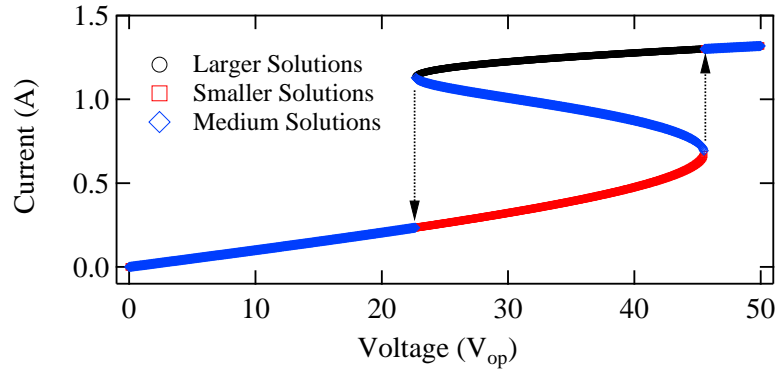


Figure 6.7: Simulation of jumping in current-voltage curve; the arrows mark the jumping directions.

With increasing voltage, current jumps from smaller roots to larger roots at $45.5 V_{op}$; with decreasing voltage, current jumps from larger roots to smaller roots at $22.5 V_{op}$.

Table 6.2: Parameters used in the simulation: voltage sweeping.

ω (rad/s)	L (mH)	R_0 (Ω)	C_0 (nF)
99500	100	10	1

Similar to the previous section, given a certain set of parameters, the nonlinear level is determined by the two nonlinear coefficients ξ and η . The influence on the current-voltage curve of ξ and η is given in Fig. 6.8. As shown in Fig. 6.8(a), when η is limited to 0, $\xi = 0$ results in a linear current (the current is on log plot). When ξ is negative, with increasing absolute value of ξ the frequency range with three real roots shrinks and the current amplitude decreases. On the opposite, when ξ is positive, the increasing ξ results in the decreasing current amplitude, as shown in Fig. 6.8(b). When ξ is limited to 0, the influence of η is presented in Fig. 6.8(c); larger η results in smaller current. When ξ is -1000 and η are not 0, the current amplitude also decreases; meanwhile the threshold voltage shifts to larger voltage before the jumping disappears, as shown in Fig. 6.8(d).

6.5 Methods of Estimating Nonlinear Level

In high power operated piezoelectrics, except for the conventional characteristics, nonlinear level needs to be estimated. In chapters 4-5, we've studied the nonlinearity using the burst mode method and admittance curve test. In this section, we want to discuss about the estimation method of nonlinear level (characterized by p and

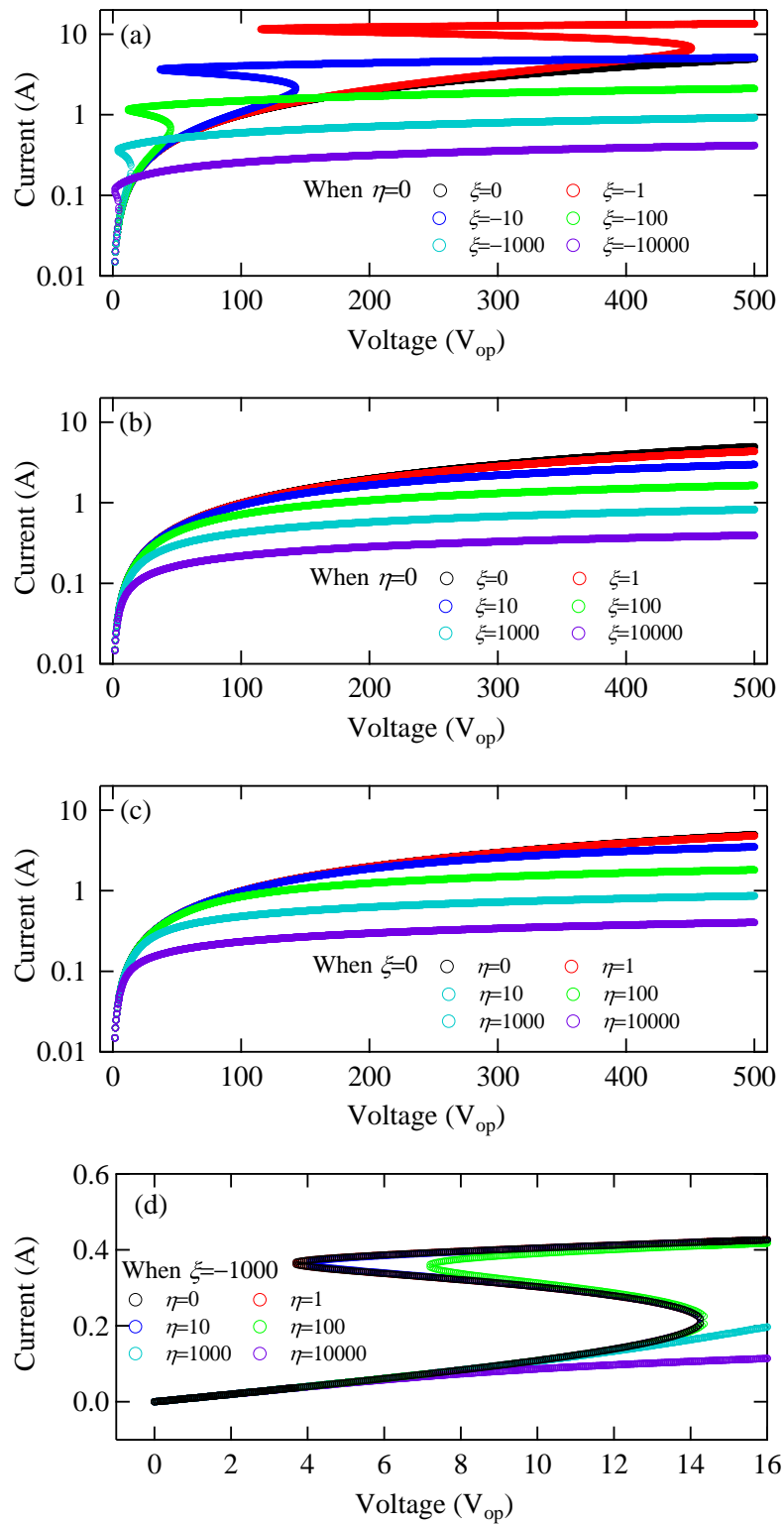


Figure 6.8: Influence of ξ and η to jumping in current-voltage curve: (a) $\xi < 0, \eta = 0$, (b) $\xi < 0, \eta = 0$, (c) $\xi = 0, \eta > 0$, and (d) $\xi = -1000, \eta > 0$.

q). Since the experimental equipment for the burst mode method is not available everywhere, here we only use the admittance curve results. In previous chapters, curve fitting was used (fitting programs seen in the appendices), in which at least one admittance curve at high voltage is required. Although the fitting is useful, it is inconvenient and sometimes unavailable; for quicker estimation, here we present a better method. For the estimation, we need to measure the admittance curves at least twice: one at low voltage (e.g. $0.5 V_{pp}$ in this study) and one at high voltage (for accuracy, the voltage should be as high as possible). Suppose we've obtained the two admittance curves as shown in Fig. 6.9. In Fig. 6.9(a), the admittance curve at low voltage give two feature points: resonance peak (f_r, Y_r) and antiresonance peak (f_a, Y_a); while Fig. 6.9(b) also has two feature points: the maximum points (point 1 and point 2 denoted by black circles) in upward and downward sweep, respectively. Figure 6.9(c) can be determined from Fig. 6.9(b), as explained later.

In the curve fitting, as shown in Fig. 6.10(a), given a set of ξ and η , the current amplitude i_0 , the motional conductance G_m and susceptance B_m , the total conductance G and susceptance B , the total admittance amplitude $|Y|$ and phase ϕ are determined in succession; comparison with measured admittance or phase curve decides the best set of ξ and η . Of course, from the measured admittance curve, the current i_0 and phase θ also can be calculated if C_d is given, as illustrated in Fig. 6.10(b).

As mentioned in chapter 2, based on the equivalent circuit, we can obtain the parameters L , C , R , and C_d using the following equations.

$$C_d = \frac{\sqrt{Y_r Y_a}}{\omega_a}, \quad (6.13)$$

$$R = \frac{1}{\sqrt{Y_r^2 - C_d^2 \omega_r^2}}, \quad (6.14)$$

$$C = C_d \frac{f_a^2 - f_r^2}{f_r^2}, \quad (6.15)$$

$$L = \frac{1}{4\pi^2 C_d (f_a^2 - f_r^2)}. \quad (6.16)$$

The force factor A is determined by L and equivalent mass m . It is noticed that A and C_d obtained from the low voltage and high voltage admittance curves are almost the same, as shown in Table 6.3. It suggests that we can use the values of A and C_d from the low voltage admittance curve to simplify the calculation of other parameters.

Now, use current i_0 and phase θ calculated from the high voltage admittance curve to determine ξ and η . Since both point 1 (i_1, θ_1) and 2 (i_2, θ_2) in Fig. 6.9(c)

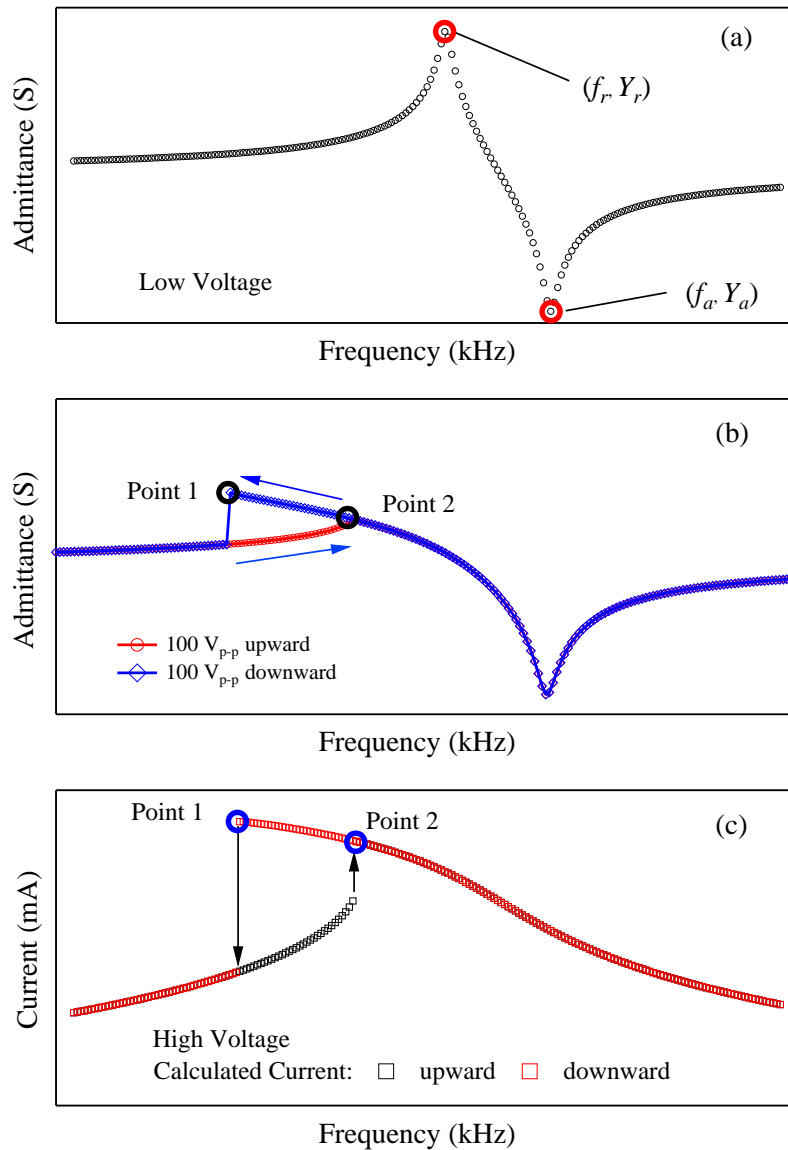


Figure 6.9: Feature points in (a) low voltage admittance curve, (b) high voltage admittance curve, and (c) motional current determined from (b).

Table 6.3: Comparison of A and C_d from low voltage and high voltage admittance curves.

Sample	Low voltage		High voltage	
	A (N/V)	C_d (pF)	A (N/V)	C_d (pF)
CuO-KNN	0.0189	96.8	0.0189	96.9
Hard PZT	0.153	2030	0.152	2060
Soft PZT	0.190	3150	0.191	3120

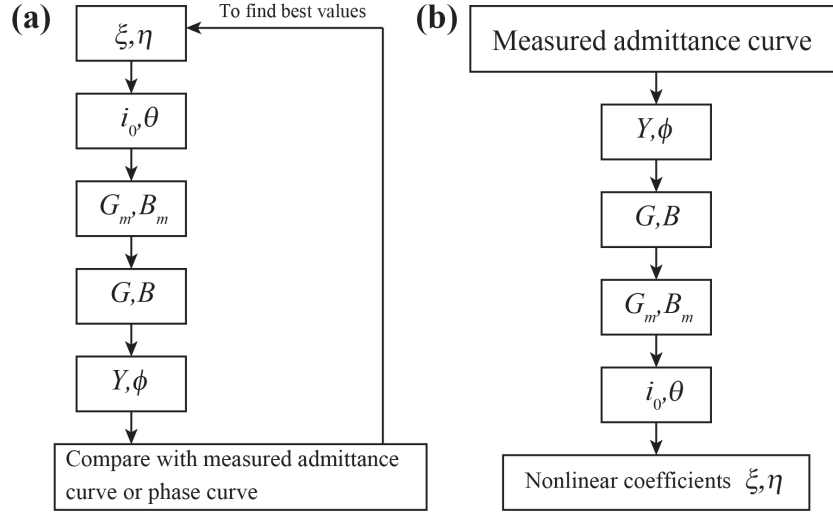


Figure 6.10: Flow diagrams of (a) admittance curve fitting and (b) calculation of i_0 .

satisfy the current and phase equations, as expressed by

$$\left(-\omega Li_0 + \frac{i_0}{\omega C_0} + \frac{3\xi i_0^3}{4}\right) = V_0 \sin \theta, \quad (6.17)$$

$$\left(R_0 i_0 + \frac{3\eta i_0^3}{4}\right) = V_0 \cos \theta. \quad (6.18)$$

Based on

$$\left(-\omega_1 Li_1 + \frac{i_1}{\omega_1 C_0} + \frac{3\xi i_1^3}{4}\right) = V_0 \sin \theta_1, \quad (6.19)$$

$$\left(-\omega_2 Li_2 + \frac{i_2}{\omega_2 C_0} + \frac{3\xi i_2^3}{4}\right) = V_0 \sin \theta_2, \quad (6.20)$$

we have

$$\xi = \frac{4}{3} \times \frac{V_0 \sin \theta_1 \times \frac{i_2}{\omega_2} + \frac{\omega_1}{\omega_2} Li_1 i_2 - V_0 \sin \theta_2 \times \frac{i_1}{\omega_1} - \frac{\omega_2}{\omega_1} Li_1 i_2}{\frac{i_1^3 i_2}{\omega_2} - \frac{i_1 i_2^3}{\omega_1}}, \quad (6.21)$$

$$C_0 = \frac{i_1}{\omega_1} \times \frac{1}{V_0 \sin \theta_1 - \frac{3\xi i_1^3}{4} + \omega_1 Li_1}, \quad (6.22)$$

$$\omega_0 = \frac{1}{\sqrt{LC_0}}. \quad (6.23)$$

Similarly, based on

$$\left(R_0 i_1 + \frac{3\eta i_1^3}{4}\right) = V_0 \cos \theta_1, \quad (6.24)$$

$$\left(R_0 i_2 + \frac{3\eta i_2^3}{4}\right) = V_0 \cos \theta_2, \quad (6.25)$$

we have

$$\eta = \frac{4}{3} \times \frac{i_2 V_0 \cos \theta_1 - i_1 V_0 \cos \theta_2}{i_1^3 i_2 - i_1 i_2^3}, \quad (6.26)$$

$$R_0 = \frac{1}{i_1} \left(V_0 \cos \theta_1 - \frac{3}{4} \eta i_1^3 \right), \quad (6.27)$$

$$\beta_0 = \frac{R_0}{2L}. \quad (6.28)$$

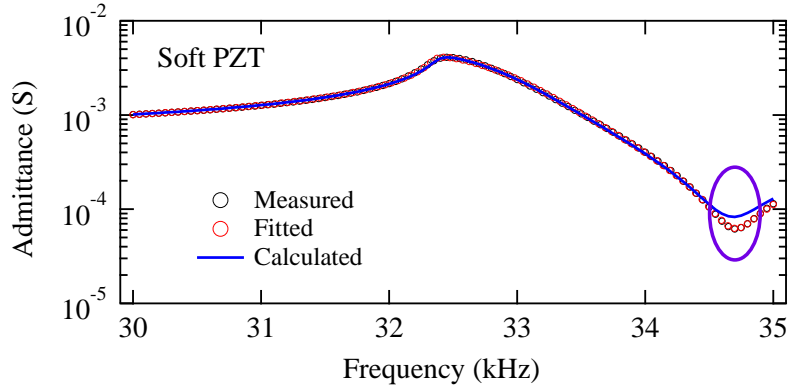


Figure 6.11: Comparison of measured, fitted, and calculated admittance curves; the purple ellipse marks the deviation of measured and calculated curves.

Table 6.4: Nonlinear parameters determined from the calculation of feature points and curve fitting of high voltage admittance curves.

Calculation from feature Points						
Sample	A (N/V)	β_0 (s^{-1})	η (ΩA^{-2})	ω_0 (rad/s)	ξ (ΩA^{-2})	C_d (pF)
CuO-KNN	0.0189	864	2.08×10^5	2.862×10^6	-2.39×10^6	96.8
Hard PZT	0.153	54	5.04×10^3	2.27×10^5	-9.72×10^4	2030
Soft PZT	0.190	1371	2.60×10^5	2.06×10^5	-8.29×10^5	3150
Fitting Results						
Sample	A (N/V)	β_0 (s^{-1})	η (ΩA^{-2})	ω_0 (rad/s)	ξ (ΩA^{-2})	C_d (pF)
CuO-KNN	0.0189	864	2.08×10^5	2.862×10^6	-2.39×10^6	96.9
Hard PZT	0.152	54	5.07×10^3	2.27×10^5	-9.57×10^4	2060
Soft PZT	0.191	1037	4.09×10^5	2.06×10^5	-8.83×10^5	3120

Using Eqs. 6.21 and 6.26, the nonlinear coefficients ξ and η were determined and shown in Table 6.4. The coefficients determined from the calculation and curve fitting show consistence except for β_0 and η of soft-type PZT. The comparison of measured, fitted, and calculated admittance curves of soft-type PZT are shown in Fig. 6.11. Near the resonance frequency the calculated curve (from the calculated

parameters) overlaps with the measured and fitted curves; however, around the antiresonance frequency a significant deviation appears (measured minimum value: $6.266 \times 10^{-5} \mu\text{S}$, calculated minimum value: $8.2877 \times 10^{-5} \mu\text{S}$). Considering that only soft-type sample has this deviation, the difference might come from the larger nonlinear coefficients.

As seen in Fig. 6.12(a)-(b), despite of the small admittance amplitude around the antiresonant frequency, the motional current amplitude at the antiresonant frequency is not the minimum. The motional current amplitudes of hard- and soft-type PZTs at the antiresonant frequency are 0.0025 and 0.0034 A, respectively. Considering the larger absolute values of nonlinear coefficients in soft-type PZT transducer, the influence of nonlinear behavior on soft-type PZT is more obvious than that on hard-type PZT. In one word, for hard-type samples, this estimation method proves to be efficient; when applying this method to soft-type samples we should be cautious.

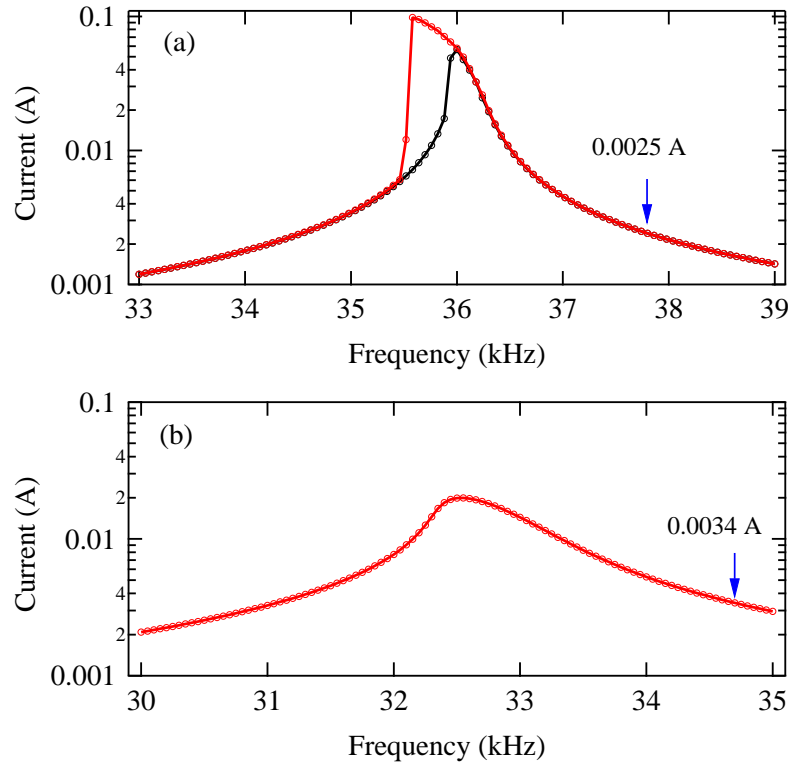


Figure 6.12: Motional current of (a) hard-type PZT and (b) soft-type PZT at $10 V_{pp}$; the arrows mark the antiresonant frequencies.

At last, the other two nonlinear coefficients p and q can be determined from ξ and η . Once again, dimensionless p and q can be used for the comparison between different samples and size-dependent ξ and η cannot.

6.6 High Power Characteristics

6.6.1 Quality factor

Owing to abovementioned nonlinear phenomena, the conventional characteristics need reconsideration because at high power operation the parameters cannot be taken as constants anymore. For instance, the definition of quality factor Q_m should be discussed. Normally, Q_m at low voltage can be determined by the equivalent circuit parameters

$$Q_m = \frac{2\pi f_r L}{R}. \quad (6.29)$$

As illustrated in chapter 3, Q_m can be calculated by the resonant frequency divided by the half bandwidth (3dB method), as expressed by

$$Q_m = \frac{f_r}{\Delta f}, \quad (6.30)$$

where Δf satisfies

$$i \left(f_r \pm \frac{\Delta f}{2} \right) = \frac{i_0}{\sqrt{2}}, \quad (6.31)$$

where i_0 is the maximum current amplitude.

Table 6.5: Parameters used in the simulation of admittance curve.

ξ (ΩA^{-2})	η (ΩA^{-2})	L (mH)	R_0 (Ω)	C_0 (nF)
-100	10	100	10	1

However, at high voltages, these equations are inapplicable considering the deformation and jumping in the admittance curves. Subsequent to the simulation, here we give the simulated admittance curves (around the resonance frequency) at different voltages (Fig. 6.13) using the same parameters and $(\xi, \eta)=(-100,10)$, as listed in Table 6.5. As shown in Fig. 6.13(a), at $0.5 V_{pp}$ the resonance peak is symmetric and it's easy to determine the half bandwidth (or 3dB point). At $10 V_{pp}$ the curve has slight deformation; despite of that, the definition of half bandwidth is still usable. However, at 20, 50, and $100 V_{pp}$ the half bandwidth is difficult to obtain; because unlike the curves in Fig. 6.13(a), in experiments the medium values is impossible to measure and the experimental result should be Fig. 6.13(b). Hence, it is inconvenient to calculate Q_m at high voltages.

We have two possible ways for the determination of Q_m . The first one: use the measured admittance curves to obtain the nonlinear parameters, then calculate the medium line (not measured), finally calculate the half bandwidth and Q_m .

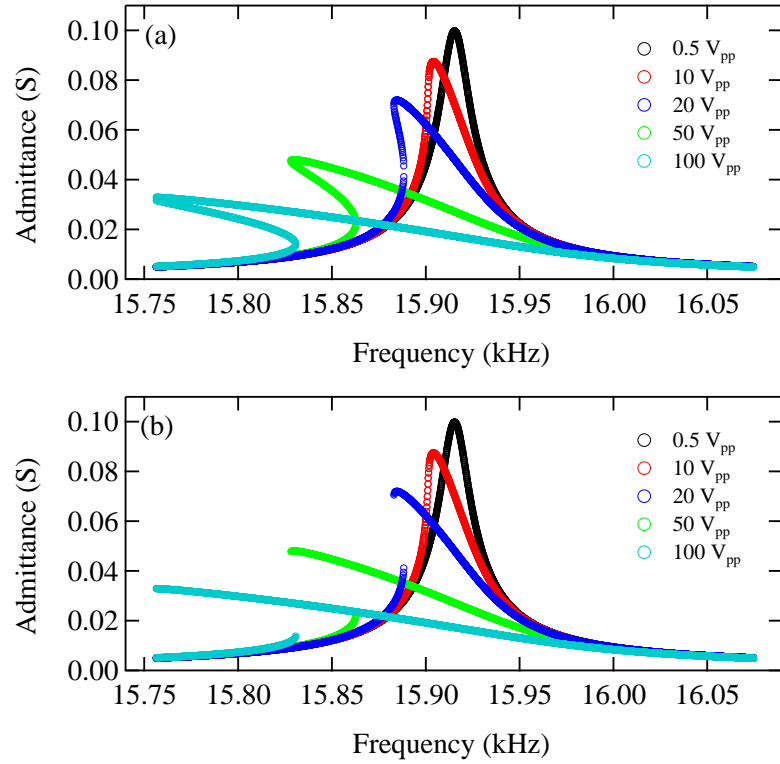


Figure 6.13: Simulated admittance curves at 0.5, 10, 20, 50, and 100 V_{pp} when $(\xi, \eta)=(-100,10)$.

The second method, revise Eq. 6.29 as

$$Q_m = \frac{\omega_r(i)L}{R(i)} = \frac{(\omega_0 L + \frac{1}{2}\xi i_0^2)}{(R_0 + \eta i_0^2)}, \quad (6.32)$$

where, both ω_r and R are related to the maximum current amplitude i_0 . Here we take the admittance curve at 0.5 and 50 V_{pp} in Fig. 6.13(a) as an example. At 0.5 V_{pp} , the admittance reaches the maximum (0.099813 S) at 99999 rad/s; the two frequencies with admittance nearest to 0.070578 S ($0.099813/\sqrt{2}$ S) are 99949 and 100050 rad/s, respectively. Using half bandwidth method, we have

$$Q_m = \frac{99999}{100050 - 99949} \approx 990; \quad (6.33)$$

while Eq. 6.32 gives a Q_m of 999 ($i_0=0.250$ A). Notice is taken that Q_m here is almost same as the value determined by conventional equivalent circuit parameters (1000), indicating the negligible nonlinearity at low voltage. The difference might come from the limited discrete data points; for a certain current amplitude usually we cannot obtain the exact frequency, but only a frequency range.

At 50 V_{pp}, the admittance reaches the maximum (0.048035 S) at 99461 rad/s; the two frequencies with admittance nearest to 0.034157 S (0.048035/√2 S) are 99603 and 99851 rad/s, respectively. So Q_m is determined to be

$$Q_m = \frac{99461}{99851 - 99603} \approx 401; \quad (6.34)$$

while using Eq. 6.32 Q_m is about 406 ($i_0=1.200875$ A); two values show acceptable consistence. So, the Q_m at high power operation can be calculated by these two methods. In addition, these two methods might be also instructive in determining other parameters.

Since we have

$$T_m = \rho c v_0, \quad (6.35)$$

$$A = \frac{i_0}{v_0}, \quad (6.36)$$

or

$$i_0 = \frac{AT_m}{\rho c}, \quad (6.37)$$

Eq. 6.32 can be revised as

$$Q_m = \frac{\omega_r(i)L}{R(i)} = \frac{\left(\omega_0 L + \frac{1}{2}\xi A^2 \frac{T_m^2}{\rho^2 c^2}\right)}{\left(2L\beta_0 + \eta A^2 \frac{T_m^2}{\rho^2 c^2}\right)}. \quad (6.38)$$

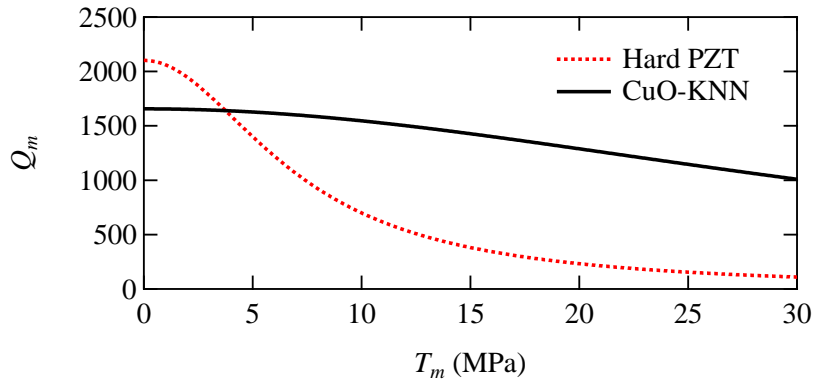


Figure 6.14: Q_m of hard-type PZT and CuO-KNN transducers as functions of T_m .

Using the determined parameters of hard-type PZT and CuO-KNN transducers (Table 6.4), the T_m -dependent Q_m of them are shown in Fig. 6.14. At low stress ($T_m \approx 0$), the Q_m of hard-type PZT transducer is about 2100 and that of CuO-KNN

transducer is about 1660, respectively. With increasing T_m , the Q_m of hard-type PZT decreases much faster than CuO-KNN does. When T_m is higher than 3.9 MPa, the Q_m of CuO-KNN is larger than that of hard-type PZT transducer, consistent with our previous conclusion that CuO-KNN is more stable than hard-type PZT.

6.6.2 Energy density

For high power applications, the energy density Γ is one key performance parameter, as expressed by

$$\Gamma = \frac{\int_{-\frac{l}{2}}^{\frac{l}{2}} \frac{1}{2} \rho v_0^2 \sin^2 kx w h dx}{lwh} = \frac{1}{4} \rho v_0^2 = \frac{1}{4} \frac{T_m^2}{E}, \quad (6.39)$$

where E is the Young's modulus.

The energy density of the hard-type PZT and CuO-KNN transducers as the functions of T_m are shown in Fig. 6.15. At the same stress, the energy density of hard-type PZT is larger than CuO-KNN, corresponding to the larger density. This relative low density is one disadvantage of most lead-free materials. However, it should be noticed that in different samples the same electrical field may results in different T_m . Again, Eq. 6.7 was adopted to calculate T_m as a function of electrical field. For the comparison between samples with different sizes, the size dependence of the parameters in Eq. 6.7 was taken into account. For a transducer with length l , width w , and thickness h , v_0 is independent on the size, and i_0 is proportional to w because

$$i_0 = A v_0 = \frac{2wd_{31}}{s_{11}^E} v_0 \propto w. \quad (6.40)$$

The size dependence of other parameters in Eq. 6.7 follows:

$$\omega L = \omega \frac{m}{A^2} \propto \frac{1}{l} \frac{lwh}{w^2} \propto \frac{h}{w}; \quad (6.41)$$

$$R_0 = 2\beta_0 L \propto \frac{1}{l} \frac{lh}{w} \propto \frac{h}{w}; \quad (6.42)$$

$$\omega C_0 = \frac{m\omega_0^2}{\omega A^2} \propto \frac{lwhl^{-2}}{l^{-1}w^2} \propto \frac{h}{w}; \quad (6.43)$$

$$\xi = \frac{2qL}{lA^2} \propto \frac{lh w^{-1}}{l w^2} \propto \frac{h}{w^3}; \quad (6.44)$$

$$\eta = \frac{2pL}{lA^2} \propto \frac{lh w^{-1}}{l w^2} \propto \frac{h}{w^3}; \quad (6.45)$$

where p and q are independent on size, as demonstrated in chapter 4. The first three terms of Eq. 6.7 are proportional to h^2 ; suggesting that the last term V_0^2 should also

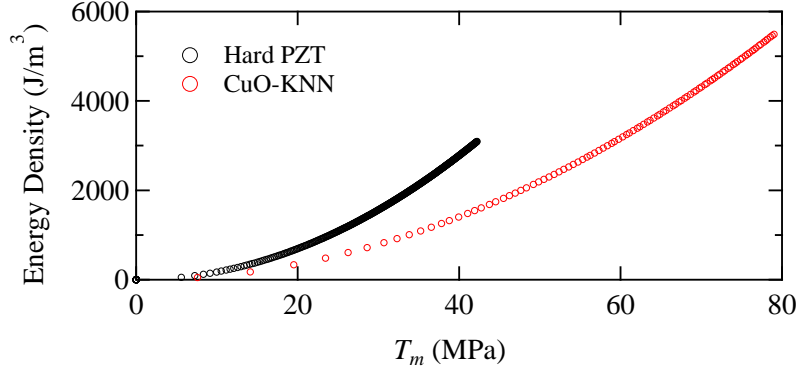


Figure 6.15: Energy density of the hard-type PZT and CuO-KNN transducers as functions of T_m .

be proportional to h^2 , or

$$V_0^2 = \left(\frac{V_0}{h} \times h \right)^2 = \left(\frac{V_0}{h} \right)^2 h^2, \quad (6.46)$$

where V_0/h happens to be the applied electrical field.

Figure 6.16 shows the energy density of both transducers as functions of electrical field. As seen in Fig. 6.16(a), at the same electrical field, the energy density of CuO-KNN transducer is larger than that of hard-type PZT transducer. Although we should notice that at low electrical field, the energy density of hard-type PZT is larger than that of CuO-KNN transducer, as seen in Fig. 6.16(b). Based on above results, CuO-KNN is a promising material for high power applications.

6.7 Simulation of Hysteresis Loops

Different from the admittance hysteresis investigated in this study, polarization-field loop and strain-field loop are also widely used and discussed. In chapter 4, we mentioned that the modeling for them is different from each other. Here we also perform the simulation for polarization-field loops and strain-field loops to illustrate the modeling discrepancy.

6.7.1 Polarization-field loop

A ferroelectric capacitor is equivalent to a circuit constructed by the parallel of a linear capacitor and a nonlinear capacitor (in series to a resistor) [157], as shown in Fig. 6.2(a). The Landau-Khalatnikov equation determines the time response of net

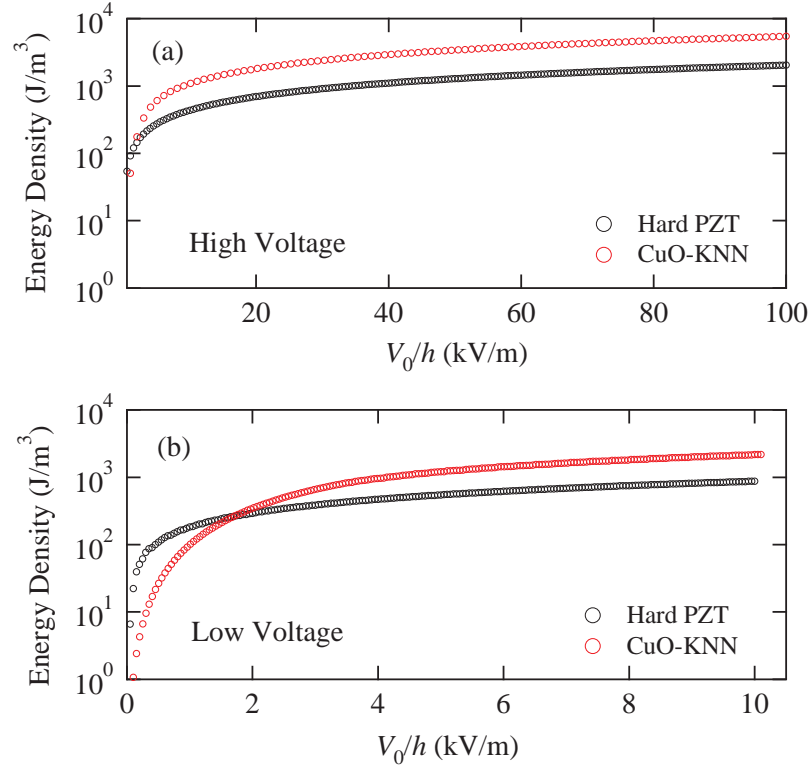


Figure 6.16: Energy density of the hard-type PZT and CuO-KNN transducers as functions of electric field.

polarization P , as expressed by

$$\rho \frac{dP}{dt} + \frac{\partial F(P, T)}{\partial P} = \frac{V_0}{h} \sin \omega t, \quad (6.47)$$

where T , ρ , F , V_0/h , and ω are stress, resistivity, free energy, electrical field, and driving angular frequency, respectively. The expression of Landau energy is

$$F(P) = \frac{1}{8\chi_0 P_s} (P^2 - P_s^2)^2, \quad (6.48)$$

where P_s and χ_0 are the polarization and electric susceptibility at a zero electric field. Simplify Eq. 6.47 to

$$\frac{dy}{dt} + \gamma (y^2 - 1) y = e_0 \sin \omega t, \quad (6.49)$$

where

$$y = \frac{P}{P_s}, x = \frac{\chi_0 V}{P_s h}, \gamma = \frac{1}{2\chi_0 \rho}, e_0 = \frac{V_0}{\rho P_s h}. \quad (6.50)$$

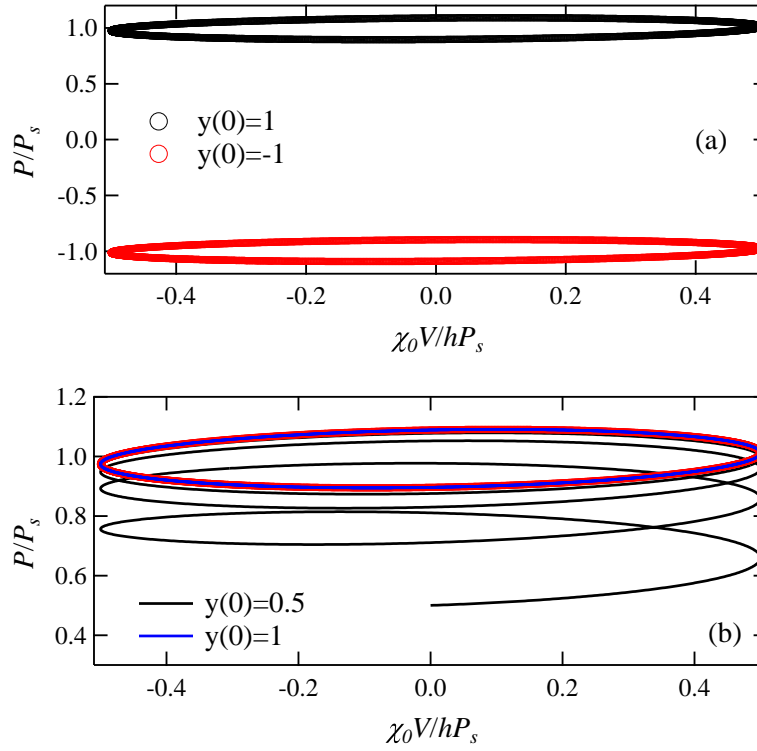


Figure 6.17: Simulated P - E loops: $y(0) =$ (a) ± 1 and (b) 0.5 and $(\gamma, e_0) = (10, 10)$.

Runge-Kutta method is adopted to simulate the discrete approximate solutions of the differential equations. For an initial value problem specified as

$$\frac{dy}{dt} = f(t, y), y(t_0) = y_0, \quad (6.51)$$

where $y(t)$ is an unknown function of time t that we would like to approximate, $y(t_0)$ is the initial value of y , the approximate solution can be obtained as follows. Pick a step $h > 0$ and define

$$y_{n+1} = y_n + \frac{h}{6} (k_1 + 2k_2 + 2k_3 + k_4), \quad (6.52)$$

$$t_{n+1} = t_n + h. \quad (6.53)$$

For $n=0, 1, 2,$ and 4 , k_n is given by

$$k_1 = f(t_n, y_n), \quad (6.54)$$

$$k_2 = f\left(t_n + \frac{h}{2}, y_n + \frac{k_1 h}{2}\right), \quad (6.55)$$

$$k_3 = f\left(t_n + \frac{h}{2}, y_n + \frac{k_2 h}{2}\right), \quad (6.56)$$

$$k_4 = f(t_n + h, y_n + k_3 h). \quad (6.57)$$

Given a certain (γ, e_0) and an initial value of y_0 , we can obtain the time response of polarization. When $(\gamma, e_0) = (10, 10)$, the hysteresis loops with different initial conditions are shown in Fig. 6.17. As shown in Fig. 6.17(a), when $y(0) = \pm 1$, the loops are closed and located near $y = \pm 1$, respectively; similar to the polarized ferroelectric materials, in which small electrical field cannot switch the polarization. When the initial condition is not $y(0) = \pm 1$, e.g., $y(0) = 0.5$, the polarization would gradually fall to the two stable states in Fig. 6.17(a), depending on the sign of $y(0)$. As shown in Fig. 6.17(b), the end of the hysteresis loop (denoted by red points) overlaps with the loop simulated from $y(0) = 1$ (denoted by blue line).

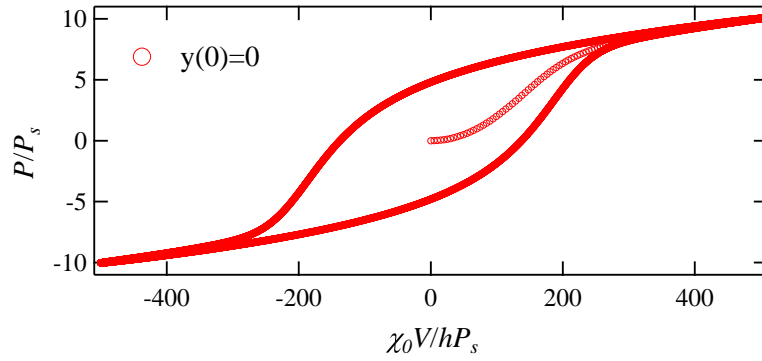


Figure 6.18: Simulated P - E loops: $y(0)$ is 0 when $(\gamma, e_0) = (10, 10000)$.

When e_0 is large enough and the initial condition is $y(0) = 0$, the simulation gives a hysteresis loop shown in Fig. 6.18. The change of polarization perfectly exhibits the P - E hysteresis loop [153, 170, 171]. Notice is taken that even the initial condition $y(0) \neq 0$, the polarization falls to this state quickly (not shown here).

6.7.2 Strain-field loop

Since we have

$$S = \alpha P^2, \quad (6.58)$$

where α is a constant dependent on the material [20]. Given a certain α , still using the Runge-Kutta method, the strain-field loop can be simulated. For $\alpha = 0.1$, the strain-field curve is shown in Fig. 6.19, which shows great similarity with the butterfly phenomena [153].

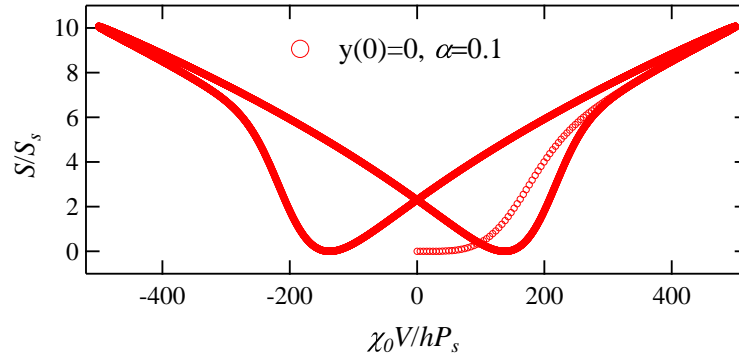


Figure 6.19: Simulated S - E loops: $y(0)$ is 0, $(\gamma, e_0) = (10, 10000)$ and $\alpha = 0.1$.

In both polarization-field and strain-field hysteresis loops, electrical field is the only source of nonlinearity, corresponding to the dielectric nonlinearity (related to the polarization switching and domain wall movements). This mechanism is different from the nonlinearity in admittance curves and burst mode results.

6.8 Brief Summary

The nonlinear phenomena were further investigated in this chapter. We summarize the characteristics at high power operation and suggest an easy method for estimating the nonlinear level. The simulation of jumping hysteresis in admittance curves and other hysteresis loops helps the understanding of nonlinearity. Three main conclusions were as follows:

(1) G - B circles were depicted to illustrate the jumping in PZT transducers. Using the proposed nonlinear model, the simulation of current jumping in frequency response and voltage response were realized. It is found that ξ , η , and V_0 can affect the jumping phenomenon separately and together: shift of resonance frequency, change of half bandwidth, appearing and disappearing of the jumping.

(2) A simplified method for estimating the nonlinear level was proposed. Using the feature points in low voltage and high voltage admittance curves, the nonlinear coefficients can be obtained via simple calculation, which was demonstrated by the comparison with fitting results. In addition, the calculation of quality factor were discussed; based on the nonlinear level it is possible to determine Q_m at high power condition.

(3) The simulation of polarization-field hysteresis loop and strain-field loop were realized. The results support our discussion that admittance hysteresis and polarization-field hysteresis has different originations.

CHAPTER 7

Conclusions and Prospects

7.1 Conclusions

Lead-free piezoelectric material potassium sodium niobate (KNN) has proved to be a promising substitute for lead-based piezoelectrics. In this thesis, CuO-doped KNN ceramics were synthesized using the hydrothermal method; and a method was proposed to enhance the quality factor Q_m on the basis of acceptor doping. To estimate the high power properties of the CuO-KNN ceramics, the phenomena and mechanism at high power condition were systematically studied. A nonlinear model on the basis of burst mode results was proposed and proved to be efficient in estimating the high power characteristics. Simulations were given to help the comprehension of the exhibited phenomena and the physical mechanism. The main results are as follows:

In chapter 1, the principle, categories, constitutive equations, applications, and the lead-free tendency of the piezoelectrics were introduced. Niobate piezoelectrics (especially potassium niobate KNbO_3 and sodium niobate NaNbO_3), as one family of the most promising lead-free substitutes for PZT, and hydrothermal methods adopted in this study were then introduced. The serious limitation of high power characteristics and thus developed evaluation methods were presented at last.

In chapter 2, the hydrothermal synthesis processes of KNbO_3 and NaNbO_3 powders and the ensuing solid state reaction of $(\text{K}_{0.48}\text{Na}_{0.52})\text{NbO}_3$ ceramics were listed first. Then the experimental details of the burst mode method, the estimation of various properties, and their calculation methods were explained.

In chapter 3, pure and CuO-doped KNN ceramics were prepared on the basis of KNbO_3 and NaNbO_3 powders fabrication. CuO-KNN ceramics was fabricated via a hydrothermal method and solid state sintering. The crystal structure of CuO-KNN was similar to that of pure KNN and corresponds to an orthorhombic single phase without impurities. It was found that the extra post-annealing process did not change the phase of the CuO-KNN ceramics; however, the intense transitions of the domains in the ceramics that occurred after post-annealing caused a change in Q_m . Q_m was decreased to a small value by the post-annealing process and recovered gradually over several hours; which can be attributed to the rearrangement of oxygen vacancies in the domains. The validity of a new method to enhance the Q_m of CuO-KNN ceramics was then investigated and discussed. A post-annealing process in an oxygen-deficient atmosphere was used to increase the amount of oxygen vacancies, which could impede the movement of the domain structures, and thus increased Q_m . In the case of annealing in argon, Q_m was increased to approximately 1500 from 870, whereas post-annealing in oxygen resulted in a decrease of Q_m .

In chapter 4, prior to the estimation of the high power characteristics for CuO-KNN ceramics, the investigation on nonlinear behavior in PZT transducers

was carried out. Nonlinearity in high voltage admittance curves and burst mode method were presented and discussed consecutively. The burst mode method was used at first to measure the vibration velocity of the transducers after excitation by a burst voltage. The determined equivalent mechanical loss and equivalent spring constant were found to be functions of velocity amplitude, suggesting that nonlinearity should be considered when the transducers are driven at high power. Admittance curves at high voltages corroborated the presence of nonlinearity in the PZT transducers. In the admittance curves of the hard-type transducer, a jumping behavior appeared as well as an admittance hysteresis between different sweeps. A model taking into account the nonlinearity was proposed and adopted to fit the admittance curves, which yielded the nonlinear coefficients. It was demonstrated to be effective in describing the admittance hysteresis and the jumping observed in the case of the hard-type PZT transducer and the deformation admittance curve for both PZT transducers. In the admittance curve, the mechanical nonlinearity was the main source instead of the dielectric and piezoelectric nonlinearities. Through the theoretical derivation of the piezoelectric constitutive equations, dimensionless coefficients were suggested for the comparison of samples with different sizes.

In chapter 5, using the proposed nonlinear model in chapter 4, the estimation of fabricated CuO-KNN transducers were carried out. The comparison of nonlinear levels between PZT and CuO-KNN transducers was then given and discussed. Similar to the hard-type PZT, the admittance curves of the CuO-KNN transducers at high voltages also have serious deformation, significant jumping, and admittance hysteresis. The proposed nonlinear model enabled the determination of nonlinear coefficients; using which the prediction of admittance curves at other voltages was realized. In the burst-mode method, the nonlinearity at high voltages was confirmed. The results obtained from the burst mode results were found to be consistent with the admittance curve measurements. Compared with the PZT transducers, lead-free CuO-KNN transducers were less dependent on high-velocity condition, which makes CuO-KNN a promising material for high-power applications.

This method can be used to analyze the nonlinearity in piezoelectrics, and the two nonlinear coefficients can be regarded as the criteria for assessing the piezoelectric transducers driven at high voltage. The comparable results of the admittance curve measurement and burst mode method suggest that the two methods can be substitutes for each other in estimating the nonlinearity level. The feasibility of the model without considering the dielectric nonlinearity and piezoelectric nonlinearity also indicates that the jumping and admittance hysteresis in the admittance curve results from the mechanical nonlinearity.

In chapter 6, the simulations of nonlinear circuits were carried out for better understanding of the appeared nonlinear phenomena. The nonlinear behavior was further investigated in this chapter; G - B circles of hard-type and soft-type PZT

transducers were depicted to illustrate the jumping behavior. Using the proposed nonlinear model, the simulations of current jumping in frequency response and voltage response were performed. The parameters ξ , η , and V_0 can affect the nonlinear phenomena (shift of resonance frequency, change of half bandwidth, appearing, and disappearing of the jumping) separately and together. For practical usage, a simplified method for estimating the nonlinear level was proposed; the nonlinear coefficients can be obtained via simple calculation from the feature points in the low voltage and high voltage admittance curves. The determination of quality factor under high power operation was discussed; based on the nonlinear coefficients it is also possible to calculate Q_m at high power condition. Comparison of the nonlinearities between the present studies and other conditions was also presented. The results supported our discussion that the admittance hysteresis and P - E hysteresis were different in essence.

This thesis mainly proposed and verified the estimation method for high power characteristics in the piezoelectrics; detailed discussion and derivation was also performed to explain the source of nonlinear phenomena. The conventional criteria employed under low power level are insufficient under high power condition because they fail to explain the nonlinear behavior. Through modeling, derivation, and discussion, the nonlinear phenomena can be described by a nonlinear model and be quantized by two coefficients, which can be taken as new criteria under high power condition. The main nonlinearity here is the mechanical nonlinearity, corresponding to the large stress generated in the resonant drive condition.

7.2 Prospects

For further investigation, the following two points might be important.

(1) Under high power operation, the proposed nonlinear model is applicable to describe the behavior of the plate transducers. However, disk transducers, bar transducers, and piezoelectric devices with other shapes are also widely employed. In further study, we would like to compare the nonlinear behaviors in different piezoelectric devices.

(2) The nonlinear model is a phenomenological model; in further study, the piezoelectric constitutive equations with the nonlinear terms should be solved so that the appearing behavior can be considered together with other elements (e.g. dielectric nonlinearity, or second harmonics).

Acknowledgments

It is a pleasure to convey my gratitude to the people who contributed in different ways to the present research. Foremost I thank all the participants of this research for their effort and time to help out with this research, I sincerely acknowledge their contribution.

First of all, and the most of all, I would like to express my deepest gratitude to my supervisor Dr. Takeshi Morita, Department of Human and Engineered Environmental Studies, The University of Tokyo for his supervision. I would like to thank him for his patient guidance, valuable advice, constructive comments, continuous encouragement, and time-consuming modification of journal articles throughout this study, and also for critical reading of this manuscript. Moreover thanks for the trust and confidence in the three years.

I would like to thank to the valuable comments and suggestions from the defense committee: Dr. Ken Sasaki, Department of Human and Engineered Environmental Studies, The University of Tokyo; Dr. Toshihiro Itoh, Department of Human and Engineered Environmental Studies, The University of Tokyo; Dr. Shin-ichi Warisawa, Department of Human and Engineered Environmental Studies, The University of Tokyo; and Dr. Kentaro Nakamura, Precision and Intelligence Laboratory, Tokyo Institute of Technology. Also I want to express my appreciation to Dr. Hiroshi Hosaka, Department of Human and Engineered Environmental Studies, The University of Tokyo, for his comments and advice in the group meetings.

I would like to gratefully acknowledge Dr. Mikio Umeda, Department of Electronics, Niigata Polytechnic College and Dr. Sadayuki Takahashi, Applied Micro Systems Inc., for their valuable and fruitful discussion and suggestion. I am also very grateful to Dr. Ho-Yong Lee, Department of Materials Science and Engineering, Sunmoon University for his single crystal samples and meaningful cooperation. I want to thank Dr. James Friend, Department of Mechanical and Aerospace Engineering, the University of California-San Diego for his kind inspiring discussion and textbook recommendation. I am also very grateful for technical support provided by NF Corporation.

I want to express my gratitude to Dr. Takafumi Maeda, Ms. Yuriko Yokouchi, both graduated from our group, for their systematic teaching the hydrothermal synthesis of piezoelectric materials. Especially I feel very grateful to Dr. Takafumi Maeda for sharing with me his research experience and life wisdom. Thanks to Ms. Yukiko Fujiuchi and Mr. Ryo Kudo, who also graduated from our group, for their helpful tutoring on daily life at the beginning of my doctoral course.

I would like to thank all the members of Morita group for the comfortable and vibrant environment. I will always remember good memories with you: special researcher: Dr. Thithi Lay, doctoral course students: Dr. Takafumi Maeda, and Mr. Kazuhiko Inoue; master course students: Mr. Yuuki Iiduka, Mr. Takami Yokose, Mr. Teppei Uchiho, Mr. Gaku Isobe, Ms. Kanako Ohta, Ms. Yuriko Yokouchi, Mr. Ryo Kudo, Ms. Yukiko Fujiuchi, Mr. Yohei Tadano, Mr. Masafumi Mutou, Mr. Kohei Okubo, Mr. Katsuhiro Saigusa, Mr. Hiroki Yokozawa, Mr. Ryouhei Ozaki, Mr. Ryuichi Mizukami, Mr. Susumu Miyake, and Mr. Rikuri Takayama.

I would like to thank secretaries Ms. Haruko Kinoshita, Ms. Yukiko Morimoto, and Ms. Takako Saegusa for buying the lab supplies and arranging the travel and reimbursement on expenses associated with the conferences.

I want to thank to China Scholarship Council (CSC) for the financial support.

Finally, I would like to thank my parents and relatives for supporting my student life and research activities. Especially I am extremely thankful to my wife Xu Jian for her understanding and patience, for her programing suggestion and support.

May 2015
LIU Yaoyang

Publications and Conferences

Publications

Yaoyang Liu*, Takafumi Maeda, Yuriko Yokouchi, and Takeshi Morita: *The hardening of CuO-(K,Na)NbO₃ via post annealing with argon*; Japanese Journal of Applied Physics Vol. 53, 015503, 2014.

Yaoyang Liu, Ryohei Ozaki, and Takeshi Morita*: *Investigation of nonlinearity in piezoelectric transducers*; Sensors and Actuators A Vol. 227, 31-38, 2015.

Yaoyang Liu* and Takeshi Morita: *Nonlinear coefficients in lead-free CuO-(K,Na)NbO₃ transducers*; Japanese Journal of Applied Physics Vol. 54, 07HC01, 2015.

Yaoyang Liu* and Takeshi Morita: *Simplified determination of nonlinear coefficients in piezoelectric transducers*; Japanese Journal of Applied Physics (accepted).

International Conferences

Yaoyang Liu*, Takafumi Maeda, Yuriko Yokouchi, and Takeshi Morita: *The hardening of CuO-(K,Na)NbO₃ via post-annealing with argon*; The 2nd International Conference on Advanced Electromaterials (ICAE2013), 29, 2013.

Yaoyang Liu* and Takeshi Morita: *Nonlinear coefficients in lead-free materials*; The 35th Symposium on Ultrasonic Electronics (USE2014), 251-252, 2014.

Yaoyang Liu and Takeshi Morita*: *Simplified determination of nonlinear coefficients in piezoelectric transducers*; The 32th Meeting on Ferroelectric Materials and Their Applications (FMA32), 145-146, 2015.

Yaoyang Liu and Takeshi Morita*: *Estimation of nonlinear level in piezoelectric transducers*; The 12th International Workshop on Piezoelectric Materials and Applications in Actuators (IWPMA 2015), 51, 2015.

Yaoyang Liu and Takeshi Morita*: *Nonlinear behavior in piezoelectric transducers*; 68th ICAT International Smart Actuator Symposium, 2015.

Domestic Conferences

Yaoyang Liu*, Takafumi Maeda, Yuriko Yokouchi, and Takeshi Morita: *Post-annealing for CuO-(K,Na)NbO₃ hard type piezoelectric ceramics*; The 50th fall conference of Japan Electronic Materials Society (JEMS50), 21, 2013.

Yaoyang Liu* and Takeshi Morita: *CuO-(K,Na)NbO₃ hard type piezoelectric ceramics for high power applications*; 2014 spring conference of The Japan Society for Precision Engineering, 829-830, 2014.

Yaoyang Liu* and Takeshi Morita: *Investigation on nonlinearity in piezoelectric transducer*; 2014 fall conference of The Japan Society for Precision Engineering (JSPE), 183-184, 2014.

Yaoyang Liu* and Takeshi Morita: *Nonlinear behavior in piezoelectric transducers*; The 51th fall conference of Japan Electronic Materials Society (JEMS51), 7, 2014.

Yaoyang Liu, Ryohei Ozaki, and Takeshi Morita*: *High power piezoelectric vibration characterization*; 2015 Symposium on Piezoelectric Materials and Devices, 47-50, 2015.

Yaoyang Liu*, Ryohei Ozaki, and Takeshi Morita: *Investigation on nonlinear vibration with lead-free piezoelectric transducer*; 2015 spring conference of The Japan Society for Precision Engineering (JSPE), 573-574, 2015.

Yaoyang Liu and Takeshi Morita*: *Modeling of nonlinear admittance curve in lead-free piezoelectrics*; The 27th Symposium on Electromagnetism And Dynamics (SEAD27), 2015.

Appendices

In chapter 3-6 we adopted some programs for data analysis and the simulations, including the fitting program for low voltage admittance curves, the fitting program for current-time, velocity-time curve, the fitting program for high voltage admittance curves, the simulation program for jumping phenomena, and the simulation program for polarization hysteresis loops, as shown in the follows.

Fitting of low voltage admittance curves

```
1 #pragma rtGlobals=1 // Use modern global access method.
3 Function Fit_admittance(w,t) : FitFunc
4     wave w
5     variable t
7     // PARAMETERS: L1, R1, C1, Cd
8     variable /c ii, YY
9     variable y, tt
10    ii=cplx(0,1)
11    tt=t
13    // Admittance
14    YY=ii * tt *w[3]+1/(w[1]+ ii * tt *w[0]- ii / tt /w[2])
15    // Amplitude
16    y=(sqrt((real(YY)^2+imag(YY)^2)))
17    return y
18 End
19
20 Function admittance()
21     wave wy=root:soft05 // y wave name
22     wave wt=root:soft_f // x wave name
23     variable i
25     // wave for initial values
26     wave W_coef=root:admittancecoef
```

```

27 // To carry out fitting
29 FuncFit/L=101/H="0000"/NTHR=0 Fit_admittance W_coef wy /X=wt /D
end
31
Function Fit_phase(w,t) : FitFunc
33 wave w
variable t
35
// PARAMETERS: L1, R1, C1, Cd
37 variable /c ii, YY
variable y, tt
39 ii=cmplx(0,1)
tt=t
41
YY=ii*tt*w[3]+1/(w[1]+ii*tt*w[0]-ii/tt/w[2])
43 // Phase
y=atan(imag(YY)/real(YY))/pi*180
45 return y
End
47
Function phase()
49 wave wy=root:soft05_phase // y wave name
wave wt=root:soft_f // x wave name
51 variable i
53 // wave for initial values
wave W_coef=root:admittancecoef
55
// To carry out fitting
57 FuncFit/L=101/H="1111"/NTHR=0 Fit_phase W_coef wy /X=wt /D
end

```

Fitting current-time and velocity-time curves

```

#pragma rtGlobals=3 // Use modern global access method and
strict wave access.
2
// v(t) = v0*sin(wr*t+phi)*exp(-beta*(t-t0))+y0
4 // v0 wr phi beta t0 y0
6 Function fitcurr(point_s, fit_num)
variable point_s, fit_num
8 string wy, wt // name of current wave
wy="C6_curr0"

```

```

10  wt="C6_time"           // name of time wave
    fit_current (point_s , fit_num , wy, wt)
12  end

14  Function fit_current (point_s , fit_num , wy, wt)
    variable point_s , fit_num
16  string wy, wt
    variable fit_start
18  variable i , imax
    imax=(numpnts ($(wt))-point_s)/fit_num-1
20  make $("curr_0_" + wy)
    make $("beta_num_" + wy)
22  make $("beta_error_" + wy)
    make $("beta_time_" + wy)
24  make $("freq_" + wy)
    make $("iop_" + wy)
26  wave curr_0=$("curr_0_" + wy)
    wave beta_num=$("beta_num_" + wy)
28  wave beta_error=$("beta_error_" + wy)
    wave beta_time=$("beta_time_" + wy)
30  wave freq=$("freq_" + wy)
    wave iop=$("iop_" + wy)
32  redimension /N=0 curr_0 , beta_num , beta_error , beta_time , freq , iop

34  // Fitting in separated sections
    for (i=0; i<imax; i=i+1)
36      fit_start=point_s+i*fit_num
        fit_sinex (fit_start , fit_num , wy, wt)
38      redimension /N=(numpnts (beta_num)+1) curr_0 , beta_num ,
        beta_error , beta_time , freq , iop
        wave w_coef=W_coef
40      wave w_sigma=W_sigma
        wave t=$(wt)
42      curr_0[i]=w_coef[0]
        beta_num[i]=w_coef[4]
44      beta_error[i]=w_sigma[4]
        beta_time[i]=t[fit_start+fit_num/2]
46      freq[i]=w_coef[1]
        iop[i]=abs (curr_0[i]*exp(-beta_num[i]*(beta_time[i]-0)))
48  endfor

50  //Draw figures
    Display beta_num vs beta_time
52  ModifyGraph mode=3, marker=19, rgb ($("beta_num_" + wy))=(0,0,0)
    ErrorBars $("beta_num_" + wy) Y, wave=($("beta_error_" + wy), $("
        beta_error_" + wy))
54  display freq vs beta_time
    display beta_num vs iop

```

```

56  ModifyGraph mode=3,marker=19,rgb($"beta_num_"+wy)=(0,0,0)
ErrorBars $"beta_num_"+wy Y,wave=($"beta_error_"+wy,$("
    beta_error_"+wy))
58 end

60 Function fit_sinx ( fit_start , fit_num ,wy, wt)
    variable fit_start , fit_num
62    string wy, wt
    variable i
64    wave W_coef=W_coef
    for ( i=0;i <20;i=i+1)
66        FuncFit /L=(fit_num) /H="000001" /NTHR=0 sinexp W_coef $(wy)[
            fit_start , fit_start+fit_num] /X=$(wt) /D
    endfor
68 end

70 Function sinexp(w, t) : FitFunc
    Wave w
72    Variable t

74    //CurveFitDialog/ These comments were created by the Curve
        Fitting dialog. Altering them will
    //CurveFitDialog/ make the function less convenient to work with
        in the Curve Fitting dialog.
76    //CurveFitDialog/ Equation:
    //CurveFitDialog/  $f(t) = A \cdot \sin(f \cdot t + \phi) \cdot \exp(-\beta \cdot (t - t_0)) + y_0$ 
78    //CurveFitDialog/ End of Equation
    //CurveFitDialog/ Independent Variables 1
80    //CurveFitDialog/ t
    //CurveFitDialog/ Coefficients 6
82    //CurveFitDialog/ w[0] = A
    //CurveFitDialog/ w[1] = f
84    //CurveFitDialog/ w[2] = phi
    //CurveFitDialog/ w[3] = y0
86    //CurveFitDialog/ w[4] = beta
    //CurveFitDialog/ w[5] = t0

88    return w[0]*sin(2*pi*w[1]*t+w[2])*exp(-w[4]*(t-w[5]))+w[3]
90 End

92 Function fitvelo (point_s , fit_num)
    variable point_s , fit_num
94    string wy, wt
    wy="C6_velo0" //name of velocity wave
96    wt="C6_time" //name of time wave
    fit_velocity ( point_s , fit_num ,wy, wt)
98 end

```



```

100 Function fit_velocity ( point_s , fit_num , wy, wt)
    variable point_s , fit_num
102 string wy, wt
    variable fit_start
104 variable i , imax
    variable den , len , wid
106 den=7650 // density
    len=0.043 // length
108 wid=0.007 // width
    imax=(numpts($ (wt))-point_s)/fit_num-1
110 make $("velo_0_" +wy)
    make $("beta_num1_" +wy)
112 make $("beta_error1_" +wy)
    make $("beta_time1_" +wy)
114 make $("freq1_" +wy)
    make $("vop_" +wy)
116 make $("Qm_" +wy)
    make $("s11_" +wy)
118 make $("d31_" +wy)
    make $("Tm_" +wy)
120 wave velo_0=$("velo_0_" +wy)
    wave beta_num1=$("beta_num1_" +wy)
122 wave beta_error1=$("beta_error1_" +wy)
    wave beta_time1=$("beta_time1_" +wy)
124 wave freq1=$("freq1_" +wy)
    wave vop=$("vop_" +wy)
126 wave Qm=$("Qm_" +wy)
    wave s11=$("s11_" +wy)
128 wave d31=$("d31_" +wy)
    wave Tm=$("Tm_" +wy)
130 wave iop=$("iop_C6_curr0")
    wave freq=$("freq_C6_curr0")
132 wave beta_num=$("beta_num_C6_curr0")
    redimension /N=0 velo_0 , beta_num1 , beta_error1 , beta_time1 , freq1 ,
        vop , Qm , s11 , d31 , Tm
134
    // Fitting in separated sections
136 for ( i=0; i<imax; i=i+1)
    fit_start=point_s+i*fit_num
138 fit_sinex ( fit_start , fit_num , wy, wt)
    redimension /N=(numpts(beta_num1)+1) velo_0 , beta_num1 ,
        beta_error1 , beta_time1 , freq1 , vop , Qm , s11 , d31 , Tm
140 wave w_coef=W_coef
    wave w_sigma=W_sigma
142 wave t=$(wt)
    velo_0 [ i ]=w_coef [ 0 ]
144 beta_num1 [ i ]=w_coef [ 4 ]
    beta_error1 [ i ]=w_sigma [ 4 ]

```

```

146     beta_time1[i]=t[fit_start+fit_num/2]
      freq1[i]=w_coef[1]
148     vop[i]=abs(velo_0[i]*exp(-beta_num1[i]*(beta_time1[i]-0)))
      Qm[i]=freq[i]*pi/beta_num[i]
150     s11[i]=1/4/den/len^2/freq1[i]^2
      d31[i]=s11[i]*iop[i]/2/wid/vop[i]
152     Tm[i]=sqrt(den/s11[i])*vop[i]
endfor
154
//Draw figures
156 Display beta_num1 vs beta_time1
ModifyGraph mode=3,marker=19,rgb($"beta_num1_"+wy)=(0,0,0)
158 ErrorBars $"beta_num1_"+wy Y,wave($"beta_error1_"+wy),($"
      beta_error1_"+wy)
display freq1 vs beta_time1
160 display beta_num1 vs vop
ModifyGraph mode=3,marker=19,rgb($"beta_num1_"+wy)=(0,0,0)
162 ErrorBars $"beta_num1_"+wy Y,wave($"beta_error1_"+wy),($"
      beta_error1_"+wy)
end

```

Fitting of high voltage admittance curves

```

1 #pragma rtGlobals=1 // Use modern global access method.
3 Function Fit_solution(w,t) : FitFunc
  wave w
5  variable t
7  // A0=w[0], ksi=w[1], beta=w[2], wr=w[3], Cd=w[4], eta=w[5]
  variable L, beta_, wr, i0, V0
9
  L=0.0023177
11  beta_=w[2]
  wr=w[3]
13
  // Change if using other voltage admittance curves
15  V0=5
17  variable C0, L0, R0, theta_,j,i
19  make Pcoef
  redimension/N=4 Pcoef
21  make /D/O Pwave
  setscale /I x -2e-8, 2e-8, Pwave

```

```

23  make /N=(0,3) /C Icoef
24  redimension /N=(0, 3) Icoef
25  wave W_polyRoots=W_polyRoots

27  make/N=0 ww, III , III1 , III2
28  make/N=0 IV
29  redimension /N=0 ww, IIII , III1 , IV , III2

31  // To calculate circuit parameters
32  L0=L/w[0]^2
33  C0=w[0]^2/L/wr^2
34  R0=2*beta_*L/w[0]^2

35
36  // Define polynomial equation
37  Pcoef[0]=-V0^2
38  Pcoef[1]=(t*L0-1/t/C0)^2+R0^2
39  Pcoef[2]=3*w[1]/C0/t/2-3*w[1]*t*L0/2+3*w[5]*R0/2
40  Pcoef[3]=9*w[1]^2/16+9*w[5]^2/16

41
42  // Solve polynomial equation
43  Pwave=Poly(Pcoef, x)
44  FindRoots /P=Pcoef
45  redimension /N=((dimsize(Icoef,0)+1),3) Icoef
46  redimension /N=(numpts(ww)+1) ww, III , III1 , IV , III2

47
48  // To give amplitude in upward sweep
49  for (i=numpts(W_PolyRoots);i>0;i=i-1)
50      Icoef[dimsize(Icoef,0)-1][i-1]=W_PolyRoots[i-1]
51      if (imag(Icoef[dimsize(Icoef,0)-1][i-1])==0)
52          i0=sqrt(real(Icoef[dimsize(Icoef,0)-1][i-1]))
53          theta_=atan((-t*L0+1/t/C0+3*w[1]*i0^2/4)/(R0+3*w[5]*i0^2/4))
54      endif
55  endfor

57  G=i0*cos(theta_)/V0 // real part of admittance
58  B=i0*sin(theta_)/V0+t*w[4] // imaginary part
59  return log(sqrt(G^2+B^2)) // return log(Y)

End

61 Function finalone()
62  wave wy=root:hard10 // y wave name
63  wave wt=root:hard_f // x wave name
64  variable i
65  wave W_coef=root:fitsolutioncoef2

66
67  // To carry out fitting
68  FuncFit/L=101 /H='111111'/NTHR=0 Fit_solution W_coef wy /X=wt
69  /D

```

```

end
71
Function Fit_solution_phase(w,t) : FitFunc
73   wave w
   variable t
75
   // A0=w[0], ksi=w[1], beta=w[2], wr=w[3], Cd=w[4], eta=w[5]
77   variable L, beta_, wr, i0, V0

79   L=0.0023177
   beta_=w[2]
81   wr=w[3]

83   // Change if using other voltage admittance curves
   V0=5

85   variable C0, L0, R0, theta_,j,i

87   make Pcoef
89   redimension /N=4 Pcoef
   make /D/O Pwave
91   setscale /I x -2e-8, 2e-8, Pwave
   make /N=(0,3) /C Icoef
93   redimension /N=(0, 3) Icoef
   wave W_polyRoots=W_polyRoots

95   make /N=0 ww, III , III1 , III2
97   make /N=0 IV
   redimension /N=0 ww, IIII , III1 ,IV , III2

99   // To calculate circuit parameters
101  L0=L/w[0]^2
   C0=w[0]^2/L/wr^2
103  R0=2*beta_*L/w[0]^2

105  // Define polynomial equation
   Pcoef[0]=-V0^2
107  Pcoef[1]=( t*L0-1/t/C0)^2+R0^2
   Pcoef[2]=3*w[1]/C0/t/2-3*w[1]*t*L0/2+3*w[5]*R0/2
109  Pcoef[3]=9*w[1]^2/16+9*w[5]^2/16

111  // Solve polynomial equation
   Pwave=Poly(Pcoef, x)
113  FindRoots /P=Pcoef
   redimension /N=((dimsize(Icoef ,0)+1),3) Icoef
115  redimension /N=(numpts(ww)+1) ww, III , III1 ,IV , III2

117  // To give phase in upward sweep

```

```

119 for (i=numpts(W_PolyRoots);i>0;i=i-1)
    Icoef[ dimension(Icoef,0)-1][i-1]=W_PolyRoots[i-1]
    if ( imag(Icoef[ dimension(Icoef,0)-1][i-1])==0)
121       i0=sqrt( real(Icoef[ dimension(Icoef,0)-1][i-1]))
        theta_ =atan((-t*L0+1/t/C0+3*w[1]*i0^2/4)/(R0+3*w[5]*i0^2/4))
123     endif
  endfor

125 G=i0*cos(theta_)/V0 // real part of admittance
127 B=i0*sin(theta_)/V0+t*w[4] // imaginary part
  return ( atan(B/G)*180/pi) // return phase
129 End

131 Function finalphase()
133 wave wy=root:hard10_phase // y wave name
  wave wt=root:hard_f // x wave name
135 variable i
  wave W_coef=root:fitsolutioncoef2

137 // To carry out fitting
139 FuncFit/L=101 /H='111111'/NTHR=0 Fit_solution_phase W_coef wy
  /X=wt /D
  end

141

143 Function Fit_solution_down(w,t) : FitFunc
  wave w
145 variable t

147 // A0=w[0], ksi=w[1], beta=w[2], wr=w[3], Cd=w[4], eta=w[5]
  variable L, beta_, wr, i0, V0

149 L=0.0023177
151 beta_=w[2]
  wr=w[3]

153 // Change if using other voltage admittance curves
155 V0=5

157 variable C0, L0, R0, theta_,j,i

159 make Pcoef
  redimension /N=4 Pcoef
161 make /D/O Pwave
  setscale /I x -2e-8, 2e-8, Pwave
163 make /N=(0,3) /C Icoef
  redimension /N=(0, 3) Icoef

```

```

165 wave W_polyRoots=W_polyRoots
167 make/N=0 ww, III , III1 , III2
169 make/N=0 IV
169 redimension/N=0 ww, IIII , III1 ,IV , III2
171 // To calculate circuit parameters
171 L0=L/w[0]^2
173 C0=w[0]^2/L/wr^2
173 R0=2*beta_*L/w[0]^2
175
175 // Define polynomial equation
177 Pcoef[0]=-V0^2
177 Pcoef[1]=( t*L0-1/t/C0)^2+R0^2
179 Pcoef[2]=3*w[1]/C0/t/2-3*w[1]*t*L0/2+3*w[5]*R0/2
179 Pcoef[3]=9*w[1]^2/16+9*w[5]^2/16
181
181 // Solve polynomial equation
183 Pwave=Poly(Pcoef , x)
183 FindRoots/P=Pcoef
185 redimension/N=((dimsize(Icoef ,0)+1),3) Icoef
185 redimension/N=(numpts(ww)+1) ww, III , III1 ,IV , III2
187
187 // To give amplitude in downward sweep
189 for (i=0;i<numpts(W_PolyRoots);i=i+1)
189 Icoef[dimsize(Icoef ,0)-1][i]=W_PolyRoots[i]
191 if (imag(Icoef[dimsize(Icoef ,0)-1][i])==0)
191 i0=sqrt(real(Icoef[dimsize(Icoef ,0)-1][i]))
193 theta_=atan((-t*L0+1/t/C0+3*w[1]*i0^2/4)/(R0+3*w[5]*i0^2/4))
193 endif
195 endfor
197
197 G=i0*cos(theta_)/V0 // real part of admittance
197 B=i0*sin(theta_)/V0+t*w[4] // imaginary part
199 return log(sqrt(G^2+B^2)) // return log(Y)
201 End
201
201 Function finalone_down()
203 wave wy=root:hard10down // y wave name
203 wave wt=root:hard_f // x wave name
205 variable i
205 wave W_coef=root:fitsolutioncoef2 //change
207
207 // To carry out fitting
209 FuncFit/L=101 /H="000000"/NTHR=0 Fit_solution_down W_coef wy /X
209 =wt /D
211 end

```

```

213 Function Fit_solution_downphase(w,t) : FitFunc
      wave w
215 variable t

217 // A0=w[0], ksi=w[1], beta=w[2], wr=w[3], Cd=w[4], eta=w[5]
      variable L, beta_, wr, i0, V0

219
      L=0.0023177
221 beta_=w[2]
      wr=w[3]

223 // Change if using other voltage admittance curves
225 V0=5

227 variable C0, L0, R0, theta_,j,i

229 make Pcoef
      redimension /N=4 Pcoef
231 make /D/O Pwave
      setscale /I x -2e-8, 2e-8, Pwave
233 make /N=(0,3) /C Icoef
      redimension /N=(0, 3) Icoef
235 wave W_polyRoots=W_polyRoots

237 make/N=0 ww, III , III1 , III2
      make/N=0 IV
239 redimension /N=0 ww, IIII , III1 , IV , III2

241 // To calculate circuit parameters
      L0=L/w[0]^2
243 C0=w[0]^2/L/wr^2
      R0=2*beta_*L/w[0]^2

245 // Define polynomial equation
247 Pcoef[0]=-V0^2
      Pcoef[1]=(t*L0-1/t/C0)^2+R0^2
249 Pcoef[2]=3*w[1]/C0/t/2-3*w[1]*t*L0/2+3*w[5]*R0/2
      Pcoef[3]=9*w[1]^2/16+9*w[5]^2/16

251 // Solve polynomial equation
253 Pwave=Poly(Pcoef, x)
      FindRoots /P=Pcoef
255 redimension /N=((dimsize(Icoef,0)+1),3) Icoef
      redimension /N=(numpts(ww)+1) ww, III , III1 , IV , III2

257 // To give phase in downward sweep
259 for (i=0;i<numpts(W_PolyRoots);i=i+1)

```

```

Icoef[ dimsize(Icoef,0) -1][i]=W_PolyRoots[i]
261 if (imag(Icoef[ dimsize(Icoef,0) -1][i])==0)
    i0=sqrt(real(Icoef[ dimsize(Icoef,0) -1][i]))
263     theta_=atan((-t*L0+1/t/C0+3*w[1]*i0^2/4)/(R0+3*w[5]*i0^2/4))
    endif
265 endfor

G=i0*cos(theta_)/V0 // real part of admittance
B=i0*sin(theta_)/V0+t*w[4] // imaginary part
269 return (atan(B/G)*180/pi) // return phase
End
271
Function finalone_downphase()
273 wave wy=root:hard10down_phase // y wave name
wave wt=root:hard_f // x wave name
275 variable i
wave W_coef=root:fitsolutioncoef2
277
// To carry out fitting
279 FuncFit/L=101 /H='111111'/NTHR=0 Fit_solution_downphase W_coef
    wy /X=wt /D
end

```

Simulation of the jumping

```

#pragma rtGlobals=1 // Use modern global access method.
2
Function FindCurrent(ksi, eta)
4 variable ksi, eta
variable V0, C0, L0, R0
6 variable j, i, w

8 // Fix the voltage amplitude
V0=25

10 // Set circuit parameters
12 C0=1E-9
L0=0.1
14 R0=10

16 make Pcoef
redimension/N=4 Pcoef
18 make /D/O Pwave
setscale /I x -2e-8, 2e-8, Pwave
20 make /N=(0,3) /C Icoef

```



```

22 redimension /N=(0, 3) Icoef
23 wave W_polyRoots=W_polyRoots
24 make/N=0 ww, VI, VII, VI2
25 make/N=0 IV
26 redimension/N=0 ww, VI, VII, VI2
27 for(j=0; j<2001; j=j+1)
28     // Set frequency range
29     w=99000+j*1
30
31     // Define polynomial equation
32     Pcoef[0]=-V0^2
33     Pcoef[1]=(w*L0-1/w/C0)^2+R0^2
34     Pcoef[2]=3*ksi/C0/w/2-3*ksi*w*L0/2+3*eta*R0/2
35     Pcoef[3]=9*ksi^2/16+9*eta^2/16
36
37     // Solve polynomial equation
38     Pwave=Poly(Pcoef, x)
39     FindRoots/P=Pcoef
40     redimension /N=((dimsize(Icoef,0)+1),3) Icoef
41     redimension /N=(numpts(ww)+1) ww, VI, VII, VI2
42     ww[numpts(ww)-1]=w
43
44     // Find the solutions for current
45     for (i=0; i<numpts(W_PolyRoots); i=i+1)
46         Icoef[dimsize(Icoef,0)-1][i]=W_PolyRoots[i]
47         if (imag(Icoef[dimsize(Icoef,0)-1][i])==0)
48             VI[numpts(ww)-1]=sqrt(real(Icoef[dimsize(Icoef,0)-1][i]))
49             VII[numpts(ww)-1]=sqrt(real(Icoef[dimsize(Icoef,0)-1][i]))
50         endif
51     endfor
52     for (i=numpts(W_PolyRoots); i>0; i=i-1)
53         if (imag(Icoef[dimsize(Icoef,0)-1][i-1])==0)
54             VII[numpts(ww)-1]=sqrt(real(Icoef[dimsize(Icoef,0)-1][i-1]))
55         endif
56     endfor
57
58     for (i=numpts(VI); i>0; i=i-1)
59         if (VI[i-1]-VII[i-1]!=0)
60             VI2[i-1]=sqrt(real(Icoef[i-1][1]))
61         endif
62     endfor
63 endfor
64 end

```

```
1 #pragma rtGlobals=1 // Use modern global access method.
```

```

3 Function FindCurrent_V(ksi , eta)
4   variable ksi , eta
5   variable V0, C0, L0, R0
6   variable j ,i ,w
7
8   // Fix the frequency
9   w=99500
10
11  // Set circuit parameters
12  C0=1E-9
13  L0=0.1
14  R0=10
15
16  make Pcoef1
17  redimension /N=4 Pcoef1
18  make /D/O Pwave1
19  setscale /I x -2e-8, 2e-8, Pwave1
20  make /N=(0,3) /C Icoef1
21  redimension /N=(0, 3) Icoef1
22  wave W_polyRoots=W_polyRoots
23  make /N=0 voltage , Curr1 , Curr2 , Curr3
24
25  redimension /N=0 voltage , Curr1 , Curr2 , Curr3
26  for (j=0; j<1001; j=j+1)
27    // Set voltage range
28    V0=0.050*j
29
30    // Define polynomial equation
31    Pcoef1[0]=-V0^2
32    Pcoef1[1]=(w*L0-1/w/C0)^2+R0^2
33    Pcoef1[2]=3*ksi /C0/w/2-3*ksi*w*L0/2+3*eta*R0/2
34    Pcoef1[3]=9*ksi^2/16+9*eta^2/16
35
36    // Solve polynomial equation
37    Pwave1=Poly(Pcoef1 , x)
38    FindRoots /P=Pcoef1
39    redimension /N=(( dimsize(Icoef1 ,0)+1) ,3) Icoef1
40    redimension /N=(numpts(voltage)+1) voltage , Curr1 , Curr2 , Curr3
41    voltage [numpts(voltage)-1]=V0
42
43    // Find the solutions for current
44    for ( i=0; i<numpts(W_PolyRoots); i=i+1)
45      Icoef1 [dimsize(Icoef1 ,0)-1][i]=W_PolyRoots[i]
46      if (imag(Icoef1 [dimsize(Icoef1 ,0)-1][i])==0)
47        Curr1 [numpts(voltage)-1]=sqrt(real(Icoef1 [dimsize(Icoef1
          ,0)-1][i]))

```

```

        Curr3[numpts(voltage)-1]=sqrt(real(Icoef1[ dimsize(Icoef1
        ,0)-1][i]))
49     endif
    endfor
51   for (i=numpts(W_PolyRoots);i>0;i=i-1)
        if (imag(Icoef1[ dimsize(Icoef1,0)-1][i-1])==0)
53       Curr2[numpts(voltage)-1]=sqrt(real(Icoef1[ dimsize(Icoef1
        ,0)-1][i-1]))
        endif
55   endfor

57   for (i=numpts(Curr1);i>0;i=i-1)
        if (Curr1[i-1]-Curr2[i-1]!=0)
59       Curr3[i-1]=sqrt(real(Icoef1[i-1][1]))
        endif
61   endfor
    endfor
63 end

```

Simulation of polarization-filed loop

```

1 #pragma rtGlobals=1 // Use modern global access method.

3 Function ThirdOrder(pw, xx, yw, dydx)
    wave pw
5    variable xx
    wave yw
7    wave dydx

9    // To define the differential equation
    // dy/dx=gamma*(y-y^3)+e0*sin(omega*t)
11   // omega=100
    dydx[0] =pw[0]*yw[0]-pw[0]*yw[0]^3+pw[1]*sin(100*xx)
13 End

15 Function PE()

17   make/D/O/N=10001 YY
    YY[0] =0 // initial condition
19   variable E0, gamma0, j
    gamma0=10
21   E0=10000
    make/D/O PP={gamma0,E0} // set constants
23   duplicate/O/D YY,Xwave,Ywave, Zwave
    setscale/I x,0,1,Xwave,Ywave, Zwave

```

```

25 Xwave=x
    Ywave=sin(100*x)*E0/2/gamma0
27
    // Runge-Kutta method
29 IntegrateODE/X=Xwave ThirdOrder , PP, YY

31 // To calculate strain
    for(j=0; j<numpts(YY); j=j+1)
33     Zwave[j]=YY[j]^2*0.1
    endfor

35
    checkdisplayed/A YY
37 // NVAR V_flag
    if (V_flag==0)

39
        // To draw P-E loop and modify the formats
41 Display YY vs Ywave
        ModifyGraph mode=4,marker=19,msize=2
43 ModifyGraph tick=2,mirror=1,fSize=14,standoff=0,font="Times
            New Roman"
        Label left "\\Z16\\f02P\\f00/\\f02P\\Bs"
45 Label bottom "\\Z16\\f02\\F'Symbol'c\\F'Times New Roman'\\B0\\
            M\\Z16E\\f00/\\f02P\\Bs"
        ModifyGraph margin(top)=14,margin(right)=20

47
        // To draw S-E loop and modify the formats
49 Display Zwave vs Ywave
        ModifyGraph mode=4,marker=19,msize=2
51 ModifyGraph tick=2,mirror=1,fSize=14,standoff=0,font="Times
            New Roman"
        Label left "\\Z16\\f02P\\f00/\\f02P\\Bs"
53 Label bottom "\\Z16\\f02\\F'Symbol'c\\F'Times New Roman'\\B0\\
            M\\Z16E\\f00/\\f02P\\Bs"
        ModifyGraph margin(top)=14,margin(right)=20
55 endif
End

```

References

- [1] J. Curie and P. Curie, Bulletin de la Socit minrologique de France **91**, 294 (1880).
- [2] G. Lippmann, Annales de chimie et de physique **24**, 145 (1881).
- [3] J. Curie and P. Curie, Comptes rendus hebdomadaires des sances de l'Acadmie des sciences **93**, 1137 (1881).
- [4] Piezoelectricity, <https://en.wikipedia.org/wiki/Piezoelectricity>.
- [5] W. Voigt, *Lehrbuch der kristallphysik* (B.G. Teubner, Berlin, 1910).
- [6] G. H. Haertling, Journal of the American Ceramic Society **82**, 797 (1999).
- [7] R. Guo, L. E. Cross, S.-E. Park, B. Noheda, D. E. Cox, and G. Shirane, Physical Review Letters **84**, 5423 (2000).
- [8] J. F. Scott, Science **315**, 954 (2007).
- [9] D. Damjanovic, Reports on Progress in Physcis **61**, 1267 (1998).
- [10] J.-F. Wang, Z.-T. Jiang, and R.-D. Shi, in *Piezoelectric Vibration*, 1 ed., edited by X. Wang and B.-G. Zhang (Science Press, Beijing, China, 1989), (in Chinese).
- [11] C. R. Bowen, H. A. Kim, P. M. Weaver, and S. Dunn, Energy & Environmental Science **7**, 25 (2014).
- [12] J. Filipiak, L. Solarz, and G. Steczko, Sensors **11**, 11809 (2011).
- [13] T. Morita, S. Takahashi, H. Asama, and T. Niino, Vacuum **70**, 53 (2003).
- [14] S. Kudo, Japanese Journal of Applied Physics **46**, 4704 (2007).
- [15] L. Bei, G. I. Dennis, H. M. Miller, T. W. Spaine, and J. W. Carnahan, Progress in Quantum Electronics **28**, 67 (2004).
- [16] T. Morita, Sensors and Actuators A **103**, 291 (2003).
- [17] K. Uchino, Smart Materials Structures **7**, 273 (1998).
- [18] J. Wallaschek, Journal of Intelligent Material Systems and Structures **6**, 71 (1995).
- [19] J. Wallaschek, Smart Materials Structures **7**, 369 (1998).

- [20] K. Uchino, *Ferroelectric devices* (Marcel Dekker, Inc., New York, 2000).
- [21] N. Aurelle, D. Guyomar, C. Richard, P. Gonnard, and L. Eyraud, *Ultrasonics* **34**, 187 (1996).
- [22] K. Nakamura *et al.*, in *High performance piezoelectric materials and advanced application technologies*, 2 ed., edited by K. Nakamura (Science & Technology Co., Ltd., Tokyo, Japan, 2010).
- [23] T. Shrout and S. Zhang, *Journal of Electroceramics* **19**, 113 (2007).
- [24] P. K. Panda and B. Sahoo, *Ferroelectrics* **474**, 128 (2015).
- [25] M. I. Morozov and D. Damjanovic, *Journal of Applied Physics* **104**, 034107 (2008).
- [26] Y. Yamashita, *Japanese Journal of Applied Physics* **33**, 5328 (1994).
- [27] S.-E. Park and T. R. Shrout, *IEEE transactions on ultrasonics, ferroelectrics, and frequency control* **44**, 1140 (1997).
- [28] W.-P. Tai, Y.-H. Kim, Y.-P. Ok, H.-N. Ji, S.-K. Kang, and J.-S. Lee, *Intergrated Ferroelectrics* **114**, 1 (2010).
- [29] T. Takenaka and H. Nagata, *Journal of the European Ceramic Society* **25**, 2693 (2005).
- [30] J. Rodel, W. Jo, K. T. P. Seifert, E.-M. Anton, and T. Granzow, *Journal of the American Ceramic Society* **92**, 1153 (2009).
- [31] J. Kwak, A. I. Kingon, and S.-H. Kim, *Materials Letters* **82**, 130 (2012).
- [32] B. T. Matthias, *Energy* **75**, 1771 (1949).
- [33] G. Shirane, H. Danner, A. Pavlovic, and R. Pepinsky, *Physical Review* **93**, 672 (1954).
- [34] A. W. Hewat, *J. Phys. C: Solid State Phys.* **6**, 2559 (1973).
- [35] F. Z. Kang Sun, in *Piezoelectricity*, edited by Q. Yang (National Defend Industy Press, Beijing, China, 1984), (in Chinese).
- [36] B. T. Matthias and J. P. Remeika, *Physical Review* **82**, 727 (1951).
- [37] K. E. Johnston, C. C. Tang, J. E. Parker, K. S. Knight, P. Lightfoot, and S. E. Ashbrook, *Journal of the American Chemical Society* **132**, 8732 (2010).

- [38] X. Wang, J. Wu, D. Xiao, J. Zhu, X. Cheng, T. Zheng, B. Zhang, X. Lou, and X. Wang, *Journal of the American Chemical Society* **136**, 2905 (2014).
- [39] S. O. Leontsev and R. E. Eitel, *Sci. Technol. Adv. Mater.* **11**, 044302 (2010).
- [40] Y. G. Lv, C. L. Wang, J. L. Zhang, L. Wu, M. L. Zhao, and J. P. Xu, *Materials Research Bulletin* **44**, 284 (2009).
- [41] D. Lin, K. W. Kwok, and H. L. W. Chan, *Journal of Alloys and Compounds* **461**, 273 (2008).
- [42] B. Malic, J. Bernard, J. Holc, D. Jenko, and M. Kosec, *Journal of the European Ceramic Society* **25**, 2707 (2005).
- [43] F. Jona and G. Shirane, in *Ferroelectric Crystals*, Vol. 1 of *International Series of Monographs on Solid State Physics*, edited by R. Smoluchowski and N. Kurti (The Macmillan Company, Great Britain, 1962).
- [44] M. Matsubara, K. Kikuta, and S. Hirano, *Journal of Applied Physics* **97**, 114105 (2005).
- [45] E. M. Alkoy, *Journal of Applied Physics* **108**, 094104 (2010).
- [46] G. Han, J. Ryu, C.-W. Ahn, W.-H. Yoon, J.-J. Choi, B.-D. Hahn, J.-W. Kim, J.-H. Choi, and D.-S. Park, *Journal of the American Ceramic Society* **95**, 1489 (2012).
- [47] F. Kurokawa, R. Yokokawa, H. Kotera, F. Horikiri, K. Shibata, T. Mishima, M. Sato, and I. Kanno, *Micro & Nano Letters* **7**, 1223 (2012).
- [48] Y. Fujiuchi and T. Morita, *IEEE transactions on ultrasonics, ferroelectrics, and frequency control* **61**, 1593 (2014).
- [49] K. H. Lam, D. M. Lin, and H. L. W. Chan, *Review of Scientific Instruments* **78**, 115109 (2007).
- [50] E. Li, H. Kakemoto, T. Hoshina, and T. Tsurumi, *Japanese Journal of Applied Physics* **47**, 7702 (2008).
- [51] E. A. Patterson and D. P. Cann, *IEEE transactions on ultrasonics, ferroelectrics, and frequency control* **58**, 1835 (2011).
- [52] S. Zhang, R. Xia, and T. R. Shrout, *Journal of Applied Physics* **100**, 104108 (2006).

- [53] T. Maeda, N. Takiguchi, T. Morita, M. Ishikawa, and T. Hemsell, *Journal of the Korean Physical Society* **57**, 924 (2010).
- [54] Y. Guo, K. ichi Kakimoto, and H. Ohsato, *Japanese Journal of Applied Physics* **43**, 6662 (2004).
- [55] P. Zhao, B.-P. Zhang, R. Tu, and T. Goto, *Journal of the American Ceramic Society* **91**, 3078 (2008).
- [56] Y. Watanabe, K. Sumida, S. Yamada, S. Sago, S. Hirano, and K. Kikuta, *Japanese Journal of Applied Physics* **47**, 3556 (2008).
- [57] B. C. Park, I. K. Hong, H. D. Jang, V. D. N. Tran, W. P. Tai, and J.-S. Lee, *Materials Letters* **64**, 1577 (2010).
- [58] T. Maeda, Ph.D. thesis, The University of Tokyo, 2013.
- [59] L. Liu, H. Fan, L. Fang, X. Chen, H. Dammak, and M. P. Thi, *Materials Chemistry and Physics* **117**, 138 (2009).
- [60] S. Uchida, Y. Inoue, Y. Fujishiro, and T. Sato, *Journal of Materials Science* **33**, 5125 (1998).
- [61] G. Li, X. Wu, W. Ren, X. Yan, P. Shi, X. Chen, and X. Yao, *Ferroelectrics* **404**, 63 (2010).
- [62] D. Zhang and Z. Zhang, *Ferroelectrics* **466**, 8 (2014).
- [63] J. Acker, H. Kungl, R. Schierholz, S. Wagner, R.-A. Eichel, and M. J. Hoffmann, *Journal of the European Ceramic Society* **34**, 4213 (2014).
- [64] Y. Liu, X. Lu, Y. Jin, S. Peng, F. Huang, Y. Kan, T. Xu, K. Min, and J. Zhu, *Applied Physics Letters* **100**, 212902 (2012).
- [65] K. Byrappa and M. Yoshimura, in *Handbook of hydrothermte technology a technology for crystal growth and material processing*, edited by G. E. McGuire, S. M. Rossmagel, and R. F. Bunshah (Noyes publications, Park Ridge, New Jersey, U.S.A., 2001).
- [66] M. Yoshimura and K. Byrappa, *Journal of Materials Science* **43**, 2085 (2008).
- [67] K. Shimomura, T. Tsurumi, Y. Ohba, and M. Daimon, *Japanese Journal of Applied Physics* **30**, 2174 (1991).
- [68] M. Yoshimura, S.-E. Yoo, M. Hayashi, and N. Ishizawa, *Japanese Journal of Applied Physics* **28**, 2007 (1989).

- [69] J. O. E. Jr., C. C. Hung-Houston, B. L. Gersten, M. M. Lencka, and R. E. Riman, *Journal of the American Ceramic Society* **79**, 2929 (1996).
- [70] J.-H. Cho, Y.-J. Ma, Y.-H. Lee, M.-P. Chun, and B.-I. Kim, *Journal of Ceramic Processing Research* **7**, 91 (2006).
- [71] G. K. L. Goh, F. F. Lange, S. M. Haile, and C. G. Levi, *Journal of Materials Research* **18**, 338 (2003).
- [72] T. Morita, M. K. Kurosawa, and T. Higuchi, *Sensors and Actuators* **83**, 225 (2000).
- [73] W. L. Suchanek and R. E. Riman, *Advances in Science and Technology* **45**, 184 (2006).
- [74] T. Morita, *Materials* **3**, 5236 (2010).
- [75] R. Ageba, Y. Kadota, T. Maeda, N. Takiguchi, T. Morita, M. Ishikawa, P. Bornmann, and T. Hemsell, *Journal of the Korean Ceramic Society* **57**, 918 (2010).
- [76] K. Kanie, Y. Numamoto, S. Tsukamoto, H. Takahashi, H. Mizutani, A. Terabe, M. Nakaya, J. Tani, and A. Muramatsu, *Materials Transactions* **52**, 2119 (2011).
- [77] C. Richard, A. Catlow, S. T. Bromley, S. Hamad, M. Mora-Fonz, A. A. Sokol, and S. M. Woodley, *Physical Chemistry Chemical Physics* **12**, 773 (2010).
- [78] S. Y. Wu, W. Zhang, and X. M. Chen, *Journal of Material Science: Material Electron* **21**, 450 (2010).
- [79] H. Zhu, Z. Zheng, X. Gao, Y. Huang, Z. Yan, J. Zou, H. Yin, Q. Zou, S. H. Kable, J. Zhao, Y. Xi, W. N. Martens, and R. L. Frost, *Journal of the American Chemical Society* **128**, 2373 (2006).
- [80] Piezoelectric ceramics typical values (at room temp. and low signal data), <http://www.fujicera.co.jp/product/j/index.html>.
- [81] A. Inoue, T. Zhang, and A. Takeuchi, *Materials Transactions* **37**, 1731 (1996).
- [82] A. Inoue, T. Zhang, W. Zhang, and A. Takeuchi, *Materials Transactions* **37**, 99 (1996).
- [83] M. A. McGuire, O. Rios, N. J. Ghimire, and M. Koehler, *Applied Physics Letters* **101**, 202401 (2012).

- [84] G. Sebald, L. Leburn, and D. Guyomar, *IEEE transactions on ultrasonics, ferroelectrics, and frequency control* **52**, 596 (2005).
- [85] M. Tani, M. Akamatsu, Y. Yasuda, H. Fujita, and H. Toshiyoshi, in *A combination of fast resonant mode and slow static deflection of SOI-PZT actuators for MEMS image projection display* (PUBLISHER, ADDRESS, 2006), pp. 25–26.
- [86] K. Uchino, J. Zheng, A. Joshi, Y. han Chen, S. Yoshikawa, S. Hirose, S. Takahashi, and J. W. C. D. Vries, *Journal of Electroceramics* **2**, 33 (1998).
- [87] K. Nagata, J. Thongrueng, and K. Kato, *Japanese Journal of Applied Physics* **36**, 6103 (1997).
- [88] S. Kawada, H. Ogawa, M. Kimura, K. Shiratsuyu, and H. Niimi, *Japanese Journal of Applied Physics* **45**, 7455 (2006).
- [89] T. Watanabe, Y. Hiruma, H. Nagata, and T. Takenaka, *Ferroelectrics* **385**, 6135 (2010).
- [90] H. Nagata, M. Seki, Y. Noumura, Y. Hiruma, and T. Takenaka, *Japanese Journal of Applied Physics* **50**, 09ND05 (2011).
- [91] H.-C. Song, T. Morita, S.-J. Yoon, and D.-Y. Jeong, *Japanese Journal of Applied Physics* **49**, 111502 (2010).
- [92] D. A. Hall, *Journal of Materials Science* **36**, 4575 (2001).
- [93] T. Ikeda, *Fundamentals of Piezoelectricity* (Oxford University Press, New York, 1990).
- [94] A. Rajapurkar, S. O. Ural, Y. Zhuang, H.-Y. Lee, A. Amin, and K. Uchino, *Japanese of Journal of Applied Physics* **49**, 071502 (2010).
- [95] H. Ogawa, S. Kawada, M. Kimura, Y. Higuchi, and H. Takagi, *Japanese Journal of Applied Physics* **48**, 09KD05 (2009).
- [96] S. Tashiro, K. Ishii, and K. Nagata, *Journal of the Ceramic Society of Japan* **110**, 649 (2002).
- [97] J. F. Blackburn and M. G. Cain, *Journal of Applied Physics* **100**, 114101 (2006).
- [98] H. Shimizu, Y. Doshida, Y. Mizuno, S. Tanaka, K. Uematsu, and H. Tamura, *Japanese Journal of Applied Physics* **51**, 09LD02 (2012).

- [99] S. Tashiro, M. Ikehiro, and H. Igarashi, *Japanese Journal of Applied Physics* **36**, 3004 (1997).
- [100] R. Ramesh, R. K. Kumar, and T. K. V. Kumar, *Journal of Electroceramics* **30**, 251 (2013).
- [101] M. Umeda, K. Nakamura, and S. Ueha, *Japanese Journal of Applied Physics* **37**, 5322 (1998).
- [102] K. Uchino, *IEEE transactions on ultrasonics, ferroelectrics, and frequency control* **48**, 307 (2001).
- [103] ANSI/IEEE Standard 176-1987 (1988).
- [104] *IEEE transactions on ultrasonics, ferroelectrics, and frequency control* **43**, 717 (1996).
- [105] Y. Yokouchi, T. Maeda, P. Bornmann, T. Hemsel, and T. Morita, *Japanese Journal of Applied Physics* **52**, 07HB03 (2013).
- [106] X-ray crystallography, https://en.wikipedia.org/wiki/X-ray_crystallography.
- [107] Density, <http://en.wikipedia.org/wiki/Density>.
- [108] Archimedes' principle, https://en.wikipedia.org/wiki/Archimedes'_principle.
- [109] Y. Fujiuchi, Master's thesis, The University of Tokyo, 2014.
- [110] M. Umeda, Technical report, (unpublished), (in Japanese).
- [111] Soft vs. hard ceramics, <https://www.americanpiezo.com/piezo-theory/soft-vs-hard-ceramics.html>.
- [112] H. Takao, Y. Saito, Y. Aoki, and K. Horibuchi, *Journal of the American Ceramic Society* **89**, 1951 (2006).
- [113] Z.-Y. Shen, Y. Xu, and J.-F. Li, *Ceramics International* **38S**, S331 (2012).
- [114] M. Matsubara, T. Yamaguchi, W. Sakamoto, K. Kikuta, T. Yogo, and S. ichi Hirano, *Journal of the American Ceramic Society* **88**, 1190 (2005).
- [115] D. Tanaka, J. Yamazaki, M. Furukawa, and T. Tsukada, *Japanese Journal of Applied Physics* **49**, 09MD03 (2010).
- [116] J. B. Lim, S. Zhang, H. J. Lee, J.-H. Jeon, and T. R. ShROUT, *Journal of the American Ceramic Society* **93**, 2519 (2010).

- [117] M. Matsubara, T. Yamaguchi, K. Kikuta, and S. ichi Hirano, *Japanese Journal of Applied Physics* **44**, 258 (2005).
- [118] N. M. Hagh and K. Kerman, *Journal of the European Ceramic Society* **29**, 2325 (2009).
- [119] T. Maeda, T. Hemsel, and T. Morita, *Japanese Journal of Applied Physics* **50**, 07HC01 (2011).
- [120] Y. Yokouchi, Master's thesis, The University of Tokyo, 2013.
- [121] Y. Gao, K. Uchino, and D. Viehland, *Japanese Journal of Applied Physics* **45**, 9119 (2006).
- [122] I. K. Yoo and S. B. Desu, *Physical Status Solidi A* **133**, 565 (1992).
- [123] D. C. Lupascu, Y. A. Genenko, and N. Balke, *Journal of the American Ceramic Society* **89**, 224 (2006).
- [124] D. Lin, K. W. Kwok, and H. L. W. Chan, *Applied Physics Letters* **90**, 232903 (2007).
- [125] S. M. Ke, H. T. Huang, H. Q. Fan, H. K. Lee, L. M. Zhou, and Y.-W. Mai, *Applied Physics Letters* **101**, 082901 (2012).
- [126] Y. A. Genenko and D. C. Lupascu, *Physical Review B* **75**, 184107 (2007).
- [127] M. I. Morozov and D. Damjanovic, *Journal of Applied Physics* **107**, 034106 (2010).
- [128] T. Granzow, E. Suvaci, H. Kungl, and M. J. Hoffmann, *Applied Physics Letters* **89**, 262908 (2006).
- [129] H.-Q. Wang, Y.-J. Dai, and X.-W. Zhang, *Journal of the American Ceramic Society* **95**, 1182 (2012).
- [130] D.-Y. Jeong, J. Ryu, and D.-S. Park, *Materials Science and Engineering B* **163**, 88 (2009).
- [131] C. Liu, D. Xiao, J. Wu, Z. Wang, F. Li, T. Huang, and J. Zhu, *Ferroelectrics* **458**, 31 (2014).
- [132] K. Ishii, N. Akimoto, S. Tashiro, and H. Igarashi, *Journal of the European Ceramic Society* **19**, 1157 (1999).
- [133] K. Ishii, N. Akimoto, S. Tashiro, and H. Igarashi, *Journal of the Ceramic Society of Japan* **106**, 555 (1998).

- [134] K. Ishii and S. Tashiro, *Journal of the Ceramic Society of Japan* **119**, 29 (2011).
- [135] K. Ishii, T. Yamada, S. Tashiro, and H. Igarashi, *Japanese Journal of Applied Physics* **38**, 5572 (1999).
- [136] M. Umeda, K. Nakamura, S. Takahashi, and S. Ueha, *Japanese Journal of Applied Physics* **39**, 5623 (2000).
- [137] D. Banerjee and J. K. Bhattacharjee, *American Journal of Physics* **78**, 142 (2010).
- [138] A. Chatterjee, (teaching resource) (unpublished).
- [139] R. Perez and A. Albareda, *Journal of the Acoustical Society of America* **100**, 3561 (1996).
- [140] A. Albareda, R. Perez, J.-H. Kayombo, E. Minguella, J.-A. Casals, and F. M. de Espinosa, *Ultrasonics* **38**, 151 (2000).
- [141] A. Albareda, P. Gonnard, V. Perria, R. Briot, and D. Guyomar, *IEEE transactions on ultrasonics, ferroelectrics, and frequency control* **47**, 844 (2000).
- [142] A. Albareda, R. Perez, J. A. Casals, J. E. Garcia, and D. A. Ochoa, *IEEE transactions on ultrasonics, ferroelectrics, and frequency control* **54**, 2175 (2007).
- [143] A. Albareda, R. Perez, J. E. Garcia, and D. A. Ochoa, *Journal of Electroceramics* **19**, 427 (2007).
- [144] M. Masaki, H. Hashimoto, W. Masahiko, and I. Suzuki, *Journal of the European Ceramic Society* **28**, 133 (2008).
- [145] J. Nosek, *IEEE transactions on ultrasonics, ferroelectrics, and frequency control* **46**, 823 (1999).
- [146] M. Hagiwara, T. Hoshina, H. Takeda, and T. Tsurumi, *Japanese Journal of Applied Physics* **51**, 09LD01 (2012).
- [147] M. Maeda, M. Washihira, H. Hashimoto, and I. Suzuki, *Journal of the Physical Society of Japan* **76**, 084704 (2007).
- [148] M. Umeda, K. Nakamura, and S. Ueha, *Japanese Journal of Applied Physics* **38**, 3327 (1999).

- [149] Y. Sasaki, S. Takahashi, M. Umeda, K. Nakamura, and S. Ueha, *Transactions of the Materials Research Society of Japan* **27**, 259 (2002).
- [150] D. Parenthoine, L. Haumesser, F. V. Meulen, M. Lethiecq, and L.-P. Tran-Huu-Hue, *IEEE transactions on ultrasonics, ferroelectrics, and frequency control* **56**, 167 (2009).
- [151] M. Hagiwara, S. Takahashi, T. Hoshina, H. Takeda, and T. Tsurumi, *IEEE transactions on ultrasonics, ferroelectrics, and frequency control* **58**, 1721 (2011).
- [152] A. V. Mezheritsky, *IEEE transactions on ultrasonics, ferroelectrics, and frequency control* **51**, 695 (2004).
- [153] M. Kamlah, *Continuum Mechanical and Thermodynamics* **13**, 219 (2001).
- [154] Y. Ishikiriyama and T. Morita, *Journal of Advanced Mechanical Design, Systems, and Manufacturing* **4**, 143 (2010).
- [155] H. Jung and D.-G. Gweon, *Review of Scientific Instruments* **71**, 1896 (2000).
- [156] D. Croft, G. Shed, and S. Devasia, *Journal of Dynamic Systems, Measurement, and Control* **123**, 35 (2001).
- [157] S. Sivasubramanian, A. Widom, and Y. Srivastava, *IEEE transactions on ultrasonics, ferroelectrics, and frequency control* **50**, 950 (2003).
- [158] H. Nagata, Y. Hiruma, and T. Takenaka, *Integrated Ferroelectrics* **115**, 63 (2010).
- [159] Y. Hiruma, T. Watanabe, H. Nagata, and T. Takenaka, *Japanese Journal of Applied Physics* **47**, 7659 (2008).
- [160] Y. Noumura, Y. Hiruma, H. Nagata, and T. Takenaka, *Japanese Journal of Applied Physics* **50**, 07HB06 (2011).
- [161] H. Ogawa, S. Kawada, M. Kimura, K. Shiratsuyu, and Y. Sakabe, *IEEE transactions on ultrasonics, ferroelectrics, and frequency control* **54**, 2500 (2007).
- [162] M. Brazier, S. Mansour, and M. McElfresh, *Applied Physics Letters* **74**, 4032 (1999).
- [163] B. Ducharne, D. Guyomar, and G. Sebald, *Journal of Physics D: Applied Physics* **40**, 551 (2007).

- [164] G. Peng, J. Yu, Y. Wang, L. Wang, and J. Li, *Integrated Ferroelectrics* **89**, 45 (2007).
- [165] Y. Kadota and T. Morita, *Japanese Journal of Applied Physics* **51**, 09LE08 (2012).
- [166] H. Ikeda, Y. Kadota, and T. Morita, *Japanese Journal of Applied Physics* **51**, 09MD01 (2012).
- [167] W. Zhang and K. Bhattacharya, *Acta Materialia* **53**, 185 (2005).
- [168] S. Fan, *Nature Science Journal of Hainan Teachers College* **2**, 91 (1989).
- [169] Y. Doshida, H. Hashimoto, Y. Mizuno, and H. Tamura, *Ceramics International* **39**, S721 (2013).
- [170] C. M. Landis, *Current Opinion in Solid State and Materials Science* **8**, 59 (2004).
- [171] S. C. Hwang, J. E. Huber, R. M. McMeeking, and N. A. Fleck, *Journal of Applied Physics* **84**, 1530 (1998).